5-2018

Synthetically Guided Investigation of Lanthanide and Actinide Redox and Bonding Properties

Scott A. Pattenaude
Purdue University

Recommended Citation

Pattenaude, Scott A., "Synthetically Guided Investigation of Lanthanide and Actinide Redox and Bonding Properties" (2018). *Open Access Dissertations*. 1789.
https://docs.lib.purdue.edu/open_access_dissertations/1789

SYNTHETICALLY GUIDED INVESTIGATION OF LANTHANIDE AND ACTINIDE REDOX AND BONDING PROPERTIES

by

Scott A. Pattenaude

A Dissertation

Submitted to the Faculty of Purdue University
In Partial Fulfillment of the Requirements for the degree of

Doctor of Philosophy

Department of Chemistry
West Lafayette, Indiana
May 2018

THE PURDUE UNIVERSITY GRADUATE SCHOOL
STATEMENT OF COMMITTEE APPROVAL

Dr. Suzanne C. Bart, Chair
Department of Chemistry
Dr. Jonathan Wilker
Department of Chemistry
Dr. Jianguo Mei
Department of Chemistry
Dr. David R. McMillin
Department of Chemistry

Approved by:
Dr. Christina A. Hrycyna
Head of the Graduate Program

ACKNOWLEDGMENTS

I have a lot of people to thank for my success. I would first like to thank my wife, Shannon. You have always been patient and supportive of my goals, even as you went through similar struggles of graduate school. We have truly been a team, and I couldn’t have done this without you, Maggie, Pasha, and Rex by my side. Actually, it probably would have been easier without the doggies, but they have been fun to have around, and I wouldn’t have had it any other way. I look forward to the next chapter of our life together, and am excited to start a family with you.

I next want to thank my wonderful advisor, Suzanne Bart. I’m really glad that I decided to switch into inorganic chemistry and take a chance to do some really unique chemistry in your lab. I don’t think I could have made a better decision. You have gone out of your way to support me and have been largely instrumental in my success. You have given me so many opportunities for success, from my diverse projects to the chance to collaborate with a variety of other research groups. You have truly been my biggest fan.

Some of the most unique experiences that I had during graduate school were my summers working at Los Alamos National Laboratory with Andrew Gaunt. I am really appreciative of the trust you had in me during my time there. Your selfless desire to give the younger generation experiences like that for the betterment of the field is inspiring. Most people don’t see the sacrifices and hard work you put in to support these students, but I do and I couldn’t be more thankful to have worked with you.

I want to thank all of the current and former Bart group members: Nick Anderson, John Kiernicki, Sara Johnson, Chris Clark, Kristen Gettys, Shane Galley, Caleb Tatebe, Ezra Coughlin, Eve Martinez, Adharsh Raghavan, Aria Bredt, and Tyler Collins. The group mentality of the Bart group was central to my success, and daily interactions with each and every one of you were valuable to me. I want to give particular thanks to Nick and John; you were both important mentors to me when I started in the Bart Group. You guys taught me that you could work hard and still “have a good time” if you were excited about your research. (By the way John, it only took me two pens to complete my Ph.D.) Also thank you Ezra for sharing an office with me and teaching me patience and modesty in my own research. You were never afraid to give me constructive criticism and never seemed to be intimidated by new techniques. I would also like to thank my

undergraduate students Chris Kuehner and Logan Cook. I’m excited to see what the future holds for both of you.

I also couldn’t have done any of this without the instrumentation support at Purdue. This includes Phil Fanwick (X-ray), Matt Zeller (X-ray), John Harwood (NMR), Hartmut Hedderich (Raman), and Pat Bishop (Research Instrumentation Center). Matt, your work in renovating the X-ray facility has been extremely beneficial to our group, and you have added significantly to the impact of our work, not to mention make it more enjoyable.

Also adding to the significance of my work was the group of collaborators that had my back. This includes Eric Schelter, Walter Dorfner, Kimberly Mullane, and Yusen Qiao who ran magnetism on my samples; Tom Albrecht-Schmitt and Shane Galley who did transuranic chemistry with us; Laura Gagliardi and Carlo Alberto Gaggioli who did computation for us; and Stosh Kozimor, Maryline Ferrier, Ben Stein, Sharon Bone, and Juan Lezama Pacheco who were all a part of the XAS dream team.

I would also like to thank my committee members Jon Wilker, Jianguo Mei, and Dave McMillin (and Suzanne). Special thanks to Suzanne, Dave, Andy Gaunt, Tom Albrecht-Schmitt, and Matt Zeller for writing letters of recommendation on my behalf. Also, thank you Dave for allowing me to TA your classes with you.

I need to especially thank my parents Jim and Kathy who have been exceptionally supportive during this long journey. Thank you both for your support and help through undergrad, and thanks for being patient with me.

Finally, I’d like to thank the funding agencies that have allowed me to do my work. Special thanks to Purdue University, the Department of Energy (award number DE-SC0008479), the Center for Actinide Science and Technology (an Energy Frontier Research Center funded by the U.S. Department of Energy; award number DE-SC0016568), and the Seaborg Institute at Los Alamos National Laboratory.

TABLE OF CONTENTS

LIST OF TABLES

LIST OF FIGURES

LIST OF SCHEMES

ABSTRACT

Author: Pattenaude, Scott, A. PhD
Institution: Purdue University
Degree Received: May 2018
Title: Synthetically Guided Investigation of Lanthanide and Actinide Redox and Bonding Properties
Committee Chair: Suzanne Bart

The complex bonding and redox properties of actinide elements are much less understood compared to common main group and transition metal elements. This is likely the result of fewer chemical studies, due to the challenges of working with these radioactive elements. Nevertheless, understanding the chemical behavior of these elements, and how they differ from the lanthanide series, is crucial for nuclear materials processing and waste management.

Along these lines, the first chapter discusses the interactions of an ONO-chelating redox-active ligand with uranium. Uranium derivatives of a dioxophenoxazine ligand, $(DOPO^{q})_2UO_2$, $(DOPO^{sq})UI_2(THF)_2$, $(DOPO^{cat})UI(THF)_2$, and $Cp^*U(DOPO^{cat})(THF)_2$ (DOPO = 2,4,6,8-tetra-*tert*-butyl-1-oxo-1*H*-phenoxazin-9-olate), have been synthesized from U(VI) and U(III) starting materials. Full characterization of these species show uranium complexes bearing ligands in three different oxidation states. The electronic structures of these complexes have been explored using ^{1}H NMR and electronic absorption spectroscopies, and where possible, X-ray crystallography and SQUID magnetometry.

The second chapter describes the stability imparted by this dioxophenoxazine ligand in the formation of tris(DOPO) complexes. This chapter involves the discussion of the first non-aqueous isostructural series of coordination compounds for members across the *f*-block, including thorium uranium, plutonium, americium, berkelium, and californium, which is the broadest, most well-studied series of trivalent metals known. While californium would be expected to show purely electrostatic contributions to bonding due to its location in the series, spectroscopic, structural, and computational analyses shows higher degrees of covalent bonding compared to its neighbors to the left. This work provides a greater understanding of bonding between organic ligands and actinides, which can aid in the design of new ligands for encapsulation and separation of metals at the bottom of the periodic table.

The third chapter addresses subtle electronic characteristics associated with redox-active ligand uranium complexes. Uranium complexes ($(^{Mes}DAE)_2U(THF)$ (**1-DAE**) and $Cp_2U(^{Mes}DAE)$ (**2-DAE**), bearing redox-innocent α-diamine ligands, have been synthesized and characterized for a full comparison with previously published, redox-active α-diamine complexes, $(^{Mes}DAB^{Me})_2U(THF)$ (**1-DAB**) and $Cp_2U(^{Mes}DAB^{Me})$ (**2-DAB**). These redox-innocent analogues maintain a similar steric environment to their redox-active ligand counterparts to facilitate a study aimed at determining the differing electronic behavior around the uranium center. Structural analysis by X-ray crystallography showed **1-DAE** and **2-DAE** have a very similar structural environment to **1-DAB** and **2-DAB,** respectively. The main difference occurs with coordination of the ene-backbone to the uranium center in the latter species. Electronic absorption spectroscopy reveals these new DAE complexes are nearly identical to each other. X-ray absorption spectroscopy of all four species notes that there is a significant difference between the bis(diamide)-THF uranium complexes as opposed to those that only contain one diamide and two cyclopentadienyl rings, but there is little difference in valency between the two ligand systems. Finally, magnetic measurements reveal that all complexes display temperature dependent behavior consist with uranium(IV) ions that are not supported by ligand radicals. Overall, this study determines that there is no significant bonding difference between the redox-innocent and redox-active ligand frameworks on uranium. Furthermore, there is no data to suggest covalent bonding character using the latter ligand framework on uranium, despite what is known for transition metals.

The fourth chapter describes the synthesis of redox-active pyridine(diimine) (PDI) lanthanide complexes with an aim to bring redox activity to the notoriously redox non active metal centers. A full reduction series of the $^{Mes}PDI^{Me}$ ligated to neodymium was accomplished using $NdI_3(THF)_{3.5}$ as a starting material. This series included the three electron reduced dimer, $[^{Mes}PDI^{Me}Nd(THF)]_2$, which is an interesting structural analogue to known uranium compounds. Also, this dimer has demonstrated high reactivity towards a variety of substrates, making it an exciting platform with which to explore redox chemistry at a lanthanide center.

The fifth chapter describes the synthesis and reactivity of new uranyl complexes containing novel alkyl amide ligands. New uranyl derivatives featuring the amide ligand, $-N(SiHMe_2)^tBu$, were synthesized and characterized by X-ray crystallography, multinuclear NMR spectroscopy, and absorption spectroscopies. Steric properties of these complexes were also quantified using the computational program Solid-G. The increased basicity of the free ligand -$N(SiHMe_2)^tBu$ was demonstrated by direct comparison to -$N(SiMe_3)_2$, a popular supporting ligand for uranyl. Substitutional lability on a uranyl center was also demonstrated by exchange with the -$N(SiMe_3)_2$ ligand. Reactions of these complexes with substituted anilines promotes new reactivity, and sets the ground work for the isolation of a uranyl imido.

Finally, the sixth chapter discusses the development of new molecular neptunium halide complexes that can be used as an entry into nonaqueous chemistry. Solvent exchange of $NpCl_4(DME)_2$ with THF yielded the THF adduct, $NpCl_4(THF)_3$, whereas $PuCl_4(DME)_2$ appears to be unstable in THF, partially decomposing through disproportionation to the mixed valent plutonium salt, $[PuCl_2(THF)_5][PuCl_5(THF)]$. Reduction of $NpCl_4(THF)_3$ led to the isolation and structural and spectroscopic characterization of $NpCl_3(py)_4$, which is a rare example of a trivalent neptunium halide that was sourced from neptunium oxides rather than Np^0.

CHAPTER 1. SYNTHESIS, CHARACTERIZATION, AND REACTIVITY OF HETEROLEPTIC DIOXOPHENOXAZINE COMPLEXES

Adapted with permission from Pattenaude, S. A.; Kuehner, C. S.; Dorfner, W. L.; Schelter, E. J.; Fanwick, P. E.; Bart, S. C. *Inorg. Chem.*, **2015**, *54* (13), 6520-6527. Copyright 2015 American Chemical Society.

1.1 Introduction

With the recent activity aimed towards understanding redox non-innocent ligands and their cooperative participation in metal mediated transformations has emerged new ligand frameworks to be tested.[1,2] One such class is dioxophenoxazine ligands (DOPO), which has recently been synthesized[3] and studied with transition metals.[4,5] These ligands are an improvement over the related 3,5-di-*tert*-butyl-1,2-quinone-1-(2-oxy-3,5-di-*tert*-butylphenyl)imine frameworks (ONO), as the DOPO class contains an additional ether linkage that introduces rigidity and prevents bending of the π-system needed for electron storage.[6–8] The DOPO ligands are stable in their monoanionic (quinone, $\mathrm{DOPO^{q}}$), dianionic (semiquinone, $\mathrm{DOPO^{sq}}$), and trianionic (catecholate, $\mathrm{DOPO^{cat}}$) forms, potentially serving to stabilize metals while still capable of mediating multi-electron processes (Scheme 1.1).

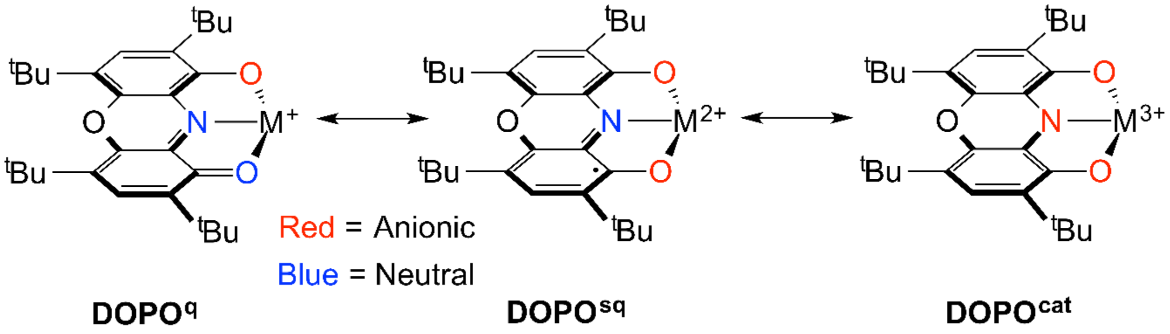

Scheme 1.1. Redox noninnocence of the DOPO ligand.

Recently, several studies have reported the utility of the bis(DOPO) ligand framework to support transition metals in a variety of oxidation states. Studies by Minkin and co-workers describe the synthesis of divalent, first-row transition metal bis(ligand) complexes, M(DOPO)$_2$ (M = Mn, Fe, Co, Ni, Cu, Zn), bearing the monoanionic DOPO^{q} form of the ligand.[5] The manganese, iron, and cobalt derivatives are all high spin, and it is hypothesized that the rigid DOPO framework prevents interconversion between the redox-isomeric forms of the complexes. More recently, Brown and co-workers have shown analogous hexavalent octahedral molybdenum and tungsten bis(ligand) species, supported by the fully reduced, trianionic form of the dioxophenoxazine ligand, DOPO^{cat}.[4] Interestingly, the chromium analogue shows an unusual electronic structure, with one ligand in the reduced semiquinone form, DOPO^{sq}, and the other in the oxidized DOPO^{q}, generating a C_{2v} symmetric chromium(III) species, Cr(DOPO^{q})(DOPO^{sq}). Despite this recent interest in the DOPO family of ligands, the ability of this framework to support f-block elements has not yet been explored.

The DOPO class of ligands is related to the iminoquinone (^{R}iq) /amidophenolate (^{R}ap) (iq = 4,6-di-*tert*-butyl-2-[(R)-iminoquinone)]; ap = 4,6-di-*tert*-butyl-2-[(R)-amidophenolate]; R = ^{t}Bu, Ad, dipp; Ad = 1-adamantyl, dipp = 2,6-diisopropylphenyl) family, which has recently been used to perform multi-electron oxidative addition[9] and reductive elimination on uranium.[10] For instance, the bidentate amidophenolate ligands in (^{R}ap)$_2$U(THF)$_2$ can mediate oxidative addition of chlorine or iodine at monomeric U(IV) complexes, where the two reducing equivalents necessary for bond cleavage are derived from the ligand. Thus, radical iminosemiquinone ligands (^{R}isq)) support the products from oxidative addition, dimeric [(^{R}isq)$_2$UCl]$_2$(μ-Cl)$_2$ and monomeric (^{R}isq)$_2$UI$_2$.[9] Alternately, radical reductive elimination of bibenzyl occurs from tetrabenzyluranium using the iminoquinone form of the ligand. These are subsequently reduced to generate the corresponding amidophenolate uranium dialkyls, (^{R}ap)U(CH$_2$Ph)$_2$.[10]

With this multi-electron chemistry at uranium established for similar redox-active ligands, exploration of the reactivity of uranium complexes with the DOPO ligand was sought. It was rationalized that it could be an improvement over the iminoquinone systems since it has an additional phenoxy substituent to make more robust tridentate uranium complexes with the potential to store up to three accessible electrons in the ligand (compared to two electrons in a fully reduced iminoquinone ligand). Of particular interest was how the addition of another oxygen chelate would affect the redox chemistry. Along these lines the DOPO ligand could be an improvement over other nitrogen based redox-active ligands that have been highly useful in facilitating new chemistry at uranium. One perhaps undesirable feature of these nitrogen based ligands (and also iminoquinone ligands) is that a neutral form of the ligand is accessible, which makes these ligand highly labile in the oxidized form. Upon deprotonation, the DOPO ligand is monoanionic in the most oxidized form, perhaps preventing ligand loss through competition with solvent binding. Initial experiments were aimed at isolating and characterizing uranium complexes in each available ligand oxidation state. This would establish a baseline for characterization of potential reactivity products.

1.2 Experimental

General Considerations. All air- and moisture-sensitive manipulations were performed using standard Schlenk techniques or in an MBraun inert atmosphere drybox with an atmosphere of purified nitrogen. The MBraun drybox was equipped with a cold well designed for freezing samples in liquid nitrogen as well as two -35 °C freezers for cooling samples and crystallizations. Solvents for sensitive manipulations were dried and deoxygenated using literature procedures with a Seca solvent purification system.[11] Benzene-d_6 and pyridine-d_5 were purchased from Cambridge Isotope Laboratories. Benzene-d_6 was dried with molecular sieves and sodium, and degassed by three freeze-pump-thaw cycles. Pyridine-d_5 was dried with molecular sieves and degassed by three freeze-pump-thaw cycles. 2,4,6,8-tetra-*tert*-butyl-9-hydroxy-1*H*-phenoxazin-1-one ($HDOPO^q$),[4] $UO_2[N(SiMe_3)_2]_2(THF)_2$,[12] KCH_2Ph,[13] potassium pentamethylcyclopentadienide (KCp*),[14] $UI_3(THF)_4$,[15,16] $UI_4(dioxane)_2$,[15] $UO_2I_2(THF)_3$,[17] $NdI_3(THF)_{3.5}$,[18] and KC_8[19] were prepared according to literature procedures.

^1H NMR spectra were recorded on a Varian Inova 300 spectrometer at 299.992 MHz. All chemical shifts are reported relative to the peak for $SiMe_4$, using ^1H (residual) chemical shifts of the solvent as a secondary standard. The spectra for paramagnetic molecules were obtained by using an acquisition time of 0.5 s; thus the peak widths reported have an error of ±2 Hz. For paramagnetic molecules, the ^1H NMR data are reported with the chemical shift, followed by the peak width at half height in Hertz, the integration value, and, where possible, the peak assignment. Elemental analyses were performed by Complete Analysis Laboratories, Inc., Parsippany, New Jersey. Electronic absorption measurements were recorded at 294 K in THF in sealed 1 cm quartz cuvettes with a Jasco V-6700 spectrophotometer. Infrared spectra were recorded using a PerkinElmer FT-IR Spectrum RX I spectrometer. Samples were made by crushing the solids, mixing with dry KBr, and pressing into a pellet.

Solid-state magnetic data were collected in collaboration with Eric Schelter at the University of Pennsylvania using a Quantum Design Multi-Property Measurement System (MPMS-7) warmed from 2–300 K and cooled from 300–2 K at 1 T and at 2 K from 0–7 T. Drinking straws were used to house the samples for measurement and were dried under a dynamic vacuum overnight before use in an inert atmosphere (N_2) drybox. While empty, the straws were crimped using a hot pair of tweezers to melt the straw together. The samples were added directly into the crimped straw and were massed to the nearest 0.1 mg using a calibrated and leveled Mettler-Toledo AL-204 analytical balance. Approximately 10.0 mg of quartz wool was added to the straw above the sample to hold it in place. The straw was then crimped above the sample with hot tweezers to complete the seal. The samples, contained in the sealed drinking straws for measurement, were transferred to the MPMS under inert atmosphere and immediately loaded into the inert atmosphere of the measurement chamber with three evacuation/purge cycles. Corrections for the intrinsic diamagnetism of the samples were made using Pascal's constants.[20]

The resonance Raman system was based on SpectraCode optical rail design. A Melles-Griot HeNe laser (632.8 nm, 25 mW) was used as an excitation source. The laser was coupled into a SpectraCode optical rail via an optical fiber. Semrock MaxLine® Laser-line and Stopline® Single-notch filters were used to select and guide the laser beam through an objective (Nikon 100x EPlan, Olympus 20x LMPlanFL and Mitutoyo 50x MPlan) to the sample. A video system was used to choose the sample area for data collection. Backscattered Raman photons were guided through a second fiber into an Acton Research SpectraPro 300i spectrograph (1200 g/mm grating). Spectra were collected as a solution in benzene-d_6 in a sealed cuvette between 300 and 1565 rel. cm^{-1} using Roper Scientific WinbSpec software.

Single crystals of $Cp^*U(DOPO^{cat})(THF)_2$, $(DOPO^{sq})UI_2(THF)_2$, and $(DOPO^{q})NdI_2(THF)_2$ for X-ray diffraction were coated with poly(isobutene) oil in a glovebox and quickly transferred to the goniometer head of a Nonius KappaCCD image plate diffractometer equipped with a graphite crystal, incident beam monochromator. Preliminary examination and data collection were performed with Mo Kα radiation ($\lambda = 0.71073$ Å). Single crystals of $(DOPO^{q})_2UO_2$, $(DOPO^{q})_2UI_2$, and $(DOPO^{sq})UO_2(OPPh_3)_2$ were coated with polybutenes oil in a glovebox and quickly transferred to the goniometer head of a Rigaku Rapid II image plate diffractometer equipped with a MicroMax002+ high intensity copper X-ray source with confocal optics. Preliminary examination and data collection were performed with Cu K_α radiation (λ = 1.54184 Å). Cell constants for data collection were obtained from least-squares refinement. The space group was identified using the program XPREP.[21] The structures were solved by direct methods using either SIR2004[22] or SHELXT.[21] Refinement was performed on a LINUX PC using SHELX-2013.[21] The data were collected at a temperature of either 150(1) K or 200(1) K.

Preparation of KDOPO^q(THF) (KDOPO^q = potassium 2,4,6,8-tetra-*tert*-butyl-1-oxo-1*H*-phenoxazin-9-olate). A 100 mL round bottom flask was charged with HDOPO^q (1.816 g, 4.15 mmol) and 30 mL of THF, and was cooled to -35 °C. An orange solution of KCH_2Ph (0.544 g, 4.15 mmol) in 15 mL of THF was also cooled to -35 °C and added dropwise to the HDOPO^q solution, causing a color change from violet to dark blue. After stirring for 1 hour the volatiles were removed *in vacuo* yielding a blue powder (quantitative yield) assigned as KDOPO^q(THF). Analysis for $C_{32}H_{46}KNO_4$: Calcd. C, 70.16; H, 8.46; N, 2.56. Found C, 69.99; H, 8.39; N, 2.76. ^1H NMR (C_6D_6, 25 °C): δ = 1.40 (m, 4H, THF-CH_2), 1.58 (br s, 36H, -C(CH_3)$_3$), 3.54 (m, 4H, THF-CH_2), 7.62 (s, 2H, Ar-C*H*).

Preparation of (DOPO^q)$_2$UO$_2$. A 20 mL scintillation vial was charged with $UO_2[N(SiMe_3)_2]_2(THF)_2$ (0.050 g, 0.069 mmol) and 5 mL of THF. This orange solution was stirred for 5 minutes before a solution of HDOPO^q (0.060 g, 0.138 mmol) in 5 mL of THF was added dropwise. The resulting green solution was stirred for 1 hour, then the volatiles were removed *in vacuo*. This green powder was taken up in 3 mL of pentane and stirred for 10 minutes. The solution was then cooled to -35 °C, causing precipitation of a dark-green powder. This was collected by filtration and assigned as (DOPO^q)$_2$UO$_2$ (0.068 g, 0.059 mmol, 86%). Green crystals suitable for X-ray analysis were grown by slow evaporation from toluene/THF (10:1) overnight at 25 °C. Analysis for $C_{56}H_{76}N_2O_8U$: Calcd. C, 58.83; H, 6.70; N, 2.45. Found C, 59.01; H, 6.77; N, 2.62. Raman (C_6D_6 , cm^{-1}) 843 (s, U=O symmetric stretch). IR (KBr pellet, cm^{-1}): 2958 (s), 1591 (w), 1498 (s), 1357 (s), 1290 (s), 1253 (s), 1203 (m), 1041 (w), 937 (w, U=O asymmetric stretch). ^1H NMR (C_6D_6, 25 °C): δ = 1.55 (s, 36H, -C(CH_3)$_3$), 1.93 (s, 36H, -C(CH_3)$_3$), 7.92 (s, 4H, Ar-C*H*).

Preparation of (DOPO^{sq})UI$_2$(THF)$_2$. A 20 mL scintillation vial was charged with UI$_3$(THF)$_4$ (0.083 g, 0.091 mmol) and KDOPO^q(THF) (0.050 g, 0.091 mmol). To this mixture, 8 mL of diethyl ether were added, and the resulting emerald green solution was stirred for 5 minutes before it was filtered over Celite. After removing volatiles *in vacuo*, an emerald green powder (0.097 g, 0.090 mmol, 99%) was collected and assigned as (DOPO^{sq})UI$_2$(THF)$_2$. Green crystals suitable for X-ray analysis were grown by slow evaporation from pentane/toluene (5:1) overnight at 25°C. Analysis for $C_{36}H_{54}I_2NO_5U$: Calcd. C, 40.31; H, 5.07; N, 1.31. Found C, 40.47; H, 5.17; N, 1.47. ^{1}H NMR (C_6D_6, 25 °C): δ = -248.69 (141, 2H, Ar-CH), -5.38 (9, 18H, -C(CH_3)$_3$), 37.66 (19, 18H, -C(CH_3)$_3$).

Preparation of (DOPO^{cat})UI(THF)$_2$. A 20 mL scintillation vial was charged with UI$_3$(THF)$_4$ (0.248 g, 0.273 mmol) and KDOPO^q(THF) (0.150 g, 0.274 mmol). To this mixture, 15 mL of diethyl ether were added, and the resulting emerald green solution was stirred for 15 minutes before it was cooled to -35 °C. A suspension of KC$_8$ (0.033 g, 0.244 mmol) in 5 mL of ether was also cooled to -35 °C and was added to the emerald green solution dropwise, yielding a dark green solution. After stirring for 15 minutes, the resulting brown solution was filtered over Celite. Upon removal of volatiles *in vacuo*, a yellow-brown powder was collected (0.240 g, 0.253 mmol, 93%) and assigned as (DOPO^{cat})UI(THF)$_2$. To obtain analytically pure sample the compound was taken up in 10 mL of pentane and stirred for 10 minutes. This solution was cooled to -35 °C and then filtered. Upon removal of volatiles *in vacuo*, a yellow-brown powder was collected (0.105 g, 0.111 mmol, 41%). Analysis for $C_{36}H_{54}INO_5U$: Calcd. C, 45.72; H, 5.76; N, 1.48. Found C, 45.67; H, 5.60; N, 1.59. ^{1}H NMR (C_6D_6, 25 °C): δ = -1.73 (4, 18H, -C(CH_3)$_3$), 15.99 (5, 2H, Ar-CH), 36.32 (6, 18H, -C(CH_3)$_3$).

Alternative Preparation of (DOPO^{cat})UI(THF)$_2$. A 20 mL scintillation vial was charged with (DOPO^{sq})UI$_2$(THF)$_2$ (0.050 g, 0.047 mmol) and 15 mL of diethyl ether. This solution was cooled to -35 °C before KC$_8$ (0.006 g, 0.047 mmol) was added as a solid. After stirring for 15 minutes, the resulting brown solution was filtered over Celite. Upon removal of volatiles *in vacuo*, a yellow-brown powder was collected (0.038 g, 0.035 mmol, 74%) and assigned as (DOPO^{cat})UI(THF)$_2$ based on ^{1}H NMR spectroscopic data.

Preparation of Cp*U(DOPO^{cat})(THF)$_2$. A 20 mL scintillation vial was charged with UI$_3$(THF)$_4$ (0.300 g, 0.331 mmol), KCp* (0.058 g, 0.331 mmol), and 8 mL of THF. This blue solution was stirred for 3 hours before a solution of KDOPO^q(THF) (0.181 g, 0.331 mmol) in 6 mL of THF was slowly added. After stirring for one minute, KC_8 (0.045 g, 0.331 mmol) was added quickly as a solid. This brown solution was stirred for 1 hour then filtered over Celite. After removing volatiles *in vacuo*, a brown powder (0.272 g, 0.285 mmol, 86%) was collected and assigned as $Cp^*U(DOPO^{cat})(THF)_2$. Brown crystals suitable for X-ray analysis were grown by slow evaporation from pentane overnight at -35 °C. Analysis for $C_{46}H_{69}NO_5U$: Calcd. C, 57.91; H, 7.29; N, 1.47. Found C, 57.76; H, 7.4; N, 1.63. ^1H NMR (C_6D_6, 25 °C): δ = -65.83 (7, 8H, THF-CH_2), -20.10 (3, 18H, -C(CH_3)$_3$), -9.70 (13, 8H, THF-CH_2), 7.20 (4, 15H, Cp*-CH_3), 7.57 (4, 2H, Ar-C*H*), 16.52 (4, 18H, -C(CH_3)$_3$).

Conditions that resulted in isolation of $(DOPO^q)_2UI_2$. A 20 mL scintillation vial was charged with $KDOPO^q(THF)$ (0.100 g, 0.183 mmol) and diethyl ether, forming a dark blue solution. A large excess of KC_8 (0.080 g, 0.593 mmol) was added causing a color change to translucent yellow with dark solid. This yellow solution was filtered directly into an orange solution of $UI_4(dioxane)_2$ (0.168 g, 0.182 mmol) in diethyl ether, causing a color change to yellow-brown. This solution was filtered and concentrated *in vacuo* to yield a dark yellow-brown powder. Analysis by ^1H NMR yielded no tractable products. Yellow single crystals were grown from a concentrated diethyl ether solution at -35°C. Instead of the desired product, $(DOPO^{cat})UI(Et_2O)_n$, analysis of the crystal by X-ray diffraction revealed the structure was $(DOPO^q)_2UI_2$.

Preparation of $(DOPO^q)NdI_2(THF)_2$. A 20 mL scintillation vial was charged with $NdI_3(THF)_{3.5}$ (0.140 g, 0.180 mmol). The blue-grey solid was suspended in THF and cooled to -35 °C. Another vial was charged with $KDOPO^q(THF)$ (0.100 g, 0.183 mmol) and THF, forming a dark blue solution. This solution was also cooled to -35 °C. After cooled, this solution was added slowly to the $NdI_3(THF)_{3.5}$ suspension, resulting in little change to the solution color. The white precipitate (KI) was filtered off, and the resulting blue solution was concentrated *in vacuo*, resulting in a blue powder assigned as $(DOPO^q)NdI_2(THF)_2$. It should be noted that when dissolved in benzene, the solution appears green. Single crystals suitable for X-ray analysis were grown from the slow evaporation of a concentrated diethyl ether solution at -35 °C. ^1H NMR (C_6D_6, 25 °C): δ = 2.78 (3, 18H, -C(CH_3)$_3$), 9.83 (7, 18H, -C(CH_3)$_3$), 14.60 (4, 2H, Ar-C*H*).

Preparation of $(DOPO^q)UO_2[N(SiMe_3)_2]$. A 20 mL scintillation vial was charged with $(DOPO^q)_2UO_2$ (0.050 g, 0.044 mmol) and 5 mL of THF. A solution of $UO_2[N(SiMe_3)_2]_2(THF)_2$ (0.031 g, 0.044 mmol) in 5 mL of THF was slowly added to the stirring solution of $(DOPO^q)_2UO_2$ resulting in a green solution. After stirring for 24 hours, the volatiles were removed *in vacuo* resulting in a green powder (0.073 g, 0.084 mmol, 96%) that was assigned as (DOPO^q)UO$_2$[N(SiMe$_3$)$_2$]. ^{1}H NMR (C$_6$D$_6$, 25 °C): δ = 0.89 (2, 18H, SiC*H*$_3$), 1.41 (2, 18H, -C(C*H*$_3$)$_3$), 1.73 (3, 18H, -C(C*H*$_3$)$_3$), 7.87 (3, 2H, Ar-C*H*).

Preparation of (DOPO^q)UO$_2$I(THF). A 20 mL scintillation vial was charged with (DOPO^q)$_2$UO$_2$ (0.012 g, 0.010 mmol) and 5 mL of THF. A solution of UO$_2$I$_2$(THF)$_3$ (0.008 g, 0.011 mmol) in 5 mL of THF was slowly added to the stirring solution of (DOPO^q)$_2$UO$_2$ resulting in a lime-green solution. After stirring for 24 hours, the volatiles were removed *in vacuo* resulting in a green powder in quantitative yield that was assigned as (DOPO^q)UO$_2$I(THF). Green crystals suitable for X-ray analysis were grown from a concentrated diethyl ether solution overnight at -35°C. Analysis of crystals revealed that the THF ligand exchanged with an ether ligand, resulting in the formula (DOPO^q)UO$_2$I(Et$_2$O). Analysis for C$_{32}$H$_{46}$INO$_6$U: Calcd. C, 42.44; H, 5.12; N, 1.55. Found C, 42.19; H, 4.96; N, 1.31. ^{1}H NMR (C$_6$D$_6$, 25 °C): δ = 1.35 (3, 9H, -C(C*H*$_3$)$_3$), 1.42 (3, 9H, -C(C*H*$_3$)$_3$), 1.64 (4, 9H, -C(C*H*$_3$)$_3$), 1.75 (4, 9H, -C(C*H*$_3$)$_3$), 3.90 (49, 4H, THF-C*H*$_2$), 5.01 (18, 4H, THF-C*H*$_2$), 7.87 (4, 1H, Ar-C*H*), 7.94 (4, 1H, Ar-C*H*).

Preparation of (DOPO^{sq})UO$_2$(THF)$_n$. A 20 mL scintillation vial was charged with (DOPO^q)UO$_2$I(THF) (0.025 g, 0.028 mmol) and 5 mL of THF. KC$_8$ (0.004 g, 0.030 mmol) was added as a solid, resulting in no color change to the green solution. After stirring for one hour, the solution was filtered (to remove graphite and KI) and concentrated *in vacuo* to a dull green powder. No resonances are observed in the ^{1}H NMR spectrum for this product, but the formula is hypothesized to be (DOPO^{sq})UO$_2$(THF)$_n$. Single crystals of the related complex (DOPO^{sq})UO$_2$(OPPh$_3$)$_2$ were grown from an ether solution layered with toluene at -35 °C.

1.3 Results and Discussion

1.3.1 Isolation of Uranium Complexes with Each Ligand Oxidation State

Studies commenced with the synthesis of the protonated DOPO^q ligand, HDOPO^q, which was accomplished using a recently improved procedure[4] that differs from the initial synthesis.[3] For the synthesis, 3,5-di-*tert*-butylcatechol and 2,6-dihydroxy-3,5-di-tert-butylaniline were stirred in benzene overnight with a catalytic amount of triethylamine. This new synthesis differs only by the addition of a catalytic amount of triethylamine, and, though this synthesis is rather straight forward, the yield is quite modest (25%). If $HDOPO^q$ were to be viable as a ligand, an efficient synthesis with respectable yield must be attainable. Much of this initial work involved analysis of possible mechanisms for this transformations in order to improve the yield.

First, it was observed that the reaction did not yield any desired product when performed under an inert atmosphere. This signified that molecular oxygen was a necessary oxidant in this reaction. However, addition of dry oxygen bubbled through the reaction did not affect the yield of the reaction. Also, addition of 2,3-dichloro-5,6-dicyano-1,4-benzoquinone (DDQ) as an internal oxidant yielded no product, which was assumed to be the result of over oxidation. Alternatively, it was hypothesized that instead of oxygen in the air, it could be moisture that is involved in the reaction. It was found that addition of water to the reaction yielded no product, yet performing the reaction over sodium sulfate as a drying agent had no effect on the yield. In general, many conditions were attempted including varying the solvent, reaction time, and the addition of various acids/bases with no improvement in yield. Ultimately, since the starting materials were cheap and the synthesis was not time restrictive, the published procedure was simply scaled up to attain a moderate amount of $HDOPO^q$ for initial metallation and reactivity studies.

Deprotonation of purple $HDOPO^q$ was accomplished using benzylpotassium at -35 ˚C and confirmed by ^1H NMR spectroscopy (benzene-*d*$_6$), which showed overlapping resonances for the two *tert*-butyl groups at 1.58 ppm and signals for the aryl-C*H* at 7.62 ppm. Two additional resonances (4H each) signify a coordinated THF molecule, making the overall formula, $KDOPO^q(THF)$.

With the protonated and potassiated forms of the ligand in hand, uranium complexes that feature the DOPO ligand in each of its possible oxidation states were planned. To generate a uranium complex with the most oxidized form of the ligand, $DOPO^q$, a bis(ligand) uranyl species was targeted. In this case, there are no additional electrons on uranium that can reduce the ligand, thus eliminating ambiguity of ligand oxidation states. Treating an orange toluene solution of $UO_2[N(SiMe_3)_2]_2(THF)_2$[12] with two equivalents of $HDOPO^q$ resulted in a color change to emerald green (Scheme 1.2). Concentration of this solution facilitated precipitation of a dark green powder assigned as $(DOPO^q)_2UO_2$ in high yield (86%).

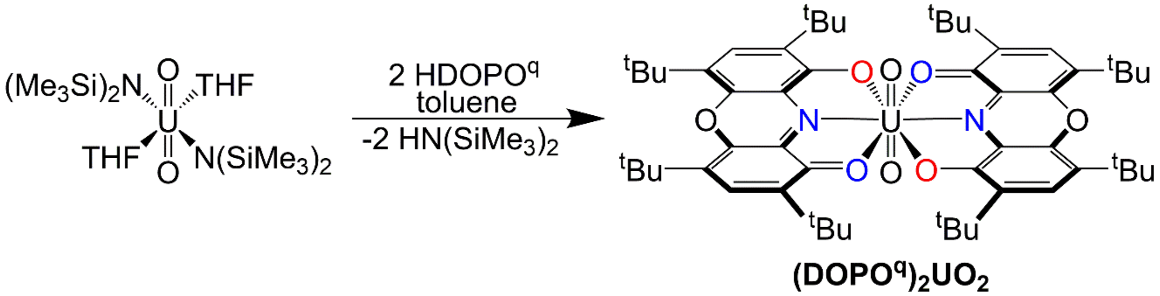

Scheme 1.2. Synthesis of $(DOPO^q)_2UO_2$.

Characterization of $(DOPO^q)_2UO_2$ by ^1H NMR spectroscopy shows a spectrum consistent with a diamagnetic, D_{2h} symmetric molecule. Two resonances (36H each) for *tert*-butyl groups are visible at 1.55 and 1.93 ppm, as well as a signal for the aryl-C*H* at 7.92 ppm (4H). Vibrational spectroscopic data supports a U(VI) center in $(DOPO^q)_2UO_2$, with a U=O absorption at 843 cm^{-1} for the symmetric stretch (Raman) as well as one at 937 cm^{-1} for the asymmetric stretch (infrared). These data are as expected based on other uranyl compounds.[23]

In order to provide baseline structural parameters for the $DOPO^q$ ligand, a single crystal of $(DOPO^q)_2UO_2$ was grown from slow evaporation of a concentrated toluene/THF solution (10:1) at 25 °C and analyzed by X-ray crystallography (Figure 1.1, bond distances in Figure 1.2). Refinement of the data confirmed the assignment of $(DOPO^q)_2UO_2$, showing a molecular structure with two $DOPO^q$ ligands *trans* to one another in the plane perpendicular to the uranyl moiety. The solid-state structure shows a pseudo-hexagonal bipyramidal uranium center, with some distortions from planarity in the $DOPO^q$ ligands. This distortion likely relieves steric strain from the *tert*-butyl groups on the *trans* $DOPO^q$ ligand. The uranyl U-O bonds of 1.765(4) and 1.768(5) Å are as expected for other uranyl species, including the starting material, $UO_2[N(SiMe_3)_2]_2(THF)_2$.[24]

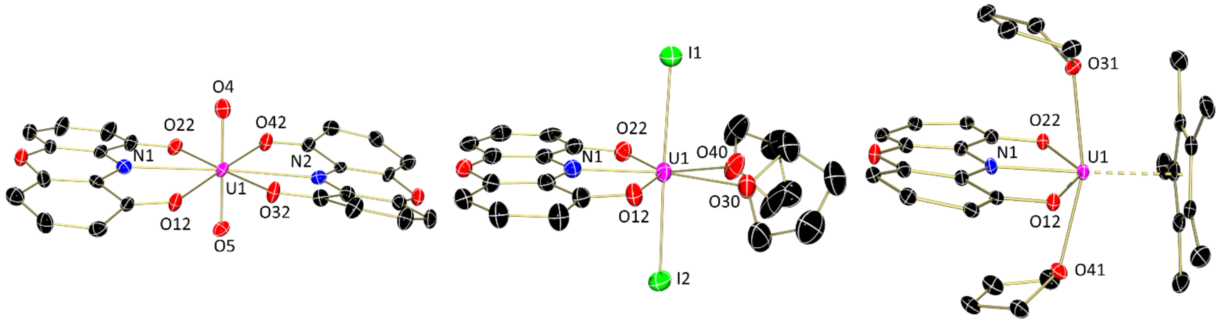

Figure 1.1. Molecular structures of $(DOPO^{q})_2UO_2$ (left), $(DOPO^{sq})UI_2(THF)_2$ (center), and $Cp^*U(DOPO^{cat})(THF)_2$ (right) shown at 30% probability ellipsoids. Hydrogen atoms, *tert*-butyl groups, and cocrystallized solvent molecules have been omitted for clarity.

Previous work has demonstrated that uranium-ligand distances are an accurate gauge for determining the extent of ligand reduction.[25–27] As shown in Scheme 1.1. Redox noninnocence of the DOPO ligand., the oxidized form of the ligand would have one monoanionic and one dative U-O interaction, which should be delocalized. Thus, the combination of the two resonance structures would produce U-O distances between anionic and dative bonds for uranium, which is observed. The U-O distances of 2.480(4) and 2.518(4) Å (Figure 1.2) are longer than a typical aryloxide ligand for uranium.[28] The U-N distance of 2.676(6) Å is quite long as compared to a uranium-amide; it is more consistent with a dative uranium-nitrogen bond, as would be expected for the oxidized $DOPO^{q}$ ligand.[28]

The intraligand parameters for $(DOPO^{q})_2UO_2$ (Figure 1.2) also support the DOPO ligand is in the quinone resonance form. For instance, the C-O distances of 1.273(7) and 1.261(7) Å are elongated from C=O double bonds due to the resonance contribution. Similarly, the C-N bond lengths of 1.335(7) and 1.344(7) Å are the same within error. These parameters are on the order of those observed for $Pb(DOPO^{q})_2$, which has C-O distances of 1.297(4) and 1.246(4) Å and C-N distances of 1.347(4) and 1.316(4) Å.[4] Similarly, Minkin reports values for $Mn(DOPO)_2$ through $Zn(DOPO)_2$ with C-O values that range from 1.266(2) – 1.294(5) Å and C-N distances from 1.315(1) – 1.333(5) Å.[5] These structural parameters measured for the ligands in $(DOPO^{q})_2UO_2$ were used to determine the metrical oxidation states (MOS) as established by Brown and co-workers for the DOPO ligand, which is useful due to the sensitivity of this method for the degree of π bonding in a molecule.[4] Applying that model to (DOPO^{q})$_2$UO$_2$ gave an MOS value of -1.25(19), which is consistent with other reports describing the quinone form of the ligand, including Pb(DOPO^{q})$_2$ (MOS = -1.06(15)).[4] Accordingly, the assignment of a hexavalent uranyl with two monoanionic, DOPO^{q} ligands is well supported by crystallographic and spectroscopic data.

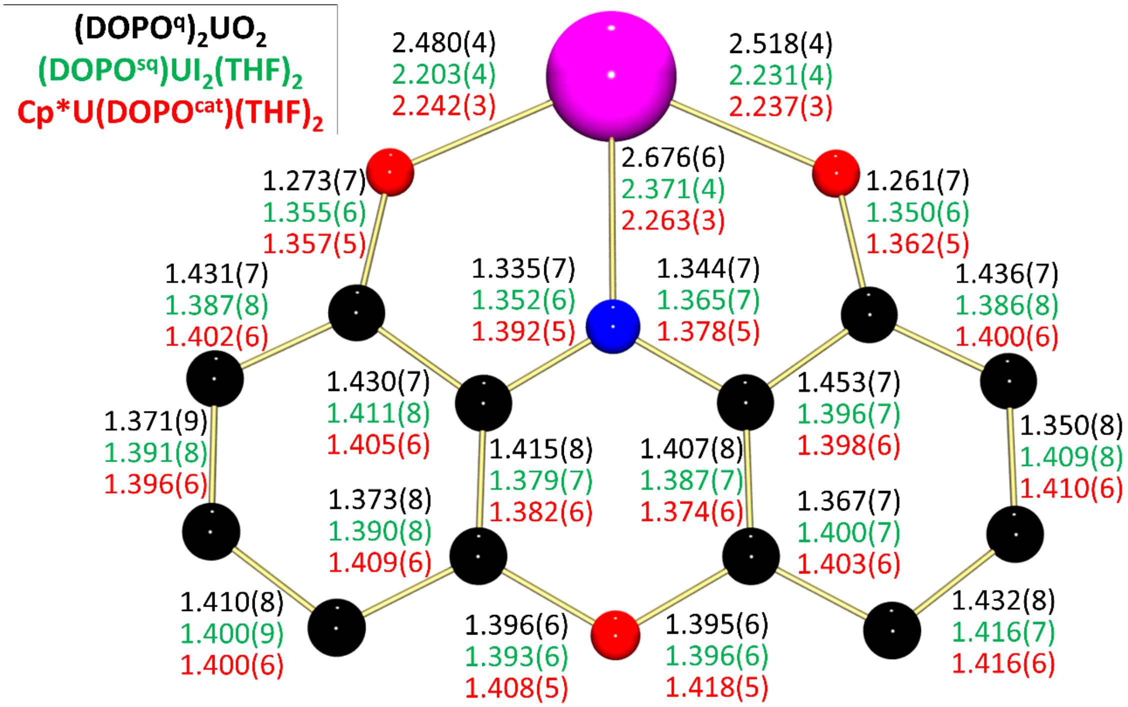

Figure 1.2. Bond distance comparison (Å) for (DOPO^{q})$_2$UO$_2$, (DOPO^{sq})UI$_2$(THF)$_2$, and Cp*U(DOPO^{cat})(THF)$_2$.

Low-valent derivatives of the DOPO ligand were also attempted by metallation with trivalent UI$_3$(THF)$_4$. Previously shown by the Bart group, treating UI$_3$(THF)$_4$ with the related iminoquinone ligand, ^{R}iq, resulted in electron transfer from the uranium to the ligand, forming the uranium(IV) iminosemiquinone product, (^{R}isq)UI$_3$(THF)$_2$ (R = dipp), as confirmed by magnetometry experiments.[10] In this case, addition of one equivalent of blue KDOPO^{q}(THF) to a blue diethyl ether suspension of UI$_3$(THF)$_4$ at -35 ˚C (Scheme 1.3) produced an emerald green powder following workup. Analysis by ^{1}H NMR spectroscopy shows a paramagnetically broadened and shifted spectrum, indicative of a C_{2v} symmetric molecule. Two resonances (18H each) for the *o*- and *p*-*tert*-butyl groups appear at -5.38 and 37.66 ppm, respectively, along with a smaller resonance (2H) shifted drastically to -248.69 ppm for the aryl-C*H* protons. This extreme upfield shift has been noted previously for uranium species bearing radical ligands,[27,29,30] leading to the assignment of the green product as (DOPO^{sq})UI$_2$, with a semiquinone radical ligand by analogy to (^{R}isq)UI$_3$(THF)$_2$.

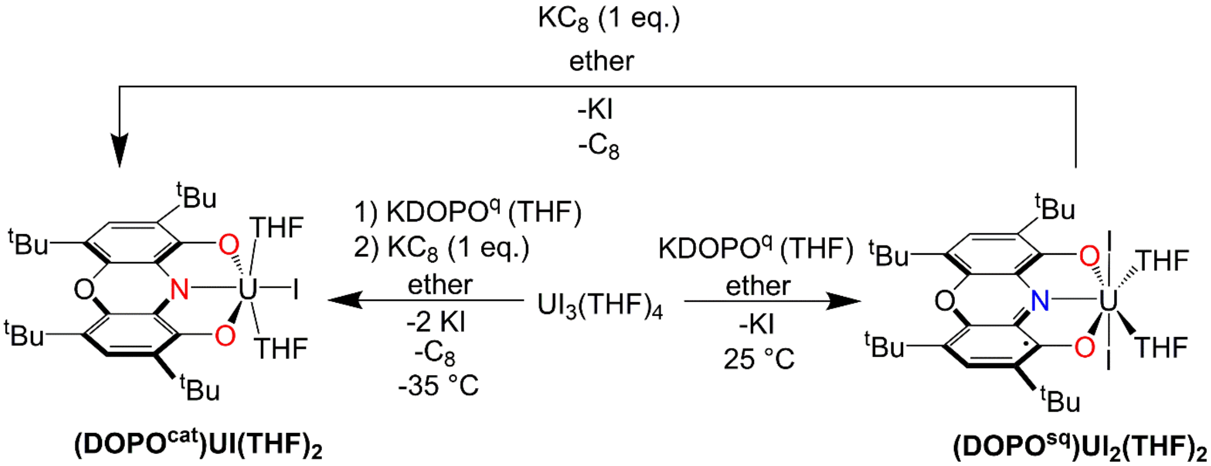

Scheme 1.3. Synthesis of low-valent DOPO complexes (DOPO^{sq})UI$_2$(THF)$_2$ and (DOPO^{cat})UI(THF)$_2$.

No THF resonances were noted in the ^{1}H NMR spectrum, likely due to dissociation/association of labile THF ligands on the NMR timescale. This hypothesis was tested by addition of pyridine-d_5 to an NMR tube containing a known amount of (DOPO^{sq})UI$_2$. Immediately, resonances for uncoordinated THF were apparent, indicating ligand substitution was operative. Quantification of the liberated THF was possible by integration against a mesitylene internal standard. This experiment established the presence of two equivalents of THF for each equivalent of (DOPO^{sq})UI$_2$, leading to the more accurate assignment of (DOPO^{sq})UI$_2$(THF)$_2$.

Confirmation for the assignment of (DOPO^{sq})UI$_2$(THF)$_2$ was obtained by X-ray diffraction of a single crystal grown from slow evaporation of a concentrated pentane solution with several drops of toluene at 25 °C. Refinement revealed a pentagonal bipyramidal uranium species with two iodide ligands and two THF molecules, in addition to the DOPO ligand (Figure 1.1, structural parameters in Figure 1.2). The idealized C_{2v} symmetry of $(DOPO^{sq})UI_2(THF)_2$ in the solid state is consistent with the solution structure as determined by ^1H NMR spectroscopy. The U-O distances of 2.203(4) and 2.231(4) Å are significantly contracted from those in $(DOPO^{q})_2UO_2$, pointing towards ligand reduction as indicated by the shorter U-O distance that is not expected for the larger uranium(IV) center. These distances are consistent with those for uranium(IV)-aryloxide interactions.[31] Accordingly, the U-N bond has also decreased (2.371(4) Å) displaying a distance that is intermediate of a U(IV)-amide and a U(IV)-amine.[27,31,32] The intraligand distances corroborate a higher degree of reduction as compared to $(DOPO^{q})_2UO_2$, with C-O distances (1.350(6) and 1.355(6) Å) that are elongated by ~0.1 Å, in agreement with single bond character that is expected for the iminosemiquinone resonance structure shown in Scheme 1.1. The corresponding C-N bonds are very similar to those in $(DOPO^{q})_2UO_2$, showing that they are less sensitive to ligand oxidation state changes. Accordingly, the semiquinone ligand in $Cr(DOPO^{q})(DOPO^{sq})$ has respective C-O and C-N averages of 1.335(2) and 1.349(2) Å. Thus, the ligand in **2** is most consistent with a U(IV) center ligated by a dianionic $DOPO^{sq}$ ligand. The calculated MOS value of -2.67(21) for the DOPO ligand in $(DOPO^{sq})UI_2(THF)_2$ suggests a higher degree of reduction in the ligand than predicted by the U-N and U-O distances. Based on the U(IV) assignment, the $U\text{-}O_{THF}$ and U-I distances are as expected compared to $UI_4(1,4\text{-dioxane})_2$.[15]

To further corroborate the presence of the iminosemiquinone in $(DOPO^{sq})UI_2(THF)_2$, self-consistent solid-state magnetic measurements of two independently prepared, analytically pure samples were made (Figure 1.3) in collaboration with Eric Schelter at the University of Pennsylvania. The low temperature effective magnetic moment of $(DOPO^{sq})UI_2(THF)_2$ was determined to be 1.81 μ_B (2 K), which was close to the expected spin-only moment predicted for a ligand based doublet, 1.73 μ_B, assuming g = 2.0.[33] The U(IV) ion is well-established to have a singlet ground state in low symmetry ligand fields.[34] The assignment of a magnetic singlet U(IV) ion and ligand-based doublet for $(DOPO^{sq})UI_2(THF)_2$ is consistent with the low temperature moment. Field-dependent data were measured at 2 K and achieved a limit at 0.79 μ_B at 7 T, which also supported assignment of a single ligand-based unpaired electron per molecule.

Overall the magnetic measurements were consistent with a configuration of (DOPO^{sq})UI$_2$(THF)$_2$ comprising S = ½ DOPO$^{sq\bullet}$ radical and a 5f^2 U(IV) singlet at low temperature: (DOPO^{sq})$^\bullet$-U(IV).

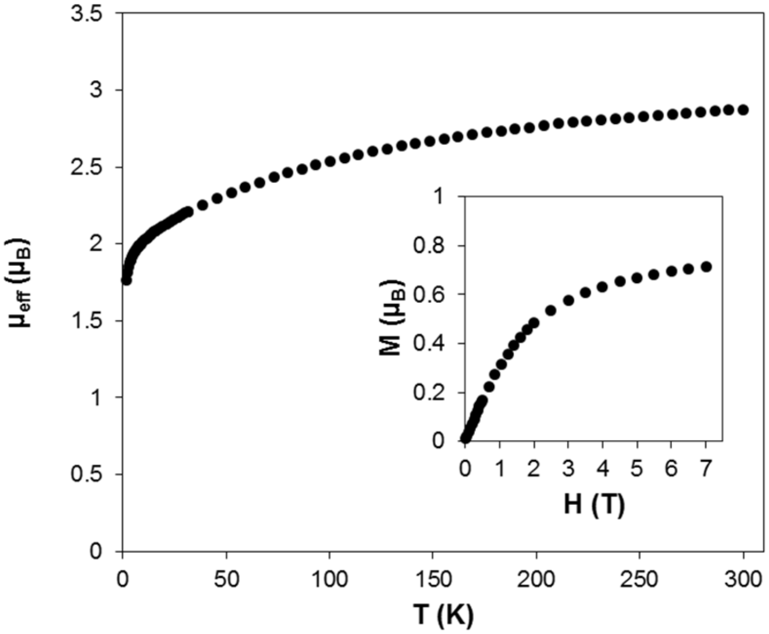

Figure 1.3. Variable temperature molar magnetic data for (DOPO^{sq})UI$_2$(THF)$_2$ between 300 and 2 K at 1 T. The inset is a plot of variable field data collected at 2 K.

Reduction of (DOPO^{sq})UI$_2$(THF)$_2$ was attempted to generate a uranium species bearing the most reduced form of the ligand, DOPO^{cat}. Performing the analogous reaction for the synthesis of (DOPO^{sq})UI$_2$(THF)$_2$ with an equivalent of potassium graphite (KC$_8$) afforded a yellow-brown powder (Scheme 1.3). As in the case for (DOPO^{sq})UI$_2$(THF)$_2$, ^{1}H NMR spectroscopic analysis showed a C_{2v} symmetric molecule with two resonances at -1.73 and 36.32 ppm for the *tert*-butyl groups on the ligand; however, in this case the C*H* protons for the DOPO aryl groups appeared at 15.99 ppm, indicating loss of radical character. With the addition of an external reductant, the product was assigned as (DOPO^{cat})UI bearing a triply reduced catecholate ligand. By charge balance considerations, a U(IV) ion is hypothesized.

No THF resonances were noted in the ^{1}H NMR spectrum for (DOPO^{cat})UI, again likely due to dissociation/association of labile THF ligands on the NMR timescale. Once again, addition of pyridine-d_5 to (DOPO^{cat})UI caused THF dissociation. Quantification by integration (mesitylene internal standard) showed two equivalents of THF were present for each equivalent of (DOPO^{cat})UI, thus the more accurate assignment is as (DOPO^{cat})UI(THF)$_2$. Compound (DOPO^{cat})UI(THF)$_2$ could also be generated by addition of KC$_8$ to (DOPO^{sq})UI$_2$(THF)$_2$ (Scheme 1.3). Unfortunately, difficulty in obtaining single crystals precluded characterization of (DOPO^{cat})UI(THF)$_2$ by X-ray diffraction.

To circumvent the crystallization issues for (DOPO^{cat})UI(THF)$_2$, the pentamethylcyclopentadienyl analogue, Cp*U(DOPO^{cat})(THF)$_2$, was synthesized. Addition of KDOPO^q(THF) to *in situ* generated Cp*UI$_2$(THF)$_3$,[35] followed immediately by one equivalent of KC$_8$ generated the desired product as a brown solid after workup (Scheme 1.4). Characterization by ^{1}H NMR spectroscopy showed a C_{2v} symmetric molecule, with resonances for the *tert*-butyl protons at -20.10 and 16.52 ppm, along with a resonance at 7.20 ppm assignable to the Cp*-CH_3 protons. The aryl-CH resonance appeared close to this at 7.57 ppm, which is also similar to that found for (DOPO^{cat})UI(THF)$_2$, again supporting the absence of a ligand radical.

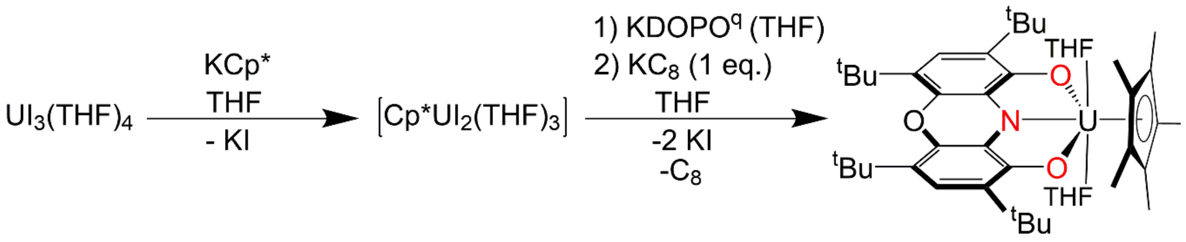

Cp*U(DOPO^{cat})(THF)$_2$

Scheme 1.4. Synthesis of Cp*U(DOPO^{cat})(THF)$_2$.

Brown crystals of Cp*U(DOPO^{cat})(THF)$_2$ were obtained from a concentrated pentane solution at -35 ˚C and analyzed by X-ray crystallography. The molecular structure features a uranium with the DOPO and Cp* ligands in a *trans* arrangement (Figure 1.1, structural parameters in Figure 1.2). Two THF molecules lie perpendicular to the DOPO ligand plane, and are *trans* with respect to each other. The solid state structure shows the THF rings are bent away from the Cp* ring, presumably relieving steric interactions. This is most likely a crystal packing effect, as inequivalency in the THF protons is not observed in the solution ^{1}H NMR spectrum. The U-Cp*$_{cent}$ distance of 2.493 Å is on the order for other U(IV)-Cp* complexes.[27,32,36] As in the case for (DOPO^{sq})UI$_2$(THF)$_2$, the U-O distances (2.237(3) and 2.242(3) Å) point to anionic uranium-oxygen bonds as would be expected for a reduced ligand framework. Divergent from (DOPO^{sq})UI$_2$(THF)$_2$, however, is the U-N distance of 2.263(3) Å, which is 0.1 Å shorter, and reflective of a uranium-amide linkage[32] resulting from a further degree of reduction. The intraligand C-O distances of 1.357(5) and 1.362(5) Å are indistinguishable from those in (DOPO^{sq})UI$_2$(THF)$_2$, once again supporting a reduced ligand. However, the C-N distance of 1.392(5) Å is statistically longer than those in (DOPO^{sq})UI$_2$(THF)$_2$, as would be consistent with C-N single bonds and consistent with the DOPO^{cat} resonance structure. The corresponding distances for Mo(DOPO^{cat})$_2$ and W(DOPO^{cat})$_2$, which have been established to contain trianionic catecholate ligands, have C-O average distances of 1.366(6) and 1.376(4) Å, respectively, which match well with those in Cp*U(DOPO^{cat})(THF)$_2$.[4] The average C-N distances for these transition metal analogues of 1.362(9) and 1.372(4) Å are within error of those for the uranium species, Cp*U(DOPO^{cat})(THF)$_2$. This structural support, along with the similar spectroscopic properties of (DOPO^{cat})UI(THF)$_2$ and Cp*U(DOPO^{cat})(THF)$_2$, point to a trianionic DOPO^{cat} ligand in both cases. This is supported by the value obtained for Cp*U(DOPO^{cat})(THF)$_2$ using the MOS model (-2.87(16)), which is on the order of those for Mo(DOPO^{cat})$_2$ (-2.83(23), -2.60(18)) and W(DOPO^{cat})$_2$ (-3.00(22), -2.80(19)).

Further confirmation for the oxidation states of the DOPO complexes was gathered using electronic absorption spectroscopy (Figure 1.4). Data in the UV-visible regions for the DOPO uranium series and KDOPO^q(THF) showed intense absorptions throughout the UV region, as has been noted previously.[4] Striking differences are found in the visible region, which shows an absorption for KDOPO^q(THF) at 735 nm with a high molar absorptivity (9,750 cm^{-1}M^{-1}) similar to what was observed for the corresponding sodium salt (λ_{max} = 695 nm).[3] For the uranium complexes, (DOPO^q)$_2$UO$_2$ shows a strong π-π* absorption at 719 nm with a high molar absorptivity (14,400 cm^{-1}M^{-1}). This large absorbance is characteristic of a transition into an empty DOPO^q -based π* orbital. For compound (DOPO^{sq})UI$_2$(THF)$_2$, there is a much weaker (ε = 874 cm^{-1}M^{-1}) π-π* absorption noted at 704 nm, consistent with the half-filled π* orbital of DOPO^{sq}. These bands are absent in complexes (DOPO^{cat})UI(THF)$_2$ and Cp*U(DOPO^{cat})(THF)$_2$, confirming the closed shell DOPO^{cat} ligand with a filled π* orbital. Data obtained in the NIR region for the low valent uranium complexes show sharp but weak f-f transitions consistent with U(IV), f^2 centers (Figure 1.4). For $(DOPO^{q})_2UO_2$, no peaks are noted in the NIR region, indicating the absence of f-f transitions, which would be expected for a U(VI), f^0 center.

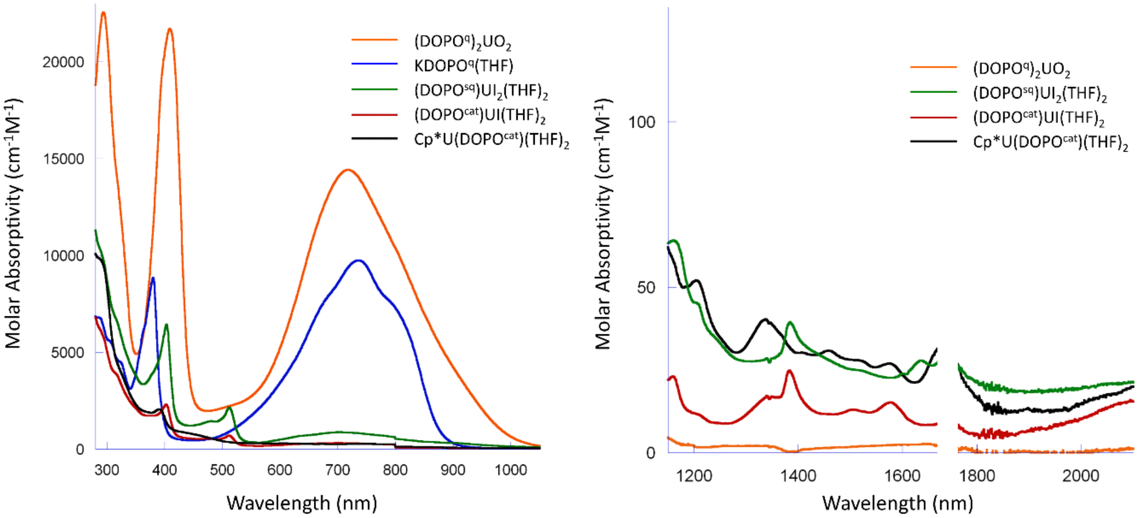

Figure 1.4. Electronic absorption spectra in the UV/visible region (left) and NIR region (right) for the DOPO series collected as solutions in THF at ambient temperature.

1.3.2 Isolation of $(DOPO^{q})_2UI_2$ as a Side Product

In an attempt to isolate “$(DOPO^{cat})UI(Et_2O)_n$” from $UI_4(dioxane)_2$, a different product was instead crystallized. Prereduction of $KDOPO^{q}(THF)$ with excess KC_8 (presumably forming “K_3DOPO^{cat}” *in situ*) followed by addition to $UI_4(dioxane)_2$ yielded crystals of the bis(DOPO) product, $(DOPO^{q})_2UI_2$. No meaningful bond metrics could be obtained from the structural analysis, but a U(IV) assignment can be inferred in analogy to $(DOPO^{sq})(DOPO^{q})_2U$ (see Section 2.3.3). No ^1H NMR data was obtained for this product, and independent syntheses using correct stoichiometry failed to reproduce this product. The mechanism of its formation is currently unknown.

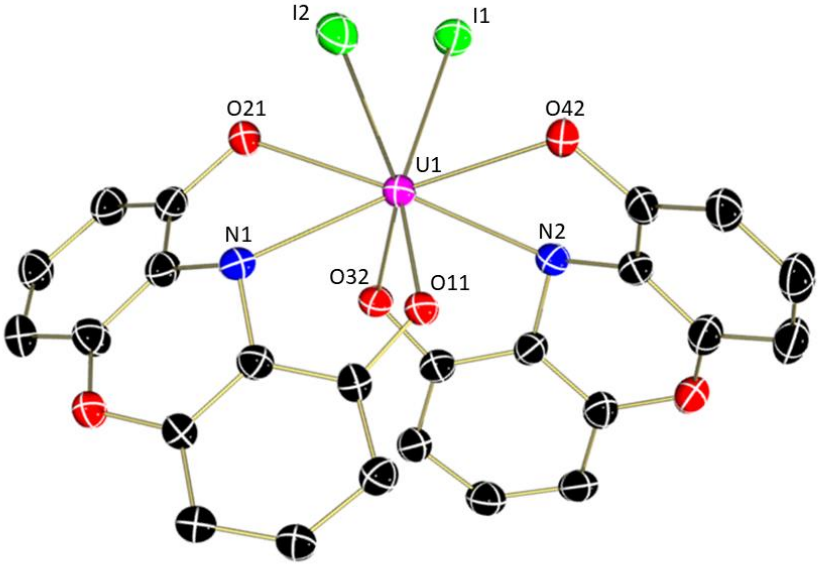

Figure 1.5. Molecular structure of $(DOPO^q)_2UI_2$ shown at 30% probability ellipsoids. Hydrogen atoms, *tert*-butyl groups, and cocrystallized solvent molecules have been omitted for clarity.

1.3.3 Isolation of a Mono(DOPO) Neodymium Complex

Also of interest was the study of the DOPO ligand on other f-block elements for a comparison of reactivity with the actinides. It was rationalized that redox-active ligands would allow for new reactivity at lanthanide elements, which are notorious for being redox inactive (see CHAPTER 4). Isolation of mono(DOPO) products were attempted for various lanthanides through different routes. Controllable metallation of one DOPO ligand to lanthanides proved difficult; over metallation was often observed from salt metathesis of $K(DOPO^q)(THF)$ with anhydrous lanthanide chlorides as described in Section 2.3.1.

The solvent adduct $NdI_3(THF)_{3.5}$ proved to be more versatile than the anhydrous lanthanide chlorides as a starting material for these reactions. Addition of a cold (-35 °C) THF solution of $K(DOPO^q)(THF)$ to a cold (-35 °C) THF suspension of $NdI_3(THF)_{3.5}$ resulted in the formation of a blue solution (Scheme 1.5). After workup, a blue powder was isolated. Analysis by ^1H NMR spectroscopy showed a highly symmetric spectrum with two large singlets at 2.78 and 9.83 ppm (18 H each) along with a small singlet shifted to 14.60 ppm (2H). This was consistent with the symmetry expected for a DOPO ligand, although multi(DOPO) products often exhibit similarly symmetric spectra. However, the wide NMR shifts suggested that the product did include a neodymium, so it initially appeared as though the metallation worked.

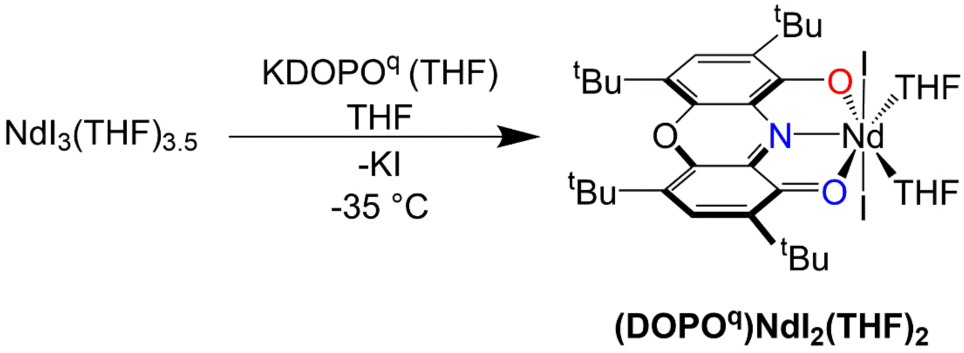

Scheme 1.5. Synthesis of $(DOPO^q)NdI_2(THF)_2$.

To determine the identity of the product, single crystals were grown from a concentrated diethyl ether solution at -35 °C. Analysis of the crystal revealed that the product was indeed the mono(DOPO) product, $(DOPO^q)NdI_2(THF)_2$, in a pentagonal bipyramidal geometry with axial iodide ligands (Figure 1.6). In fact, the structure is isostructural to $(DOPO^{sq})UI_2(THF)_2$. The Nd-I distances of 3.0744(9) and 3.0758(10) Å are similar to other Nd(III)-I distances.[18] The difference between these distances and the U(IV)-I distances in $(DOPO^{sq})UI_2(THF)_2$ (3.0480(5) and 2.9980(5) Å) are on the order of the difference in ionic radii of Nd(III) and U(IV).[37] The Nd-N distance (2.509(4) Å) is typical for a neutral nitrogen interaction, while the Nd-O distances (2.375(4) and 2.385(4) Å) are intermediate neutral and ionic Nd-O interactions reported in literature.[18] This resonance is as expected for a $DOPO^q$ ligand. The MOS analysis also supports the assignment of a monoanionic ligand with and average MOS value of -1.28(13).[4] Overall, the structural analysis is quite consistent with the expected Nd(III) center containing a monoanionic $DOPO^q$ ligand.

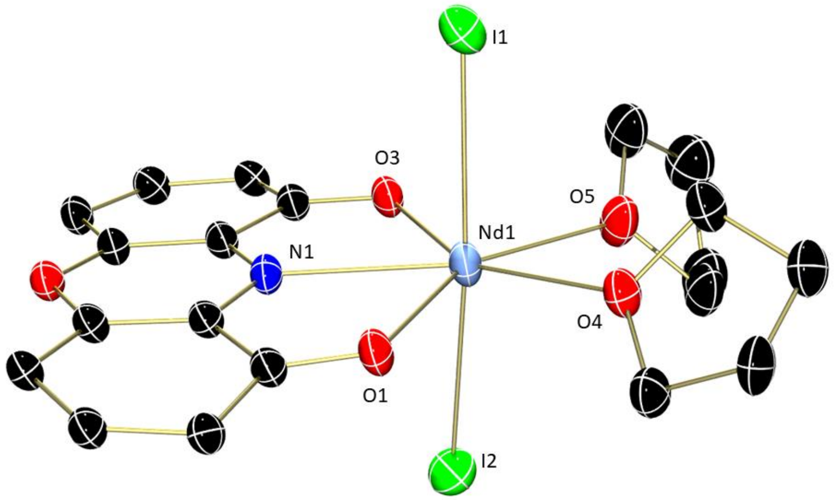

Figure 1.6. Molecular structure of $(DOPO^q)NdI_2(THF)_2$ shown at 30% probability ellipsoids. Hydrogen atoms, *tert*-butyl groups, and cocrystallized solvent molecules have been omitted for clarity.

1.3.4 Reactivity of Select Complexes

1.3.4.1 Comproportionation Reactions with $(DOPO^q)_2UO_2$

Attempts to isolate a mono(DOPO) uranyl species were unsuccessful from the direct protonation reaction of $UO_2[N(SiMe_3)_2]_2(THF)_2$ with $HDOPO^q$ or from salt metathesis of $KDOPO^q(THF)$ with $UO_2I_2(THF)_3$. This is likely due to the kinetically favorable formation of $(DOPO^q)_2UO_2$. Performing the reactions at reduced temperatures and adding $HDOPO^q$ or $KDOPO^q(THF)$ slowly always yielded a mixture of a mono(DOPO) product, $(DOPO^q)_2UO_2$, and leftover starting material as determined by ^{1}H NMR spectroscopy.

Interestingly, it was observed that a sealed NMR sample of the protonation route mixture in benzene-d_6 would eventually convert to the mono(DOPO) product after one week. It was hypothesized that this was the effect of a comproportionation between $(DOPO^q)_2UO_2$ and the remaining $UO_2[N(SiMe_3)_2]_2(THF)_2$ starting material present in the solution. To test this hypothesis a solution of $UO_2[N(SiMe_3)_2]_2(THF)_2$ in THF was added to a solution of $(DOPO^q)_2UO_2$ in THF and stirred overnight (Scheme 1.6). After removing the volatiles, a green powder was obtained in high yield. ^{1}H NMR spectroscopic analysis confirmed the assignment of (DOPO^q)UO$_2$[N(SiMe$_3$)$_2$] with a peak at 0.89 ppm from the N(Si(C*H*$_3$)$_3$)$_2$ group, two peaks at 1.41 and 1.73 ppm from the two inequivalent *tert*-butyl groups, and a peak at 7.87 ppm from the Ar-*H*. The steric pressure in the equatorial plane of (DOPO^q)$_2$UO$_2$ likely causes the DOPO ligands to have increased lability, which promotes this ligand substitution reaction. Due to the extreme solubility of this silyl amide complex, single crystals weren't obtained for structural analysis.

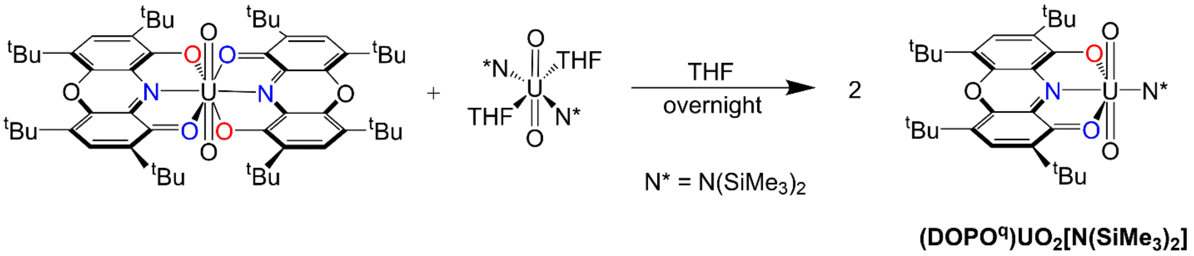

Scheme 1.6. Synthesis of (DOPO^q)UO$_2$[N(SiMe$_3$)$_2$].

To test the versatility of this route, the comproportionation was also attempted with a uranyl halide starting material. Addition of UO$_2$I$_2$(THF)$_3$ to a THF solution of (DOPO^q)$_2$UO$_2$ resulted in the formation of the desired product, (DOPO^q)UO$_2$I(THF) (Scheme 1.7). In this case, the additional THF ligand in the product causes asymmetry in the complex that is observed in the ^{1}H NMR spectrum (C$_6$D$_6$, 25 °C). All four *tert*-butyl groups in (DOPO^q)UO$_2$I(THF) are inequivalent, appearing at 1.35, 1.42, 1.64, and 1.75 ppm. Similarly, the aromatic protons of the DOPO ligand appear at 7.87 and 7.94 ppm. Two broad peaks at 3.90 and 5.01 ppm are observed for the bound THF molecule.

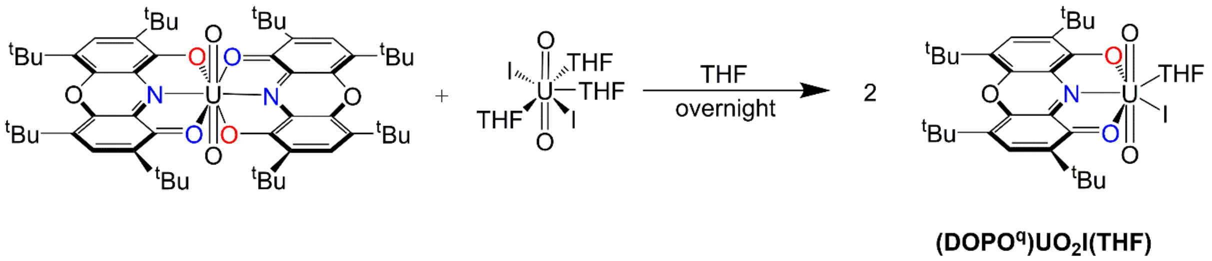

Scheme 1.7. Synthesis of (DOPO^q)UO$_2$I(THF) complexes.

Single crystals suitable for X-ray analysis were grown from a concentrated diethyl ether solution of (DOPO^q)UO$_2$I(THF). Analysis of a crystal revealed the desired structure, except that the THF ligand was replaced with a diethyl ether molecule, making the overall formula (DOPO^q)UO$_2$I(Et$_2$O) (Figure 1.7). This exchange was expected due to the presumed lability of the THF molecule, as evident by the broad signals observed in the ^{1}H NMR spectrum. The uranium oxygen distances (2.384(7) and 2.355(6) Å) and uranium nitrogen distance (2.510(8) Å) to the DOPO ligand are consistently shorter than those in (DOPO^q)$_2$UO$_2$ (2.480(4), 2.518(4), and 2.676(6) Å, respectively). This is presumably due to differing steric environments as (DOPO^q)UO$_2$I(Et$_2$O) is much less crowded in the equatorial plane. The uranyl U-O bonds (1.767(7) and 1.766(7) Å) are consistent with those in (DOPO^q)$_2$UO$_2$ (1.765(4) and 1.768(5) Å). Metrical Oxidation State (MOS) analysis reveals a computed ligand oxidation state of -1.44(22), consistent with the formulation of a uranium (VI) canter supported by a monoanionic, DOPO^q ligand.

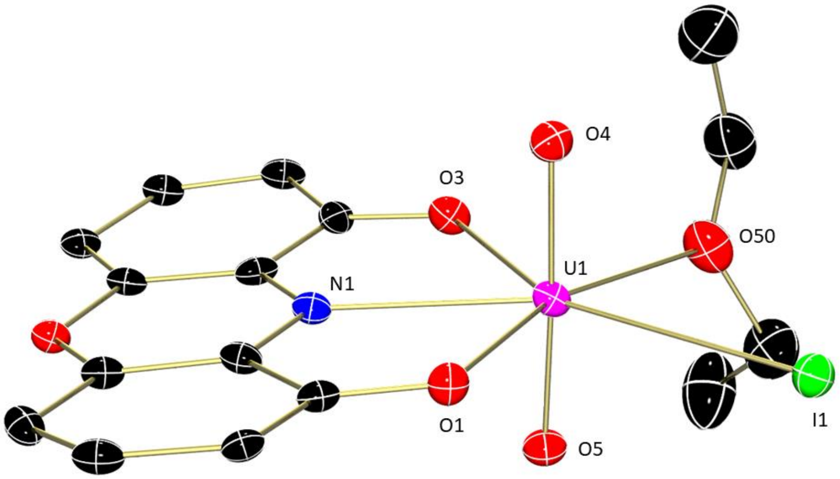

Figure 1.7. Molecular structure of (DOPO^q)$UO_2I(Et_2O)$ shown at 30% probability ellipsoids. Hydrogen atoms and *tert*-butyl groups have been omitted for clarity.

1.3.4.2 Reduction Chemistry of (DOPO^q)UO_2I(THF)

The main goal for the utility of redox-active DOPO ligated to high-valent uranyl derivatives would be aimed at activation of the notoriously stable U=O bonds in the uranyl[38] or to at least gain a better understanding of this reductive process. After metallation of the ligand onto a uranyl fragment, the ligand needed to be reduced, as it has been hypothesized by the Bart group that adding electron density to the equatorial plane of the uranyl could interrupt the inverse trans influence (ITI) that stabilizes the U=O bonds.[38] These additional electrons could also be used as reducing equivalents for processes to activate the uranyl moiety.

Initial investigations into the reduction of (DOPO^q)$UO_2[N(SiMe_3)_2]$ with KC_8 were unsuccessful (no tractable products), likely due to the loss of $K[N(SiMe_3)_2]$ that could cause side reactions. Therefore the focus on this reduction chemistry was aimed at (DOPO^q)UO_2I(THF) that could eliminate KI cleanly upon reduction. Addition of one equivalent of KC_8 to a THF solution of (DOPO^q)UO_2I(THF) resulted in no color change to the green solution. After workup to remove graphite (and presumably KI), a dull green powder was isolated. ^1H NMR analysis showed no significant peaks. Only small, broadened peaks for THF were sometimes observed for some samples. Certainly, no peaks were observed for a DOPO ligand, which typically have peaks representing 18 hydrogens (compared to four hydrogens for a THF molecule). However, it was evident that there was a significant amount of DOPO ligand in the NMR sample due to the dark green color of the C_6D_6 solution. This absence of signals in the ^1H NMR spectra was attributed to its paramagnetic nature. Upon reduction, the resultant unpaired electron could either reside in the π system of the DOPO ligand (similar to $(DOPO^{sq})UI_2(THF)_2$) or on the uranium center. The latter case would create an f^1 electronic structure for the uranium, which often exhibit paramagnetism that broadens ^1H NMR spectra in the baseline so that they are not observable. However, no other evidence supported the assignment of U(V) in this compound. Particularly, no f-f transitions were ever observed in the near-IR region of absorption spectra, and the uranyl asymmetric stretching frequency (IR spectroscopy) doesn't appreciably change upon reduction (926 cm^{-1} for $(DOPO^q)UO_2I(THF)$ compared to 927 cm^{-1} for this product). This lead to the assignment of this compound as $(DOPO^{sq})UO_2(THF)_n$ (Scheme 1.8).

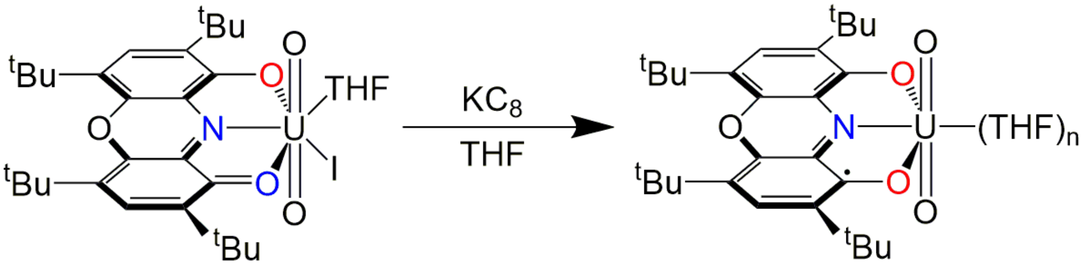

Scheme 1.8. Reduction of $(DOPO^q)UO_2I(THF)$.

To help infer the identity of this compound, single crystals of the related triphenylphosphine oxide adduct were grown. Single crystals of the THF adduct wouldn't form. However, addition of approximately two equivalents of triphenylphosphine oxide to a THF solution of $(DOPO^{sq})UO_2(THF)_n$ yielded a complex that produced crystals upon layering a diethyl ether solution with toluene and cooling to -35 °C. Analysis of a crystal revealed the related complex $(DOPO^{sq})UO_2(OPPh_3)_2$ (Scheme 1.9).

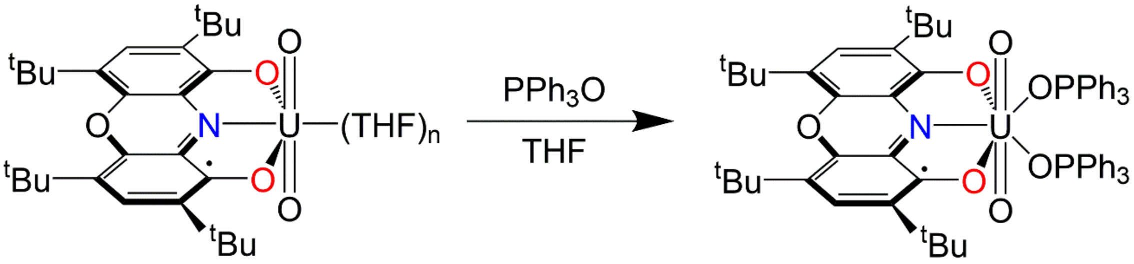

Scheme 1.9. Formation of (DOPO^{sq})UO$_2$(OPPh$_3$)$_2$.

The structure (Figure 1.8) displays axial oxo ligands (1.763(7) and 1.762(7) Å) that are within the bond distance range for U(VI) uranyl U-O bonds.[38] In fact, they are statistically unchanged from (DOPO^q)UO$_2$I(Et$_2$O) (1.767(7) and 1.766(7) Å). The U-O (2.365(5) and 2.367(6) Å) and U-N (2.455(7) Å) distances to the DOPO ligand are also statically indistinguishable from (DOPO^q)UO$_2$I(Et$_2$O). However, MOS analysis indicates a ligand oxidation state of -2.02(22), consistent with ligand reduction to the DOPO^{sq} form. A comparison of metal-ligand and intraligand bond distances is shown in Figure 1.9.

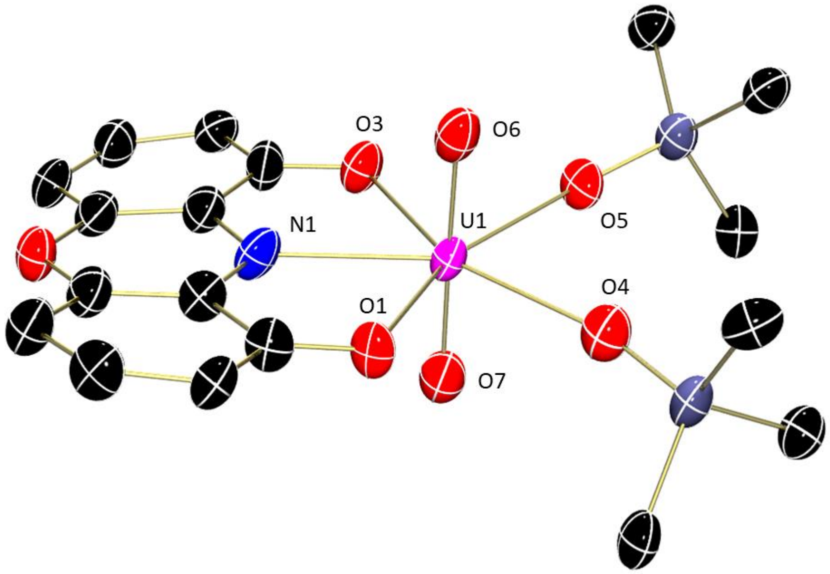

Figure 1.8. Structure of (DOPO^{sq})UO$_2$(OPPh$_3$)$_2$ shown at 30% probability ellipsoids. Hydrogen atoms, *tert*-butyl groups, and phenyl groups have been omitted for clarity.

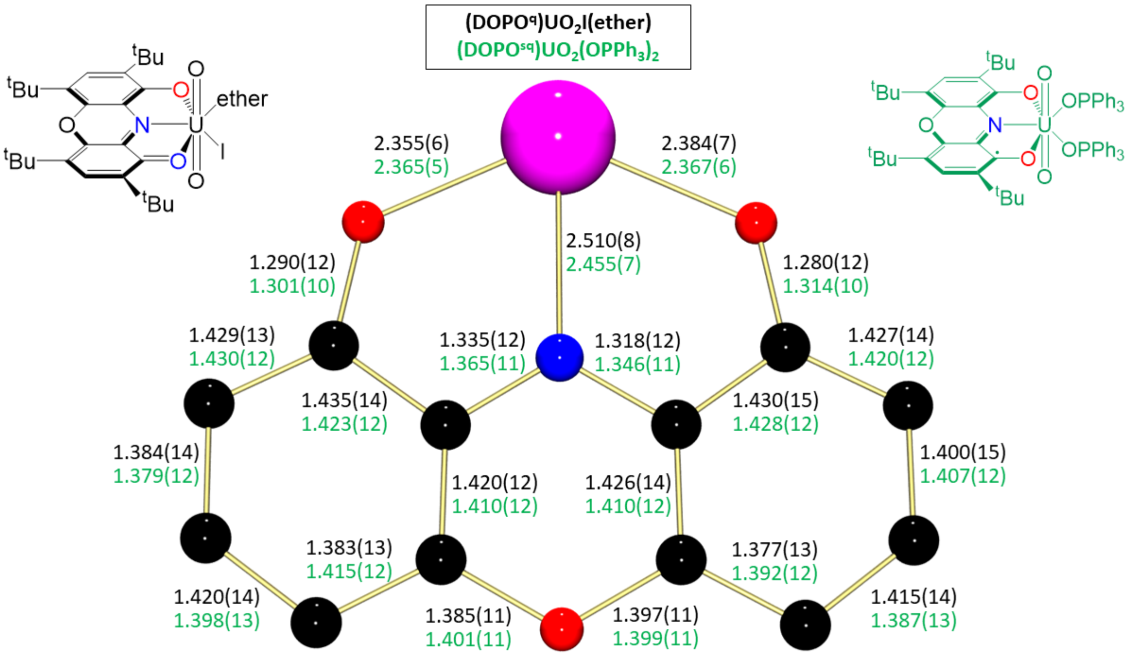

Figure 1.9. Metal-ligand and intraligand bond distance comparison (in Å) for $(DOPO^{q})UO_2I(Et_2O)$ (black) and $(DOPO^{sq})UO_2(OPPh_3)_2$ (green).

To examine the reversibility of this reduction, oxidation of $(DOPO^{sq})UO_2(THF)_n$ was demonstrated. This reactivity also helped support the assignment of this complex, which isn't observed by NMR spectroscopy. Addition of one half equivalent of I_2 (assuming n=2 for $(DOPO^{sq})UO_2(THF)_n$) to a THF solution of $(DOPO^{sq})UO_2(THF)_n$ results in clean conversion back to $(DOPO^{q})UO_2I(THF)$ as observed by ^{1}H NMR spectroscopy.

Additional reduction of $(DOPO^{sq})UO_2(THF)_n$ was attempted. However, with the lack of NMR spectroscopy and inability to grow crystals of the resultant products, it was unclear if additional reductions were possible with this platform.

1.3.4.3 Oxidation Chemistry of $Cp^*U(DOPO^{cat})(THF)_2$

$Cp^*U(DOPO^{cat})(THF)_2$ was chosen for reactivity studies based on its complete characterization and fully reduced nature of the $DOPO^{cat}$ ligand. These studies sought to explore if the electrons in the ligand could be used for reactivity. Oxidations with both TMSI and MeI were largely unsuccessful. After one day of stirring in THF, only starting material remained, and after much longer, the complex appeared to decompose. Oxidation with I_2 appeared to be much cleaner as the ^{1}H NMR of the reaction mixture appeared to contain two or three DOPO containing complexes. However, the identity of these products was never elucidated.

It quickly became clear that the DOPO ligand wasn't as reactive when coordinated to uranium when compared to nitrogen based redox-active ligands such as pyridine diimines. This observation was rationalized by the oxophilicity of the uranium center. Once the ligand was reduced and contained anionic oxygen chelates, it was difficult to get the electrons back to make dative interactions. A better use of the DOPO ligand was found in stabilizing actinide and lanthanide metals (see CHAPTER 2).

1.4 Conclusions

To confirm that the DOPO ligand was stable in multiple oxidation states on uranium, a series of dioxophenoxazine uranium complexes, $(DOPO^{q})_2UO_2$, $(DOPO^{sq})UI_2(THF)_2$, $(DOPO^{cat})UI(THF)_2$, and $Cp^*U(DOPO^{cat})(THF)_2$ were synthesized in high yield and characterized. Data obtained using ^{1}H NMR spectroscopy, electronic absorption spectroscopy, X-ray crystallography, and SQUID magnetometry suggest that $(DOPO^{q})_2UO_2$ contains two monoanionic $DOPO^{q}$ ligands at a U(VI) center, while $(DOPO^{sq})UI_2(THF)_2$ has a dianionic $DOPO^{sq}$ chelate and a U(IV) center. Both $(DOPO^{cat})UI(THF)_2$ and $Cp^*U(DOPO^{cat})(THF)_2$ feature a trianionic $DOPO^{cat}$ framework, also ligated to a U(IV) center. Ligand oxidation states were also established by using the intraligand bond distances as determined by X-ray crystallography to calculate the Metrical Oxidation State (MOS) of each ligand.[4] These calculations supported, within error, the assignments of the ligand oxidation states based on experimental data as compared to previously established examples with transition metals.[4,5] Near-infrared absorption data support that the uranium center is tetravalent for $(DOPO^{sq})UI_2(THF)_2$, $(DOPO^{cat})UI(THF)_2$, and $Cp^*U(DOPO^{cat})(THF)_2$ and maintains its +6 oxidation state for $(DOPO^{q})_2UO_2$.

With this baseline series known, other DOPO products were isolated. Comproportionation reactions with $(DOPO^{q})_2UO_2$ produced a variety of mono(DOPO) uranyl products including $(DOPO^{q})UO_2[N(SiMe_3)_2]$, $(DOPO^{q})UO_2I(THF)$, and $(DOPO^{q})UO_2I(Et_2O)$. Reduction of $(DOPO^{q})UO_2I(THF)$ produced the reduced product, $(DOPO^{sq})UO_2(THF)_n$, which was trapped and crystallized with two equivalents of triphenylphosphine oxide, producing $(DOPO^{sq})UO_2(OPPh_3)_2$. Although these compounds are not observable by NMR spectroscopy, other characterization techniques suggest that the reduction occurs at the DOPO ligand rather than the uranium center.

The dioxophenoxazine uranium and neodymium species described here are exciting new additions to the collection of known uranium species bearing redox-active ligands, as the oxygen donor atoms make the DOPO ligand a strong chelator for the oxophilic uranium center. Further studies focused on using the DOPO ligand to stabilize homoleptic actinide and lanthanide complexes (CHAPTER 2).

CHAPTER 2. SYNTHESIS AND CHARACTERIZATION OF HOMOLEPTIC DIOXOPHENOXAZINE COMPLEXES

2.1 Introduction

It was rationalized that the DOPO ligand, an oxygen containing chelate, would create robust complexes with highly oxophilic lanthanide and actinide elements and that this added stability would allow for the isolation of a broad class of stable lanthanide and actinide compounds. These studies would be useful in understanding general periodic trends that could be applied to new strategies for recycling of used nuclear fuels.

Recycling of used nuclear fuels represents significant contributions to the cost and waste generation of nuclear fuel cycles.[39,40] The application of ligands designed to have a high specificity for separating targeted isotopes from the complex mixture of elements in used fuel has been successful, but lack of understanding about the basic coordination chemistry of certain heavy elements, especially those beyond uranium, has hindered progress.[40–43] As established by studies in the d-block, ionic radius, oxidation state, electronegativity, valence electron configuration, and other factors determine the coordination environment of a metal. Thus, to effectively design ligands for binding transuranic elements, these characteristics must be understood on a fundamental level.

Trends for these properties have been well established for *d*-block elements, and many studies have repeatedly highlighted contrasting chemistry between early and late transition metals. The relatively fewer studies on actinides suggest that elements early in the series take on covalent character, due to mixing of the 6p, 6d, and 5f orbitals for bonding to organic ligands.[44,45] As the actinide series is traversed, the later elements begin to behave more like lanthanides, where the 3+ oxidation state and ionic bonding character dominates. Elements past plutonium are known to have similar chemical properties to lanthanides, causing separation of so-called minor actinides (Np, Am, Cm) and lanthanides present in used nuclear fuel to be challenging. While actinides are typically associated with higher degrees of covalency in their metal-ligand bonds as compared to the lanthanides, leveraging this property for separations of trivalent ions is challenging because the degree of covalency is known to decrease with the lowering of the oxidation state for actinides.

Recent work in the actinide series featuring tris(dipicolinate) (Hdpa) derivatives, $An(Hdpa)_3$ (An = Am, Cm, Cf, Bk), has demonstrated that while the above trend is generally true for transuranic elements, the availability of the +2 oxidation state for californium causes a deviation in this trend that overrides the minor contraction of the 5*f* orbitals that is typically observed.[46,47] It was hypothesized that this trend could be further perturbed using redox-active ligands that accept electron density into their π^* orbitals. Such a class of ligands have been shown to produce highly-covalent transition-metal derivatives, and thus offers an opportunity to study covalency in metal-ligand bonds for transuranium elements.

The DOPO is an appropriate choice, given its widespread use on d-[4,5] and f-block[48–50] metals. This ligand's planar coordination mode, its ability to form robust metal-oxygen bonds, and its analogy to dipicolinate make it attractive for this study. The redox flexibility of this ligand is key to its function, as it can take on three different oxidation states. The redox activity of the DOPO ligand should also allow for isostructural comparisons between metals of different oxidation states. This is especially important when comparing actinides that have different stable oxidation states. It was postulated that the large ionic radii of the f-block metals would permit formation of tris(DOPO) complexes and that the redox flexibility of the ligands would allow for the isolation of an isostructural set across the lanthanide and actinide series. Tris-ligand complexes of similar ONO-chelating ligands (ONO = 3,5-di-*tert*-butyl-1,2-quinone-1-(2-oxy-3,5-di-*tert*-butylphenyl)imine) have been characterized for strontium and samarium, while bis-ligand complexes for both DOPO and ONO are reported for many other metals.[16] The homoleptic tris(ligand) derivatives, of the form $M(DOPO)_3$, reported here have been fully characterized using structural, spectroscopic, and magnetic techniques as well as electronic structure theory calculations. The findings highlight differences in bonding and covalency between the different regions of the f-block.

2.2 Experimental

General Considerations. All manipulations were performed using standard Schlenk techniques or in an MBraun inert atmosphere drybox with an atmosphere of purified nitrogen (lanthanides, transition metals, main group metals, thorium, and uranium) or ultra high purity argon (transuranics). Gadolinium chloride, neodymium chloride, cerium chloride, hafnium chloride, bismuth chloride, and europium (II) bromide were purchased from Strem Chemicals. Pentane, toluene, and THF were dried and deoxygenated using literature procedures with a Seca solvent purification system.[11] Anhydrous pyridine was purchased from Sigma Aldrich and was used without further purification. Benzene-d_6 was purchased from Cambridge Isotope Laboratories and was degassed by three freeze-pump-thaw cycles and dried over molecular sieves and sodium. $U[N(SiMe_3)_2]_3$,[16] $ThCl_4(DME)_2$,[51] KC_8,[19] $HDOPO^q$,[4] and $KDOPO^q(THF)$[48] were prepared according to literature procedures.

Caution! ^{239}Pu ($t_{1/2}$=24110 years) ^{243}Am ($t_{1/2}$=7380 years), ^{249}Bk ($t_{1/2}$=320 days), and ^{249}Cf ($t_{1/2}$=351 years) represent serious health risks due to their α emission and the radiotoxicity associated with their α, β, and γ emitting daughters. All studies with these actinides were conducted in a laboratory dedicated to studies on transuranic elements in collaboration with Thomas Albrecht-Schmitt and his group. This laboratory is located in a nuclear science facility at Florida State University and is equipped with HEPA-filtered hoods and gloveboxes. A series of instruments continually monitor the radiation levels in the laboratory. All free-flowing actinide solids are handled in gloveboxes, and products are only examined when coated with immersion or krytox oil. Significant limitations exist to accurately determining yields of these actinide compounds because drying, isolating, and weighing a solid is required, which creates an inhalation hazard and manipulation difficulties given the small quantities of products from these reactions.

All ^{1}H NMR spectra were recorded on a Varian Inova 300 spectrometer at 299.992 MHz. All chemical shifts are reported relative to the peak for $SiMe_4$, using ^{1}H (residual) chemical shifts of the solvent as a secondary standard. The spectra for paramagnetic molecules were obtained using an acquisition time of 0.5 s; thus, the peak widths reported have an error of ±2 Hz. For paramagnetic molecules, the ^{1}H NMR data are reported with the chemical shift, followed by the peak width at half height in Hertz, the integration value, and, where possible, the peak assignment.

Electronic absorption measurements were recorded at 294 K with a Craic Technologies microspectrophotometer. Single crystals of each compound were placed on a quartz slide in immersion oil, and the data were collected from 300 nm to 1100 nm.

A single crystals of $Ce(DOPO^q)_3$ and $Eu(DOPO^q)(DOPO^{sq})(py)_3$ for X-ray diffraction were coated with poly(isobutene) oil in a glovebox and transferred to the goniometer head of a Bruker AXS D8 Quest CMOS diffraction equipped with a complementary metal-oxidesemiconductor (CMOS) detector and an I-μ-S Mo Kα microsource X-ray tube (λ = 0.71073 Å) operated at 50 kV and 1 mA with laterally graded multilayer (Goebel) mirror X-ray optics. Data were collected, reflections were indexed and processed, and the files scaled and corrected for absorption using SADABS.[52] The space group was assigned and the structure was solved by direct methods using XPREP within the SHELXTL suite of programs[21] and refined by full matrix least squares against F^2 with all reflections using Shelxl2014[21] using the graphical interface Shelxle.[21] A solvate toluene molecule is disordered. Its two moieties were restrained to have similar geometries as another not disordered toluene molecule, and the atoms of the disordered moieties were subjected to a rigid bond restraint (RIGU in Shelxl). Subject to these conditions the occupancy ratio refined to 0.624(6) to 0.376(6).

A single crystals of Nd(DOPO^{q})$_3$, U(DOPO^{q})$_2$(DOPO^{sq}), and Bi(DOPO^{q})$_3$ for X-ray diffraction were coated with poly(isobutene) oil in a glovebox and quickly transferred to the goniometer head of a Rigaku Rapid II image plate diffractometer equipped with a MicroMax002+ high intensity copper X-ray source with confocal optics. Preliminary examination and data collection were performed with Cu Kα radiation (λ = 1.54184 Å). Data were collected using the dtrek option of CrystalClear.[53] The data set was processed using HKL3000 and data were corrected for absorption and scaled using Scalepack.[54] The space group was assigned and the structure was solved by direct methods using XPREP within the SHELXTL suite of programs[21] and refined by full matrix least squares against F^2 with all reflections using Shelxl2014[21] using the graphical interface Shelxle.[21]

A single crystals of Gd(DOPO^{q})$_3$ and Hf(DOPO^{q})$_2$(DOPO^{sq}) for X-ray diffraction were coated with poly(isobutene) oil in a glovebox and quickly transferred to the goniometer head of a Nonius KappaCCD image plate diffractometer equipped with a graphite crystal, incident beam monochromator. Preliminary examination and data collection were performed with Mo Kα radiation (λ = 0.71073 Å). Data were collected using the Nonius Collect software.[55] The data set was processed using HKL3000 and data were corrected for absorption and scaled using Scalepack.[54] The space group was assigned and the structure was solved by direct methods using XPREP within the SHELXTL suite of programs[21] and refined by full matrix least squares against F^2 with all reflections using Shelxl2014[21] using the graphical interface Shelxle.[21] Two of four solvate pyridine rings were refined as disordered over two slightly rotated orientations. The geometries of all four pyridine rings were restrained to be similar, and the U^{ij} components of the

ADPs of disordered atoms were restrained to be similar for atoms closer to each other than 1.7 Å. Subject to these conditions the occupancy ratio for the rings involving N6 refined to 0.338(10); the ones involving N7 refined to 0.428(8).

Single crystals of Am(DOPO^q)$_3$, Bk(DOPO^q)$_3$, Cf(DOPO^q)$_3$, Pu(DOPO^q)$_2$(DOPO^{sq}), and Cf(DOPO^q)$_2$(NO$_3$)(py) were mounted on a Mitegen mount with krytox oil, and the crystals were optically aligned on a Bruker D8 Quest X-ray Diffractometer using a built in camera. Preliminary measurements were performed using an I-μ-S X-ray source (Mo Kα, $\lambda = 0.71073$ Å) with high-brilliance and high-performance focusing quest multilayer optics. Data were collected, reflections were indexed and processed, and the files scaled and corrected for absorption using APEX2.[52] The reflection's intensities of a sphere were collected by a mixture of four sets of frames. Each set had a different omega angle for the crystal, and each exposure covered a range of 0.50 in ω, totaling to 1464 frames. The frames were collected with an exposure time of 5-25 seconds which was dependent on the crystal. SAINT software was used for data integration including polarization and Lorentz corrections.[56] The files scaled and corrected for absorption using SADABS[52] The space groups were assigned and the structures were solved by direct methods using XPREP within the SHELXTL suite of programs[21] and refined by full matrix least squares against F^2 with all reflections using Shelxl2016 or 2017[21] using the graphical interface Shelxle.[21] Structure factors for Bk, Am and Cf were not defined in the Shelxl software and were manually defined using the values published in the International tables of Crystallography, Vol. C, defined based on the published values from the International Tables Vol C Tables 4.2.6.8 (entries a1 to c of the scattering factor line), 6.1.1.4 (f' and f") and 4.2.4.2 (mu). For the atomic weight, the value of the actually used isotope was used (not necessarily that of the longest lived isotope). The structures of Am and Bk are isomorphous and were refined against a common model. Neither exhibits any disorder. In the Cf structure one of the DOPO ligands undergoes a rotating motion around californium. It was refined as disordered over two orientations. Both moieties were restrained to have a similar geometry as the second not disordered DOPO ligand. Atoms C49 and C49B were constrained to have identical ADPs. A pyridine solvate molecule is disordered around an inversion center. Another pyridine solvate molecule is disordered in a general position. A third pyridine solvate molecule was refined as partially occupied. Ill-defined diffuse electron density around the first and third pyridine molecules could not be assigned to any additional solvate molecules and was ignored in the structural model (it might be the cause for partial occupancy of the third pyridine molecule). U^{ij} components of all disordered atoms were restrained to be similar for atoms closer to each other than 1.7 Å. Subject to these conditions the occupancy ratios for the DOPO moieties refined to 0.522(13) to 0.478(13). That of the disordered pyridine to 0.584(12) to 0.416(12). The occupancy rate for the partially occupied pyridine molecule refined to 0.707(5).

A single crystal of $Th(DOPO^{q})_2(DOPO^{sq})$ suitable for X-ray diffraction, was coated with poly(isobutylene) oil in a glovebox and quickly transferred to the goniometer head of a Bruker Quest diffractometer with a fixed chi angle, a sealed tube fine focus X-ray tube, single crystal curved graphite incident beam monochromator and a Photon100 CMOS area detector. Examination and data collection were performed with Mo Kα radiation ($\lambda = 0.71073$ Å). Data were collected, reflections were indexed and processed, and the files scaled and corrected for absorption using APEX3.[52] The data were collected with Oxford Cryosystems low temperature devices operating at 150 K. The space groups were assigned and the structures were solved by direct methods using XPREP within the SHELXTL suite of programs and refined by full matrix least squares against F^2 with all reflections using Shelxl2016[21] using the graphical interface Shelxle.[21]

Magnetic data were collected on a Quantum Design Magnetic Property Measurement System (MPMS-7). Temperature-dependent data were collected under applied 1 T DC fields from 2 to 300 K, and field dependent data were performed at 2 K with varying applied magnetic field strengths ranging from 0 to 7 T. Corrections for the intrinsic diamagnetism of the samples were made using Pascal's constants.[20] Each magnetism sample was prepared in the glovebox and placed in a heat-sealed compartment of a plastic drinking straw. The plastic drinking straws were evacuated overnight prior to use. These straws were then sealed at one end (~ 9.5 cm from the top) by heating a pair of forceps and crimping the sides of the straw until the two sides were fused together. Microcrystalline compound (10 ~ 40 mg) was loaded into the straw, capped with < 10 mg of quartz wool (dried at 250 °C prior to use), and packed in tightly using a Q-tip. The other end of the plastic drinking straw was then sealed directly above the quartz wool, forming a small compartment (<1 cm). The sample and quartz wool were massed four times each to the nearest 0.1 mg, and the values used were the averages of these mass measurements.

Geometry optimizations were performed for a model Metal-DOPO complex (in which the *t*-Bu groups have been replaced with hydrogen atoms), for the maximum spin multiplicity with density functional theory (DFT) using the ADF2016 software package, employing the B3LYP functional in combination with UFF dispersion. A TZP quality was used for the lanthanides or actinides, while a DZP quality basis was employed for all other atoms (H, C, O, N). Scalar relativistic effects were included by means of the Zeroth-Order-Regular-Approximation (ZORA). The electronic structures were analyzed with Complete Active Space SCF (CASSCF) calculations on top of the DFT optimized structures using the Molcas 8.2 software package. Small-core relativistic Effective Core Potentials (ECP) of the Stuttgart-Cologne group were applied for all elements, along with segmented basis sets for lanthanides with the following contraction (14s, 13p, 10d, 8f, 6g)/[10s, 8p, 5d, 4f, 3g], the following contraction for actinides (14s, 13p, 10d, 8f, 6g)/[10s, 9p, 5d, 4f, 3g], the following contraction for N and C (4s, 4p)/[2s, 2p], the following contraction for oxygen (4s, 5p)/[2s, 3p], and the following contraction for hydrogen (4s,)/[4s]. Resolution of Identity Cholesky Decomposition (RICD) was used for reducing the computational cost of computing the two-electron integrals.

Preparation of Gd(DOPO^q)$_3$. A 20 mL scintillation vial was charged with anhydrous $GdCl_3$ (0.030 g, 0.114 mmol) and 5 mL of pyridine. To this suspension was added a violet solution of HDOPO^q (0.150 g, 0.343 mmol) in 5 mL of pyridine, resulting in a color change to dark blue after 5 minutes. After stirring for 2 hours, the resulting solution was concentrated *in vacuo* to a dark blue powder. The product was extracted into 20 mL of pentane, and the solution was filtered to remove the pyridinium chloride byproduct. This solution was concentrated *in vacuo*, resulting in a blue powder assigned as Gd(DOPO^q)$_3$ (0.119 g, 0.081 mmol, 71%). Paramagnetism of the sample precluded analysis by ^{1}H NMR spectroscopy.

Crystallization of Gd(DOPO^q)$_3$. X-ray quality crystals were grown directly from a small scale reaction mixture. A 20 mL scintillation vial was charged with anhydrous $GdCl_3$ (0.010 g, 0.038 mmol) and 5 mL of pyridine. To this suspension was added a violet solution of HDOPO^q (0.050 g, 0.114 mmol) in 5 mL of pyridine, resulting in a color change to dark blue after 5 minutes. After stirring for an additional 5 minutes, the cap was removed, and the solution was removed from the stir plate. After 24 hrs, blue X-ray quality crystals were isolated from the solution.

Preparation of Nd(DOPO^q)$_3$. A 20 mL scintillation vial was charged with anhydrous $NdCl_3$ (0.029 g, 0.116 mmol) and 5 mL of pyridine. To this suspension was added a violet solution of HDOPO^q (0.150 g, 0.343 mmol) in 5 mL of pyridine, resulting in an immediate color change to dark blue. After stirring for 2 hours, the resulting solution was concentrated *in vacuo* to a dark blue powder. The product was extracted into 20 mL of pentane, and the solution was filtered to remove the pyridinium chloride byproduct. This solution was concentrated *in vacuo,* resulting in a blue powder assigned as Nd(DOPO^q)$_3$ (0.112 g, 0.077 mmol, 68%). ^{1}H NMR (C_6D_6, 25 °C): δ = 1.03 (6, 54H, -C(C*H*$_3$)$_3$), 1.84 (3, 54H, -C(C*H*$_3$)$_3$), 9.09 (4, 6H, Ar-C*H*).

Crystallization of Nd(DOPO^q)$_3$. X-ray quality crystals were grown directly from a small scale reaction mixture. A 20 mL scintillation vial was charged with anhydrous $NdCl_3$ (0.010 g, 0.040 mmol) and 5 mL of pyridine. To this suspension was added a violet solution of HDOPO^q (0.050 g, 0.114 mmol) in 5 mL of pyridine, resulting in an immediate color change to dark blue. After stirring for an additional 5 minutes, the cap was removed, and the solution was removed from the stir plate. After 24 hrs, blue X-ray quality crystals were isolated from the solution.

Preparation of Ce(DOPO^q)$_3$. A 20 mL scintillation vial was charged with anhydrous $CeCl_3$ (0.028 g, 0.114 mmol) and 5 mL of pyridine. To this suspension was added a violet solution of HDOPO^q (0.150 g, 0.343 mmol) in 5 mL of pyridine, resulting in an immediate color change to dark blue. After stirring for 2 hours, the resulting solution was concentrated *in vacuo* to a dark blue powder. The product was extracted into 20 mL of pentane, and the solution was filtered to remove the pyridinium chloride byproduct. This solution was concentrated *in vacuo,* resulting in a blue powder assigned as Ce(DOPO^q)$_3$ (0.126 g, 0.087 mmol, 76%). ^{1}H NMR (C_6D_6, 25 °C): δ = 0.69 (3, 54H, -C(C*H*$_3$)$_3$), 1.92 (2, 54H, -C(C*H*$_3$)$_3$), 8.64 (2, 6H, Ar-C*H*).

Crystallization of Ce(DOPO^q)$_3$. Ce(DOPO^q)$_3$ (about 0.050 g) was dissolved in 2 mL of toluene, creating a dark blue solution. 1 mL of pentane was added, and the solution was filtered and placed in the freezer at -35 °C, yielding small crystals over the course of 1 week.

General Comments for (DOPO^q)$_3$Ln Crystallizations. These crystallization conditions are optimized for maximum crystal size and yield. Performing the reactions too concentrated leads to microcrystalline materials that aren't useful for single crystal X-ray diffraction. Curiously, no crystals or solid of any form are obtained if the reaction mixture is placed in the freezer (-35 °C).

Preparation of Am(DOPO^q)$_3$. A 7 ml scintillation vial was charged with $^{243}AmBr_3$ (0.005 g, 0.010 mmol) and 1 ml of pyridine. A solution of HDOPO^q (0.0135 g, 0.031 mmol) dissolved in 2 mL of pyridine was added to the vial, causing a color change from yellow to dark purple. The solution sat overnight to allow evaporation of solvent. Dark purple block crystals suitable for X-ray analysis formed, and were analyzed immediately.

Preparation of Bk(DOPO^q)$_3$. A 7 ml scintillation vial was charged with ^{249}BkCl$_3$ (0.00433 g, 0.012 mmol) and 1 ml of pyridine. A solution of HDOPO^q (0.0192 g, 0.044 mmol) and 1 ml of anhydrous pyridine was added to the vial, causing a color change from green to blue. The solution was dried to a residue, and 10 equivalents of HDOPO^q (0.0525 g, 0.120 mmol) in 1 mL of pyridine was added. The solution was transferred to a 20 ml scintillation vial via pasteur pipet. Upon standing blue rod crystals formed which were suitable for X-ray analysis.

Preparation of Cf(DOPO^q)$_3$. A 20 ml scintillation vial was charged with ^{249}CfCl$_3$ (0.005 g, 0.014 mmol) and 1 ml of pyridine. A solution of HDOPO^q (0.061 g, 0.140 mmol) in 1 ml of anhydrous pyridine was added to the vial, causing a color change from green to blue. The solution was dried to a residue and the product was extracted with 1 ml of pentane. The blue pentane solution was transferred to a 20 mL scintillation vial and dried. The residue was then redissolved in 1 mL of pyridine. Upon standing, dark blue platelet crystals formed which were suitable for X-ray analysis.

Preparation of U(DOPO^q)$_2$(DOPO^{sq}). A 20 mL scintillation vial was charged with U[N(SiMe$_3$)$_2$]$_3$ (0.025 g, 0.035 mmol) and 5 mL of THF. A solution of HDOPO^q (0.046 g, 0.105 mmol) in 5 mL of THF was slowly added to the stirring solution of U[N(SiMe$_3$)$_2$]$_3$ resulting in a color change from violet to green. After stirring for one hour, the volatiles were removed *in vacuo* resulting in a green powder (0.051 g, 0.033 mmol, 94%) that was assigned as U(DOPO^q)$_2$(DOPO^{sq}). Green crystals suitable for X-ray analysis were grown by slow evaporation from pentane over a week at room temperature. Analysis for $C_{84}H_{114}N_3O_9U$: Calcd. C, 65.18; H, 7.42; N, 2.71. Found C, 65.07; H, 7.28; N, 2.82. ^{1}H NMR (C_6D_6, 25 °C): $\delta = -82.80$ (38, 6H, Ar-C*H*), 0.45 (3, 54H, -C(C*H*$_3$)$_3$), 1.52 (4, 54H, -C(C*H*$_3$)$_3$).

Preparation of Pu(DOPO^q)$_2$(DOPO^{sq}). A 7 mL scintillation vial was charged with ^{239}PuBr$_3$ (0.005 g, 0.0104 mmol) and 2 mL of pyridine. A solution of HDOPO^q (0.0135 g, 0.0311 mmol) dissolved in 2 mL of pyridine was added to the vial, causing a color change from yellow to dark purple. Overnight, dark-purple, block crystals suitable for X-ray analysis formed and were immediately analyzed.

Preparation of Th(DOPO^q)$_2$(DOPO^{sq}). A 20 mL scintillation vial was charged with ThCl$_4$(DME)$_2$ (0.084 g, 0.152 mmol) and 5 mL of THF. A solution of KDOPO^q(THF) (0.250 g, 0.456 mmol) dissolved in 5 mL of THF was added to the vial, causing a color change from blue to green. One equivalent of KC$_8$ (0.021 g, 0.155 mmol) was added, and the solution was allowed to stir for one hour before it was concentrated *in vacuo*. The resulting green powder was extracted into toluene, filtered to remove KCl and graphite, and concentrated *in vacuo* to a dark green powder assigned as Th(DOPO^q)$_2$(DOPO^{sq}). Single crystals for X-ray crystallography were grown from a concentrated pyridine solution at room temperature.

Preparation of Hf(DOPO^q)$_2$(DOPO^{sq}). A 20 mL scintillation vial was charged with $HfCl_4$ (0.010 g, 0.031 mmol) and 5 mL of THF. A solution of KDOPO^q(THF) (0.058 g, 0.106 mmol) dissolved in 5 mL of THF was added to the vial, causing a color change from blue to green. One equivalent of KC_8 (0.005 g, 0.037 mmol) was added, and the solution was allowed to stir for one hour before it was concentrated *in vacuo*. The resulting green powder was extracted into toluene, filtered to remove KCl and graphite, and concentrated *in vacuo* to a dark green powder assigned as Hf(DOPO^q)$_2$(DOPO^{sq}). Single crystals for X-ray crystallography were grown from a concentrated pyridine solution at room temperature.

Preparation of Bi(DOPO^q)$_3$. A 20 mL scintillation vial was charged with $BiCl_3$ (0.012 g, 0.038 mmol) and 5 mL of pyridine. To this suspension was added a violet solution of HDOPO^q (0.050 g, 0.114 mmol) in 5 mL of pyridine, resulting in a color change to dark blue after 5 minutes. After stirring for an additional 5 minutes, the cap was removed, and the solution was removed from the stir plate. After 24 hrs, blue X-ray quality crystals were isolated from the solution.

Preparation of Cf(DOPO^q)$_2$(NO$_3$)(py). A 7 ml scintillation vial was charged $^{249}CfCl_3$ (0.005 g, 0.0141 mmol) and 2 ml of pyridine. A solution of HDOPO^q (0.0135 g, 0.031 mmol) dissolved in 2 ml of pyridine was added to the vial, causing a color change from green to dark teal. The solution sat overnight to allow evaporation of solvent. Teal plate crystals suitable for X-ray analysis formed, and were analyzed immediately.

Preparation of Eu(DOPO^q)(DOPO^{sq})(py)$_3$. A 20 mL scintillation vial was charged with $EuBr_2$ (0.012 g, 0.038 mmol) and 5 mL of pyridine. To this suspension was added a violet solution of HDOPO^q (0.050 g, 0.114 mmol) in 5 mL of pyridine, resulting in a color change to dark green. After stirring for an additional 5 minutes, the solution was filtered and concentrated in vacuo to a green powder assigned as Eu(DOPO^q)(DOPO^{sq})(py)$_3$. Green crystals suitable for X-ray analysis deposited upon slow diffusion of pentane into the pyridine solution at -35 °C.

2.3 Results and Discussion

2.3.1 Trivalent Lanthanide Complexes

Initial synthetic efforts focused on the synthesis of lanthanide tris(ligand) derivatives that would serve as model compounds for transuranic elements. An efficient synthesis using high boiling solvents that would quickly and reliably yield the desired tris(ligand) complexes was required for eventual extension to the appropriate transuranic materials. Treating stirring pyridine solutions of either CeCl$_3$, NdCl$_3$, or GdCl$_3$ with three equivalents of HDOPO^q generated deep blue solutions in each case, indicative of ligand metallation. Removal of the volatiles *in vacuo* followed by extraction with pentane and filtration to remove pyridinium chloride produced the corresponding tris(ligand) products, Ln(DOPO^q)$_3$ (Ln = Ce, Nd, Gd) as teal blue solids in good yields (76%, 68% and 71% respectively) (Scheme 2.1). Analysis by ^{1}H NMR spectroscopy of Gd(DOPO^q)$_3$ was not possible due to the paramagnetism stemming from the 7 unpaired electrons of Gd(III), but the Ce(III), f^1 and Nd(III), f^3 analogues produced interpretable spectra that had the appropriate number of peaks consistent with the expected symmetry of Ln(DOPO^q)$_3$ (Ln = Ce, Nd).

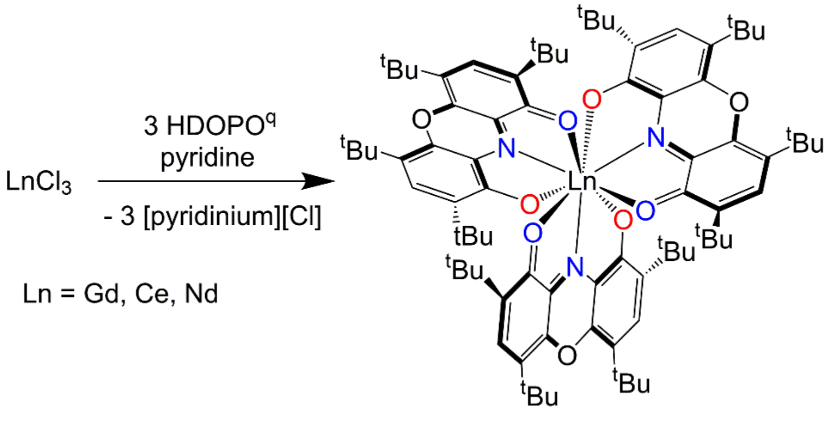

Scheme 2.1. Synthesis of Ln(DOPO^q)$_3$ (Ln = Gd, Ce, Nd) complexes.

Crystallization of Ce(DOPO^q)$_3$, Nd(DOPO^q)$_3$, and Gd(DOPO^q)$_3$ was possible directly from small scale mixtures utilizing 10 mg of LnCl$_3$ (Ln = lanthanide), three equivalents of ligand, and 5 mL of pyridine. Slow evaporation over 24 hours caused blue crystals to reliably and reproducibly precipitate from these concentrated solutions. Analysis of the crystals by X-ray diffraction confirmed the identities as Ce(DOPO^q)$_3$, Nd(DOPO^q)$_3$, and Gd(DOPO^q)$_3$, and the molecular structures are presented in Figure 2.1.

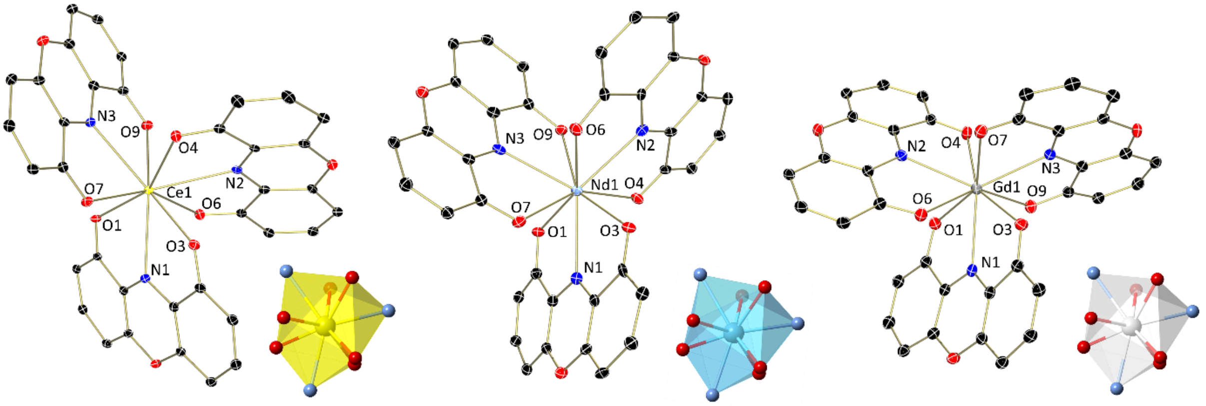

Figure 2.1. Molecular structures of Ce(DOPO^q)$_3$, Nd(DOPO^q)$_3$, and Gd(DOPO^q)$_3$ shown at 30% probability ellipsoids. Hydrogen atoms, *tert*-butyl groups, and co-crystallized solvent molecules have been omitted for clarity.

In each case, three statistically indistinguishable DOPO ligands were observed. (Table 2.1) The M-O distances, ranging from 2.4825(19) - 2.5234(18) Å for Ce(DOPO^q)$_3$, 2.463(3) - 2.492(3) Å for Nd(DOPO^q)$_3$, and 2.4206(15) - 2.4514(15) Å for Gd(DOPO^q)$_3$, are all appropriate for formulation as monoanionic quinone ligands. In this resonance form, the M-O bond distances should be averaged, as one bond has anionic character while the other is dative. Both the DOPO^{sq} and DOPO^{cat} forms of the ligand would display shorter bond distances because there would be no dative M-O interactions. Furthermore, the M-N distances are all long, with average values of 2.644, 2.588, and 2.536 Å for Ce(DOPO^q)$_3$, Nd(DOPO^q)$_3$, and Gd(DOPO^q)$_3$, respectively, again pointing towards the DOPO^q resonance form, which features a dative M-N interaction.

Table 2.1. Metal-ligand bond distances (in Å) for Ln DOPO complexes.

Bond	**Ce(DOPO^q)$_3$**	**Nd(DOPO^q)$_3$**	**Gd(DOPO^q)$_3$**
M-O1	2.4825(19)	2.463(3)	2.4276(17)
M-N1	2.644(2)	2.570(4)	2.5426(19)
M-O3	2.5204(19)	2.489(3)	2.4484(16)
M-O4	2.5058(19)	2.492(3)	2.4514(15)
M-N2	2.653(2)	2.608(4)	2.5527(19)
M-O6	2.5234(18)	2.470(3)	2.4295(16)
M-O7	2.5073(17)	2.473(3)	2.4316(17)
M-N3	2.634(2)	2.587(4)	2.514(2)
M-O9	2.4934(19)	2.474(3)	2.4206(15)

Because structural parameters are useful in assigning ligand oxidation states, analysis of the intraligand metrical parameters for each molecular structure were studied using the Metrical Oxidation State (MOS) method previously established by Brown.[4] Using this model, which takes into account the errors associated with the statistical fitting to idealized ligand oxidation states, the average ligand oxidation states were calculated. The average values of -1.08(15) (Ce(DOPO^q)$_3$), -1.03(15) (Nd(DOPO^q)$_3$), and -1.13(13) (Gd(DOPO^q)$_3$), are all consistent with the monoanionic, quinone resonance form of the ligand. By charge balance considerations, each lanthanide ion would be in the formal +3 oxidation state, as expected.

In collaboration with Laura Gagliardi at the University of Minnesota, the structures of the Ln DOPO complexes were optimized using density functional theory with the B3LYP exchange correlation functional (in combination with UFF dispersion) and DZP (TZP for Ln) set. The DFT metal-ligand bond distances along with the difference from the experimental values are reported in Table 2.2. The DFT metal-ligand bond lengths are similar to the experimental ones, even if DFT yields systematically shorter M-N bonds and longer M-O bonds. Overall the agreement is satisfactory, and DFT geometries could be used for further computational analysis.

Table 2.2. DFT (B3LYP) computed (and difference with experimental) metal-ligand bond distances (in Å) for Ln DOPO complexes.

Bond	**Ce(DOPO^q)$_3$**	**Nd(DOPO^q)$_3$**	**Gd(DOPO^q)$_3$**
M-O1	2.512 (0.030)	2.527 (0.064)	2.476 (0.048)
M-N1	2.553 (-0.091)	2.557 (-0.013)	2.495 (-0.048)
M-O3	2.515 (-0.005)	2.520 (0.031)	2.477(0.029)
M-O4	2.533 (0.027)	2.518 (0.026)	2.474 (0.023)
M-N2	2.577 (-0.076)	2.554 (-0.054)	2.494 (-0.059)
M-O6	2.530 (0.007)	2.529 (0.059)	2.477 (0.047)
M-O7	2.530 (0.023)	2.528 (0.055)	2.474 (0.042)
M-N3	2.571 (-0.063)	2.558 (-0.029)	2.493 (-0.021)
M-O9	2.521 (0.028)	2.522 (0.048)	2.472 (0.051)

Further confirmation of the ligand oxidation states for Ce(DOPO^q)$_3$, Nd(DOPO^q)$_3$, and Gd(DOPO^q)$_3$ was obtained from electronic absorption spectroscopic measurements (Figure 2.2). With experimental constraints for transuranic compounds in mind, the data for the lanthanide species were collected in the range of 300-1000 nm on single crystal samples. The data for each lanthanide derivative is analogous, showing two pronounced features in the visible region, with absorbances appearing at 399 and 716 nm for Ce(DOPO^q)$_3$, at 403 and 731 nm for Nd(DOPO^q)$_3$, and at 401 and 716 nm for Gd(DOPO^q)$_3$. The quinone form of the ligand typically shows intense ligand-to-ligand charge-transfer bands in the 650-800 range due to transitions into an empty DOPO^q -based π* orbital. The data for Ce(DOPO^q)$_3$, Nd(DOPO^q)$_3$, and Gd(DOPO^q)$_3$ are in accord with the uranium derivative, UO$_2$(DOPO^q)$_2$ (λ_{max} = 719 nm, 14,400 cm^{-1}M^{-1}),[48] as well as the alkali metal ligand salts KDOPO^q(THF) (λ_{max} = 735 nm, 9,750 cm^{-1}M^{-1})[7] and NaDOPO^q (λ_{max} = 695 nm).[3] The intensity of these ligand based transitions are such that any features from the lanthanide ion are dwarfed.

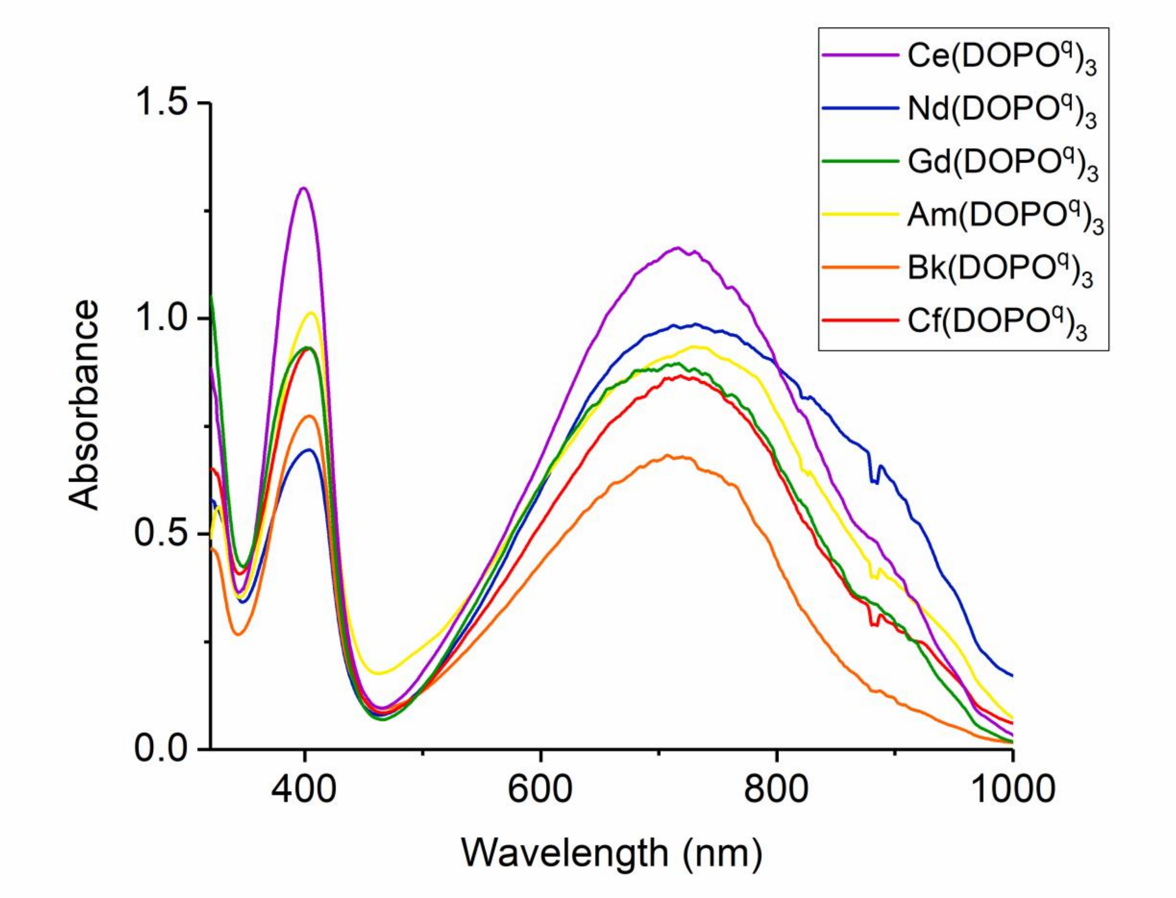

Figure 2.2. Electronic absorption spectra (collected on single crystal samples) for Ce(DOPO^q)$_3$, Nd(DOPO^q)$_3$, Gd(DOPO^q)$_3$, Am(DOPO^q)$_3$, Bk(DOPO^q)$_3$, and Cf(DOPO^q)$_3$ presented as absorbance.

To further support the ground state electronic structures in Ln(DOPO^q)$_3$ (Ln = Ce, Nd, and Gd), variable temperature magnetization and field-dependent magnetic measurements were performed (Figure 2.3). This was done in collaboration with Eric Schelter at the University of Pennsylvania. At room temperature, the μ_{eff} values of Ce(DOPO^q)$_3$, Nd(DOPO^q)$_3$, and Gd(DOPO^q)$_3$ were 2.49, 3.61, and 7.90 μ_B, respectively, in good agreement with the expected magnetic moments, 2.53, 3.62, and 7.94 μ_B for Ce^{3+}, Nd^{3+}, and Gd^{3+} cations.[49,57–62] Upon cooling, the μ_{eff} values decreased to 1.23, 1.97 and 6.49 μ_B, respectively, at 2 K. Such decreases in moments at lower temperatures for Ce(DOPO^q)$_3$ and Nd(DOPO^q)$_3$ results from the depopulation of Stark energy levels created by crystal field perturbations of the J = 5/2 and J = 9/2 manifold for the respective Ce^{3+} and Nd^{3+} cations. The behavior of Gd(DOPO^q)$_3$ was consistent with that previously reported.[49] Overall the magnetic data are consistent with monoanionic ligands that are in their quinone states ($S = 0$); the magnetic response of the Ln(DOPO^q)$_3$ complexes arise solely from the paramagnetic Ln^{3+} cations, with no open shell ligand contributions.

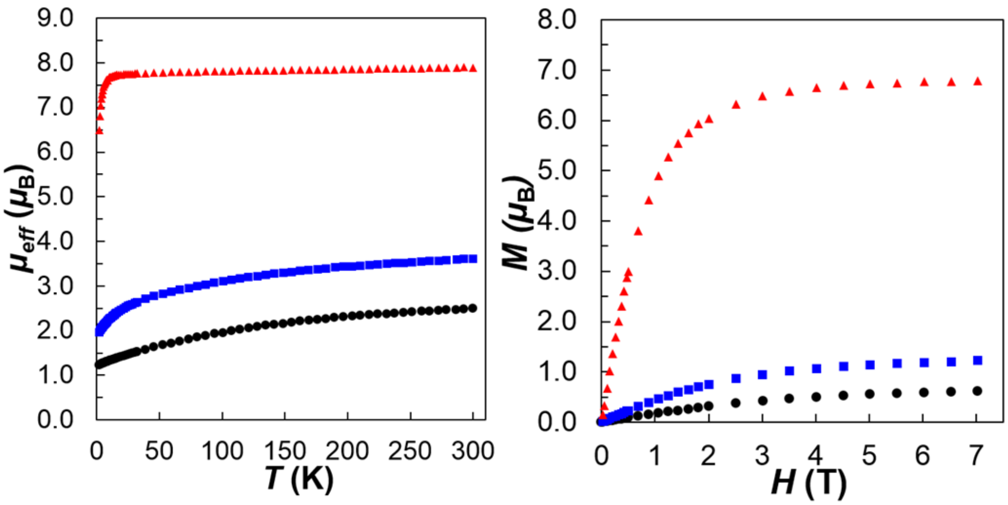

Figure 2.3. Variable-temperature molar magnetic data (μ_{eff}) for Ce(DOPO^q)$_3$ (black circles), Nd(DOPO^q)$_3$ (blue squares), and Gd(DOPO^q)$_3$ (red triangles).

2.3.2 Trivalent Actinide Complexes

With the synthetic and crystallization procedures established for the lanthanides, these protocols were scaled to perform on 5 milligram quantities of halide salts in preparation for extension to transuranic elements, including americium, berkelium, and californium. As for the lanthanide models, mixing ^{243}AmBr$_3$ and HDOPO resulted in the formation of Am(DOPO^q)$_3$ (Scheme 2.2).

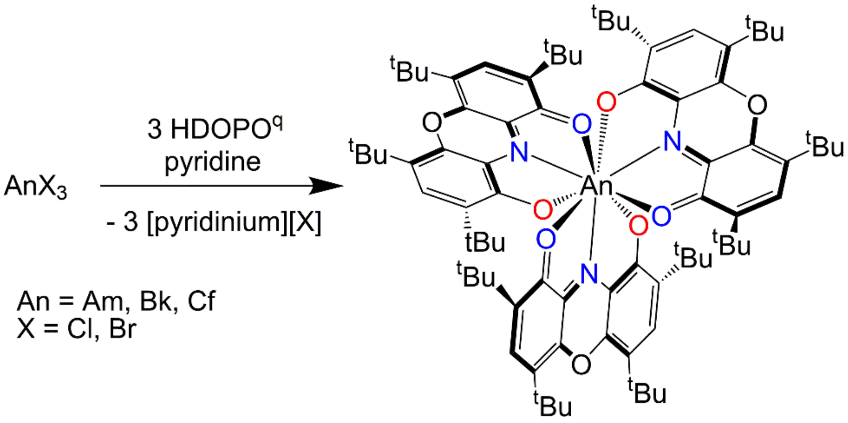

Scheme 2.2. Synthesis of An(DOPO^{q})$_3$ (An = Am, Bk, Cf) complexes.

Due to the technical challenges associated with transuranic elements, characterization by ^{1}H NMR spectroscopy was not possible. However, analysis of single crystals obtained from the analogous crystallization conditions confirmed the molecular structure of Am(DOPO^{q})$_3$. In this case, the americium has three DOPO^{q} ligands chelated to form a 9 coordinate distorted tricapped trigonal prismatic geometry (structure in Figure 2.4; bond metrics in Table 2.3). The Am-O distances range from 2.463(3)-2.494(3) Å, as the anionic and dative interactions are averaged across each ligand. For comparison, pure dative Am-O interactions range from 2.508(6)-2.525(4) Å in [Am(TMOGA)$_3$][ClO$_4$]$_3$ (TMOGA = tetramethyl-3-oxa-glutaramide).[63] No purely anionic Am-O bonds were noted in the CCDC. The Am-N bond distances range from 2.545(3)-2.591(3) Å, and are on par with those observed for [Am(PDA)(NO$_3$)(H$_2$O)$_2$]·H$_2$O[64] (H$_2$PDA = 1,10-phenanthroline-2,9-dicarboxylic acid) of 2.589(11) Å and Am(HDPA)$_3$[41] of (2.551(4), 2.591(3), 2.550(4)), both of which are established as containing Am^{3+}. The intraligand C-O bonds range from 1.265(5)-1.276(5) Å and C-N bonds range from 1.321(5)-1.342(5) Å, producing an average MOS value of -1.08(14) for the ligands. These intraligand bond metrics are in correspondence with published DOPO^{q} distances for transition metals.

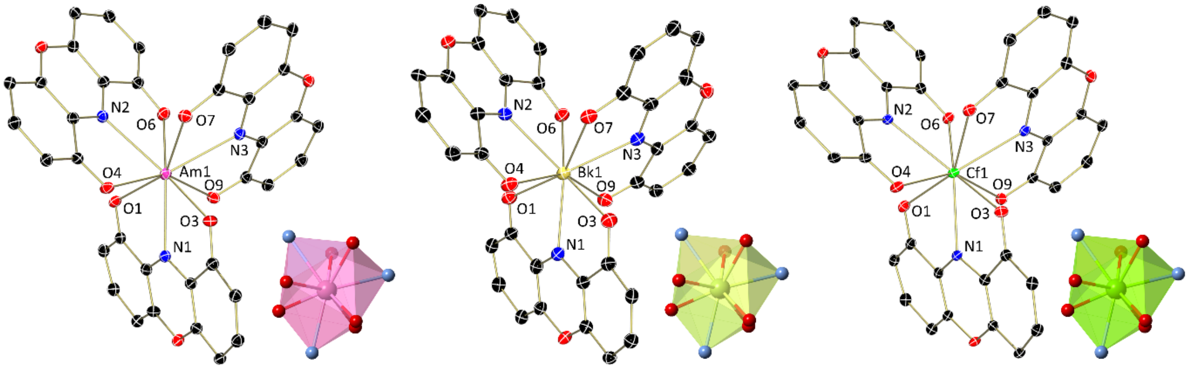

Figure 2.4. Molecular structures of Am(DOPO^q)$_3$, Bk(DOPO^q)$_3$, and Cf(DOPO^q)$_3$ shown at 30% probability ellipsoids. Hydrogen atoms, *tert*-butyl groups, and co-crystallized solvent molecules have been omitted for clarity.

Table 2.3. Metal-ligand bond distances (in Å) for An DOPO complexes.

Bond	**Am(DOPO^q)$_3$**	**Bk(DOPO^q)$_3$**	**Cf(DOPO^q)$_3$**
M-O1	2.488(3)	2.459(4)	2.448(2)
M-N1	2.554(3)	2.522(4)	2.511(2)
M-O3	2.463(3)	2.436(3)	2.423(2)
M-O4	2.493(3)	2.468(3)	2.463(2)
M-N2	2.591(3)	2.571(4)	2.549(2)
M-O6	2.747(3)	2.454(3)	2.436(2)
M-O7	2.472(3)	2.447(4)	2.435(2)
M-N3	2.582(3)	2.544(4)	2.538(2)
M-O9	2.482(3)	2.452(3)	2.456(2)

With the successful synthesis of Am(DOPO^q)$_3$, the berkelium and californium variants, Bk(DOPO^q)$_3$ and Cf(DOPO^q)$_3$, were also targeted. Treating either ^{249}BkCl$_3$ or ^{249}CfCl$_3$ with three equivalents of HDOPO in pyridine produced the same striking color change from pale green to vibrant teal, indicative of the desired products (Scheme 2.2). Furthermore, using 10 equivalents of ligand instead of three aided in crystallization, thus single crystals suitable for X-ray diffraction could be isolated within 1 hour. In the absence of excess ligand, the timescale of crystallization was too long, and radiolytic degradation of both desired compounds was observed as signified by a color change from teal to red-brown (see Section 2.3.6).

Overall, both the Bk-ligand and Cf-ligand bond distances are in accord with trivalent metals, as expected (structures in Figure 2.4; bond metrics in Table 2.3). In the berkelium and californium analogues, the Bk-O distances, ranging from 2.436(3)-2.468(3) Å, and the Cf-O bond lengths, ranging from 2.423(2)-2.463(2) Å, are within error of those reported for $Bk(HDPA)_3$ (2.410(3)-2.497(3) Å) and $Cf(HDPA)_3$ (2.387(4)-2.494(4) Å),[46] respectively. The long Bk-N (2.522(4), 2.571(4), and 2.544(4) Å) and Cf-N (2.511(2), 2.549(2) and 2.538(2) Å) distances are indicative of dative Bk-N and Cf-N interactions, suggesting a central berkelium +3 and californium +3 ions, similar to those in $Bk(HDPA)_3$ and $Cf(HDPA)_3$. This is further supported by the intraligand distance analysis that yields nearly identical average MOS values of -1.08(12) Å for $Bk(DOPO^q)_3$ and -1.08(13) Å for $Cf(DOPO^q)_3$, supporting the monoanionic, quinone resonance form of the ligands is dominant in both cases.

In collaboration with Laura Gagliardi at the University of Minnesota, the structures of the An DOPO complexes were optimized using density functional theory with the B3LYP exchange correlation functional (in combination with UFF dispersion) and DZP (TZP for An) set. The DFT metal-ligand bond distances along with the difference from the experimental values are reported in Table 2.4. The DFT metal-ligand bond lengths are similar to the experimental ones, even if DFT yields systematically shorter M-N bonds and longer M-O bonds. Overall the agreement is satisfactory, and DFT geometries could be used for further computational analysis.

Table 2.4. DFT (B3LYP) computed (and difference with experimental) metal-ligand bond distances (in Å) for An DOPO complexes.

Bond	**$Am(DOPO^q)_3$**	**$Bk(DOPO^q)_3$**	**$Cf(DOPO^q)_3$**
M-O1	2.586 (0.098)	2.505 (0.046)	2.545 (0.097)
M-N1	2.542 (-0.012)	2.441 (-0.081)	2.494 (-0.017)
M-O3	2.595 (0.132)	2.495 (0.059)	2.537 (0.114)
M-O4	2.579 (0.086)	2.590 (0.112)	2.567 (0.104)
M-N2	2.522 (-0.069)	2.494 (-0.077)	2.492 (-0.057)
M-O6	2.586 (0.112)	2.528 (0.074)	2.528 (0.092)
M-O7	2.558 (0.086)	2.532 (0.085)	2.567 (0.132)
M-N3	2.507 (-0.075)	2.492 (-0.052)	2.484 (-0.054)
M-O9	2.573 (0.091)	2.583 (0.131)	2.542 (0.086)

Characterization by electronic absorption spectroscopy on single crystals of $Am(DOPO^q)_3$, $Bk(DOPO^q)_3$, and $Cf(DOPO^q)_3$, further corroborates the formulation of the ligands as the monoanionic, $DOPO^q$ resonance form (Figure 2.2). Again, these data show absorbances for π to π* transitions for $Am(DOPO^q)_3$ at 427 and 746 nm, for $Bk(DOPO^q)_3$ at 404 and 707 nm, and for $Cf(DOPO^q)_3$ at 404 and 719 nm, which are all in accord with the lanthanide models. These ligand based transitions are so intense that any features due to the individual metal ions are not visible. This supports the similar teal-blue color that is noted for all of these derivatives.

In order to gain further insight into the bonding nature of the aforementioned synthesized compounds, Laura Gagliardi and her group performed a computational analysis by means of complete active space self consistent field, CASSCF, calculations. Initial analysis started with the lanthanide-DOPO complexes (Ce(III), Nd(III), Gd(III)). For $Ce(DOPO^q)_3$, there is only one unpaired electron on the seven 4f orbitals. Therefore, the relative energies of all possible doublet spin states were computed for a CASSCF(1,7) (one electron in seven orbitals) model. A LoProp[65] charge analysis and Mulliken spin density analysis was also performed, and this shows that the orbitals and spin density are completely localized on the cerium (4f orbitals), with no interaction with the ligand. The computational analysis for both Nd(III) and Gd(III) shows analogous results as the one for Ce(III). Thus for the lanthanide-DOPO complexes, the computational analysis reveals no significant interaction between the metal and the ligands in terms of redox flexibility, in agreement with the experimental results.

Subsequently, CASSCF calculations were also performed for the actinide-DOPO analogues (Am(III), Cf(III), Bk(III)). The $Am(DOPO^q)_3$ complex presents an electronic structure with six unpaired electrons in seven 5f orbitals, (CASSCF(6,7)), allowing analysis in all possible spin states (septets, quintets, triplets, and singlets). The high-spin septet state was determined to be the ground state, and the orbitals for the septet ground state root reveal a high localization of the unpaired electrons on the 5f orbitals of americium, (Figure 2.5 (first row)). Such localization has previously been found in related uranium(III) complexes.[66] The wave function analysis of the septet ground state root reveals multi-reference character, with all spin density located on the Am atom and a LoProp charge on Am of 2.45. No interaction of Am(III) with the DOPO ligand occurs. The computational analysis for $Bk(DOPO^q)_3$ showed a similar picture. In this case, 8 electrons were distributed among the 7 5f orbitals (CASSCF(8,7)). Overall, the system shows multi-configurational character, with the quintet state as the lowest in energy. An energetically accessible triplet state lies just 13.2 kcal/mol (0.572 eV) higher in energy. The Mulliken charge analysis for the quintet state for Bk totals 2.13, while the LoProp charge is 2.40, very similar to that for Am(DOPO^{q})$_3$, and the spin density is 3.98 for Bk. Overall, the active space orbitals are localized on berkelium(3+), and there is very little interaction between Bk and the DOPO ligands.

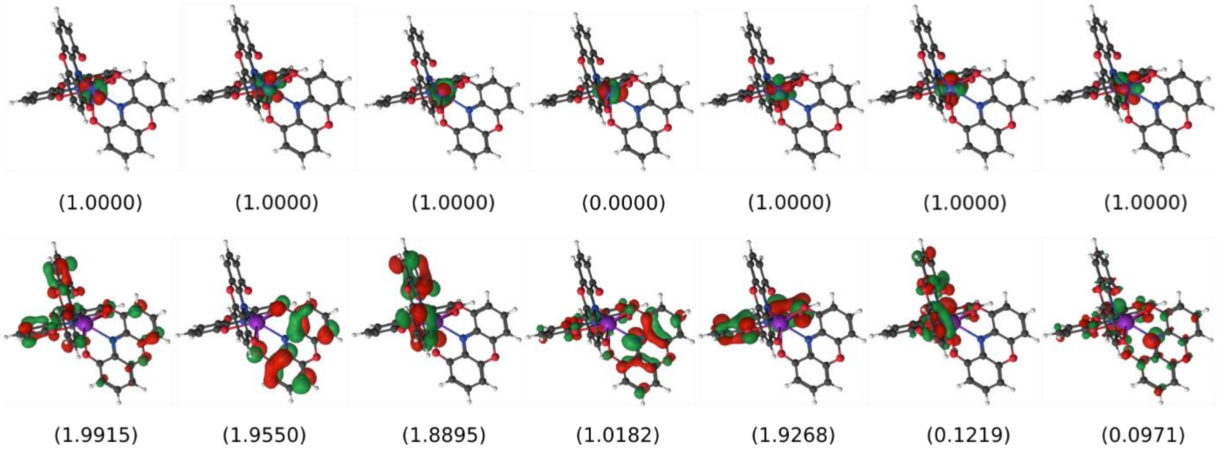

Figure 2.5. Active space orbitals (occupation numbers in parentheses) for the ground state root of Am(DOPO^{q})$_3$ (septet spin state, first row) and Cf(DOPO^{q})$_3$ (doublet spin state, second row).

Cf(DOPO^{q})$_3$ was also analyzed by means of CASSCF(9,7) calculations for the sextet, quartet and doublet spin states. In this case, the ground state is the lowest-spin one, namely the doublet, with the quartet state being perhaps still accessible (17.4 kcal mol^{-1} higher). The analysis of the active space orbitals of the ground state root of the doublet spin state (Figure 2.5, bottom) reveals that there are 4 (almost) doubly occupied orbitals, one orbital with one unpaired electron and two (almost) empty orbitals, each of them encompassing a small contribution from the Cf atom. The unpaired electron is mostly localized on the ligand, as further confirmed by the Mulliken spin density analysis. The 5f orbitals of Cf are either doubly occupied (four of them), or empty (three of them). Furthermore, the LoProp charge for Cf in the ground doublet state is 2.43, indicating a californium in the +2 oxidation state, rather than the +3 oxidation state as experimental ligand parameters indicate.

From this computational analysis, differences can be pointed out among the nature of the bonding of actinides with DOPO. Inspection of the SOMO levels for Am(DOPO^q)$_3$ shows that these orbitals are entirely f orbital based. Thus, this compound behaves similarly to the lanthanides with this ligand, with little to no ligand redox activity. However, the SOMOs for Cf(DOPO^q)$_3$ are striking, as these orbitals show ligand involvement. Clearly this element, which is later in the actinide series, is showing some covalent interaction with the ligand. This is likely due to the propensity of californium to favor the +2 oxidation state. This has been previously demonstrated with the dipicolinate derivative, Cf(Hdpa)$_3$.[46] Thus, the experimental data obtained here supports the "californium break" in the actinide series, where despite the fact that it is later in the series, it actually shows more covalent behavior than its neighbors to the left.

With this rare isostructural family in hand, it is possible to now make comparisons of structural parameters across the actinide series. As periodic trends dictate, traversing the actinide series from left to right results in a decrease in atomic radius. Theory predicts in moving from Am to Cf that there should be a decrease by 0.01 Å with each step, for a total of a 0.03 Å decrease. Examination of the difference between the average Am-N (2.572(4) Å, 2.524 Å with DFT) and Cf-N (2.533(2) Å, 2.490 Å with DFT) bonds is $\Delta = 0.04$ Å (0.034 Å with DFT), while the difference in the respective bond distances for the corresponding M-O bonds (Am: 2.475(4), 2.580 Å with DFT; Cf: 2.444(2) Å, 2.548 Å with DFT) is $\Delta = 0.03$ Å (0.032 Å with DFT). Although the magnitude of the Δ value is as expected, these values differ from what has been previously established for californium. For instance, comparing Am(Hdpa)$_3$ and Cf(Hdpa)$_3$, average values for Δ(M-O) = 0.046, 0.037 Å and Δ(M-N) = 0.042, 0.037 Å indicate that there is more contraction in these bonds as compared to the tris(DOPO^q) system. This is likely due to both steric and electronic factors. The extreme sterics imparted by the tris(DOPO^q) framework could result in slight bond elongation to alleviate strain from the large tert-butyl substituents. Electronically, the computational data supports a canonical resonance form where the californium is in the +2 oxidation state that can contribute to the overall electronic structure of Cf(DOPO^q)$_3$.

2.3.3 Tetravalent Actinide Complexes

When conducting many of the experiments for heteroleptic DOPO synthesis and reactivity for uranium (Section 1.3.1), a common minor side was often observed (before to the isolation of any other tris(DOPO) complex). This byproduct was observed in the ^{1}H NMR spectra as two equivalent peaks at 0.45 and 1.55 ppm, each integrating to 18H, and a much smaller, upfield-shifted peak at -82.80 ppm that integrated to 2H. It was hypothesized that this was a multi(DOPO) product, but initially it was unclear if it was the homoleptic bis(DOPO) or tris(DOPO) product.

With predictions of this product identity, an independent synthesis was sought to determine the identity of the product. Attempts to make a bis(DOPO) complex by addition of two equivalents of KDOPO^{q}THF to UI$_3$(THF)$_4$ yielded the targeted product (identified by ^{1}H NMR spectroscopy), but the same results were obtained with the addition of three equivalents of KDOPO^{q}THF to UI$_3$(THF)$_4$ so the two possibilities could not be distinguished. However, the addition of three equivalents of HDOPO^{q} to a stirring solution of U[N(SiMe$_3$)$_2$]$_3$ resulted cleanly in the desired product with no excess ligand present. Therefore, the product was tentatively assigned as U(DOPO)$_3$ (Scheme 2.3).

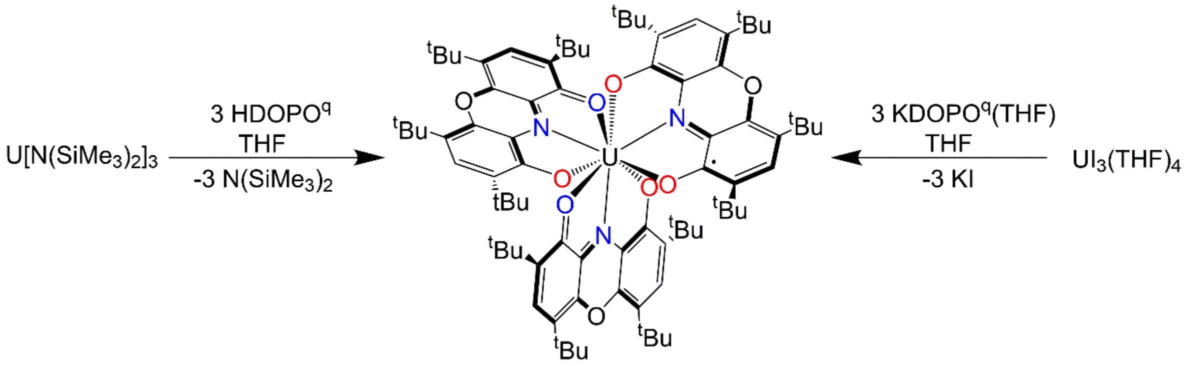

Scheme 2.3. Synthesis of U(DOPO^{q})$_2$(DOPO^{sq}) through protonation (left) and salt metathesis (right).

To confirm the identity of this product, green crystals of (DOPO)$_3$U were grown by slow evaporation from pentane and analyzed by X-ray crystallography, which confirmed the assignment as U(DOPO)$_3$ (Figure 2.6). Refinement of the data shows a pseudo tricapped trigonal prismatic geometry around the uranium center, while the idealized D_3 symmetry is consistent with the solution structure observed by ^{1}H NMR spectroscopy. The U-O bonds of 2.346(3) and 2.349(3) Å are slightly longer than those for (DOPO^{sq})UI$_2$(THF)$_2$ (2.203(4) and 2.231(4) Å). These distances are, however, in the range of typical aryloxide ligand distances for uranium 4+.[15] Similarly, the U-N bond distance of 2.522(3) Å is quite elongated from the U-N distance in (DOPO^{sq})UI$_2$(THF)$_2$ (2.371(4) Å) and is more consistent with the U-N distance of compound (DOPO^q)$_2$UO$_2$ (2.676(6) Å). These elongations in U-DOPO bonds are likely caused by steric interactions as this nine-coordinate uranium center would be quite encumbered, especially with the ligand *tert*-butyl groups pointing towards each other. Thus, electronic assignments are not possible from metal-ligand distances.

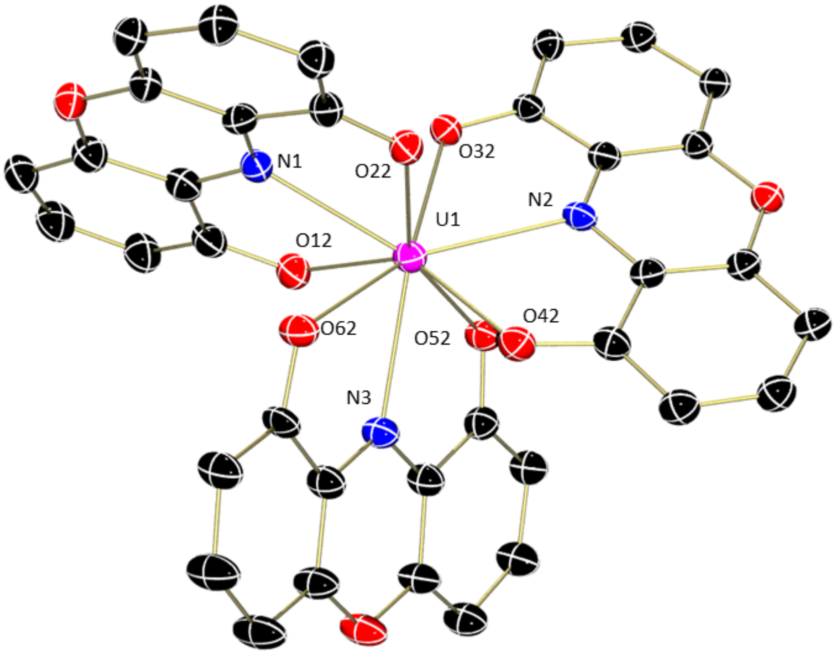

Figure 2.6. Molecular structure of U(DOPO^q)$_2$(DOPO^{sq}) shown at 30% probability ellipsoids. Hydrogen atoms, *tert*-butyl groups, and co-crystallized solvent molecules have been omitted for clarity.

In an attempt to assign the ligand and metal oxidation state for $U(DOPO)_3$, the intraligand bond distances were analyzed. These distances were summarized with the Metrical Oxidation State model.[4] This model showed an average MOS for the DOPO ligands of -1.71(18) with no spastically significant differences in each ligand oxidation state. This would imply a uranium oxidation state of +5, which is inconsistent with the sharp ^{1}H NMR spectrum. With the large errors associated with this model, it was assumed that the uranium is instead in the +4 or +6 oxidation state.

In general, the ligand and uranium oxidation states in $U(DOPO)_3$ could be quite diverse. For example, the uranium could exist in oxidation state +3, +4, +5, +6 due to the inherent redox-activity of the DOPO ligand. The uranium +6 possibility could be supported by three -2 $DOPO^{sq}$ ligands in a symmetric fashion, or it could have asymmetric DOPO ligands in different oxidation states. Similarly, the U^{+4} possibility could exist with independent DOPO ligand oxidation states in the form $U(DOPO^{q})_2(DOPO^{sq})$, or it could have the extra electron delocalized across all π* DOPO ligand orbitals. The latter case has been observed for similar transition metal complexes.[4]

Magnetic measurements were conducted to elucidate the complicated electronics of this complex. In collaboration with Eric Schelter and his group, variable temperature magnetization and field-dependent magnetic measurements were performed (Figure 2.7). The room temperature effective magnetic moment of 2.93 μ_B and low temperature (2 K) moment of 1.42 μ_B are consistent with the assignment of this compound as a uranium +4 center supported by two, monoanionic $DOPO^{q}$ ligands and one dianionic $DOPO^{sq}$ ligand. This assignment based on magnetic data is quite consistent with the similar compound, $(DOPO^{sq})UI_2(THF)_2$, that has a low temperature moment (2K) of 1.81 μ_B (Figure 1.3).

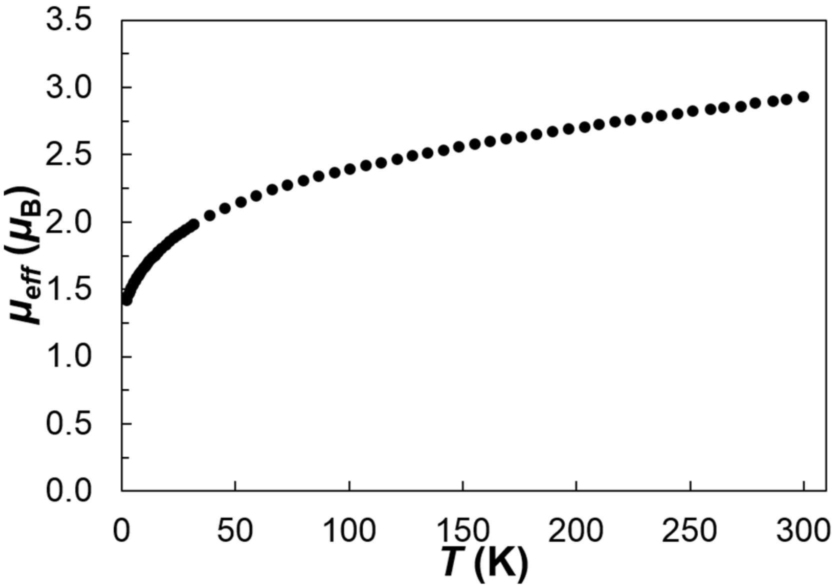

Figure 2.7. Variable-temperature molar magnetic data (μ_{eff}) for U(DOPO^q)$_2$(DOPO^{sq}).

The assignment of the uranium tris(DOPO) complex as U^{+4}(DOPO^q)$_2$(DOPO^{sq}) highlights an interesting feature for the tris(DOPO) platform. This compound is isostructural to other trivalent tris(DOPO) complexes, yet not isoelectronic. Therefore, the tris(DOPO) framework is able to stabilize a diverse array of metal centers in an isostructural series, even if the metals in the series don't have common stable oxidation states. This is particularly useful for understanding periodic trends in the transuranic series, since direct comparisons between different elements are hindered by the lack of chemical studies and structural understanding of these rare elements.

Therefore, synthesis of other actinide tris(DOPO) complexes that would likely be more stable in the tetravalent state was attempted. In an analogous fashion to the synthesis of the trivalent analogues, three equivalents of HDOPO^q were added to a pyridine solution of PuBr$_3$, resulting in a darkening of the solution. Overnight, dark purple block crystals formed from the solution. Analysis of the crystals revealed the desired product Pu(DOPO^q)$_2$(DOPO^{sq}) (Scheme 2.4, Figure 2.8).

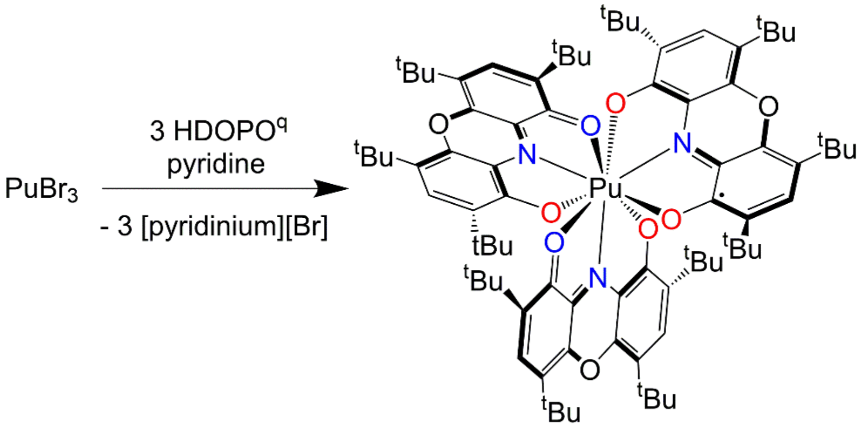

Scheme 2.4. Synthesis of Pu(DOPO^q)$_2$(DOPO^{sq}).

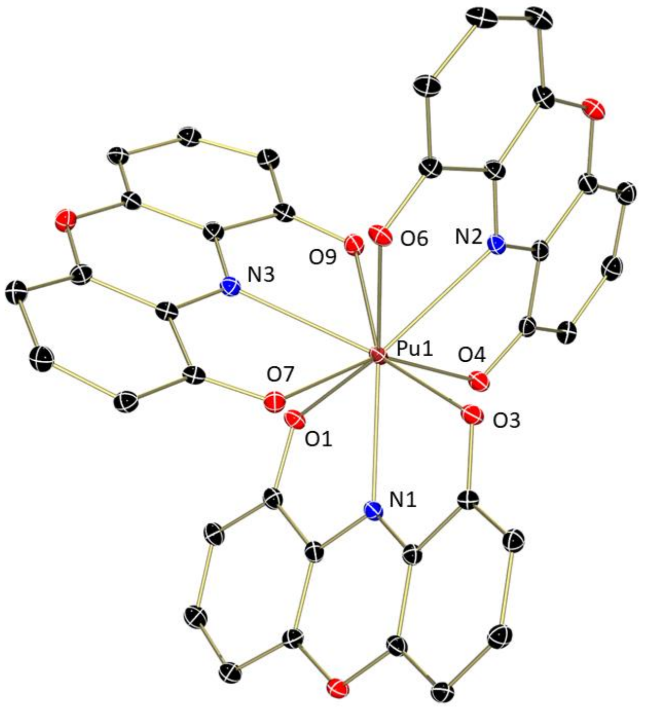

Figure 2.8. Molecular structure of Pu(DOPO^q)$_2$(DOPO^{sq}) shown at 30% probability ellipsoids. Hydrogen atoms, *tert*-butyl groups, and co-crystallized solvent molecules have been omitted for clarity.

Unlike the uranium tris(DOPO) example, this plutonium complex has a ligand that is clearly in a more reduced state. This is initially evident in the metal-ligand distances. Plutonium oxygen distances to O1 and O3 (2.2890(16) and 2.2886(17) Å) are much shorter than the other plutonium oxygen distances (2.3434(17), 2.3869(16), 2.4001(17), and 2.4253(16) Å). In a similar manner, the plutonium N1 distance is 2.4122(19) Å, shorter than the Pu-N2 (2.5428(19) Å) and Pu-N3 (2.538(2) Å) distances. This shortening is likely due to binding to a more reduced, DOPO^{sq} ligand. Analysis of the intraligand bond distances with the Metrical Oxidation State model reveals a similar conclusion.[4] Analysis reveals that two ligands have MOS values of -1.13(23) and -1.16(20), while the third ligand has an MOS value of -1.95(23). This is consistent with the electronic assignment of Pu(DOPO)$_3$ as Pu^{4+}(DOPO^q)$_2$(DOPO^{sq}).

Due to the lack of suitable trivalent starting materials for some elements in the actinide series, a new route from tetravalent elements was needed. Thorium was chosen for these initial studies, with hopes to translate the results to neptunium. This synthesis proved to be much more difficult as reductions in pyridine were not possible. Instead of protonation routes, salt metathesis was chosen (Scheme 2.5). Addition of three equivalents of KDOPO^q(THF) to a THF suspension of ThCl$_4$(DME)$_2$ resulted in a slight color change to green, and the ThCl$_4$(DME)$_2$ was fully solubilized. Addition of one equivalent of KC$_8$ resulted in very little color change. The solution was concentrated *in vacuo* to a green powder. This crude product was extracted in toluene, filtered to remove graphite and KCl and again concentrated to a green powder. The product was then dissolved in pyridine, which produced green X-ray quality crystals overnight.

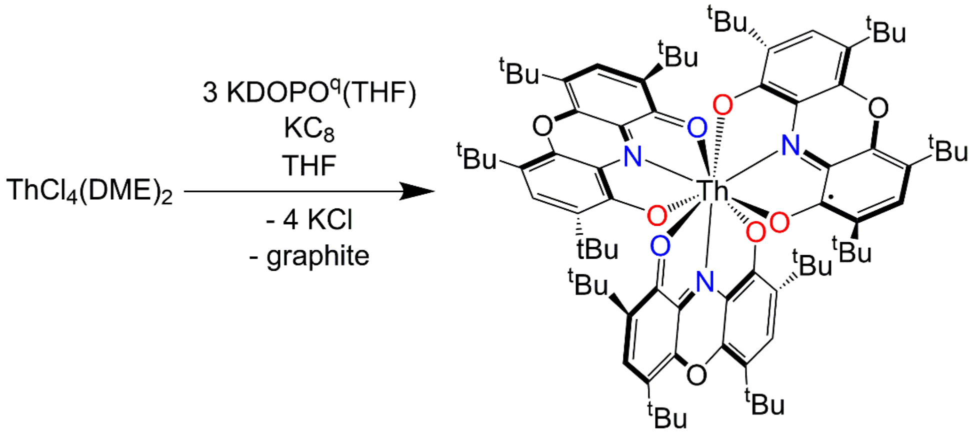

Scheme 2.5. Synthesis of Th(DOPO^q)$_2$(DOPO^{sq}).

Analysis of the crystals revealed the desired tris(DOPO) chelate (Figure 2.9). Metal-ligand distances show a similar case to the plutonium example. One ligand shows short Th-N (2.524(3) Å) and Th-O (2.365(3) and 2.372(3) Å) distances, while the other two have much longer Th-N (2.640(4) and 2.647(4) Å) and Th-O (2.453(3), 2.480(3), 2.486(3), and 2.491(3) Å) distances. Metrical Oxidation State analysis also supports the assignment of one reduced ligand with MOS values of -1.44(17), -1.26(17), and -2.12(16). Therefore, this complex was more specifically assigned as Th(DOPO^{q})$_2$(DOPO^{sq}).

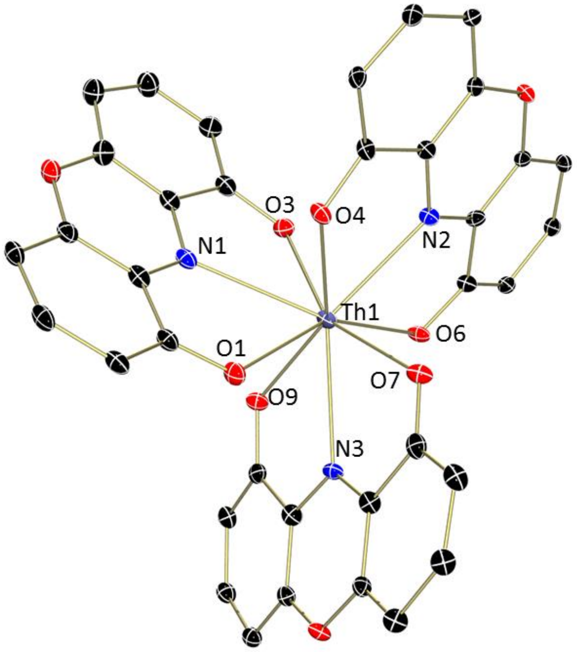

Figure 2.9. Molecular structure of Th(DOPO^{q})$_2$(DOPO^{sq}) shown at 30% probability ellipsoids. Hydrogen atoms, *tert*-butyl groups, and co-crystallized solvent molecules have been omitted for clarity.

2.3.4 Transition Metal Complex

To understand the versatility of the tris(DOPO) framework for stabilizing a variety of metal centers, transition metal analogues were targeted. Transition metal bis(DOPO) complexes were already well known, but it was hypothesized that transition metals that had large enough ionic radii could accommodate three DOPO ligands. Due to its relatively large ionic radius, hafnium was chosen as a representative example (0.085 Å for Hf^{+4}).

In a similar fashion to the synthesis of Th(DOPO^{q})$_2$(DOPO^{sq}), addition of three equivalents of KDOPO^{q}(THF) to a THF suspension of HfCl$_4$ resulted in a slight color change to green, and the HfCl$_4$ was fully solubilized. Addition of one equivalent of KC$_8$ resulted in very little color change (Scheme 2.6). The solution was concentrated *in vacuo* to a green powder. This crude product was extracted in toluene, filtered to remove graphite and KCl, and again concentrated to a green powder. This product was then dissolved in pyridine, which produced green X-ray quality crystals overnight.

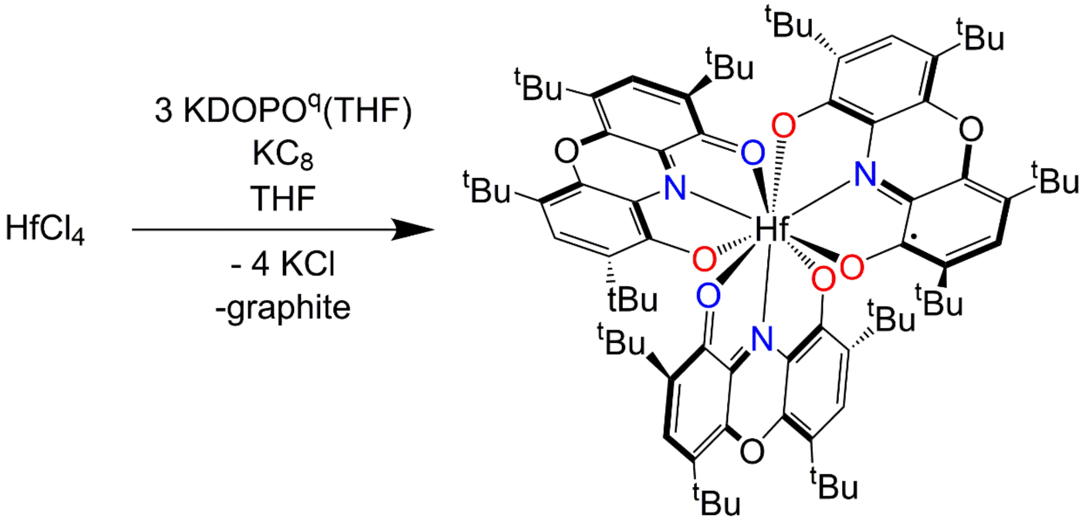

Scheme 2.6. Synthesis of Hf(DOPO^{q})$_2$(DOPO^{sq}).

Analysis of the crystals revealed the desired tris(DOPO) chelate (Figure 2.10). Metal-ligand distances show a similar case to the plutonium and thorium examples. One ligand shows short Hf-N (2.258(3) Å) and Th-O (2.167(3) and 2.159(3) Å) distances, while the other two have much longer Hf-N (2.346(4) and 2.343(4) Å) and Th-O (2.237(3), 2.253(3), 2.253(3), and 2.250(3) Å) distances. Metrical Oxidation State analysis also supports the assignment of one reduced ligand with MOS values of -1.13(23), -1.16(20), and -1.95(23). Therefore, this complex was more specifically assigned as Hf(DOPO^{q})$_2$(DOPO^{sq}). Additionally, this is the first tris(DOPO) complex that is visually distinct from the other complexes, as the steric strain of the saturated coordination sphere is evident in the crystal view depicted in Figure 2.10. For this structure, there is no view where the ligands don't overlap, highlighting the tighter bite angle to the small Hf^{4+} cation.[37]

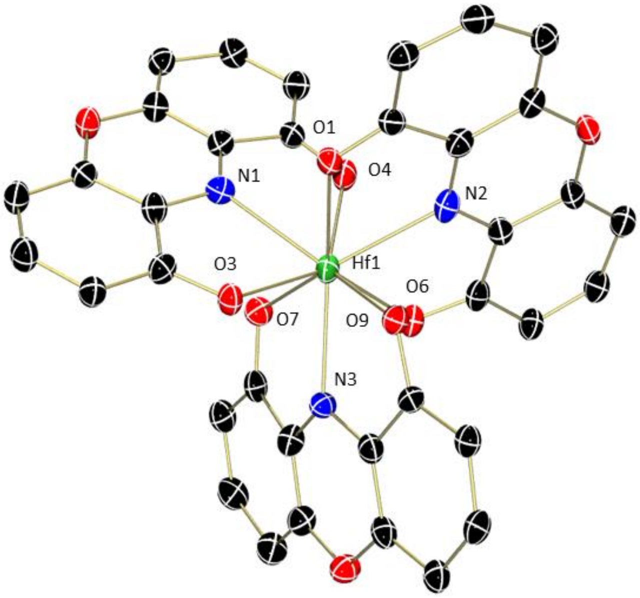

Figure 2.10. Molecular structure of $Hf(DOPO^{q})_2(DOPO^{sq})$ shown at 30% probability ellipsoids. Hydrogen atoms, *tert*-butyl groups, and co-crystallized solvent molecules have been omitted for clarity.

2.3.5 Main Group Complex

To expand this series even more, large main group elements were explored with the tris(DOPO) platform. Bismuth was chosen based on its large ionic radius (1.03 Å)[37] and preference for the 3+ oxidation state like the lanthanide series. In analogy to the synthesis of the lanthanide tris(DOPO) complexes, a solution of $HDOPO^{q}$ (3 equivalents) dissolved in pyridine was added to $BiCl_3$ in pyridine, causing a color change from purple to blue (Scheme 2.7). Upon sitting overnight, large blue block crystals suitable for X-ray crystallography formed.

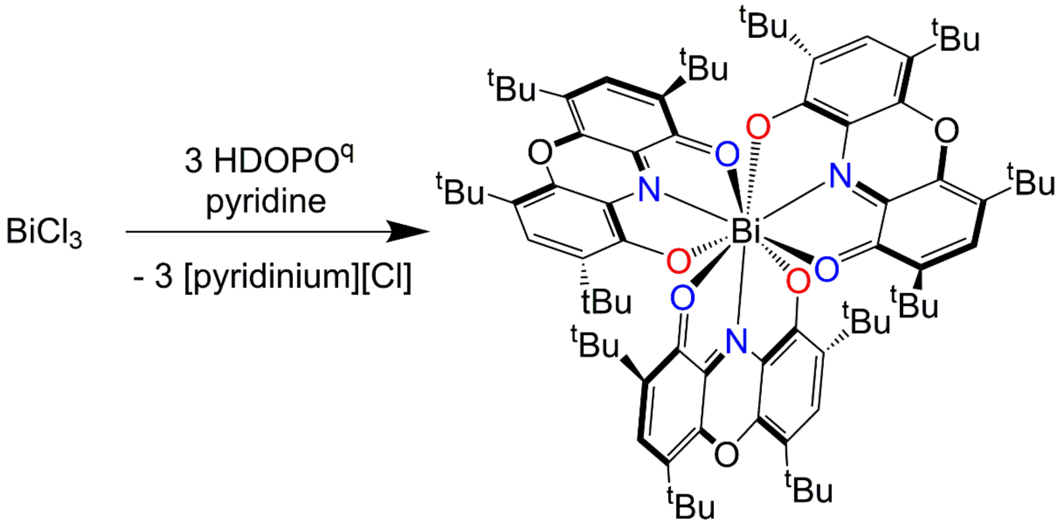

Scheme 2.7. Synthesis of Bi(DOPO^q)$_3$.

Analysis of the crystals revealed the desired tris(DOPO) chelate (Scheme 2.7). The Bi-N distances range from 2.533(3)-2.600(2) Å, while the Bi-N distances range from 2.405(2)-2.621(2). Although these ranges are statistically significant and span a large range, it is hypothesized that they vary due to steric considerations because of the limited redox-activity of bismuth 3+. This hypothesis is supported by the Metrical Oxidation State analysis, which has consistent MOS values of -1.06(14), -1.07(18), and -1.08(12).[4]

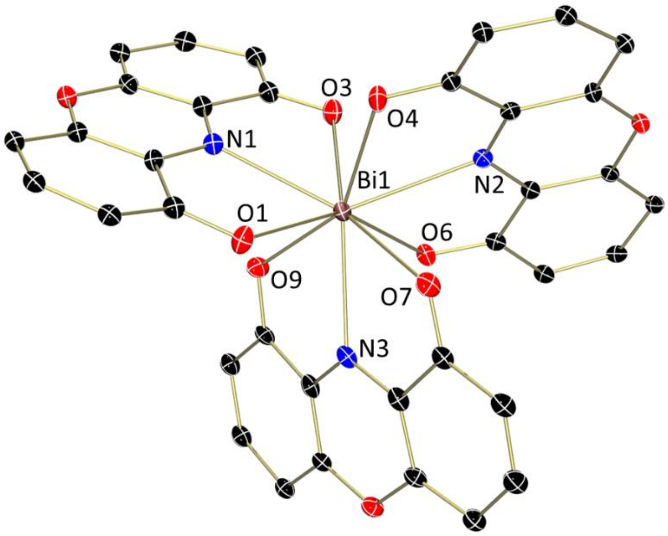

Figure 2.11. Molecular structure of Bi(DOPO^q)$_3$ shown at 30% probability ellipsoids. Hydrogen atoms, *tert*-butyl groups, and co-crystallized solvent molecules have been omitted for clarity.

2.3.6 Californium Bis(DOPO) Complex from Radiolytic Damage

Prior to the successful isolation of Cf(DOPO^q)$_3$ using excess equivalents of HDOPO^q (Section 2.3.2), another product was identified. Treating ^{249}CfCl$_3$ with three equivalents of HDOPO^q in pyridine produced a striking color change from pale green to vibrant teal, indicative of the desired product. Subjecting this material to the typical tris(DOPO) crystallization conditions resulted in isolation of crystals of Cf(DOPO^q)$_2$(NO$_3$)(py), which was confirmed by X-ray diffraction analysis. In this case, two DOPO^q ligands, one pyridine molecule, and one κ^2-nitrate fill the coordination sphere of Cf (Scheme 2.8, Figure 2.12). Overall, the californium-ligand bond distances are in accord with a trivalent Cf. The Cf-O bond lengths, ranging from 2.404(3)-2.419(3) Å, are similar to those reported for Cf(HDPA)$_3$ (2.387(4)-2.494(4) Å),[46] which is established to contain a +3 californium ion. The Cf-N distances of 2.496(4) and 2.527(4) Å in Cf(DOPO^q)$_2$(py)(NO$_3$) correspond well to those in Cf(HDPA)$_3$ of 2.508(4), 2.512(4), 2.545(4) Å. The intraligand distances for both DOPO ligands produce an average MOS value of -1.02(17), consistent with the quinone resonance form.

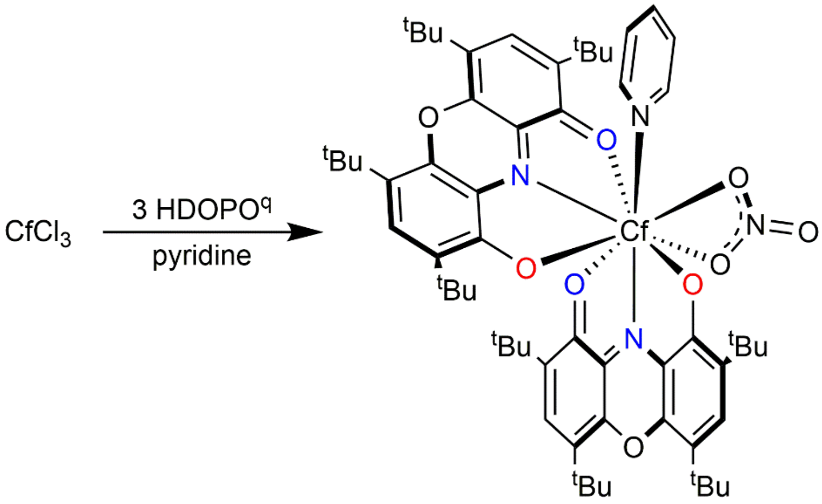

Scheme 2.8. Synthesis of Cf(DOPO^q)$_2$(NO$_3$)(py) from radiolytic degradation.

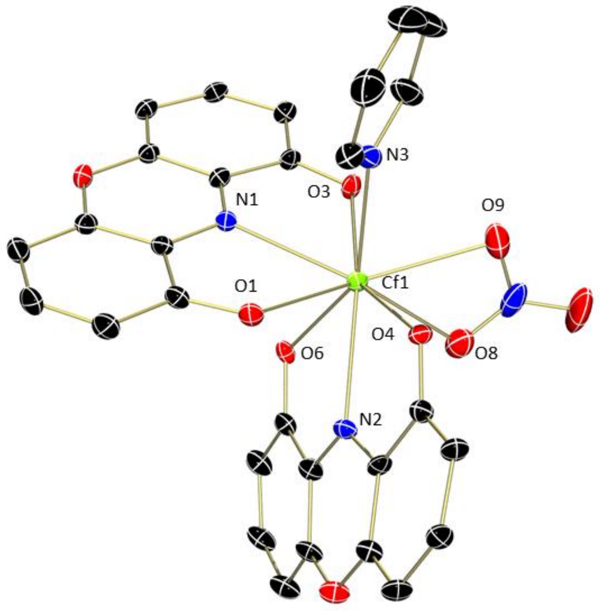

Figure 2.12. Molecular structure of Cf(DOPO^q)$_2$(NO$_3$)(py) shown at 30% probability ellipsoids. Hydrogen atoms, *tert*-butyl groups, and co-crystallized solvent molecules have been omitted for clarity.

Repeated attempts at isolation of crystals of Cf(DOPO^q)$_3$ without adding excess HDOPO^q ligand were unsuccessful, with crystals of Cf(DOPO^q)$_2$(NO$_3$)(py) obtained every time. A high resolution mass spectrum of the starting material, $^{249}CfCl_3$, reveals no nitrate incorporation, thus the nitrate is presumably formed over the course of the crystallization. This is clearly visible as the initial dark teal solution of $Cf(DOPO^q)_3$ changes to burgundy, signifying formation of $Cf(DOPO^q)_2(NO_3)(py)$. Thus the nitrate is likely formed from radiolysis of the pyridine or $DOPO^q$ ligand in the presence of water. As the nitrate concentration increases, the nitrate competes for the californium, disrupting the desired tris(chelate). Nitrate formation is not unprecedented in radiochemistry, as previous studies have shown that nitrate can form from radiolysis of N_2 by ^{239}Pu in water.[67] Generation of the californium nitrate highlights that while non-aqueous chemistry can be performed with highly radioactive elements, crystallization conditions need to be tuned to deposit crystals readily to avoid radiolysis products

2.3.7 Europium Bis(DOPO) Complex

As the homoleptic, tris(DOPO) complexes were being developed, there was also interest in exploring bis(DOPO) complexes in case the desired metal centers were too small to accommodate three DOPO ligands. Bis(DOPO) complexes are already well known for transition metals,[4] but the prospect of bis(DOPO) f-block complexes was of particular interest to this work. To explore this chemistry, europium was first targeted since it has an assessable +2 oxidation state that could allow for a synthetic route without the need for external reductant. Addition of two equivalents of $KDOPO^q(THF)$ to a pyridine solution of $EuBr_2$ resulted in a color change to green, reminiscent of the formation of dianionic $DOPO^{sq}$ (Scheme 2.9). Green crystals suitable for X-ray analysis deposited upon slow diffusion of pentane into the pyridine solution at -35 °C.

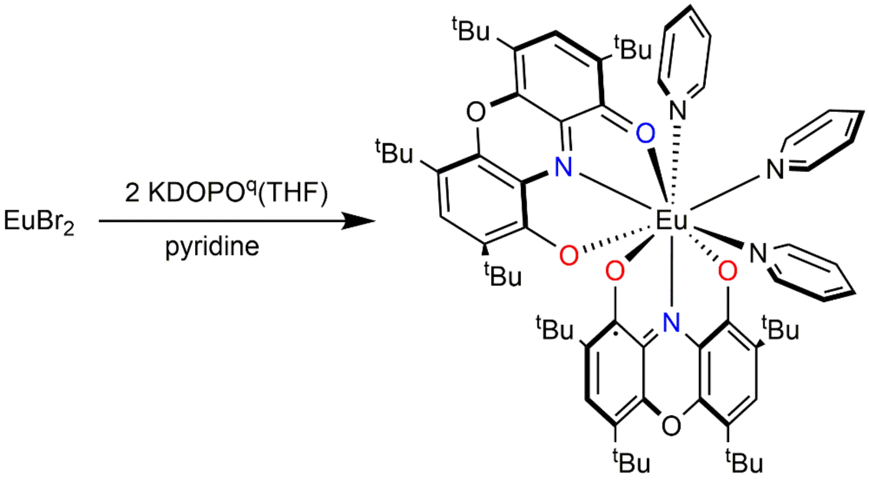

Scheme 2.9. Synthesis of Eu(DOPO^q)(DOPO^{sq})(py)$_3$.

Refinement of the data revealed the desired Eu(DOPO)$_2$ functionality with three pyridine molecules completing the coordination sphere, resulting in the structural assignment of this compound as Eu(DOPO)$_2$(py)$_3$ (Figure 2.13). The two DOPO ligands are crystallographically symmetric with Eu-N bond distances of 2.488(2) Å and Eu-O bond distances of 2.4003(18) and 2.4314(18) Å. These distances are comparable to those reported in a related complex, Eu^{3+}(pydcH)$_3$ (H$_2$pydc = 2,6-pyridinedicarboxylic acid), which has average Eu-N distances of 2.532 Å and average Eu-O distances of 2.438 Å.[68] The Eu-N bonds in Eu^{3+}(pydcH)$_3$ represent neutral nitrogen contacts, while the Eu-O bonds are resonate between neutral and ionic contacts, similar to Eu(DOPO)$_2$(py)$_3$. Therefore, the metal oxidation state is assigned as Eu^{+3}, resulting from ligand reduction upon metallation. Due to the symmetric nature of the DOPO ligands, the resulting oxidation state of the ligands is assigned as -1.5, which has been noted for related bis ligand aluminum, cobalt, iron, and gallium complexes with the ONO chelating ligand bis(3,5-di-*tert*-butyl-1-hydroxy-2-phenyl)amine.[4] This is likely the result of resonant behavior between DOPO^q and DOPO^{sq} ligands, and is supported by Metrical Oxidation State analysis, which gives average MOS values of -1.58(17). Taking this into account, the electronic structure of this complex is assigned as Eu^{3+}(DOPO^q)(DOPO^{sq})(py)$_3$.

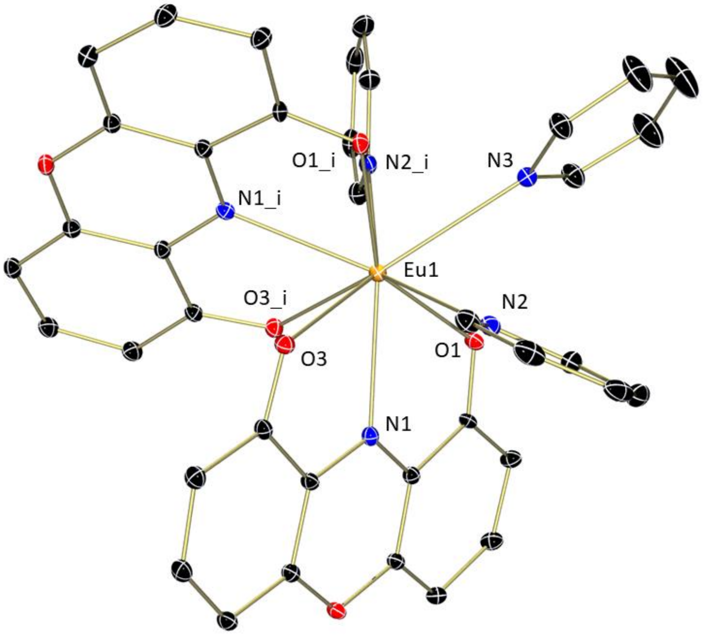

Figure 2.13. Molecular structure of Eu(DOPO^q)$_2$(DOPO^{sq})(py)$_3$ shown at 30% probability ellipsoids. Hydrogen atoms, *tert*-butyl groups, and co-crystallized solvent molecules have been omitted for clarity.

2.4 Conclusions

For the first time, a non-aqueous isostructural series of coordination compounds has been developed for members across the lanthanide and actinide series. By combining expertise in non-aqueous synthetic techniques with the knowledge and ability to manipulate elements from all throughout the f-block, redox-active ligands were used to make the broadest series known, which includes representative elements from transition metals, main group metals, lanthanides, early actinides, and transuranic. These complexes are stabilized in either trivalent or tetravalent states. Structural analysis of these representatives reveals trends across the actinide series, which are supported by spectroscopic measurements and computational analyses. These studies demonstrate that although californium appears later in the actinide series, where it would be expected to behave like a lanthanide, structural parameters and computational modeling don’t support this. Rather, unlike the americium and berkelium species, the californium derivative shows ligand involvement in its highest (singly) occupied molecular orbitals, which is unexpected given its location in the actinide series.

Through this work, the challenges of performing transuranic chemistry in nonaqueous environments have been highlighted. Isolation of $Cf(DOPO^{q})_2(NO_3)(py)$ shows the challenges of using organic solvent with these highly radioactive elements. This work will help in the understanding of organic solvent stability for aqueous-organic nuclear waste separation strategies. All-together, this combination of studies highlights the importance of blending synthesis, characterization and computational techniques to contribute to the overall understanding of bonding between organic ligands and metals at the bottom of the periodic table.

CHAPTER 3. MODEL URANIUM REDOX-INNOCENT LIGAND COMPLEXES

3.1 Introduction

Redox-active ligands, those that participate in redox chemistry with a metal rather than existing as spectators, have recently risen to the forefront of inorganic and organometallic chemistry.[69–76] These ligands serve as electron reservoirs that work in concert with metal centers to mediate multi-electron reactions that would not otherwise be possible.[72,73] Along with providing this unique capability to metals that are typically redox-restricted, these ligands also impart additional complexity to the electronic structures of coordination complexes.[77] The origin of this complexity lies in the very root of their functionality, energetically accessible π^* orbitals that can accept electron density. Pioneering studies have demonstrated the utility of combining multiple analytical tools to elucidate ground state electronic structures including NMR spectroscopy, X-ray crystallography, X-ray absorption spectroscopy, Mössbauer spectroscopy (where appropriate), computational modeling, and magnetic studies.[4,78–81]

In recent years, the Bart group[27,36,48,82–84] and others[85–88] have extended these studies to the elements of the *f*-block, and more specifically uranium, bringing additional complexity to the already electronically diverse actinide elements. By utilizing the above mentioned techniques, uranium complexes bearing redox-active ligands in a variety of ground states have been established. These highly reduced, electron-rich uranium species readily perform multi-electron transfer chemistry,[26,30,36] showing that in the correct environment, a metal that typically only does one-electron chemistry, like uranium, can behave like a late transition metal.

Studies of first row transition metal species bearing redox-active ligands conclude that electrons are highly delocalized over the entirety of the complex.[4,89–91] This is in part due to the energy match and orbital overlap between the ligand π^* orbitals and the metal *d*-orbitals, generating species that are highly covalent. It is well established that the actinides' valence 5*f*-orbitals do not participate in covalent bonding equivalently to the valence *d*-orbitals associated with the transition metals, in part due to their more limited radial extension.

Thus, there remains the question as to whether redox-active ligands impart additional covalent character to actinide complexes, given the energetically similar metal and ligand orbitals.

In 2011, it was reported a full electronic structure study of uranium complexes bearing redox-active diazabutadiene ligands, namely $(^{Mes}DAB^{Me})_2U(THF)$ (**1-DAB**) and $Cp_2U(^{Mes}DAB^{Me})$ (**2-DAB**) ($^{Mes}DAB^{Me}$ = [ArN=C(Me)C(Me)=Nar], where Ar = 2,4,6-trimethylphenyl (Mes)).[92] As determined by a combined spectroscopic, structural, and computational study, these species feature the doubly reduced ligands, $[^{Mes}DAB^{Me}]^{2-}$, along with uranium(IV) ions. An interesting structural highlight was the association of the C-C π bond of the reduced ene-diamide ligand backbone to the uranium center, which has recently also been observed for uranium[93] and the lanthanides with similar ligand frameworks.[94,95] At the time, variable temperature magnetic data that were collected for these species gave anomalous results with values that would not be expected for uranium(IV) species. As an extension of this study, it was hypothesized that generating the redox innocent version of these complexes would provide insight into this unusual magnetic behavior. Herein is presented work on the redox innocent analogues to **1-DAB** and **2-DAB**, $(^{Mes}DAE)_2U(THF)$ (**1-DAE**) and $Cp_2U(^{Mes}DAE)$ (**2-DAE**), which are simple uranium(IV) complexes with diamide chelates (^{Mes}DAE = $[ArN{=}CH_2CH_2{=}NAr]$, where Ar = Mes). To preserve the sterics of the original $^{Mes}DAB^{Me}$ system, the diamine ligand was synthesized with the bulky 2,4,6-trimethylphenyl substituents on the nitrogen atoms. Once again, a study that combines spectroscopic, structural, and magnetic measurements was undertaken to directly compare to the redox-active ligand system.

3.2 Experimental

General Considerations. All air- and moisture-sensitive manipulations were performed using standard Schlenk techniques or in an MBraun inert atmosphere drybox with an atmosphere of purified nitrogen. The MBraun drybox was equipped with a cold well designed for freezing samples in liquid nitrogen as well as two -35 °C freezers for cooling samples and crystallizations. Solvents for sensitive manipulations were dried and deoxygenated using literature procedures with a Seca solvent purification system.[11] Benzene-d_6 and chloroform-*d* were purchased from Cambridge Isotope Laboratories. Deuterated solvents were dried with molecular sieves and degassed by three freeze-pump-thaw cycles. *N,N'*-dimesitylethane-1,2-diamine dihydrochloride,[96] KCH_2Ph,[13] and UCl_4[97] were prepared according to literature procedures. NaCp solution (2.0 M in THF) was purchased from Sigma Aldrich and used as received.

^{1}H NMR spectra were recorded on a Varian Inova 300 spectrometer at 299.992 MHz. All chemical shifts are reported relative to the peak for $SiMe_4$, using ^{1}H (residual) chemical shifts of the solvent as a secondary standard. The spectra for paramagnetic molecules were obtained by using an acquisition time of 0.5 s; thus the peak widths reported have an error of ±2 Hz. For paramagnetic molecules, the ^{1}H NMR data are reported with the chemical shift, followed by the peak width at half height in Hertz, the integration value, and, where possible, the peak assignment. Elemental analyses were performed by Complete Analysis Laboratories, Inc., Parsippany, New Jersey. Electronic absorption measurements were recorded at 294 K in THF in sealed 1 cm quartz cuvettes with a Jasco V-6700 spectrophotometer. Infrared spectra were recorded using a PerkinElmer FT-IR Spectrum RX I spectrometer. Samples were made by crushing the solids, mixing with dry KBr, and pressing into a pellet.

A single crystal of $(^{Mes}DAE)_2U(THF)$ (**1-DAE**) for X-ray diffraction was coated with poly(isobutene) oil in a glovebox and quickly transferred to the goniometer head of a Bruker AXS APEXII CCD diffractometer. Preliminary examination and data collection were performed with Mo K_α radiation ($\lambda = 0.71073$ Å). Data were collected, reflections were indexed and processed, and the files scaled and corrected for absorption using APEX2.[52] The space group was assigned and the structures was solved by direct methods using XPREP[21] within the SHELXTL suite of programs[21] and refined by full matrix least squares against F^2 with all reflections using Shelxl2014/7[21] using the graphical interface Shelxle.[21]

A single crystal of $Cp_2U(^{Mes}DAE)$ (**2-DAE**) for X-ray diffraction was coated with poly(isobutene) oil in a glovebox and quickly transferred to the goniometer head of a Nonius KappaCCD diffractometer equipped with a graphite crystal incident beam monochromator. Preliminary examination and data collection were performed with Mo K_α radiation ($\lambda = 0.71073$ Å). Data were collected using the Nonius Collect Software.[55] Reflections were indexed and processed using HKL-3000,[54] and the files were scaled and corrected for absorption using SCALEPACK.[54] The space group was assigned and the structure was solved by direct methods using XPREP[21] within the SHELXTL[21] suite of programs and refined by full matrix least squares against F^2 with all reflections using Shelxl2014-7.[21]

For both compounds, if not specified otherwise, H atoms attached to carbon atoms were positioned geometrically and constrained to ride on their parent atoms, with carbon hydrogen bond distances of 0.95 Å for and aromatic C-H, 0.99 and 0.98 Å for aliphatic CH_2 and CH_3

moieties, respectively. Methyl H atoms were allowed to rotate but not to tip to best fit the experimental electron density. $U_{iso}(H)$ values were set to a multiple of $U_{eq}(C)$ with 1.5 for CH_3 and 1.2 for CH_2 units.

Solid-state magnetic data were collected using a Quantum Design Multi-Property Measurement System (MPMS-7) warmed from 2–300 K and cooled from 300–2 K at 1 T and at 2 K from 0–7 T. Drinking straws were used to house the samples for measurement and were dried under a dynamic vacuum overnight before use in an inert atmosphere (N_2) drybox. While empty, the straws were crimped using a hot pair of tweezers to melt the straw together. The samples were added directly into the crimped straw and were massed to the nearest 0.1 mg using a calibrated and leveled Mettler-Toledo AL-204 analytical balance. Approximately 10.0 mg of quartz wool was added to the straw above the sample to hold it in place. The straw was then crimped above the sample and quartz wool with hot tweezers to complete the seal. The samples, contained in the sealed drinking straws for measurement, were transferred to the MPMS under inert atmosphere and immediately loaded into the inert atmosphere of the measurement chamber with three evacuation/purge cycles. Corrections for the intrinsic diamagnetism of the samples were made using Pascal's constants.[20]

Samples of $Cs_2UO_2Cl_4$, **1-DAE**, **2-DAE**, **1-DAB**, and **2-DAB** were analyzed by U L_3-edge X-ray absorption spectroscopy measurements. Samples were prepared under an argon atmosphere. The samples were diluted with boron nitride (BN), which was dried at elevated temperature (200 °C) under vacuum (10^{-3} Torr) for 24 h prior to use. A mixture of the analyte and BN were weighed out, such that the edge jump for the absorbing atom was calculated to be at 1 absorption length in transmission (~30 to 50 mg of sample and 50 to 30 mg of BN). Samples were ground using a Wig-L-Bug ®, a Teflon bead, and a polycarbonate capsule. The finely ground powders were pressed as a pellet into a slotted aluminum sample holder equipped with a Kapton windows (1 mil), one was fixed with super glue and the other was Kapton tape. This primary holder was nested within a secondary aluminum holder equipped with Kapton (2 mil) windows that were sealed with indium wire. The samples were sealed in Mylar bags, and shipped to the Stanford Synchrotron Lightsource (SSRL). Once unpackaged, the samples were immediately attached to the coldfinger of a liquid N_2 cryostat and quickly evacuated (10^{-7} Torr). The cryostat was attached to the beamline 11-2 XAFS rail (SSRL), which was equipped with three ionization chambers through which nitrogen gas was continually flowed. One chamber (10 cm) was positioned before the cryostat to monitor the incident radiation (I_0). The second chamber (30 cm) was positioned after the cryostat so that sample transmission (I_1) could be evaluated against I_0 and so that the absorption coefficient (μ) could be calculated as $\ln(I_0/I_1)$. The third chamber (I_2; 30 cm) was positioned downstream from I_1 so that the XANES of a calibration foil could be measured against I_1. A potential of 1600 V was applied in series to the ionization chambers. Samples were calibrated in-situ to the energy of the first inflection point of the K-edge of an yttrium foil (17,038.4 eV).

The X-ray absorption near edge spectra (XANES) were measured at the Stanford Synchrotron Radiation Lightsource (SSRL), under dedicated operating conditions (3.0 GeV, 5%, 500 mA using continuous topoff injections) on end station 11-2. This beamline was equipped with a 26-pole, 2.0 tesla wiggler, utilized a liquid nitrogen-cooled double-crystal Si(220) monochromator, and employed collimating and focusing mirrors. A single energy was selected from the white beam with a liquid-N_2-cooled double-crystal monochromator utilizing Si(220) ($\varphi = 0$) crystals. Although the crystals were run fully-tuned, higher harmonics from the monochromatic light were removed using a 370 mm Rh coated harmonic rejection mirror. The Rh coating was 50 nm with 20 nm seed coating and the substrate was Zerodur. Vertical acceptance was controlled by slits positioned before the monochromator. The harmonic rejection cut-off was set by the mirror angle, thereby controlling which photons experience total external reflection. The horizontal and vertical slit sizes were 15 and 1 mm, respectively (10 mm horizontal slit for $Cs_2UO_2Cl_4$).

Data were treated as previously described.[82,84,85] Data were background subtracted by fitting a lint to the pre-edge region, which was subsequently subtracted from the experimental data to eliminate the background. Data were normalized by fitting a first-order polynomial to the post-edge region of the spectrum and setting the edge jump to an intensity of 1.0.

Preparation of $H_2(^{Mes}DAE)$. A 500 mL round-bottom flask was charged with *N,N'*-dimesitylethane-1,2-diamine dihydrochloride (1.750 g, 4.74 mmol) and 300 mL of a saturated, aqueous $NaHCO_3$ solution. This suspension was stirred until approximately 90% of the solid was dissolved (1 h) before the product was extracted with dichloromethane (3x200 mL). After drying the dichloromethane solution over $MgSO_4$ and concentration *in vacuo*, a clear, colorless oil was obtained, which solidified overnight to a crystalline, white solid assigned as $H_2(^{Mes}DAE)$ (1.100

g, 3.71 mmol, 78%). ^{1}H NMR spectrum in CD_3Cl matches previously published data.[96] ^{1}H NMR (C_6D_6, 25 °C): δ = 2.18 (s, 6H, C*H*$_3$), 2.22 (s, 12H, C*H*$_3$), 2.95 (s, 4H, C*H*$_2$), 3.40 (bs, 2H, N*H*), 6.79 (s, 4H, Ar-C*H*).

Preparation of (^{Mes}DAE)$_2$U(THF) (1-DAE). A 20 mL scintillation vial was charged with H_2(^{Mes}DAE) (0.468 g, 1.58 mmol) and 15 mL of THF. An orange solution of KCH_2Ph (0.414 g, 3.18 mmol) in 5 mL of THF was added dropwise to the H_2(^{Mes}DAE) solution, causing a color change from colorless to yellow. After stirring for 10 minutes, a yellow solid suddenly precipitated from the solution. This suspension was then added dropwise to a 100 mL round-bottom flask containing a green solution of UCl_4 (0.300 g, 0.790 mmol) in 30 mL of THF, causing an immediate color change to dark orange. After stirring for 1 hour, the solution was concentrated *in vacuo* to a sticky, orange solid. Pentane (80 mL) was added, and the solution was allowed to stir for 1 hour before KCl was removed by filtration. The resulting yellow solution was concentrated to 10 mL and cooled to -35 °C, causing the precipitation of a yellow solid. After decanting the pentane, the yellow solid was dried *in vacuo* and assigned as (^{Mes}DAE)$_2$U(THF) (**1-DAE**) (0.330 g, 0.367 mmol, 46%). Brown crystals suitable for X-ray analysis were grown by slow evaporation from diethyl ether at -35 °C. Analysis for $C_{44}H_{60}N_4OU$: Calcd C, 58.78; H, 6.73; N, 6.23. Found C, 58.61; H, 6.79; N, 6.42. ^{1}H NMR (C_6D_6, 25 °C): δ = -15.88 (38, 24H, C*H*$_3$), 5.61 (12, 12H, C*H*$_3$), 10.71 (15, 8H, Ar-C*H*), 62.03 (31, 8H, C*H*$_2$).

Preparation of Cp_2U(^{Mes}DAE) (2-DAE). A 20 mL scintillation vial was charged with H_2(^{Mes}DAE) (0.234 g, 0.789 mmol) and 10 mL of THF. An orange solution of KCH_2Ph (0.207 g, 1.59 mmol) in 5 mL of THF was added dropwise to the H_2(^{Mes}DAE) solution, causing a color change from colorless to yellow. After stirring for 10 minutes, a yellow solid suddenly precipitated from the solution. This suspension was then added dropwise to a 100 mL round-bottom flask containing a green solution of UCl_4 (0.300 g, 0.790 mmol) in 30 mL of THF, causing an immediate color change to dark orange. Quickly, NaCp (0.138 g, 1.57 mmol) was added as a solid, causing the solution to darken. After stirring for 1 hour, the solution was concentrated *in vacuo* to a sticky, brown solid. 80 mL of pentane were added, and the solution was allowed to stir for 1 hour before KCl and NaCl were removed by filtration. The resulting orange solution was concentrated to 10 mL and cooled to -35 °C causing the precipitation of an orange solid. After decanting the pentane, the orange solid was dried *in vacuo* and assigned as

$Cp_2U(^{Mes}DAE)$ (**2-DAE**) (0.212 g, 0.307 mmol, 39%). Orange crystals suitable for X-ray analysis were grown from a concentrated pentane solution at -35 °C overnight. Analysis for $C_{30}H_{36}N_4U$: Calcd C, 54.38; H, 5.48; N, 4.23. Found C, 54.27; H, 5.65; N, 4.47. ^1H NMR (C_6D_6, 25 °C): δ = -11.53 (6, 12H, C*H*$_3$), 1.18 (13, 6H, C*H*$_3$), 1.35 (9, 10H, Cp-C*H*), 4.32 (4, 4H, Ar-C*H*), 31.12 (8, 4H, C*H*$_2$).

3.3 Results and Discussion

3.3.1 Synthesis of Redox-Innocent Analogues

To build a system where redox-active and redox-innocent ligand frameworks would be directly compared on uranium, preliminary attempts focused on designing a ligand that would retain the steric properties of $^{Mes}DAB^{Me}$ while providing amine linkages for easy coordination to uranium. It was hypothesized the most straightforward method would be via reduction of $^{Mes}DAB^{Me}$ with sodium borohydride. However, upon workup, the complexity associated with separation of diastereomers precluded a suitable platform for scalable chemistry. Thus, a ligand was selected with an ethylenediamine backbone, which precludes diastereomer formation, but still allows installation of the bulky mesityl groups. This ligand was prepared by the deprotonation of previously synthesized *N,N'*-dimesitylethane-1,2-diamine dihydrochloride with excess sodium bicarbonate, yielding $H_2(^{Mes}DAE)$ ($H_2(^{Mes}DAE)$ = *N,N'*-dimesitylethane-1,2-diamine) in moderate yield as a clear oil.[96] In its purest form, $H_2(^{Mes}DAE)$ solidifies over the course of days, but no difference in spectroscopic properties or metalation reactivity was observed between the two phases.

Deprotonation of two equivalents of $H_2(^{Mes}DAE)$ was accomplished *in situ* using four equivalents of benzyl potassium in THF (Scheme 3.1), signified by precipitation of a yellow solid. Addition of this suspension to one equivalent of UCl_4 in THF at room temperature resulted in a dark-orange solution, which produced $(^{Mes}DAE)_2U(THF)$ (**1-DAE**) in moderate yield as a yellow powder following concentration, extraction, and recrystallization from pentane. It should be noted that using this ligand solution for metalation prior to precipitation of the ligand potassium salt left substantial $H_2(^{Mes}DAE)$ impurities in the final product **1-DAE**. Analysis of a KBr pellet of **1-DAE** by IR spectroscopy confirmed that no N-H functionalities were present.

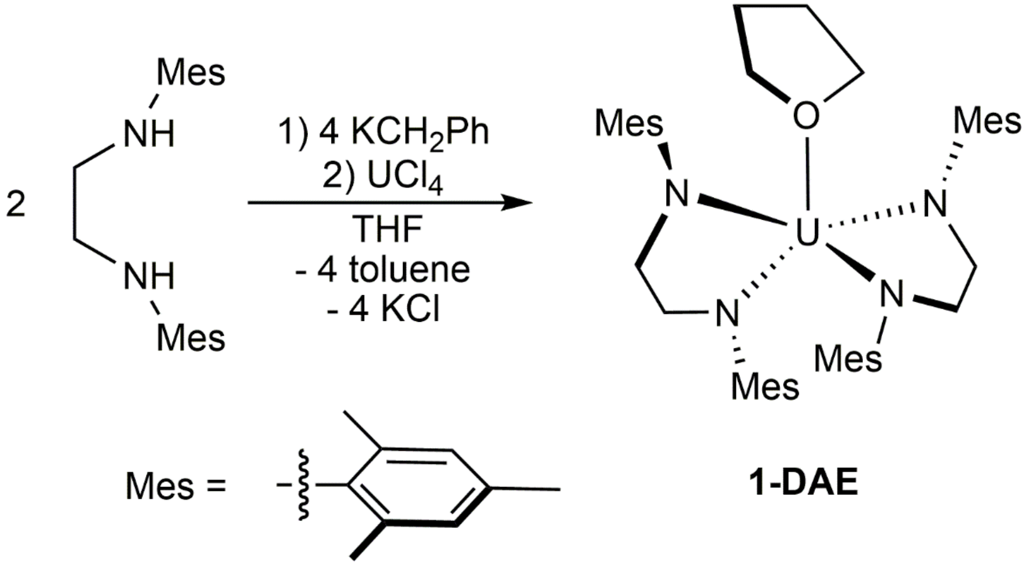

Scheme 3.1. Synthesis of $(^{Mes}DAE)_2U(THF)$ (**1-DAE**).

Analysis of **1-DAE** by ^1H NMR spectroscopy reveals a sharp, paramagnetically-shifted, C_{2v}-symmetric spectrum with all mesityl groups appearing equivalent. Peaks at -15.88 and 5.61 ppm correspond to the methyl groups of the mesityl substituents, while a peak at 10.71 ppm is observed for the aryl protons of the mesityl groups. An additional down-field shifted resonance is observed at 62.03 ppm corresponding to the backbone methylene groups. Similar to **1-DAB**, no THF resonances are observed in the spectrum at room temperature; however, addition of excess pyridine-d_5 to a known amount of **1** liberated one equivalent of THF, as determined by ^1H NMR spectroscopy by integration with a mesitylene standard. The THF resonances are likely not observable at room temperature due to broadening from dynamic behavior.

The sharpness and symmetry observed in the ^1H NMR spectrum of **1-DAE** contrasts that of **1-DAB**, which has very broad resonances. The origin of this broadness was hypothesized to originate from dynamic behavior in benzene-d_6 solution at ambient temperature, attributed to the interaction of the uranium with the ligand “ene” backbones in solution, which was corroborated by sharpening of the resonances in the low temperature ^1H NMR spectrum (toluene-d_8, 10 °C).[92]

Following the isolation of **1-DAE**, the redox-innocent ligand analogue to **2-DAB**, $Cp_2U(^{Mes}DAE)$ (**2-DAE**), was targeted. Synthesis was again accomplished by *in situ* deprotonation of one equivalent of $H_2(^{Mes}DAE)$ in THF, followed by transfer of this slurry to a

THF solution of UCl_4 with subsequent quick addition of two equivalents of solid NaCp (Scheme 3.2). Following workup, **2-DAE** was isolated in moderate yield as an orange powder, and analyzed by IR spectroscopy to confirm the absence of N-H functional groups.

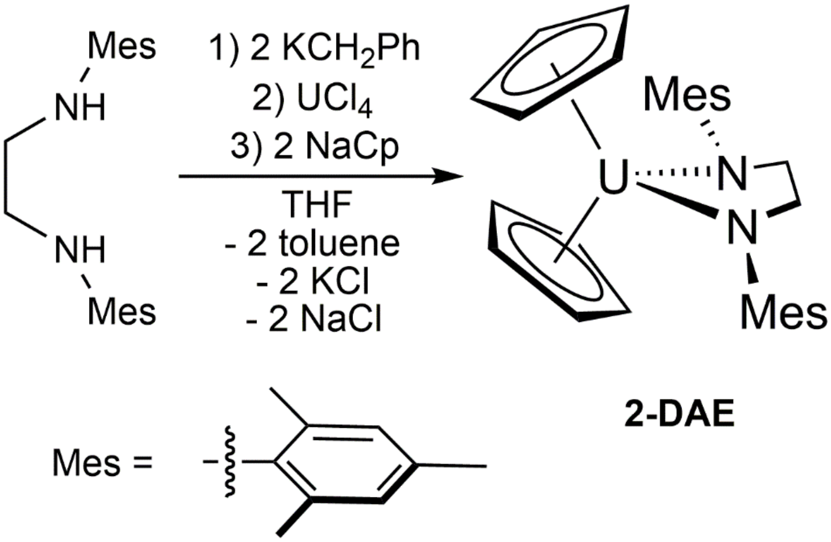

2-DAE

Scheme 3.2. Synthesis of $Cp_2U(^{Mes}DAE)$ (**2-DAE**).

The ^1H NMR spectrum of **2-DAE** was reminiscent of **1-DAE**, again showing sharp, paramagnetically shifted resonances and an overall C_{2v}-symmetric spectrum. Resonances assigned to the methyl groups for the mesityl substituents are observed at -11.53 and 1.18 ppm, while the aryl protons on the mesityl rings appear at 4.32 ppm. A large resonance, observed at 1.35 ppm, is assignable to the Cp protons, whereas the backbone methylene protons appear downfield (31.12 ppm). The symmetry of **2-DAE** in solution contrasts that of the analogous $^{Mes}DAB^{Me}$ compound, as **2-DAB** displays a C_s-symmetric spectrum, likely resulting from a static backbone interaction in solution that is missing in **2-DAE**.

3.3.2 X-Ray Crystallography

The molecular structures of newly generated **1-DAE** and **2-DAE** were interrogated by X-ray crystallography to assess their respective similarities to **1-DAB** and **2-DAB**. Although the symmetries of the ^{Mes}DAE and ^{Mes}DAB^{Me} series differ in solution, for this study it is imperative that the solid state geometries are analogous to eliminate ligand electronic influences other than the ligand backbone interactions. Furthermore, since a majority of the electronic characterization techniques are performed on solid-state samples, it is important to understand structural elements and possible molecular interactions.

Brown crystals of compound **1-DAE** suitable for single crystal X-ray analysis were grown by slow evaporation from a concentrated diethyl ether solution at -35 °C. Refinement of the data confirmed the identity of **1-DAE** as (^{Mes}DAE)$_2$U(THF) (Figure 3.1, right; Table 3.1). Similar to the structure of **1-DAB** (Figure 3.1, left; Table 3.1), compound **1-DAE** consists of a five-coordinate uranium center with pseudo square-pyramidal geometry containing a THF molecule at the apex.

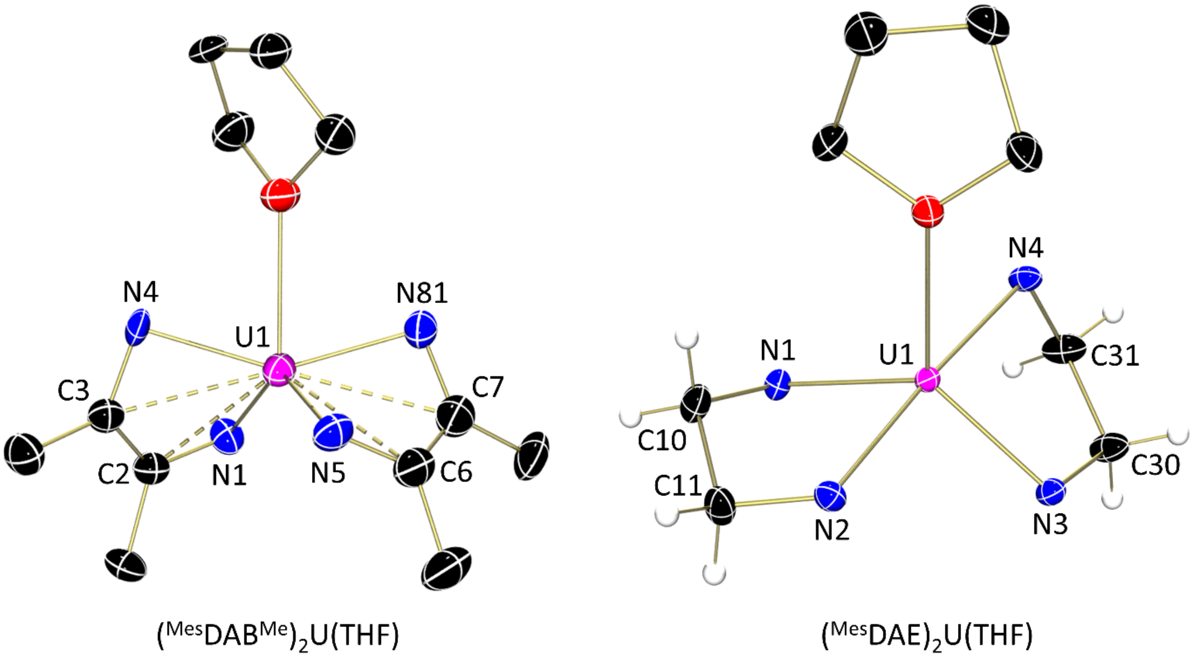

Figure 3.1. Molecular structures of (^{Mes}DAB^{Me})$_2$U(THF) (**1-DAB**) and (^{Mes}DAE)$_2$U(THF) (**1-DAE**) shown with 30% probability ellipsoids. Selected hydrogen atoms, solvent molecules, and mesityl groups have been omitted for clarity.[92]

The U-N distances of **1-DAE**, ranging from 2.242(2)-2.264(2) Å, are consistent with those observed in **1-DAB** (2.251(4)-2.255(4) Å) and are indicative of anionic nitrogen-uranium interactions. From the structural parameters it is also evident that the C-C bonds in the backbone of the ^{Mes}DAE ligands are consistent with C-C single bonds, displaying distances of 1.523(4) and 1.529(4) Å, differing significantly from those of the C=C bonds (1.361(8) and 1.364(7) Å) in **1-DAB**, which are consistent with C=C double bonds.[98–101] Additionally, in compound **1-DAE** the U-C contacts are too long (ranging from 3.022(3) to 3.171 Å) to be considered as bonded; this contrasts the U-C distances of **1-DAB**, which are much shorter at 2.749(5) to 2.788(5) Å and are clearly interacting.[102]

Orange crystals of compound **2-DAE** suitable for X-ray diffraction experiments were grown from a concentrated pentane solution at -35 °C overnight. Analysis confirmed the identity of **2-DAE** as $Cp_2U(^{Mes}DAE)$ (Figure 3.2, right; Table 3.1), featuring a distorted tetrahedral geometry (when considering the Cp centroids) similar to **2-DAB**.

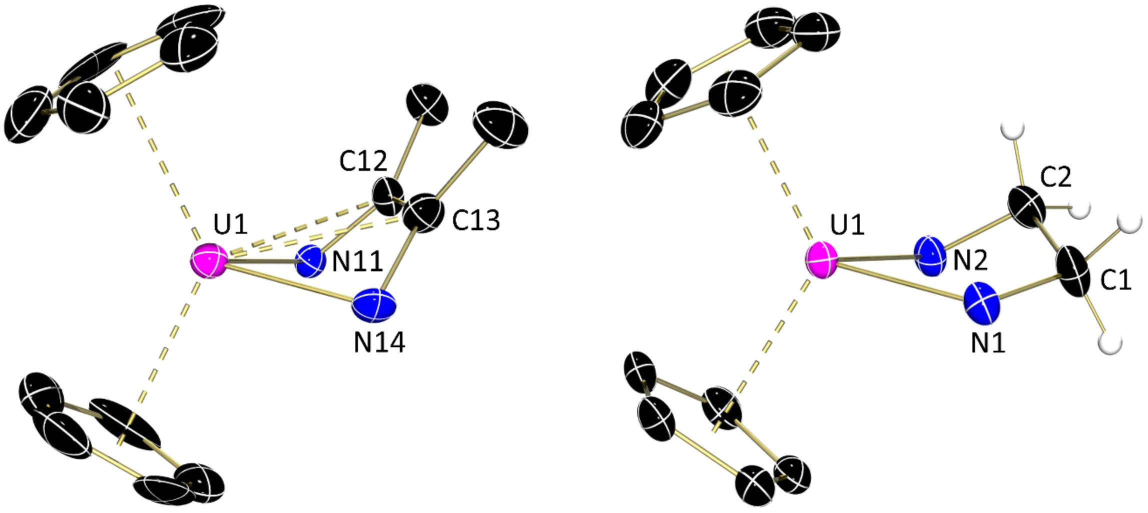

$Cp_2U(^{Mes}DAB^{Me})$ $Cp_2U(^{Mes}DAE)$

Figure 3.2. Molecular structures of $Cp_2U(^{Mes}DAB^{Me})$ (**2-DAB**) and $Cp_2U(^{Mes}DAE)$ (**2-DAE**) shown with 30% probability ellipsoids. Select hydrogen atoms, solvent molecules, and mesityl groups have been omitted for clarity.[92]

The U-N distances in **2-DAE** (2.221(3) and 2.204(3) Å) are consistent with those observed in **2-DAB** (2.224(6) and 2.198(6) Å) and are indicative of anionic uranium-nitrogen interactions. By charge balance considerations, **2-DAE** contains a U(IV) center. Similar to compound **1-DAE**, the C-C bond distance in the ligand backbone of compound **2-DAE** (1.540(5) Å) is consistent with a C-C single bond, again contrasting the C=C double bond in the backbone of **2-DAB** (1.399(11) Å). Again, the uranium interaction with the ligand backbone is diminished in compound **2-DAE**, as the U-C distances of 2.875 and 3.068 Å are substantially longer than those noted in **2-DAB** (2.637(7) to 2.685(5) Å).

Table 3.1. Bond distances (in Å) for ${}^{Mes}DAB^{Me}$ and ${}^{Mes}DAE$ compounds.[92]

Compound	C-N	C-C	U-N	U-C$_{backbone}$
$({}^{Mes}DAB^{Me})_2U(THF)$ (**1-DAB**)	1.431(7)	1.361(8)	2.251(4)	2.749(5)
	1.419(6)	1.364(7)	2.252(4)	2.773(4)
	1.432(6)	-	2.255(3)	2.787(6)
	1.418(6)	-	2.255(4)	2.788(5)
$({}^{Mes}DAE)_2U(THF)$ (**1-DAE**)	1.485(4)	1.523(4)	2.264(2)	3.022(3)
	1.471(4)	1.529(4)	2.242(2)	3.141
	1.477(4)	-	2.264(2)	3.171
	1.466(4)	-	2.259(2)	3.058(3)
$Cp_2U({}^{Mes}DAB^{Me})$ (**2-DAB**)	1.425(10)	1.399(11)	2.224(6)	2.637(7)
	1.407(9)	-	2.198(6)	2.685(5)
$Cp_2U({}^{Mes}DAE)$ (**2-DAE**)	1.473(4)	1.540(5)	2.221(3)	3.068
	1.495(4)	-	2.204(3)	2.875

3.3.3 Electronic Absorption Spectroscopy

To corroborate the assignment of U(IV) for both **1-DAE** and **2-DAE**, as well as to serve as a comparison to the ${}^{Mes}DAB^{Me}$ derivatives, electronic absorption spectroscopy was performed. Spectra for **1-DAE** and **2-DAE** were recorded in THF solution at room temperature in both the UV-visible (Figure 3.3, left) and near-infrared regions (Figure 3.3, right). In the UV-visible region, both **1-DAE** and **2-DAE** have nearly featureless spectra, except for absorbances around 300 nm that are only partially discernable. These absorbances are likely ligand-to-metal charge-transfer bands and are consistent with those observed for the ${}^{Mes}DAB^{Me}$ compounds.[92] Similarly, the near-IR region shows sharp but weakly intense bands that are characteristic of *f*-*f* transitions typically observed for U(IV), f^2 complexes.[103,104]

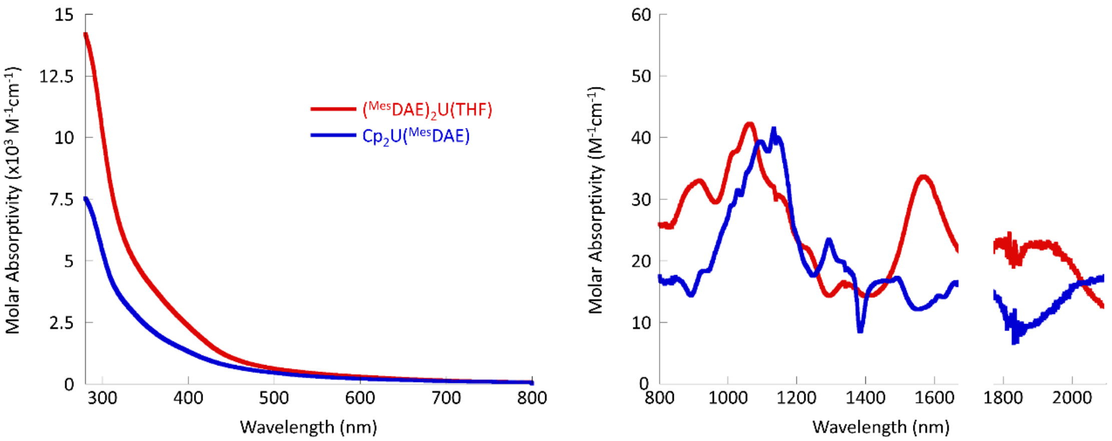

Figure 3.3. Electronic absorption spectra in the UV-visible region (left) and near infrared region (right) for $(^{Mes}DAE)_2U(THF)$ (**1-DAE**) and $Cp_2U(^{Mes}DAE)$ (**2-DAE**) in THF at ambient temperature. THF solvent overtones between 1675 and 1775 nm have been omitted for clarity.

3.3.4 X-ray Absorption Spectroscopy

For a direct comparison of the effective nuclear charge on the uranium centers for compounds containing the redox-active $^{Mes}DAB^{Me}$ and redox-innocent ^{Mes}DAE, X-ray absorption near edge structure (XANES) spectroscopy was conducted on the series of four compounds. The U L_3-edge XANES spectra from **1-DAE**, **1-DAB**, **2-DAE**, and **2-DAB** collected at 80 K were background subtracted and normalized (Figure 3.4). As characteristic for U L_3-edge XANES,[82,105–108] each spectrum was dominated by a large edge feature superimposed on a step-like absorption threshold. It has been shown that the energy of this absorption peak can be correlated with the effective nuclear charge of the absorbing uranium atom.[92,107,109–112] Data were calibrated in energy to the inflection point of the Y K-edge XANES spectrum from an Y foil measured *in-situ* (17,038.4 eV). Note, the **1-DAB** and **2-DAB** compounds had been measured previously in 2011. The original spectra were referenced to 17,032.08 eV, not the more conventional 17,083.4 eV. For this reason, the $^{Mes}DAB^{Me}$ compounds were re-evaluated experimentally, and the results are presented herein. To ensure robust calibration, the U L_3-edge XANES energies were additionally evaluated against an external standard, namely $Cs_2UO_2Cl_4$. Not only does this external calibration standard guard against energy drift over time (accompanying oxidation of the Y calibration foil), it also facilitates comparison of inflection point measurements previously reported in the literature.[105,109]

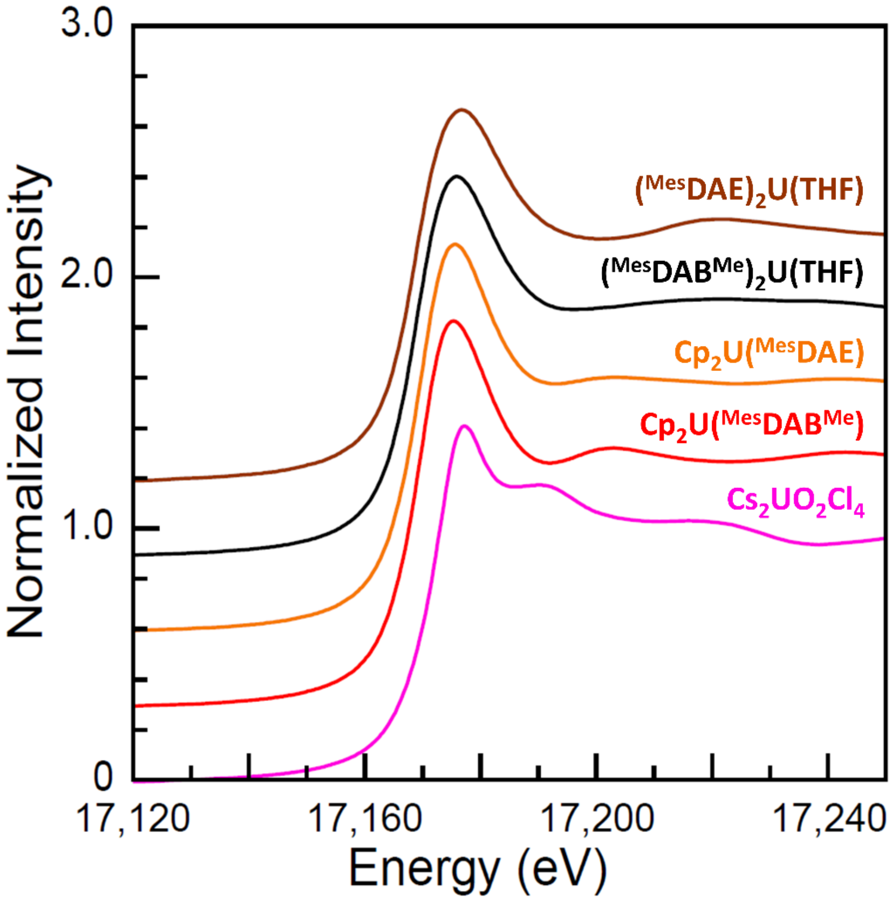

Figure 3.4. U L_3-edge XANES spectra from $Cs_2UO_2Cl_4$ (pink), **1-DAE** (brown), **1-DAB** (black), **2-DAE** (orange), and **2-DAB** (red) collected at 80 K.

Edge-positions for the four analytes were characterized by their individual inflection points. These values were defined by the point at which the second derivative of the data equaled zero. Overall, the analytes' inflection points were similar in energy, spanning only 1 eV (Table 3.2). Uncertainty associated with such inflection point measurements are typically between ± 0.5 to 0.1 eV. All of inflection point values were on the order of 4.2 to 2.8 eV lower in energy than the $Cs_2UO_2Cl_4$ external standard, which was consistent with the uranium ion being described as +4.[105] For **1-DAB** and **2-DAB**, the measured 17,169.3 ± 0.1 and 17,169.7 ± 0.6 eV inflections points were equivalent to that observed in 2011 (i.e., 17,169.3 eV), once the experimental uncertainties were considered. The inflection point energies showed no statistically relevant dependence on diamine identity, comparing ^{Mes}DAB^{Me} to ^{Mes}DAE. However, the inflection point energies dropped by 0.4 to 0.7 eV when changing from a combination of a single diamine with two cyclopentadienides (**2-DAE**) to a ligand environment comprised of two diamides and a THF molecule (**1-DAE**). The peak maxima (where the first derivative of the data equaled zero) was also determined. Again, these values spanned a small energy range (only 0.9 eV). Like the inflection points, the peak maxima could be groups in pairs, metallocenes vs. bis(diimines). However, in contrast to the inflection point measurements, moving from metallocenes to the bis(diimines) causes an approximate increase (not a decrease) in peak maxima energy of 1.2 eV, which was statistically relevant. This energy shift highlights electronic structure differences between metallocene and bis(diamine) ligand environments. Unfortunately, the resolutions associated with the U L_3-edge measurement was not sufficiently rigorous to evaluate the exact origin of this energy shift. Hence, it was concluded from X-ray absorption spectroscopy that the switch to redox-innocent ligands imparted negligible electronic differences on the uranium centers in these complexes. In other words, the redox-active ligands in this system do not appear to significantly contribute to covalency at the uranium, in contrast to transition metal examples.[4,79,90,91,113,114]

Table 3.2. U L_3-edge XANES data from **1-DAE**, **1-DAB**, **2-DAE**, and **2-DAB**.

Compound	**Inflection point**	**Analyte inflection point minus that of $Cs_2UO_2Cl_4$**	**Peak maxima**
$Cs_2UO_2Cl_4$	17,173.2 ± 0.2	0	17,177.3 ± 0.2
$(^{Mes}DAB^{Me})_2U(THF)$ (**1-DAB**)	17,170.4 ± 0.6	-2.8	17,175.8 ± 0.2
$(^{Mes}DAE)_2U(THF)$ (**1-DAE**)	17,169.7 ± 0.5	-3.5	17,175.4 ± 0.2
$Cp_2U(^{Mes}DAB^{Me})$ (**2-DAB**)	17,169.3 ± 0.1	-3.9	17,176.8 ± 0.2
$Cp_2U(^{Mes}DAE)$ (**2-DAE**)	17,169.0 ± 0.1	-4.2	17,176.7 ± 0.2

3.3.5 Magnetism

To further compare the electronic structures of compounds **1-DAE** and **2-DAE** to the previously reported unsaturated analogues, **1-DAB** and **2-DAB**, magnetic data was collected. Temperature-dependent data for compounds **1-DAE** and **2-DAE** were collected at 1 T in the range of 2–300 K (Figure 3.5, left). The data were consistent with a simple $5f^2$ U(IV) cation as evidenced by the low temperature moments of 0.51 and 0.88 μ_B which increased to 2.64 and 2.69 μ_B at room temperature. These low and room temperature moments, as well as the overall line-shape are consistent with data reported for U(IV) complexes.[34] Additionally, field-dependent data at 2 K were collected from 0–7 Tesla (Figure 3.5, right), which revealed low moments consistent with singlet ground states, expected for uranium(IV) complexes.[115–117]

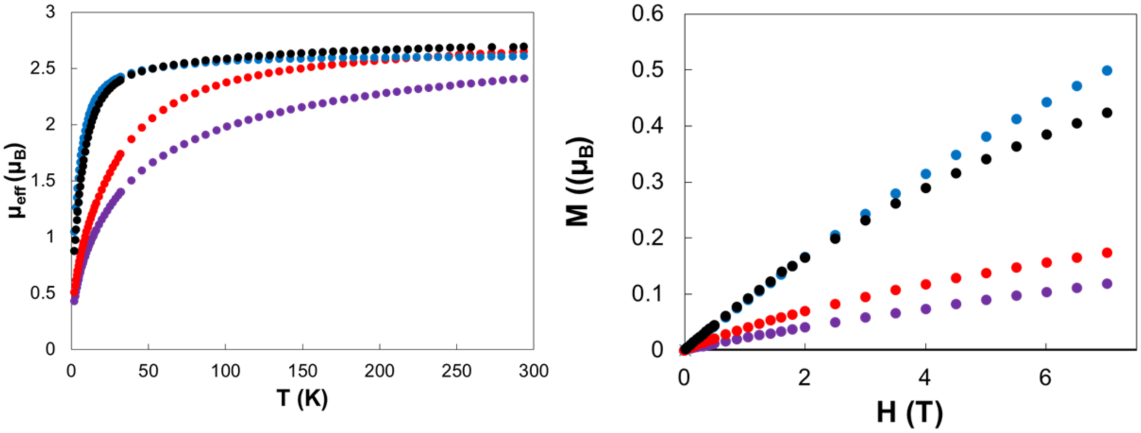

Figure 3.5. Temperature (left) and field-dependent (right) magnetic data for (${}^{\mathrm{Mes}}$DAE)$_2$U(THF) (**1-DAE**) (black), (${}^{\mathrm{Mes}}$DAB${}^{\mathrm{Me}}$)$_2$U(THF) (**1-DAB**) (blue), Cp$_2$U(${}^{\mathrm{Mes}}$DAE) (**2-DAE**) (red), and Cp$_2$U(${}^{\mathrm{Mes}}$DAB${}^{\mathrm{Me}}$) (**2-DAB**) (purple). Temperature-dependent data were collected at 1.0 T, and field-dependent data at 2K.

Previously, the temperature- and field-dependent data for **1-DAB** and **2-DAB** were reported with samples prepared using annealed gelatin capsules as sample holders.[92] While it has been shown that simple room temperature moments are not diagnostic tools alone for assigning oxidation states of uranium cations,[34] the room temperature moments for **1-DAB** and **2-DAB** were surprisingly low for U(IV) cations at 1.91 and 1.79 μ_B, respectively. The low moments were purported to arise as a result of an electronic effect from the direct structural interaction between the ene-diamine ligands and uranium cations.[92]

For the current work, magnetism data for **1-DAB** and **2-DAB** were recollected using very low background plastic straw sample holders described in the experimental section, for consistency with the sample preparation that was used in the data collection for **1-DAE** and **2-DAE** (Figure 3.5). These measurements revealed little difference between **1-DAE** and **1-DAB**, and between **2-DAE** and **2-DAB** respectively. These new results are at odds with the previous report. Upon examining new temperature dependent data, **1-DAB** has a low temperature moment of 1.04 μ_B and increases to 2.61 μ_B at room temperature, values which are quite consistent with **1-DAE**, which has a low temperature moment of 0.88 μ_B and achieves a moment of 2.69 μ_B at room temperature. Additionally, upon comparing the temperature dependent data for **2-DAB** and

2-DAE, similar moments of 0.43 and 0.51 μ_B at 2K, and moments of 2.41 and 2.64 at room temperature are observed. Field-dependent plots attained low moments for all of the derivatives without saturation. In light of these new measurements, it can be concluded that **1-DAB** and **2-DAB**, which have the potential to have redox-active ligand systems, have electronic structures that are very similar to those of **1-DAE** and **2-DAE**, which contain redox-innocent ligand frameworks. Furthermore, the low moments previously reported emerged from experimental artefacts associated with the sample holders.

3.4 Conclusions

Compounds **1-DAE** and **2-DAE**, which possess redox-innocent ligands, were synthesized as analogues to (^{Mes}DAB^{Me})$_2$U(THF) (**1-DAB**) and Cp$_2$U(^{Mes}DAB^{Me}) (**2-DAB**), which contain redox-active, α-diimine ligands that were fully reduced to their ene-diamide forms. Crystallographic analysis determined that the uranium ions in both **1-DAE** and **2-DAE** were structurally analogous to their redox-active counterparts, differing only by the absence of ligand backbone interactions in the redox-innocent series. This allowed for a detailed analysis of the electronic effects imparted by the interaction of the π system with the uranium center.

Analysis of **1-DAE** and **2-DAE** using the same spectroscopic techniques as for **1-DAB** and **2-DAB** allowed for a direct comparison to elucidate the bonding and electronic structure between the two families of compounds. Comparisons of the data obtained from electronic absorption spectroscopy, X-ray absorption spectroscopy, and magnetic measurements are all in agreement, suggesting that the additional ^{Mes}DAB^{Me} ligand interaction in the ene-diamide form has a negligible electronic influence on the uranium center. Furthermore, the updated magnetic data now shows magnetic moments consistent with typical uranium(IV) species. Current studies focus on other redox-active ligand systems in a similar fashion to better understand the electronic demands of these ligands, allowing for a more effective understanding of the reactivity and properties of these complexes.

CHAPTER 4. LANTHANIDE PYRIDINE(DIIMINE) COMPLEXES

4.1 Introduction

While actinide elements often have diverse redox chemistry, lanthanides are notorious for having limited redox-activity.[118] Cerium is known to access the +4 oxidation state, while europium, ytterbium, and samarium can reasonably access the +2 state.[118] Otherwise the chemistry of the lanthanides is restricted to the +3 oxidation state. For this reason, redox-active ligands are a good fit to impart new reactivity to these elements. It has been proposed that a variety of lanthanide moieties, including some lanthanide element multiple bonds, haven't yet been isolated, not because they don't exist, but because there is no conceivable redox-neutral routes to access these motifs.[119] Along these lines, it was hypothesized that the success the Bart group has had in using the redox-active $^{Mes}PDI^{Me}$ ligand ($^{R}PDI^{R'}$ = 2,6-(R-N=CR')$_2$C$_5$H$_3$N) with uranium to access new types of bonding arrangements can be translated to the lanthanide elements.[26,84]

Initial efforts focused on the metallation and reduction chemistry of the $^{Mes}PDI^{Me}$ ligand onto a lanthanide metal center. There were no specific preference as to which lanthanide was used, and therefore chemistry with multiple elements was explored. Cerium and europium were of particular interest due to their unique redox capability, as cerium has an accessible +4 oxidation state and Eu has an accessible +2 oxidation state. Of initial interest were these two elements since ligand cooperativity had been shown with redox processes at PDI-uranium complexes and could be possible with these redox flexible metals as well.[26] Aside from this, other redox inactive lanthanides have differing ionic radii, which makes their chemistries tunable with appropriate steric saturation of PDI-lanthanide complexes.[37] Finally, appropriate lanthanide elements were chosen based on their electronic properties, as too many unpaired electrons precluded analysis by NMR spectroscopy, a useful tool in tracking product identity.

4.2 Experimental

General Considerations. All air- and moisture-sensitive manipulations were performed using standard Schlenk techniques or in an MBraun inert atmosphere drybox with an atmosphere of purified nitrogen. The MBraun drybox was equipped with a cold well designed for freezing samples in liquid nitrogen as well as two -35 °C freezers for cooling samples and crystallizations. Solvents for sensitive manipulations were dried and deoxygenated using literature procedures with a Seca solvent purification system.[11] Benzene-*d*$_6$ and acetonitrile-*d*$_3$ were purchased from Cambridge Isotope Laboratories. Deuterated solvents were dried with molecular sieves and degassed by three freeze-pump-thaw cycles. ^{Mes}PDI^{Me},[120] KC$_8$,[19] and NdI$_3$(THF)$_{3.5}$[18] were prepared according to literature procedures. Lanthanide chlorides and neodymium metal were purchased from Strem chemicals.

^{1}H NMR spectra were recorded on a Varian Inova 300 spectrometer at 299.992 MHz. All chemical shifts are reported relative to the peak for SiMe$_4$, using ^{1}H (residual) chemical shifts of the solvent as a secondary standard. The spectra for paramagnetic molecules were obtained by using an acquisition time of 0.5 s; thus the peak widths reported have an error of ±2 Hz. For paramagnetic molecules, the ^{1}H NMR data are reported with the chemical shift, followed by the peak width at half height in Hertz, the integration value, and, where possible, the peak assignment. Elemental analyses were performed by Complete Analysis Laboratories, Inc., Parsippany, New Jersey or Robertson Microlit Laboratories in Ledgewood, New Jersey. Infrared spectra were recorded using a PerkinElmer FT-IR Spectrum RX I spectrometer. Samples were made by crushing the solids, mixing with dry KBr, and pressing into a pellet.

Preparation of ^{Mes}PDI^{Me}CeCl$_3$(NCMe). A 20 mL scintillation was charged with CeCl$_3$ (0.100 g, 0.406 mmol) and 2 mL of acetonitrile, creating a slurry. A solution of ^{Mes}PDI^{Me} (0.177 g, 0.445 mmol) in 2 mL of acetonitrile was added. Note: 1.1 equivalents of ^{Mes}PDI^{Me} were used to promote metallation; excess ^{Mes}PDI^{Me} could be washed away with pentane after metallation. This yellow solution was stirred overnight, causing solubilization of solids. After concentrating the yellow solution *in vacuo*, the resulting yellow residue was washed with pentane (3 x 5 mL) until the pentane washes came out clear. After concentrating *in vacuo*, a yellow powder was obtained and assigned as ^{Mes}PDI^{Me}CeCl$_3$(NCMe) (0.251 g, 0.366 mmol, 90%). Yellow crystals suitable for X-ray analysis were grown by slow diffusion of pentane into a concentrated acetonitrile solution at -35 °C. Analysis for $C_{29}H_{34}N_4Cl_3Ce$: Calcd C, 50.84; H, 5.00; N, 8.18. Found C, 50.70; H, 4.84; N, 7.95. ^{1}H NMR (CD$_3$CN, 25 °C): δ = -3.49 (39, 12H, Mes-C*H*$_3$), 0.33 (12, 6H, C*H*$_3$), 0.60 (6, 6H, Mes-C*H*$_3$), 2.21 (6, 1H, *p*Ar-C*H*), 3.57 (12, 4H, Mes-C*H*), 11.86 (41, 2H, *m*Ar-C*H*).

Preparation of ^{Mes}PDI^{Me}EuCl$_3$(NCMe). A 20 mL scintillation was charged with $EuCl_3$ (0.100 g, 0.387 mmol) and 2 mL of acetonitrile, creating a slurry. A solution of ^{Mes}PDI^{Me} (0.169 g, 0.425 mmol) in 2 mL of acetonitrile was added. Note: 1.1 equivalents of ^{Mes}PDI^{Me} were used to promote metallation; excess ^{Mes}PDI^{Me} could be washed away with pentane after metallation. This yellow solution was stirred overnight, causing solubilization of solids. After concentrating the yellow solution *in vacuo*, the resulting yellow residue was washed with pentane (3 x 5 mL) until the pentane washes came out clear. After concentrating *in vacuo*, a yellow powder was obtained and assigned as ^{Mes}PDI^{Me}EuCl$_3$(NCMe) (0.256 g, 0.343 mmol, 89%). Yellow crystals suitable for X-ray analysis were grown by slow diffusion of pentane into a concentrated acetonitrile solution at -35 °C. Analysis for $C_{29}H_{34}N_4Cl_3Eu$: Calcd C, 49.98; H, 4.92; N, 8.04. Found C, 49.77; H, 4.98; N, 7.92. ^{1}H NMR (CD_3CN, 25 °C): δ = 4.12 (129, 2H, *m*Ar-C*H*), 4.78 (3, 1H, *p*Ar-C*H*), 4.87 (34, 6H, Mes-CH_3), 7.74 (36, 12H, Mes-CH_3), 9.80 (4, 6H, CH_3), 12.06 (43, 4H, Mes-C*H*).

Preparation of ^{Mes}PDI^{Me}CeCl$_2$(THF)$_2$. A 20 mL scintillation vial was charged with ^{Mes}PDI^{Me}CeCl$_3$(NCMe) (0.100 g, 0.136 mmol) and 5 ml of THF. While stirring, KC_8 (0.022 g, 0.163 mmol) was added, causing an immediate darkening of the solution. After stirring for one hour, the reaction was filtered and concentrated *in vacuo* to a dark residue. This residue was brought up into 10 mL of toluene, filtered to remove KCl, and again concentrated *in vacuo* to an orange powder assigned as ^{Mes}PDI^{Me}CeCl$_2$(THF)$_2$ (0.041 g, 0.054 mmol, 40%). Orange single crystals suitable for X-ray analysis were grown from a concentrated toluene solution cooled to -35 °C. ^{1}H NMR (CD_3CN, 25 °C): δ = -3.00 (5, 1H, *p*Ar-C*H*), -2.44 (31, 12H, Mes-CH_3), 4.11 (24, 4H, Mes-C*H*), 16.13 (24, 6H, Mes-CH_3), 33.96 (34, 2H, *m*Ar-C*H*), 218.53 (4, 6H, CH_3).

Preparation of ^{Mes}PDI^{Me}NdI$_3$(NCMe). A 20 mL scintillation was charged with $NdI_3(THF)_{3.5}$ (0.147 g, 0.189 mmol) and 5 mL of toluene, creating a slurry. A solution of ^{Mes}PDI^{Me} (0.075 g, 0.189 mmol) in 2 mL of toluene was added. This cloudy yellow solution was stirred overnight, causing solubilization of solids. After concentrating the yellow solution *in vacuo*, the resulting yellow residue was washed with pentane (3 x 5 mL) until the pentane washes came out clear. After concentrating *in vacuo*, a yellow powder was obtained and assigned as ^{Mes}PDI^{Me}NdI$_3$(THF) (0.167g, 0.168 mmol, 89%). Analysis for $C_{27}H_{39}N_3OI_3Nd$: Calcd C, 37.47; H, 3.85; N, 4.23. Found C, 38.16; H, 3.86; N, 3.75. ^{1}H NMR (C_6D_6, 25 °C): δ = -4.12 (26, 12H, Mes-CH_3), 2.02

(4, 6H, Mes-CH_3), 2.69 (17, 6H, CH_3), 5.39 (9, 4H, Mes-C*H*), 14.25 (8, 1H, *p*Ar-C*H*), -15.58 (19, 2H, *m*Ar-C*H*).

Preparation of ^{Mes}PDI^{Me}NdI$_2$(THF)$_2$. A 20 mL scintillation was charged with NdI$_3$(THF)$_{3.5}$ (0.195 g, 0.251 mmol), ^{Mes}PDI^{Me} (0.100 g, 0.251 mmol), and 10 mL of THF, creating a slurry. While stirring, KC$_8$ (0.034, 0.252 mmol) was slowly added as a solid, causing an immediate color change to orange. After stirring for one hour, the reaction was filtered (to remove graphite and KI) and concentrated *in vacuo* to a dark residue. To remove any traces of free ^{Mes}PDI^{Me}, this residue was washed with pentane (3 x 10 mL), and again concentrated *in vacuo* to an orange powder assigned as ^{Mes}PDI^{Me}NdI$_2$(THF)$_2$ (0.152 g, 0.162 mmol, 83%). Orange single crystals suitable for X-ray analysis were grown from a concentrated benzene solution at room temperature. ^{1}H NMR (C_6D_6, 25 °C): δ = -237.80 (4, 1H, *p*Ar-C*H*), -8.48 (253, 12H, Mes-CH_3), 2.48 (4, 6H, Mes-CH_3), 5.72 (5, 8H, THF-CH_2), 10.20 (5, 8H, THF-CH_2), 12.72 (9, 4H, Mes-C*H*), 38.40 (91, 2H, *m*Ar-C*H*), 189.52 (4, 6H, CH_3).

Preparation of ^{Mes}PDI^{Me}NdI(THF)$_2$. A 20 mL scintillation was charged with NdI$_3$(THF)$_{3.5}$ (0.250 g, 0.322 mmol), ^{Mes}PDI^{Me} (0.128 g, 0.322 mmol), and 15 mL of THF, creating a slurry. While stirring, KC$_8$ (0.087, 0.644 mmol) was slowly added as a solid, causing an immediate color change to dark-orange. After stirring for one hour, the reaction was filtered (to remove graphite and KI) and concentrated *in vacuo* to a dark residue. To remove any traces of free ^{Mes}PDI^{Me}, this residue was washed with pentane (3 x 12 mL), and again concentrated *in vacuo* to a dark-orange powder assigned as ^{Mes}PDI^{Me}NdI(THF)$_2$ (0.144 g, 0.177 mmol, 55%). Orange single crystals suitable for X-ray analysis were grown from a concentrated Et$_2$O solution cooled to -35 °C. No signals for ^{Mes}PDI^{Me}NdI(THF)$_2$ are observed in the ^{1}H NMR spectrum at room temperature.

Preparation of [^{Mes}PDI^{Me}Nd(THF)]$_2$. A 20 mL scintillation was charged with NdI$_3$(THF)$_{3.5}$ (0.150 g, 0.251 mmol), ^{Mes}PDI^{Me} (0.076 g, 0.251 mmol), and 12 mL of THF, creating a slurry. While stirring, KC$_8$ (0.078, 0.252 mmol) was slowly added as a solid, causing an immediate color change to dark brown-green. After stirring for one hour, the reaction was filtered (to remove graphite and KI) and concentrated *in vacuo* to a dark residue. To remove any traces of bis(^{Mes}PDI^{Me}) product, this residue was washed with pentane (6 x 10 mL), and again concentrated *in vacuo* to an emerald green powder assigned as [^{Mes}PDI^{Me}Nd(THF)]$_2$ (0.100 g, 0.081 mmol, 65%). Green single crystals suitable for X-ray analysis were grown from a concentrated Et_2O solution cooled to -35 °C. ^{1}H NMR (C_6D_6, 25 °C): δ = -479.37 (5, 1H, *p*Ar-C*H*), -6.16 (103, 6H, Mes-CH_3), 2.56 (14, 8H, THF-CH_2), 3.22 (26, 8H, THF-CH_2), 7.34 (8, 6H, Mes-CH_3), 10.73 (15, 6H, Mes-CH_3), 14.22 (9, 2H, Mes-C*H*), 30.28 (110, 2H, Mes-C*H*), 160.74 (5, 2H, *m*Ar-C*H*), 227.31 (5, 6H, CH_3).

(^{Mes}PDI^{Me})$_2$Nd. A 20 mL scintillation was charged with $NdI_3(THF)_{3.5}$ (0.150 g, 0.251 mmol), ^{Mes}PDI^{Me} (0.153 g, 0.494 mmol), and 12 mL of THF, creating a slurry. While stirring, KC_8 (0.078, 0.252 mmol) was slowly added as a solid, causing an immediate color change to dark brown-green. After stirring for one hour, the reaction was filtered (to remove graphite and KI) and concentrated *in vacuo* to a dark residue assigned as (^{Mes}PDI^{Me})$_2$Nd (0.217 g, 0.231 mmol, 92%). ^{1}H NMR (C_6D_6, 25 °C): δ = -121.71 (6, 1H, *p*Ar-C*H*), -14.46 (91, 12H, Mes-CH_3), 2.39 (4, 6H, Mes-CH_3), 5.65 (10, 4H, Mes-C*H*), 27.86 (52, 2H, *m*Ar-C*H*), 117.09 (5, 6H, CH_3).

4.3 Results and Discussion

4.3.1 Lanthanide Chloride Chemistry

Due to the commercial availability of many anhydrous lanthanide chloride salts, these starting materials were chosen as a starting point for initial metallation of ^{Mes}PDI^{Me} ligand. Cerium (III) chloride was first attempted based on its availability to access the tetravalent oxidation state and perhaps exhibit ligand cooperativity in redox processes. Initial attempts to metallate ^{Mes}PDI^{Me} with $CeCl_3$ in coordinating polar solvents such as THF were unsuccessful as the THF would out compete the neutral ^{Mes}PDI^{Me} ligand. This is likely an artefact of the high oxophilicity of the lanthanides and was also observed with oxophilic uranium.[26,121] This posed a conundrum for neutral metallation, as the $CeCl_3$ wasn't soluble enough in nonpolar solvents to promote metallation, but coordinating solvents would often outcompete the neutral ligand. This problem was solved with the use of acetonitrile. As shown in Scheme 4.1, addition of ^{Mes}PDI^{Me} to an acetonitrile solution of $CeCl_3$ produced ^{Mes}PDI^{Me}CeCl$_3$(NCMe) after workup.

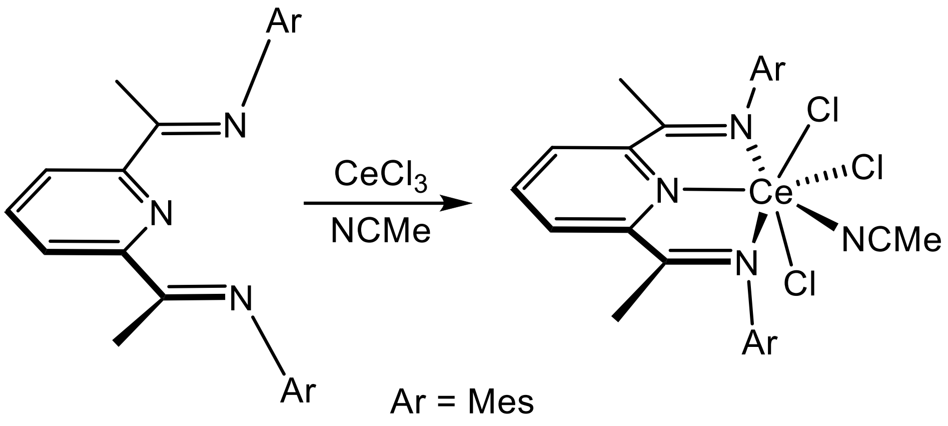

Scheme 4.1. Synthesis of $^{Mes}PDI^{Me}CeCl_3(NCMe)$.

Analysis of $^{Mes}PDI^{Me}CeCl_3(NCMe)$ by ^1H NMR spectroscopy in CD_3CN confirmed that metallation had occurred, based on the paramagnetic distribution of peaks. Significantly broadened peaks were observed in a range between -3.49 and 11.86 ppm. Yellow crystals suitable for X-ray analysis were grown by slow diffusion of pentane into a concentrated acetonitrile solution at -35 °C. Analysis of one of the crystals by X-ray crystallography confirmed the assignment as $^{Mes}PDI^{Me}CeCl_3(NCMe)$ (Figure 4.1).

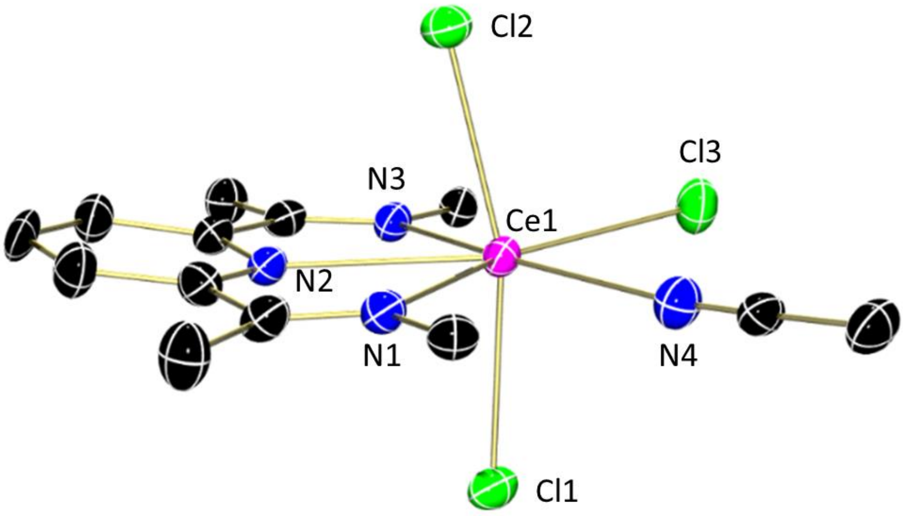

Figure 4.1. Molecular structures of $^{Mes}PDI^{Me}CeCl_3(NCMe)$ shown with 30% probability ellipsoids. Hydrogen atoms, cocrystallized solvent molecules, and mesityl groups have been omitted for clarity.

Due to the redox capability of Ce, different electronic structures are possible for $^{Mes}PDI^{Me}CeCl_3(NCMe)$. To assign the oxidation state of Ce and the $^{Mes}PDI^{Me}$ ligand, metrical parameters were analyzed. The Ce-N distances to the $^{Mes}PDI^{Me}$ ligand (2.646(5)-2.7131(16) Å) are consistent with Ce(III)-neutral nitrogen contacts.[122] Additionally, intraligand distances were consistent with a neutral $^{Mes}PDI^{Me}$ ligand. Particularly, the C-N$_{imide}$ distances (1.276(8) and 1.279(7) Å) are consistent with double bonds. Therefore, $^{Mes}PDI^{Me}CeCl_3(NCMe)$ was assigned as having a neutral $^{Mes}PDI^{Me}$ ligand chelated to a Ce^{3+} ion.

In a similar fashion, addition of $^{Mes}PDI^{Me}$ to an acetonitrile solution of $EuCl_3$ produced $^{Mes}PDI^{Me}EuCl_3(NCMe)$ after workup (Scheme 4.2). Analysis of $^{Mes}PDI^{Me}EuCl_3(NCMe)$ by ^1H NMR spectroscopy in CD_3CN again confirmed that metallation had occurred, based on the paramagnetic distribution and extreme broadening of the peaks. Significantly broadened peaks were observed in a range between 4.12 and 12.06 ppm. The broadness of the peaks is consistent with an f^6 state of a Eu^{3+} cation.

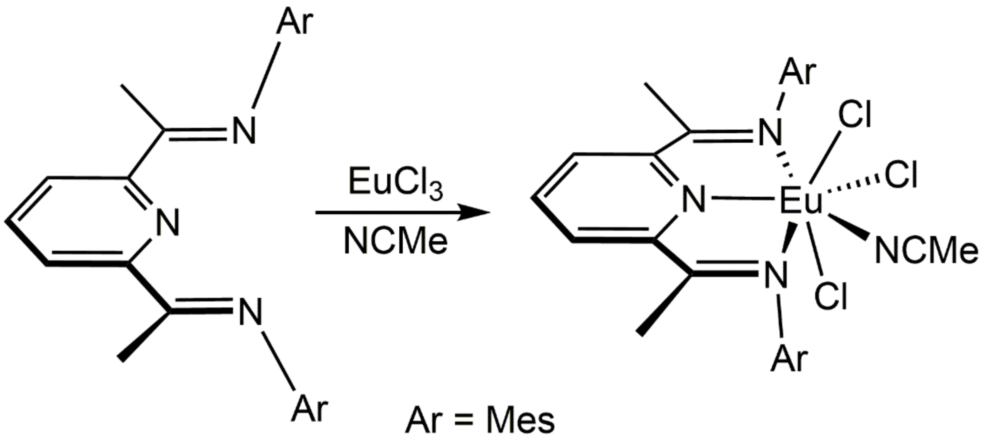

Scheme 4.2. Synthesis of $^{Mes}PDI^{Me}EuCl_3(NCMe)$.

Yellow crystals suitable for X-ray analysis were grown by slow diffusion of pentane into a concentrated acetonitrile solution at -35 °C. Analysis of one of the crystals by X-ray crystallography confirmed the assignment as $^{Mes}PDI^{Me}EuCl_3(NCMe)$ (Figure 4.2). Unfortunately, the coordinated acetonitrile molecule was disordered with an acetamide ligand; however, this does show the stability of this fully oxidized complex toward water, which is likely the cause of the acetamide formation. Metrical parameters again signify a Eu^{3+} chelated with a neutral $^{Mes}PDI^{Me}$ ligand. Specifically, U-N distances to the $^{Mes}PDI^{Me}$ ligand (2.539(6)-2.601(7) Å) are consistent with Eu(III)-neutral nitrogen contacts.[68] Additionally, intraligand distances were consistent with a neutral $^{Mes}PDI^{Me}$ ligand. Particularly, the C-N_{imide} distances (1.289(10) and 1.284(12) Å) are consistent with double bonds. This leads to the definitive assignment of $^{Mes}PDI^{Me}EuCl_3(NCMe)$ as having a Eu^{3+} cation supported by a neutral $^{Mes}PDI^{Me}$ chelate.

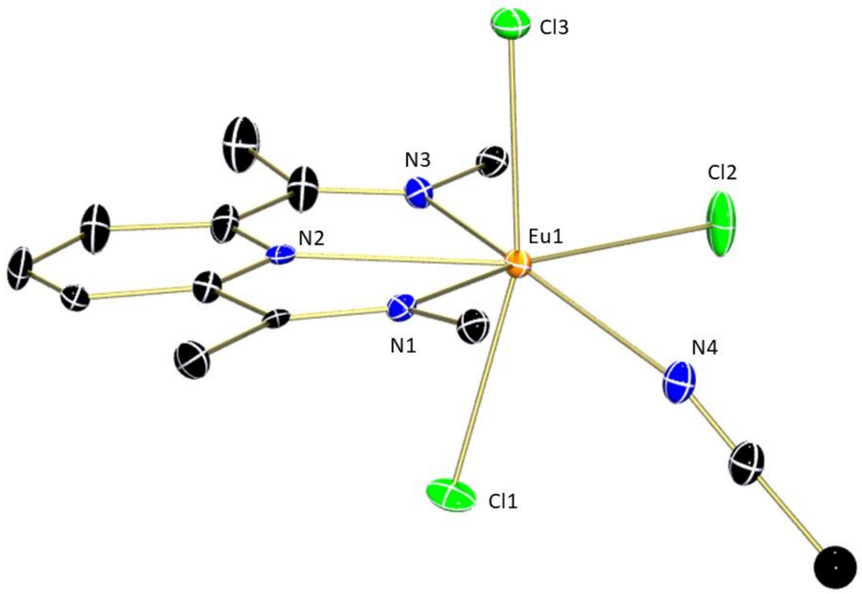

Figure 4.2. Molecular structures of $^{Mes}PDI^{Me}EuCl_3(NCMe)$ shown with 30% probability ellipsoids. Hydrogen atoms, cocrystallized solvent molecules, acetamide disorder, and mesityl groups have been omitted for clarity.

With these two different $^{Mes}PDI^{Me}$-lanthanide complexes in hand, their reduction chemistry was explored. Addition of one equivalent of KC_8 to THF solutions of $^{Mes}PDI^{Me}CeCl_3(NCMe)$ and $^{Mes}PDI^{Me}EuCl_3(NCMe)$ produced two completely different results. While a new $^{Mes}PDI^{Me}$-cerium complex was obtained, as determined by ^1H NMR spectroscopy, the europium complex didn't retain the $^{Mes}PDI^{Me}$ ligand. Only free $^{Mes}PDI^{Me}$ was identifiable from the europium reaction. This was hypothesized to be due to the accessible +2 oxidation state. Reduction to Eu^{2+} likely results in less effective charge and loss of the neutral $^{Mes}PDI^{Me}$ ligand.

Cerium doesn't have an accessible +2 oxidation state, and this is likely the reason that the reduction retains the $^{Mes}PDI^{Me}$ ligand. As shown in Scheme 4.3, addition of one equivalent of KC_8 to a stirring solution of $^{Mes}PDI^{Me}CeCl_3(NCMe)$ in THF resulted in an orange powder after workup. This product was assigned as $^{Mes}PDI^{Me}CeCl_2(THF)_2$, albeit in low yield. The low yield (40%) is presumably a result of the incompatibility of the coordinated acetonitrile in the reducing conditions.

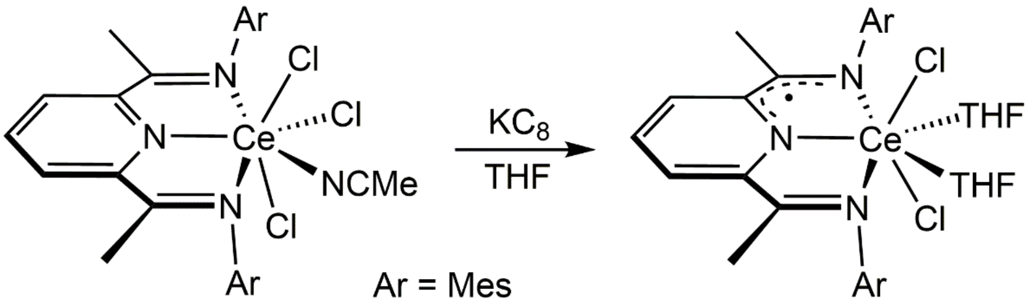

Scheme 4.3. Synthesis of $^{Mes}PDI^{Me}CeCl_2(THF)_2$.

Analysis by ^1H NMR spectroscopy reveals a different paramagnetically shifted product than $^{Mes}PDI^{Me}CeCl_3(NCMe)$. Peaks assignable to coordinated $^{Mes}PDI^{Me}$ are observed in a range from -3.00 to 218.53 ppm. Orange crystals suitable for X-ray analysis were grown a concentrated toluene solution cooled to -35 °C. Analysis of one of the crystals by X-ray crystallography confirmed the assignment as $^{Mes}PDI^{Me}CeCl_2(THF)_2$ (Figure 4.3). Metrical parameters were examined to determine if the reduction occurred at the metal or $^{Mes}PDI^{Me}$ ligand. Analysis shows Ce-N bonds (2.474(15)-2.591(6) Å) to the $^{Mes}PDI^{Me}$ ligand that are shorter than those in $^{Mes}PDI^{Me}CeCl_3(NCMe)$. This is consistent with ligand reduction as expected. Also, there is an increase in the ligand C-N$_{imine}$ bonds (1.369(14) Å), consistent with reduction as well. Overall, $^{Mes}PDI^{Me}CeCl_2(THF)_2$ is assigned as a cerium +3 center with a monoanionic $^{Mes}PDI^{Me}$ ligand.

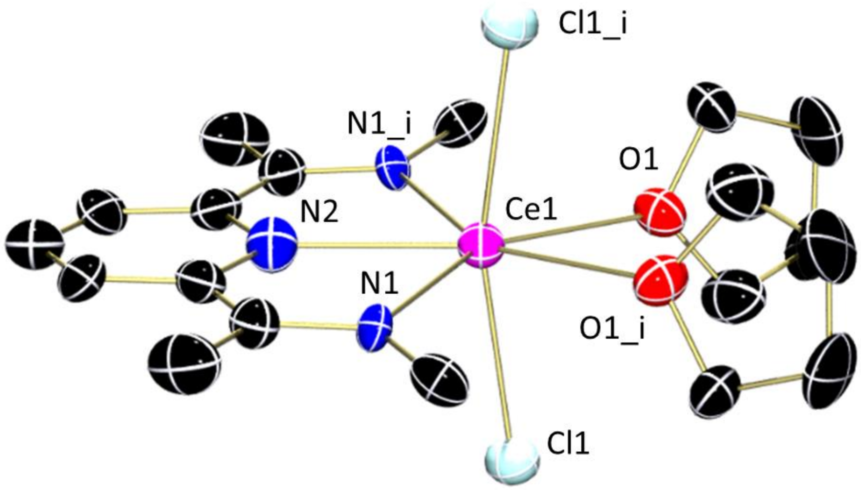

Figure 4.3. Molecular structures of $^{Mes}PDI^{Me}CeCl_2(THF)_2$ shown with 30% probability ellipsoids. Hydrogen atoms and mesityl groups have been omitted for clarity.

Unfortunately, further reductions of $^{Mes}PDI^{Me}CeCl_2(THF)_2$ was unsuccessful. No new paramagnetic products were observed with sequential KC_8 additions, and often only free $^{Mes}PDI^{Me}$ was identified from these attempts. Furthermore, the low yield of $^{Mes}PDI^{Me}CeCl_2(THF)_2$ hindered this chemistry. Routes from other lanthanide starting materials proved to be more successful in obtaining the $^{Mes}PDI^{Me}$ reduction series on lanthanides.

4.3.2 Neodymium Iodide Chemistry

To improve the reduction chemistry of PDI-Ln complexes, it was rationalized that $NdI_3(THF)_{3.5}$ would be an improved entry route into this chemistry.[18] Benefits were envisioned such as increased solubility over $LnCl_3$ salts and better reduction chemistry associated with the loss of KI (which could much more easily be extracted compared to KCl) as well. This chemistry should also better correlate to PDI chemistry using $UI_3(THF)_4$, which is well established.[26]

Coincidentally, pyridine(diimine) chemistry has already been explored on neodymium with the $^{DIPP}PDI^{Me}$ ligand.[123] In this study, oxidation of neodymium metal with iodine in the presence of $^{DIPP}PDI^{Me}$ ligand produced $^{DIPP}PDI^{Me}NdI_2(THF)$ in low yield. It was concluded that further reduction was unsuccessful, and the $^{DIPP}PDI^{Me}$ ligand was susceptible to deprotonation at the imine CH_3 group. Additional to the low yield, no ^1H NMR data was reported. It was rationalized that the recent development of well-defined $NdI_3(THF)_{3.5}$ would aid in the synthesis and allow for further exploration of reduction chemistry.[18]

In a similar fashion to the analogous uranium chemistry, stirring a mixture of $^{Mes}PDI^{Me}$ and $NdI_3(THF)_{3.5}$ in toluene overnight resulted in the isolation of $^{Mes}PDI^{Me}NdI_3(THF)$ after workup (Scheme 4.4). This product formation was evident by ^1H NMR spectroscopy, which shows broad, paramagnetically-shifted peaks assignable to a coordinated $^{Mes}PDI^{Me}$ ligand in the region of -4.12 to 15.58 ppm. X-ray crystallography of this product wasn't successful due to the lack of suitable crystals, but one coordinated THF was assumed based on analogy to the results with uranium.[26] The exact formula didn't affect further chemistry since *in situ* routes to reduced products proved to be clean and high yielding.

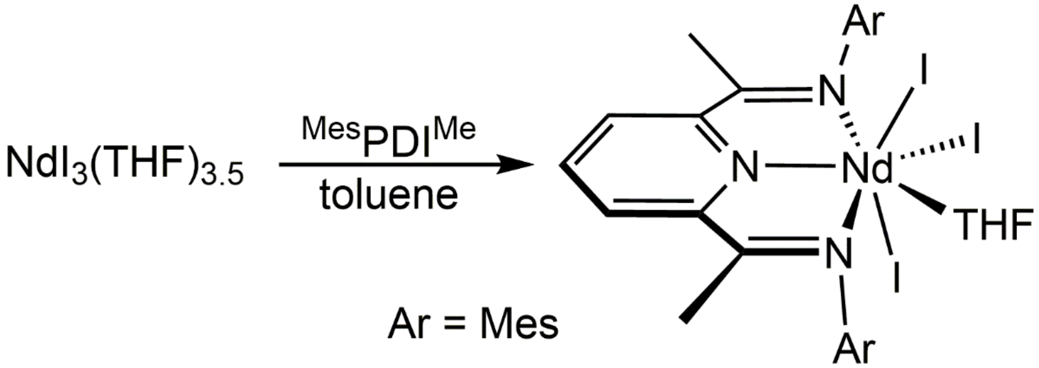

Scheme 4.4. Synthesis of $^{Mes}PDI^{Me}NdI_3(THF)$.

Instead of exploring direct reduction of $^{Mes}PDI^{Me}NdI_3(THF)$, it was rationalized that *in situ* reduction routes may be cleaner and more versatile. Along these lines, slow addition of solid KC_8 to a stirring slurry of $NdI_3(THF)_{3.5}$ and $^{Mes}PDI^{Me}$ resulted in the formation of a bright orange solution almost immediately. After workup to remove graphite and KI, an orange powder was isolated in high yield and assigned as $^{Mes}PDI^{Me}NdI_2(THF)_2$ (Scheme 4.5). This product formation was evident by ^1H NMR spectroscopy, which shows sharp, paramagnetically-shifted peaks assignable to a coordinated $^{Mes}PDI^{Me}$ ligand (different than $^{Mes}PDI^{Me}NdI_3(THF)$) in the region of -237.80 to 189.52 ppm. The extreme upfield and downfield shifts are consistent with the presence of paramagnetism associated with a ligand radical.[26,48] The monoanionic ligand is expected to have a ligand radical. Additionally, broad resonances assignable to bound-THF molecules are observed at 5.72 and 10.20 ppm.

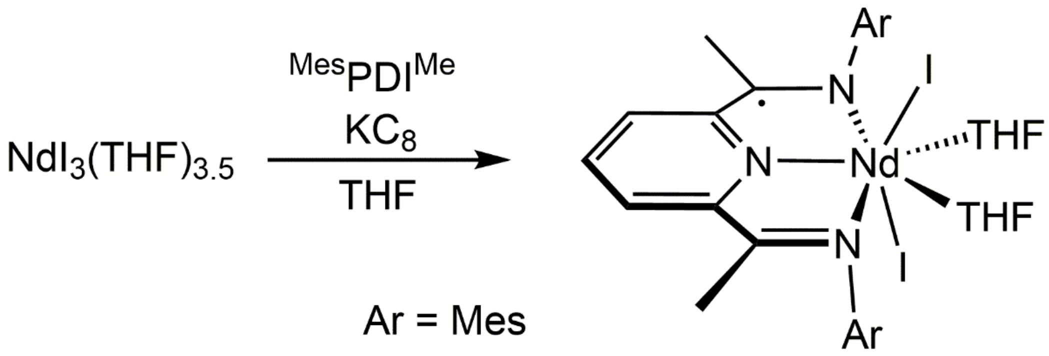

Scheme 4.5. Synthesis of $^{Mes}PDI^{Me}NdI_2(THF)_2$.

Orange crystals of $^{Mes}PDI^{Me}NdI_2(THF)_2$ were grown overnight from a concentrated benzene solution at room temperature, confirming the structural assignment (Figure 4.4). Metrical parameters were examined to confirm that the reduction occurred at the $^{Mes}PDI^{Me}$ ligand. Analysis shows Nd-N bonds (2.416(5)-2.599(5) Å) to the $^{Mes}PDI^{Me}$ ligand that are intermediate typical Nd-N ionic and Nd-N neutral bonds.[123] This is consistent with ligand reduction since the monoanionic ligand has resonance of one ionic N throughout each nitrogen contact. Also, there is an increase in the ligand C-N$_{imine}$ bonds (1.318(8) and 1.307(8) Å) compared to $^{Mes}PDI^{Me}CeCl_3(NCMe)$ (1.276(8) and 1.279(7) Å), consistent with reduction as well. Overall, $^{Mes}PDI^{Me}NdI_2(THF)_2$ is assigned as a neodymium +3 center with a monoanionic $^{Mes}PDI^{Me}$ ligand.

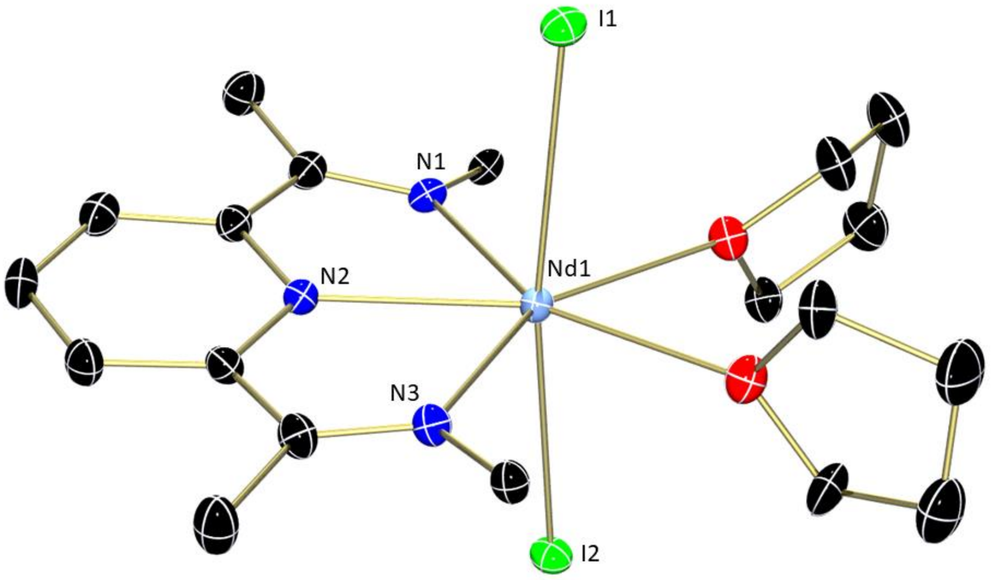

Figure 4.4. Molecular structures of $^{Mes}PDI^{Me}NdI_2(THF)_2$ shown with 30% probability ellipsoids. Hydrogen atoms, mesityl groups, and cocrystallized solvent molecules have been omitted for clarity.

In a similar fashion to the one-pot synthesis of $^{Mes}PDI^{Me}NdI_2(THF)_2$, the complex containing a dianionic $^{Mes}PDI^{Me}$ ligand was targeted. Along these lines, slow addition of two equivalents of solid KC_8 to a stirring slurry of $NdI_3(THF)_{3.5}$ and $^{Mes}PDI^{Me}$ resulted in the formation of a brown-orange solution almost immediately. After workup to remove graphite and KI, a brown powder was isolated and tentatively assigned as $^{Mes}PDI^{Me}NdI(THF)_2$ (Scheme 4.6). Interestingly, only very small peaks are ever observed for $^{Mes}PDI^{Me}NdI_2(THF)_2$ and $[^{Mes}PDI^{Me}Nd(THF)]_2$ (*vide infra*) in the ^1H NMR spectrum of this product. These two products are likely either minor impurities or perhaps even disproportionation products as they are often observed in similar ratios. Additionally, decomposition of this product with the addition of a small amount of water to the NMR sample, liberates large amounts of free $^{Mes}PDI^{Me}$. One current hypothesis as to why this product isn't observed by ^1H NMR spectroscopy at room temperature is an unusual electronic structure that creates excessive paramagnetism. This could be possible with an open-shell (diradical) dianionic $^{Mes}PDI^{Me}$ ligand. Another theory to explain the absence of ^1H NMR signals is the potential to dimerize, which could create a dynamic process in the

NMR sample. While this product is not fully understood, X-ray crystallography confirms the connectivity.

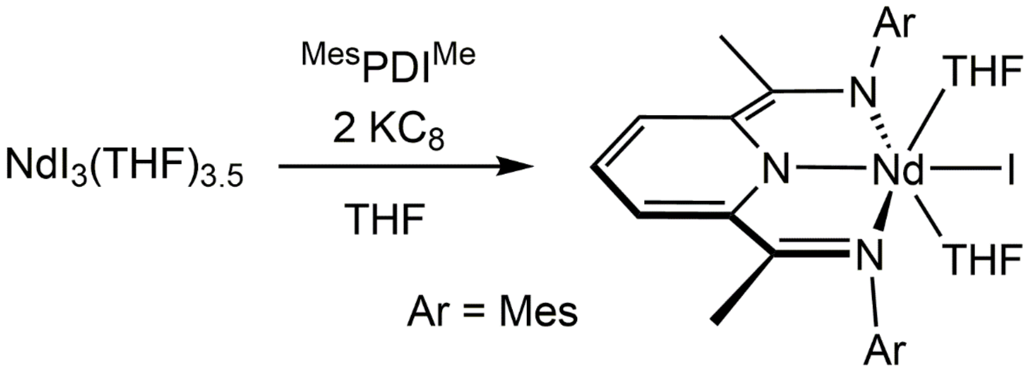

Scheme 4.6. Synthesis of $^{Mes}PDI^{Me}NdI(THF)_2$.

Orange single crystals suitable for X-ray analysis were grown from a concentrated Et_2O solution cooled to -35 °C. Analysis of one of the crystals revealed the desired product as $^{Mes}PDI^{Me}NdI(THF)_2$ (Figure 4.5). However, the data quality was poor, which precluded meaningful analysis of any metrical parameters. Based on similar Nd complexes reported here, this compound is confidently assigned as having a Nd^{3+} center supported by a dianionic $^{Mes}PDI^{Me}$ ligand.

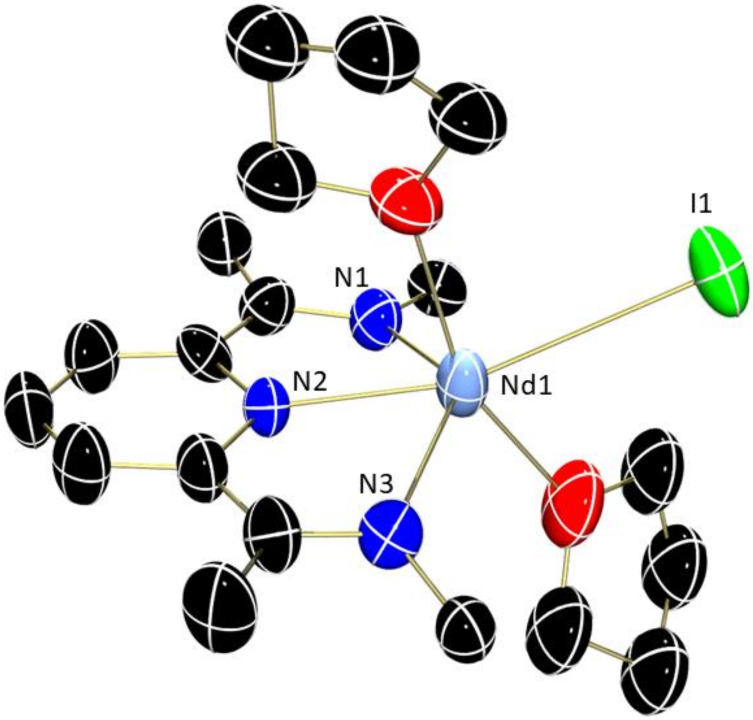

Figure 4.5. Molecular structures of $^{Mes}PDI^{Me}NdI(THF)_2$ shown with 30% probability ellipsoids. Hydrogen atoms, mesityl groups, and cocrystallized solvent molecules have been omitted for clarity.

Following a similar procedure for the one-pot synthesis of Nd-PDI complexes, the final member of this family was targeted, the most reduced complex containing a trianionic $^{Mes}PDI^{Me}$ chelate. Slow addition of three equivalents of solid KC_8 to a stirring slurry of $NdI_3(THF)_{3.5}$ and $^{Mes}PDI^{Me}$ in THF resulted in the formation of a brown-green solution almost immediately. After workup to remove graphite and KI, along with pentane washes to remove any pentane soluble products, an emerald green powder was isolated and assigned as $[^{Mes}PDI^{Me}Nd(THF)]_2$ (Scheme 4.7).

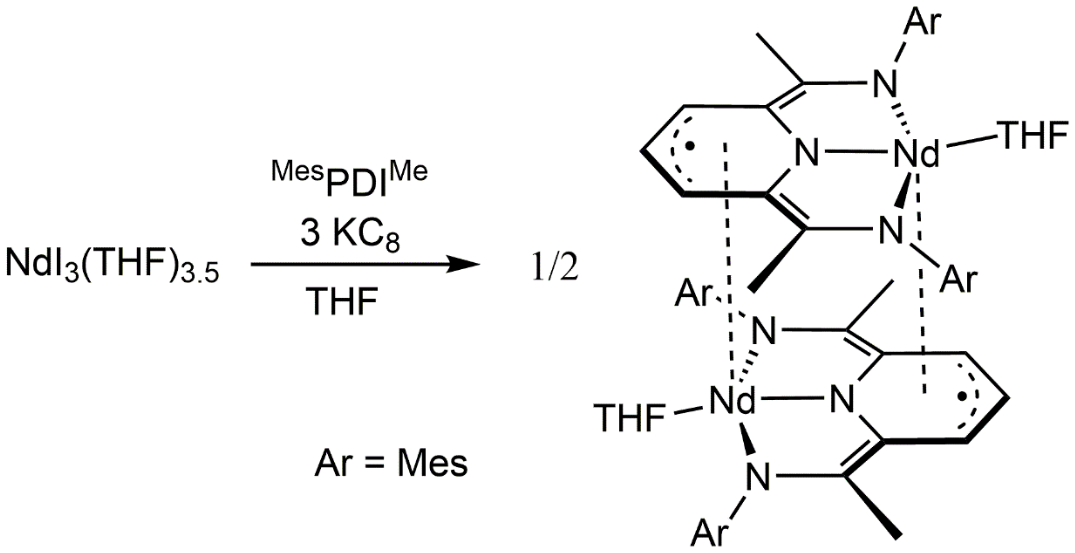

Scheme 4.7. Synthesis of $[^{Mes}PDI^{Me}Nd(THF)]_2$.

Analysis by ^{1}H NMR spectroscopy shows a new paramagnetic product with extreme upfield and downfield resonances (Figure 4.6). Resonances are observed in a region between -479.37 to 277.31 ppm. These are some of the most extreme paramagnetic shifts observed for f-block $^{Mes}PDI^{Me}$ compounds and are indicative of a ligand radical, as expected with the trianionic state of the $^{Mes}PDI^{Me}$ ligand. Interestingly, the C_{2h} symmetry of this molecule is different than the solution state symmetries of the other Nd complexes, and is consistent to the isoelectronic uranium analogue, $[^{Mes}PDI^{Me}UI]_2$.[26] This broken symmetry, likely the result of hindered rotation of the mesityl groups, suggests that this molecule exists as a dimer in the solution state.

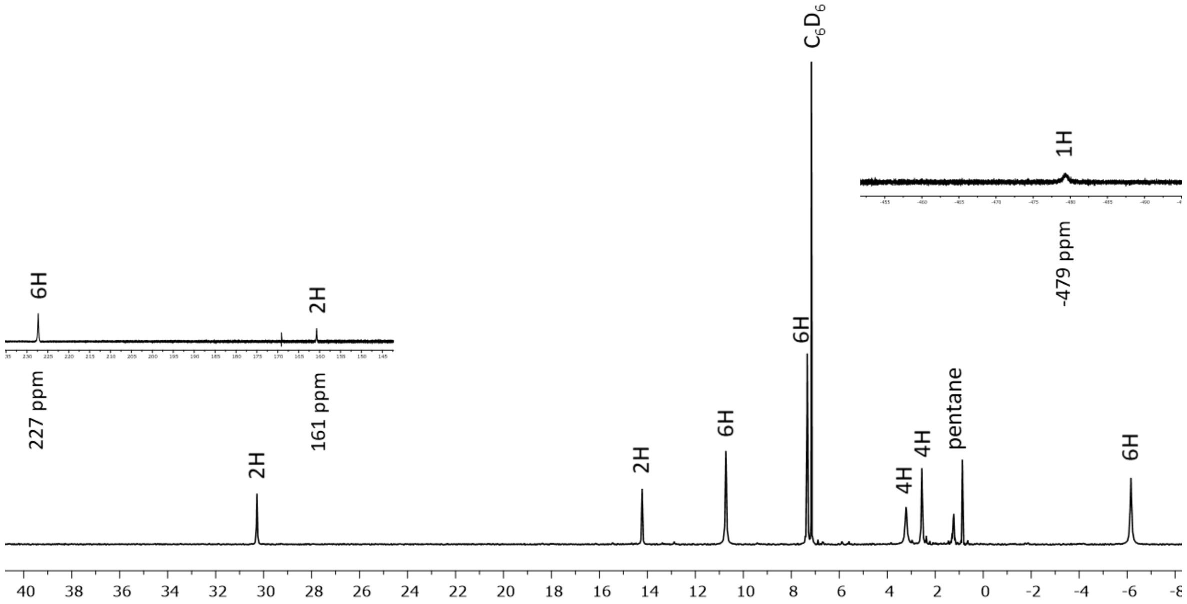

Figure 4.6. ^{1}H NMR spectrum (C_6D_6, 25 °C) of [^{Mes}PDI^{Me}Nd(THF)]$_2$, highlighting the extreme paramagnetic shifts observed for this complex.

Similar to the uranium dimer analogues, this compound has high crystallinity in many organic solvents.[26] Single crystals were grown from a concentrated Et_2O solution cooled to -35 °C. Refinement of the data revealed the desired product and confirmed the existence of a dimer in the solid state (Figure 4.7), similar to both [^{Mes}PDI^{Me}UI]$_2$ and [^{Mes}PDI^{Me}U(THF)]$_2$.[26] A molecular structure comparison of [^{Mes}PDI^{Me}Nd(THF)]$_2$ to [^{Mes}PDI^{Me}UI]$_2$ is shown in Figure 4.8, and the metrical parameter differences are highlighted in Figure 4.9. Even though [^{Mes}PDI^{Me}Nd(THF)]$_2$ is isostructural to [^{Mes}PDI^{Me}U(THF)]$_2$, a better comparison is made to [^{Mes}PDI^{Me}UI]$_2$, which has an trianionic ^{Mes}PDI^{Me} ligand similar to that of [^{Mes}PDI^{Me}Nd(THF)]$_2$ (The oxidation state of the uranium is +4 while the oxidation state of neodymium is almost certainly +3).[26,84] This comparison shows a similar bend in each of the ^{Mes}PDI^{Me} ligands to accommodate the interaction with the pyridine nitrogen to the adjacent metal center on another molecule. Once the difference in ionic radii between U^{4+} and Nd^{3+} are taken into account, the complexes have similar intermonomeric metrical parameters.[26] The intermolecular $N_{pyridine}$-Nd interaction (2.459(5) Å) is statistically shorter than the intermolecular $N_{pyridine}$-U interaction (2.441(11) and 2.461(10) Å) when a difference of 0.9 Å in ionic radii is considered.[37] However, a shorter contact is noted with the arene system of the pyridine ring in the uranium complex, even after ionic radii difference is accounted for. This could be an artefact of differing amounts of δ-interactions between the actinide and lanthanide example.[84] Minimal δ-interaction would be predicted in the neodymium due to the limited radial extent of the lanthanide 4f orbitals. Further computational studies would be needed to support this structural difference.

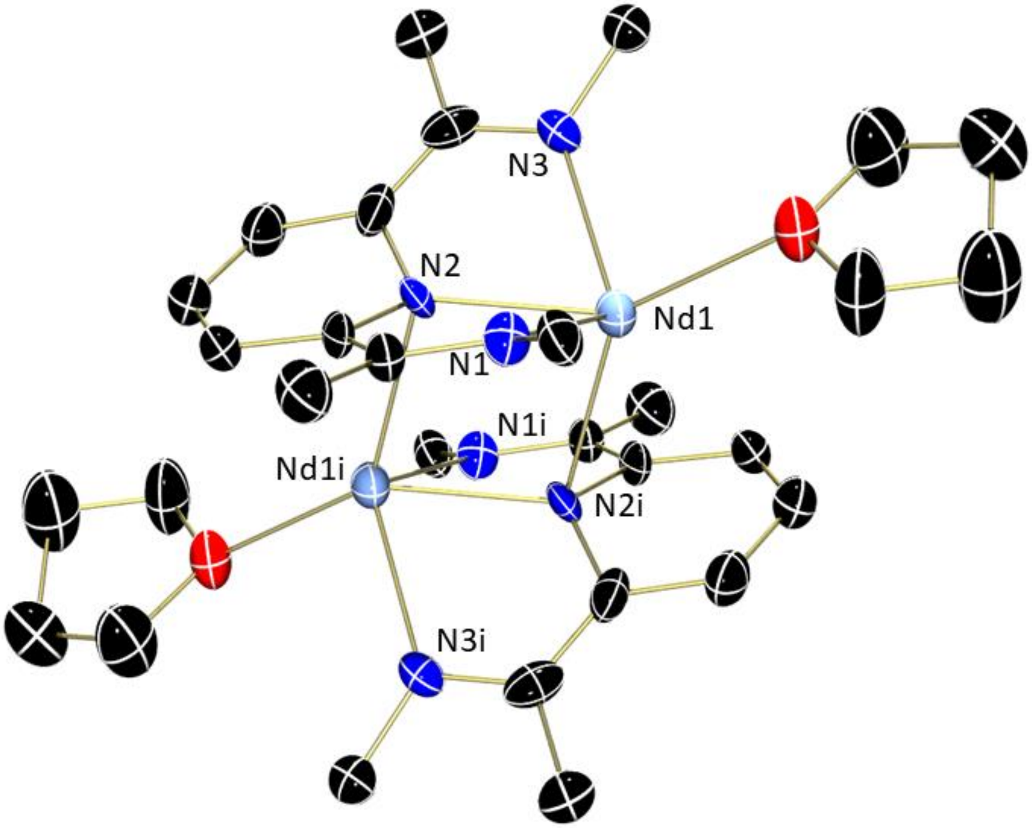

Figure 4.7. Molecular structure of [^{Mes}PDI^{Me}Nd(THF)]$_2$ shown with 30% probability ellipsoids. Hydrogen atoms and mesityl groups have been omitted for clarity.

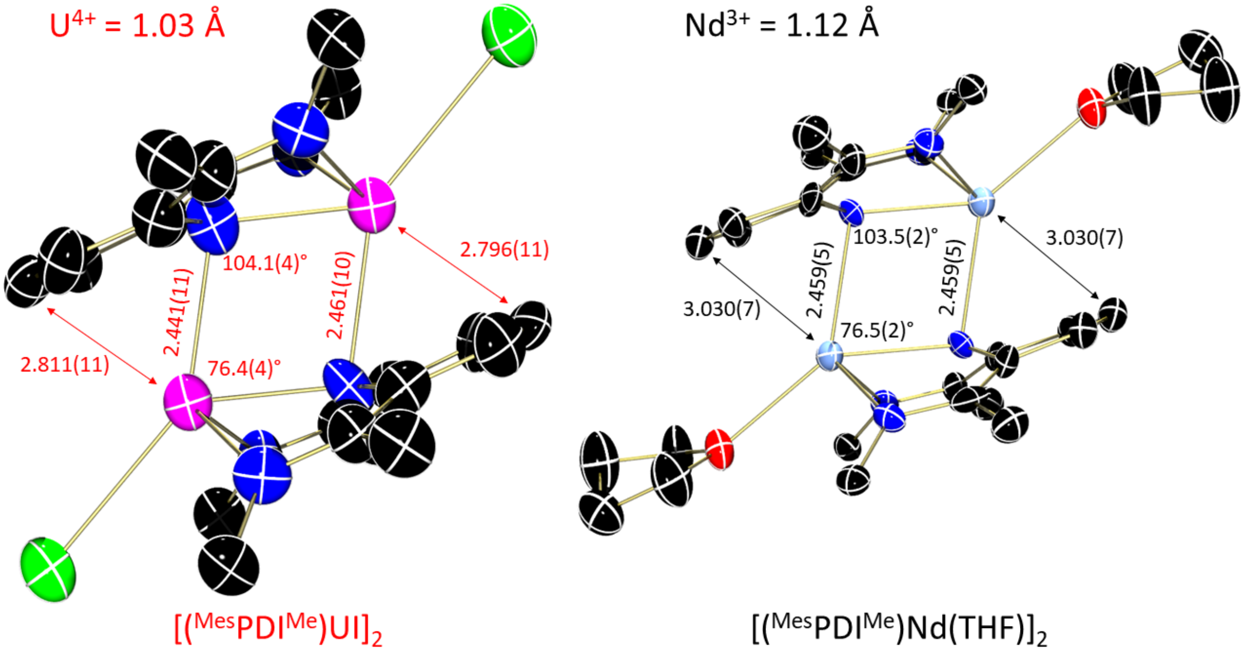

Figure 4.8. Structural comparison of $[^{Mes}PDI^{Me}UI]_2$ (left) and $[^{Mes}PDI^{Me}Nd(THF)]_2$ (right).[26]

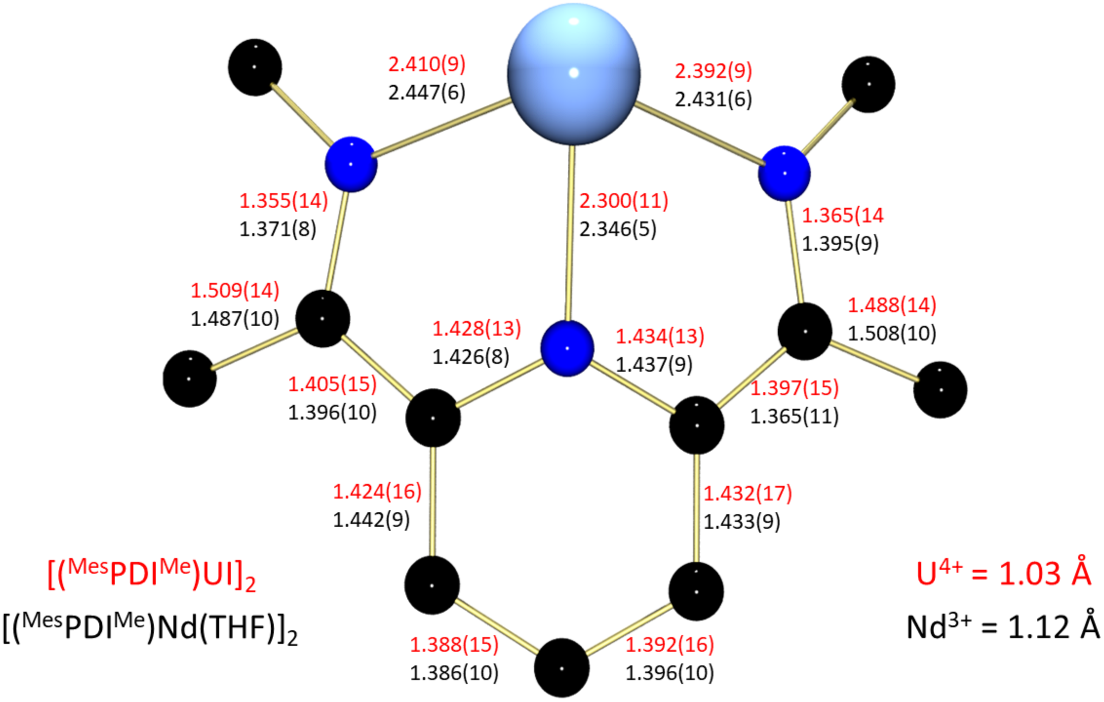

Figure 4.9. Bond distance comparison of $[^{Mes}PDI^{Me}UI]_2$ (red) and $[^{Mes}PDI^{Me}Nd(THF)]_2$ (black).[26]

Upon comparison of intraligand distances of [^{Mes}PDI^{Me}Nd(THF)]$_2$ with [^{Mes}PDI^{Me}UI]$_2$ (Figure 4.9), it is evident that the ^{Mes}PDI^{Me} ligand is in the 3+ state, as no intraligand bond is statistically different than in the uranium analogue, which is established to have a trianionic ligand.[26] Additionally, no statistical differences in metal ligand are observed when considering the differences in ionic radii between U^{4+} and Nd^{3+}.[37] When comparing bond distances of [^{Mes}PDI^{Me}Nd(THF)]$_2$ with ^{Mes}PDI^{Me}NdI$_2$(THF)$_2$, further reduction of the ^{Mes}PDI^{Me} ligand is evident for the dimer. Particularly, Nd-N distance are shortened (2.346(5)-2.447(6) vs. 2.416(5)-2.559(5) Å), while C-N$_{imine}$ distances are lengthened (1.371(8)-1.395(9) vs. 1.307(8)-1.318(8) Å). From this data, it is evident that [^{Mes}PDI^{Me}Nd(THF)]$_2$ is a Nd^{3+} center supported by a trianionic ^{Mes}PDI^{Me} ligand.

An interesting observation was made when examining crude samples of [^{Mes}PDI^{Me}Nd(THF)]$_2$ by ^{1}H NMR spectroscopy. While other compounds in the series would have a small amount of free ^{Mes}PDI^{Me} that would need to be washed away from crude reaction products, no free ^{Mes}PDI^{Me} was ever observed for the dimer. Instead, another broad paramagnetic product was observed and could be washed away with pentane washes similar to the free ligand. This product was hypothesized to be a bis ligand product. To test this theory, two equivalents (one per monomer) of ^{Mes}PDI^{Me} was added to a toluene solution of [^{Mes}PDI^{Me}Nd(THF)]$_2$ (Scheme 4.8), resulting in complete conversion to the broad peaks observed as an impurity in the synthesis of [^{Mes}PDI^{Me}Nd(THF)]$_2$.

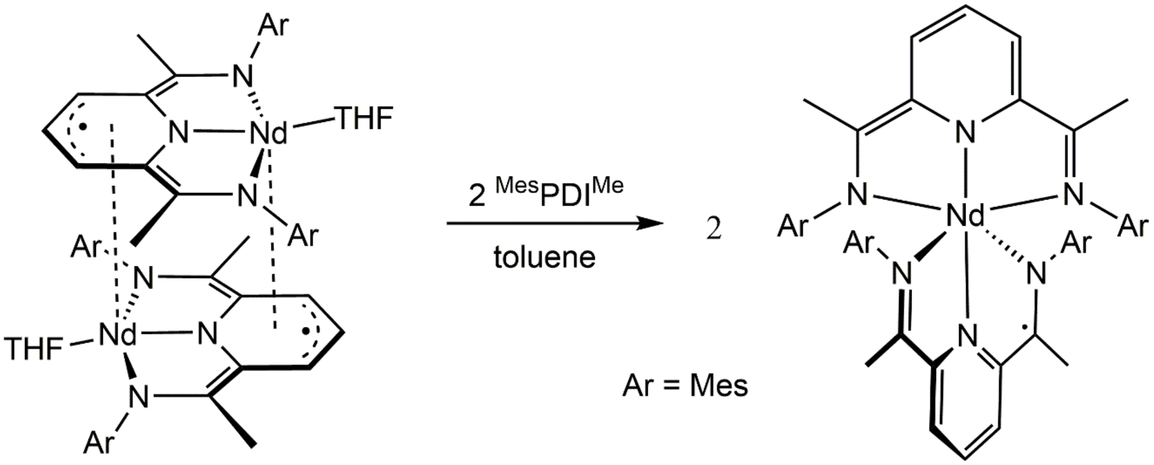

Scheme 4.8. Synthesis of $(^{Mes}PDI^{Me})_2Nd$ from $[^{Mes}PDI^{Me}Nd(THF)]_2$.

A rational, independent synthesis of this product also produced this orange compound cleanly. This was accomplished in a similar manner to the synthesis of $[^{Mes}PDI^{Me}Nd(THF)]_2$, except with an additional equivalent of $^{Mes}PDI^{Me}$ (Scheme 4.9). ^1H NMR analysis of this product shows significantly broadened, paramagnetic peaks in the region of -121.71 to 117.09 ppm. Unfortunately, due to the extreme solubility of this product, no single crystals were obtained for X-ray analysis. However, the conversion of $[^{Mes}PDI^{Me}Nd(THF)]_2$ to this product with an equivalent of $^{Mes}PDI^{Me}$ is convincing that the product is the bis ligand product, $(^{Mes}PDI^{Me})_2Nd$. This product likely has one monoanionic and one dianionic ligand, but no further claims about specific electronic structure can be made without further characterization.

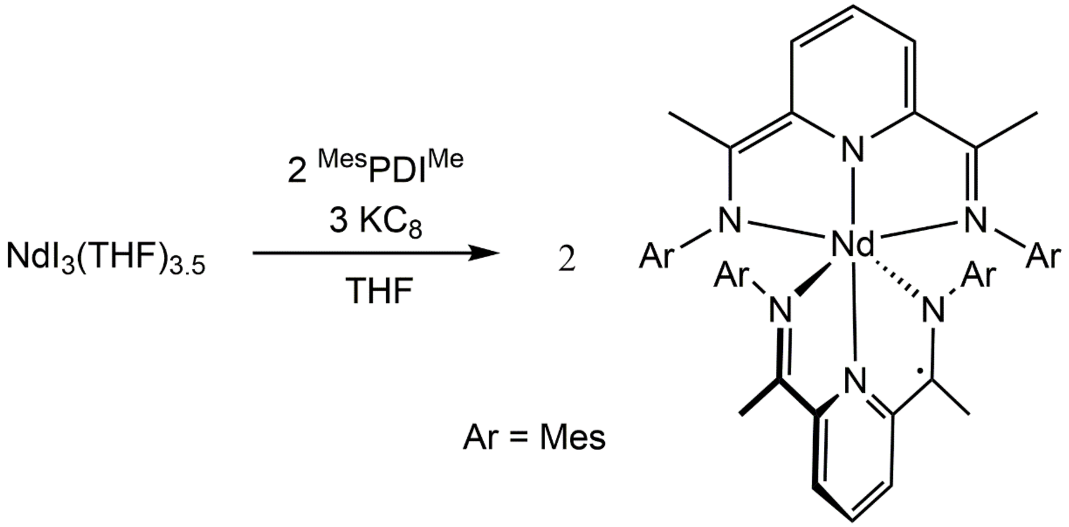

Scheme 4.9. Synthesis of $(^{Mes}PDI^{Me})_2Nd$ from $NdI_3(THF)_{3.5}$.

Formation of bis-PDI products is a common decomposition route for highly reduced transition metal complexes, while dimer formation to support triply reduced PDI ligand products appears to be unique to f-block elements.[26,84,124] Neodymium appears to be on the precipice of these two extremes. While the dimer products are certainly isolable, formation of $(^{Mes}PDI^{Me})_2Nd$ appears to facile in the presence of excess $^{Mes}PDI^{Me}$ ligand. Attempts to make $(^{Mes}PDI^{Me})_2U$ from both $[^{Mes}PDI^{Me}U(THF)]_2$ or $UI_3(THF)_4$ were completely unsuccessful, even at elevated temperatures. In these instances, the formation of dimers appeared to be favorable. On the other hand, attempts to make reduced $^{Mes}PDI^{Me}$ dimer compounds of Hf and W were unsuccessful.

4.3.3 Reactivity of $[^{Mes}PDI^{Me}Nd(THF)]_2$

4.3.3.1 Reactivity with Azides

The first reactivity sought with $[^{Mes}PDI^{Me}Nd(THF)]_2$, was the synthesis of a neodymium-imido from the activation of an azide. This would demonstrated the first use of redox chemistry at a lanthanide center to create such a rare moiety. Addition of two equivalents of N_3DIPP to a green solution of $[^{Mes}PDI^{Me}Nd(THF)]_2$ in THF results in the immediate color change to dark brown. This color change is consistent with oxidation of the $^{Mes}PDI^{Me}$ ligand, since all other

^{Mes}PDI^{Me}-Nd complexes are orange or brown. Analysis of this crude reaction mixture by ^{1}H NMR spectroscopy reveals a major paramagnetic product (Figure 4.10).

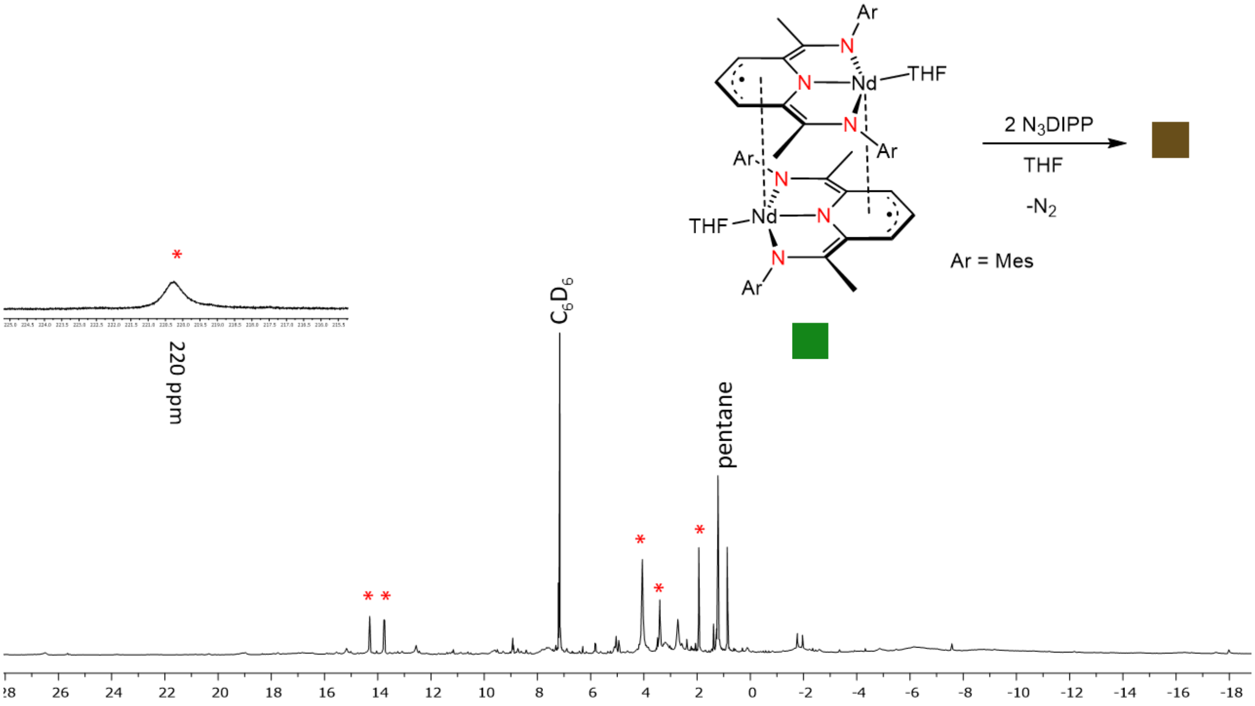

Figure 4.10. ^{1}H NMR spectrum (C_6D_6, 25 °C) showing reaction of [^{Mes}PDI^{Me}Nd(THF)]$_2$ with N_3DIPP. Red asterisks represent new paramagnetic product.

Unfortunately, analysis of this crude reaction product by IR spectroscopy shows the presence of an N-H stretch, which likely signifies decomposition of the azide (or transient imido) to an amide or amine. Low quality crystals were grown from concentrated Et_2O solutions of this crude product and were suitable for X-ray analysis. Analysis of one of these crystals revealed that the -NDIPP moiety was indeed intact with the Nd center, although this fragment was bent and heavily disordered (Figure 4.11). This group was bent at an angle of 153.5(12)° around the Nd-N-C bond, with a long Nd-N distance of 2.425(14) Å. This distance is typical of interactions to ^{Mes}PDI^{Me}NdI$_2$(THF)$_2$ and suggests a monoanionic, amide contact. Upon further examination, short contacts are noted between both C$_{imine}$-C fragments as depicted in Figure 4.11. These distances of 1.389(15) and 1.375(18) Å are consistent with double bonds, likely the result of deprotonation to create C_{imine}-CH_2, resulting in the formation of a dianionic $^{Mes}PDI^{CH2}$ ligand. This is reminiscent of the lanthanide-PDI chemistry reported by Gambarotta and Budzelaar, showing that this position is susceptible to deprotonation.[123] It appears that a nucleophilic neodymium imido is basic enough to deprotonate the $^{Mes}PDI^{Me}$ ligand to create an amide. Overall, this compound, assigned as $^{Mes}PDI^{CH2}Nd(NHDIPP(THF)_2$, is likely a decomposition product of a transient neodymium imido formed from azide activation.

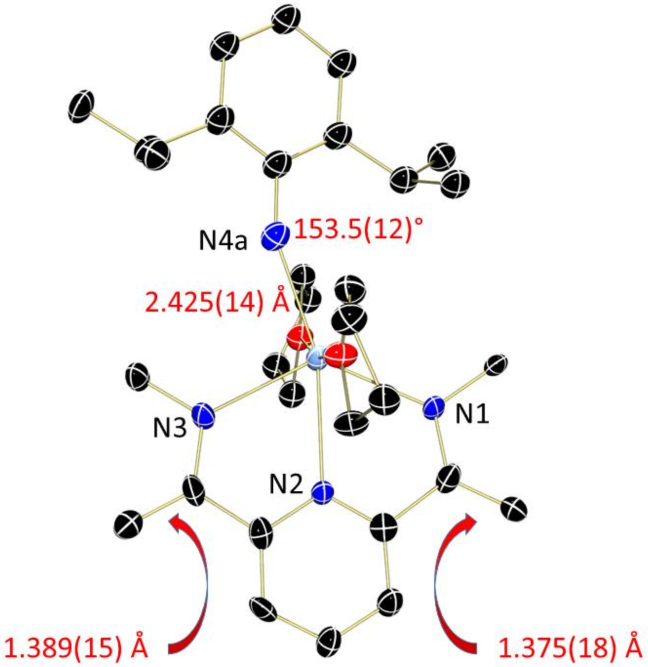

Figure 4.11. Molecular structure of $^{Mes}PDI^{CH2}Nd(NHDIPP)(THF)$ shown with 30% probability ellipsoids. Hydrogen atoms, mesityl groups, and amide disorder have been omitted for clarity.

4.3.3.2 Reactivity with Azobenzene

$[^{Mes}PDI^{Me}Nd(THF)]_2$ is also reactive towards azobenzene. Addition of two equivalents of azobenzene to a THF solution of $[^{Mes}PDI^{Me}Nd(THF)]_2$ results in the immediate formation of a brown solution. After concentrating *in vacuo*, analysis of the crude product by ^{1}H NMR spectroscopy shows a new arrangement of paramagnetic peaks (Figure 4.12). Although the peaks aren't easily assignable, this peak distribution is consistent, even when the equivalents of azobenzene are changed. The formation of monoanionic hydrazido ligands has been demonstrated on cerium, and could be one potential product of this reaction.[125]

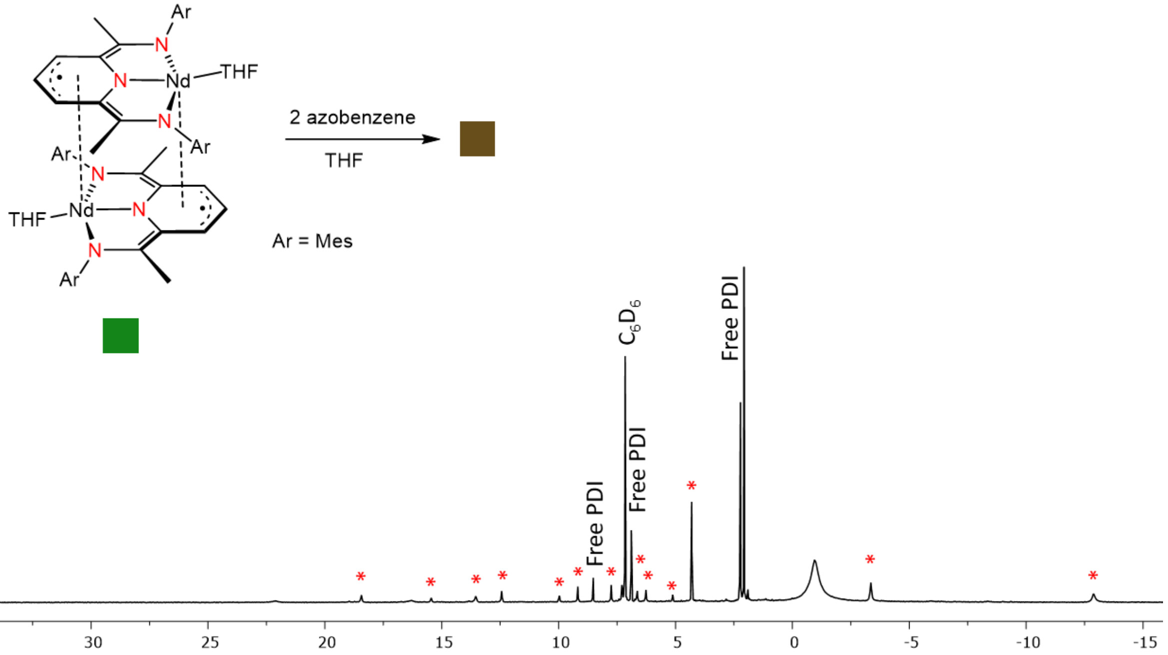

Figure 4.12. ^{1}H NMR spectrum (C_6D_6, 25 °C) showing reaction of $[^{Mes}PDI^{Me}Nd(THF)]_2$ with azobenzene. Red asterisks represent new paramagnetic product.

4.3.3.3 Reactivity with Phenazine

In an attempt to control the reactivity, phenazine, a one electron oxidant was utilized. This product has been shown to selectively oxidize divalent lanthanide compounds.[126] Addition of one equivalent of phenazine to $[^{Mes}PDI^{Me}Nd(THF)]_2$ in THF resulted in the immediate formation of a brown solution (Scheme 4.10). Analysis of this crude product by ^{1}H NMR spectroscopy showed no signals, not even for free $^{Mes}PDI^{Me}$. However, addition of water to this NMR sample liberates free $^{Mes}PDI^{Me}$ along with peaks assignable to dihydrophenazine, showing that $(^{Mes}PDI^{Me}Nd)_2(C_{12}H_8N_2)$ formation is possible. The lack of signals in the room temperature ^{1}H NMR spectrum appears to be an artefact of the dianionic $^{Mes}PDI^{Me}$ ligand coordinated to neodymium, reminiscent of $^{Mes}PDI^{Me}NdI(THF)_2$. A hypothesis for this phenomenon is that the

${}^{Mes}PDI^{Me}$ ligand adopts a highly paramagnetic open shell electronic configuration as depicted in Scheme 4.10. Unfortunately, no single crystals for X-ray analysis were obtained for this product.

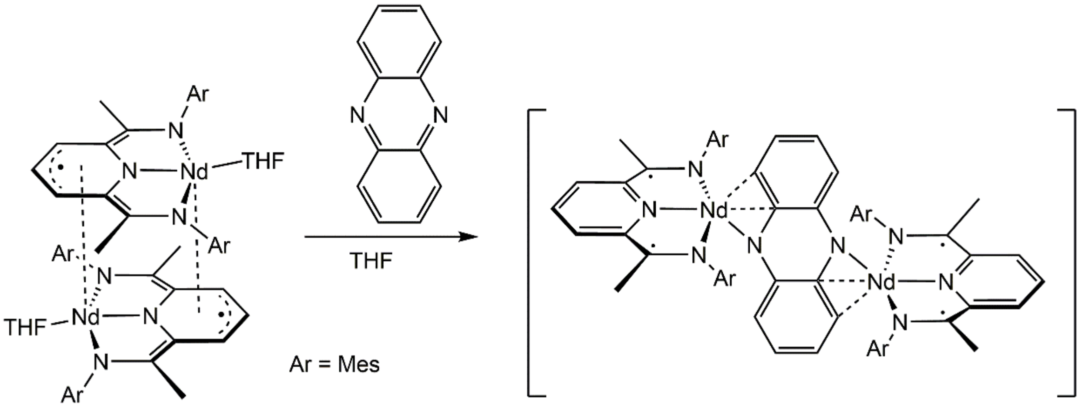

Scheme 4.10. Proposed formation of $({}^{Mes}PDI^{Me}Nd)_2(C_{12}H_8N_2)$.

4.3.3.4 Reactivity with Oxygen Atom Transfer Reagents

$[{}^{Mes}PDI^{Me}Nd(THF)]_2$ is also very reactive with oxygen atom transfer reagents such as N-methylmorpholine N-oxide or pyridine N-oxide. However, even when performing these reactions at cold well temperatures, it was difficult to isolate any neodymium products. Only free ${}^{Mes}PDI^{Me}$ was observed, likely the result of over oxidation to neodymium-odixes, which aren't soluble in organic solvents.

4.4 Conclusions

A variety of ${}^{Mes}PDI^{Me}$-lanthanide complexes were synthesized. The chloride complexes weren't useful as a route to full reduction of the ${}^{Mes}PDI^{Me}$ ligand, but the switch to $NdI_3(THF)_{3.5}$ as a starting point allowed the isolation of the full reduction series, including the highly reduced dimer, $[{}^{Mes}PDI^{Me}Nd(THF)]_2$. This molecule is interesting on two levels. From a coordination chemistry standpoint, $[{}^{Mes}PDI^{Me}Nd(THF)]_2$ is an interesting structural analogue to the uranium dimers, and could help elucidate the orbital participation involved in stabilizing these dimers. This dimer is isolable with neodymium, along with the bis ligand complex. This is an interesting combination of coordination chemistry observed for both actinides and transition metals. Also,

$[^{Mes}PDI^{Me}Nd(THF)]_2$ is interesting as a starting platform to perform redox chemistry at neodymium. This study has demonstrated the extreme reactivity of this highly reduced dimer and the accessibility of the ligand electrons for reactivity studies.

CHAPTER 5. STEPS TOWARDS URANYL ACTIVATION THROUGH NEW EQUATORIAL LIGAND BONDING

Adapted with permission from Pattenaude, S. A.; Coughlin, E. J.; Collins, T. S.; Zeller, M.; Bart, S. C. *Inorg. Chem.*, **2018**, *57*, 4543-4549. Copyright 2018 American Chemical Society.

5.1 Introduction

The uranyl moiety, UO_2^{2+}, which features strongly bonded *trans*-oxo ligands, dominates the coordination chemistry of high valent uranium.[127] In the environment, such compounds are found as inorganic salts that are highly soluble in water.[127] The low solubility of this form in common organic solvents makes its non-aqueous coordination chemistry difficult to study, which is necessary for future design of organic ligand extractants.[12] To circumvent this issue, neutral organometallic derivatives have been developed, with amide congeners being particularly advantageous due to their steric and electronic modularity. One example, $UO_2(N(SiMe_3)_2)_2(THF)_2$, originally reported by Andersen,[12] has risen to popularity because of its ease of synthesis, stability, and solubility. Furthermore, the crystallinity imparted by the bis(trimethylsilyl)amide ligands facilitates the structural characterization, typically as Lewis base derivatives.[24,128–130] More recently, Arnold and co-workers reported a variation of this compound where one methyl is replaced by a phenyl on each silyl substituent, $UO_2(N(SiMe_2Ph)_2)_2$.[131] Despite these positive attributes of amide ligands, there have been few developments in the realm of neutral amide derivatives of uranyl in recent years.

Although $UO_2(N(SiMe_3)_2)_2(THF)_2$ is a useful high-valent uranyl starting material for non-aqueous chemistry, less bulky, more basic alternatives are desirable due to the increased lability. The *tert*-butyl dimethyl silyl amide ($-N(SiHMe_2)^tBu$) is attractive in this regard, as it is more substitutionally labile as well as being sterically less demanding and has the potential to facilitate new chemistry. Furthermore, the $-N(SiHMe_2)^tBu$ ligand has more spectroscopic handles than its predecessor. While derivatives of the $-N(SiMe_3)_2$ ligand only display a singlet in the ^1H NMR spectrum and lack diagnostic infrared (IR) absorptions, the chemical shift, multiplicity and coupling constant of the Si-*H* moiety in $-N(SiHMe_2)^tBu$ can probe protonation of the ligand ($^3J_{HH}$ coupling with NH) or the presence of a secondary Si-H interaction ($^1J_{SiH}$), both of which can also be confirmed using IR spectroscopy.

Despite being well studied on the *d*-block,[132–140] less is known about the use of the -$N(SiHMe_2)^tBu$ ligand to frame *f*-block metals.[141–144] Recent work from the Sadow group highlights that this ligand effectively supports several rare earth elements, forming $RE(N(SiHMe_2)^tBu)_3$ (RE = Y, Sc, Lu).[142] In these cases, three Si-H functionalities participate in secondary interactions with the rare earth center, and their exchange rate is determined spectroscopically. Similarly, the erbium analogue, $Er(N(SiHMe_2)^tBu)_3$, is proposed to contain secondary Si-H interactions based on the fact that the *tert*-butyl groups all point away from the erbium in the molecular structure.[143] Livinghouse showed that complexes $[Li][RE(N(SiMe_2H)^tBu)_4]$ (RE = Y, La) were useful synthons to generate amide precatalysts for enantioselective hydroamination/cyclization,[144] and recently Andersen demonstrated the synthesis of the organocerium compound, $Cp^*_2CeN(SiHMe_2)^tBu$, as well.[141] Surprisingly, there are no reports of this amide ligand supporting actinide elements.

Along these lines, it was hypothesized that isolation of a class of uranyl complexes containing highly basic, kinetically accessible amides would allow for the construction of new uranyl frameworks that could allow for a better understanding of uranyl bonding and perhaps introduce new strategies for activation of this highly stable fragment. Of particular interest was the isolation of a uranyl imido, in analogy to recent work by the Bart group with imido complexes.[26,105,145] Using imido analogues to the uranyl, this work has demonstrated that heavily π-electron rich uranium centers tend to have weakened axial imido bonds.[26] This strategy of creating competing π-electron donation has also completely overcome electronic bonding preferences associated with the inverse trans influence (ITI).[105,146] In the uranyl, the ITI forces two oxo ligands trans to one another, reinforcing each ligand bonding to the uranium in a synergistic fashion.[38] This electronic influence makes activation of this moiety very difficult. Directly overcoming the thermodynamic stability of the ITI in uranyl complexes using this novel approach would be revolutionary in this field.

5.2 Experimental

General Considerations. All air- and moisture-sensitive manipulations were performed using standard Schlenk techniques or in an MBraun inert atmosphere drybox with an atmosphere of purified nitrogen. The MBraun drybox was equipped with two -35 °C freezers for cooling samples and crystallizations. Solvents for sensitive manipulations were dried and deoxygenated using literature procedures with a Seca solvent purification system.[11] Benzene-d_6 was purchased from Cambridge Isotope Laboratories, dried with molecular sieves and sodium, and degassed by three freeze–pump–thaw cycles. THF-d_8 was purchased from Cambridge Isotope Laboratories in a sealed ampule and dried over an alumina plug before it was dried additionally with sodium. Chloroform-*d* was purchased from Cambridge Isotope Laboratories and used without further purification. ^{t}BuNH$_2$, SiHMe$_2$Cl, ^{n}BuLi, ^{t}Bu$_2$bipy (^{t}Bu$_2$bipy = 4,4'-di-*tert*-butyl-2,2'-dipyridine), H$_2$NDIPP (DIPP = 2,6-diisopropylphenyl), H$_2$NAd (Ad = adamantyl), *p*-CF$_3$aniline, and BCF (BCF = tris(pentafluorophenyl)borane) were purchased from Sigma Aldrich and used without further purification. [UO$_2$Cl$_2$(THF)$_2$]$_2$ was prepared according to literature procedures[147] using UO$_3$ obtained from IBI Inc. *Caution:* U-238 is a weak α-emitter with a half-life of $t_{1/2} = 4 \times 10^9$ years. All manipulations were performed in an inert atmosphere glovebox in a laboratory equipped with proper detection equipment.

^{1}H NMR spectra were recorded on a Varian Inova 300, Bruker AV-III-400-HD, or Bruker AV-III-500-HD spectrometer operating at 299.96, 400.13, and 500.23 MHz, respectively. All chemical shifts are reported relative to the peak for SiMe$_4$, using ^{1}H (residual) chemical shifts of the solvent as a secondary standard. ^{7}Li NMR spectra were recorded on a Bruker AV-III-400-HD spectrometer operating at 155.51 MHz. ^{13}C{^{1}H} NMR spectra were recorded on a Bruker AV-III-400-HD or Bruker AV-III-500-HD spectrometer operating at 100.62 and 125.80 MHz, respectively. ^{29}Si NMR spectra were recorded on a Bruker AV-III-400-HD or Bruker AV-III-500-HD spectrometer operating at 79.49 and 99.37 MHz, respectively. ^{29}Si{^{1}H} NMR spectra were recorded on a Bruker AV-III-500-HD spectrometer operating at 99.37 MHz. For all molecules, the NMR data are reported with the chemical shift, followed by the multiplicity, any relevant coupling constants, the integration value, and the peak assignment.

Infrared spectra were recorded using a Thermo Nicolet 6700 spectrometer; samples were prepared by evaporating C$_6$D$_6$ solutions of the desired compound onto KBr salt plates. Electronic absorption measurements were recorded at 25 °C in sealed 1 cm quartz cuvettes with Cary 6000i UV-Vis-NIR spectrophotometer. Elemental analyses were performed by Midwest Microlab (Indianapolis, IN).

Single crystals of **1**, **1-crown**, **2**, and **3** suitable for X-ray diffraction, were coated with poly(isobutylene) oil in a glovebox and quickly transferred to the goniometer head of a Bruker Quest diffractometer with a fixed chi angle, a sealed tube fine focus X-ray tube, single crystal curved graphite incident beam monochromator and a Photon100 CMOS area detector. Examination and data collection were performed with Mo Kα radiation ($\lambda = 0.71073$ Å).

Data were collected, reflections were indexed and processed, and the files scaled and corrected for absorption using APEX3.[52] All data were collected with Oxford Cryosystems low temperature devices operating at 150 K. The space groups were assigned and the structures were solved by direct methods using XPREP within the SHELXTL suite of programs and refined by full matrix least squares against F^2 with all reflections using Shelxl2017[21] using the graphical interface Shelxle.[21] If not specified otherwise, H atoms attached to carbon and silicon atoms were positioned geometrically and constrained to ride on their parent atoms, with carbon hydrogen bond distances of 0.95 Å for and aromatic C-H, 0.99 and 0.98 Å for aliphatic CH_2 and CH_3 moieties, respectively, and 1.00 Å for Si-H moieties. Methyl H atoms were allowed to rotate but not to tip to best fit the experimental electron density. $U_{iso}(H)$ values were set to a multiple of $U_{eq}(C)$ with 1.5 for CH_3 and 1.2 for CH_2 and SiH units.

Synthesis of HN(SiHMe$_2$)^{t}Bu. Modified from a literature procedure.[148] In a fume hood, ^{t}BuNH$_2$ (75 mL, 0.71 mol) and Et_2O (75 mL) were added to a round-bottom flask and cooled to -78 °C in a dry ice and acetone bath. SiHMe$_2$Cl (25 mL, 0.23 mol) and Et_2O (25 mL) were added to an addition funnel and slowly added to the ^{t}BuNH$_2$ solution over the course of one hour. The resulting reaction mixture was then allowed to warm to room temperature in the acetone bath for four hours. Once warmed, the reaction mixture was vacuum filtered on a Büchner funnel and washed with Et_2O (2x10 mL). The filtrate was carefully concentrated with the aid of a fractional distillation column until all of the Et_2O was removed, leaving a clear liquid assigned as HN(SiHMe$_2$)^{t}Bu (20.2 g, 0.154 mol, 68%).

^{1}H NMR ($CDCl_3$, 300 MHz, 25 °C): δ 0.05 (d, $^3J_{HH} = 3.1$ Hz, 6 H, SiH(C*H*$_3$)$_2$), 0.48 (br s, 1 H, N*H*), 1.11 (s, 9 H, C(C*H*$_3$)$_3$), 4.49 (d sept, $^1J_{SiH} = 192.4$ Hz, 1 H, Si*H*(CH$_3$)$_2$).

^{1}H NMR (C_6D_6, 300 MHz, 25 °C): δ 0.13 (d, $^3J_{HH} = 3.0$ Hz, 6 H, SiH(C*H*$_3$)$_2$), 1.11 (s, 9 H, C(C*H*$_3$)$_3$), 4.83 (d sept, $^1J_{SiH} = 192.1$ Hz, 1 H, Si*H*(CH$_3$)$_2$).

IR (KBr, cm^{-1}): 3391 m (ν_{NH}), 2964 s, 2905 s, 2870 m, 2106 s br (ν_{SiH}), 1465 m, 1376 s, 1362 s, 1250 s, 1229 s, 1015 s, 913 s, 888 s, 839 s, 774 s, 752 m, 698 m, 686 m, 625 m.

Synthesis of LiN(SiHMe$_2$)^{t}Bu. Modified from a literature procedure.[148] A 250 mL round-bottom flask was charged with HN(SiHMe$_2$)^{t}Bu (4.500 g, 34.28 mmol) and pentane (100 mL). This clear, colorless solution was frozen in the coldwell. Upon thawing, ^{n}BuLi (2.5 M in hexanes, 13.5 mL, 33.8 mmol) was added dropwise over 5 minutes. This solution was stirred as it warmed to ambient temperature over the course of 3 hours. After concentration of the solution *in vacuo*, a white solid was collected and assigned as LiN(SiHMe$_2$)^{t}Bu (4.607 g, 33.57 mmol, 98%).

^{1}H NMR (C_6D_6, 400 MHz, 25 °C): δ 0.35 (d, $^3J_{HH}$ = 2.8 Hz, 6 H, SiH(C*H*$_3$)$_2$), 1.26 (s, 9 H, C(C*H*$_3$)$_3$), 4.86 (br m, $^1J_{SiH}$ = 169 Hz, 1 H, Si*H*(CH$_3$)$_2$).

^{7}Li NMR (C_6D_6, 155 MHz, 25 °C): δ 2.14 (*Li*).

^{13}C{^{1}H} NMR (C_6D_6, 100 MHz, 25 °C): δ 5.40 (SiH(*C*H$_3$)$_2$), 37.44 (C(*C*H$_3$)$_3$), 52.61 (*C*(CH$_3$)$_3$.

^{29}Si{^{1}H} NMR (C_6D_6, 80 MHz, 25 °C): -23.27 (*Si*H(CH$_3$)$_2$).

IR (KBr, cm^{-1}): 2953 s, 2852 m, 2043 s br (ν_{SiH}), 1465 m, 1354 m, 1244 m, 1188 m, 1037 m, 1015 m, 914 m, 884 m, 830 m, 767 m, 748 m, 692 m.

Synthesis of [Li(THF)$_3$][UO$_2$(N(SiHMe$_2$)^{t}Bu)$_3$] (1). A 20 mL scintillation vial was charged with [UO$_2$Cl$_2$(THF)$_2$]$_2$ (0.100 g, 0.103 mmol) and THF (4 mL), creating a bright yellow suspension. After stirring for 10 minutes, the solid fully dissolved, forming a light yellow solution, which was then frozen in the coldwell. In a separate 20 mL vial, LiN(SiHMe$_2$)^{t}Bu (0.085 g, 0.62 mmol) was dissolved in THF (2 mL), forming a clear, colorless solution that was also frozen in the coldwell. While thawing, the LiN(SiHMe$_2$)^{t}Bu solution was added dropwise to the thawing uranyl chloride solution. After complete addition, the resulting solution gradually darkened to red-orange over the course of one minute. The reaction mixture was stirred for one hour as it warmed to ambient temperature. This red-orange solution was then concentrated to a dark residue *in vacuo*. This residue was dissolved in Et$_2$O (6 mL), filtered to remove LiCl, and concentrated to a red-orange powder assigned as [Li(THF)$_3$][UO$_2$(N(SiHMe$_2$)^{t}Bu)$_3$] (**1**) (0.155 g, 0.175 mmol, 85%). Red crystalline needles suitable for X-ray analysis were grown from a dilute pentane solution overnight at -35 °C. Elemental analysis was attempted twice for compound **1**. Results regularly showed low C and H values, consistent with some degree of THF desolvation from the lithium cation.

^{1}H NMR (C_6D_6, 400 MHz, 25 °C): δ 0.66 (d, $^{3}J_{HH}$ = 3.3 Hz, 18 H, SiH(C*H*$_3$)$_2$), 1.28 (br s, 12 H, THF-C*H*$_2$), 1.89 (s, 27 H, C(C*H*$_3$)$_3$), 3.40 (br s, 12 H, THF-C*H*$_2$), 6.84 (sept, $^{3}J_{HH}$ = 3.3 Hz, $^{1}J_{SiH}$ = 164.5 Hz, 3 H, Si*H*(CH$_3$)$_2$).

^{7}Li NMR (C_6D_6, 155 MHz, 25 °C): δ 0.77 (*Li*(THF)$_3$).

^{13}C{^{1}H} NMR (C_6D_6, 100 MHz, 25 °C): δ 4.86 (SiH(*C*H$_3$)$_2$), 25.54 (THF-*C*H$_2$), 38.07 (C(*C*H$_3$)$_3$), 56.96 (*C*(CH$_3$)$_3$), 68.13 (THF-*C*H$_2$).

^{29}Si{^{1}H} NMR (C_6D_6, 100 MHz, 25 °C): δ -21.86 (*Si*H(CH$_3$)$_2$).

^{29}Si NMR (C_6D_6, 100 MHz, 25 °C): δ -21.89 (d sept, $^{1}J_{SiH}$ = 165.1 Hz, $^{2}J_{SiH}$ = 5.9 Hz, *Si*H(CH$_3$)$_2$). IR (KBr, cm^{-1}): 2959 s, 2901 m, 2091 s br (ν_{SiH}), 1464 w, 1356 w, 1246 m, 1187 m, 1033 m, 902 s br, 836 s, 781 m.

Synthesis of [Li(12-crown-4)$_2$][UO$_2$(N(SiHMe$_2$)^{t}Bu)$_3$] (1-crown). A 20 mL scintillation vial was charged with [Li(THF)$_3$][UO$_2$(N(SiHMe$_2$)^{t}Bu)$_3$] (0.150 g, 0.170 mmol) and THF (10 mL). 12-crown-4 (0.060 g, 0.34 mmol) was added neat, causing no change to the solution color. The resulting red-orange reaction mixture was stirred for one hour before it was concentrated *in vacuo* to an orange residue. This residue was triturated with pentane and concentrated *in vacuo* to ensure complete removal of residual THF. An orange powder assigned as [Li(12-crown-4)$_2$][UO$_2$(N(SiHMe$_2$)^{t}Bu)$_3$] (**1-crown**) was isolated in quantitative yield. Red crystalline blocks suitable for X-ray analysis were grown from a dilute benzene solution overnight at 25 °C.

^{1}H NMR (C_6D_6, 300 MHz, 25 °C): δ 0.80 (d, $^{3}J_{HH}$ = 3.3 Hz, 18 H, SiH(C*H*$_3$)$_2$), 2.07 (s, 27 H, C(C*H*$_3$)$_3$), 3.42 (br s, 32 H, 12-crown-4), 6.45 (sept, $^{3}J_{HH}$ = 3.2 Hz, 3 H, Si*H*(CH$_3$)$_2$).

^{1}H NMR (THF-d$_8$, 500 MHz, 25 °C): δ 0.25 (br s, 18 H, SiH(C*H*$_3$)$_2$), 1.58 (br s, 27 H, C(C*H*$_3$)$_3$), 3.66 (br s, 32 H, 12-crown-4), 5.77 (br m, $^{1}J_{SiH}$ = 175.8 Hz, 3 H, Si*H*(CH$_3$)$_2$).

^{7}Li NMR (C_6D_6, 155 MHz, 25 °C): δ -3.12 (*Li*(12-crown-4)$_2$).

^{13}C{^{1}H} NMR (THF-d$_8$, 125 MHz, 25 °C): δ 4.55 (SiH(*C*H$_3$)$_2$), 37.10 (C(*C*H$_3$)$_3$), 56.52 (*C*(CH$_3$)$_3$), 68.66 (12-crown-4).

^{29}Si{^{1}H} NMR (THF-d$_8$, 100 MHz, 25 °C): δ -28.07 (*Si*H(CH$_3$)$_2$).

^{29}Si NMR (THF-d$_8$, 100 MHz, 25 °C): δ -28.08 (d sept, $^{1}J_{SiH}$ = 176.0 Hz, $^{2}J_{SiH}$ = 6.5 Hz, *Si*H(CH$_3$)$_2$).

IR (KBr, cm^{-1}): 2942 m, 2899 m, 2865 m, 2034 m br (ν_{SiH}), 1445 m, 1364 m, 1347 m, 1303 w, 1288 m, 1243 m, 1229 m, 1188 m, 1134 s, 1095 s, 1024 s, 976 m, 917 s, 893 s, 824 s, 773 s, 751 s, 687 m, 637 m.

Analysis for $C_{34}H_{80}N_3O_{10}Si_3LiU$: Calcd C, 40.03; H, 7.90; N, 4.12. Found C, 39.74; H, 7.69; N, 3.91.

Synthesis of (^{t}Bu$_2$bipy)UO$_2$(N(SiHMe$_2$)^{t}Bu)$_2$ (2). A 20 mL scintillation vial was charged with $[UO_2Cl_2(THF)_2]_2$ (0.300 g, 0.309 mmol) and THF (5 mL), creating a bright yellow suspension. After stirring for 10 minutes, the solid fully dissolved, forming a light yellow solution. A solution of ^{t}Bu$_2$bipy (0.166 g, 0.618 mmol) in THF (2 mL) was added dropwise to the uranyl chloride solution, causing a color change from yellow to orange. After stirring for 10 minutes, this solution was frozen in the coldwell. In a separate 20 mL vial, LiN(SiHMe$_2$)^{t}Bu (0.170 g, 1.236 mmol) was dissolved in THF (2 mL), forming a clear, colorless solution that was also frozen in the coldwell. While thawing, the LiN(SiHMe$_2$)^{t}Bu solution was added dropwise to the thawing uranyl chloride solution. After complete addition, the resulting solution gradually darkened to red-orange over the course of one minute. The reaction mixture was stirred for 30 minutes as it warmed to ambient temperature. This red-orange solution was then concentrated to a dark residue *in vacuo*. This residue was dissolved in Et_2O (10 mL), filtered to remove LiCl, and concentrated to a red powder assigned as (^{t}Bu$_2$bipy)UO$_2$(N(SiHMe$_2$)^{t}Bu)$_2$ (**2**) (0.476 g, 0.596 mmol, 96%). Red crystalline blocks suitable for X-ray analysis were grown from a dilute pentane solution overnight at -35 °C.

^{1}H NMR (C_6D_6, 400 MHz, 25 °C): δ 0.85 (d, $^3J_{HH}$ = 3.4 Hz, 12 H, SiH(CH_3)$_2$), 0.96 (s, 18 H, CC(CH_3)$_3$), 2.26 (s, 18 H, NC(CH_3)$_3$), 6.80 (sept, $^3J_{HH}$ = 3.4 Hz, 3 H, SiH(CH$_3$)$_2$), z (dd, $^3J_{HH}$ = 5.8 Hz, $^4J_{HH}$ = 1.8 Hz, 2 H, bipy-CH), 7.73 (d, $^4J_{HH}$ = 1.7 Hz, 2 H, bipy-CH), 9.83 (d, $^3J_{HH}$ = 5.7 Hz, 2 H, bipy-CH).

^{13}C{^{1}H} NMR (C_6D_6, 100 MHz, 25 °C): δ 5.61 (SiH(CH$_3$)$_2$), 30.06 (bipy-C(CH$_3$)$_3$), 35.03 (bipy-C(CH$_3$)$_3$), 38.18 (NC(CH$_3$)$_3$), 58.38 (NC(CH$_3$)$_3$), 119.49 (bipy-C), 122.14 (bipy-C), 151.90 (bipy-C), 156.80 (bipy-C), 163.69 (bipy-C).

^{29}Si{^{1}H} NMR (C_6D_6, 100 MHz, 25 °C): δ -21.35 (SiH(CH$_3$)$_2$).

^{29}Si NMR (C_6D_6, 100 MHz, 25 °C): δ -21.36 (d sept, $^1J_{SiH}$ = 182.0 Hz, $^2J_{SiH}$ = 6.7 Hz, SiH(CH$_3$)$_2$).

IR (KBr, cm^{-1}): 2964 s, 2902 m, 2081 s br (ν_{SiH}), 1611 s, 1545 m, 1478 m, 1463 m, 1403 m, 1377 w, 1366 m , 1354 w, 1246 m, 1187 m, 1016 w, 993 w, 954 m, 899 s, 846 m, 773 m, 714 w, 692 m, 607 m.

Analysis for $C_{30}H_{56}N_4O_2Si_2U$: Calcd C, 45.10; H, 7.06; N, 7.01. Found C, 44.67; H, 6.75; N, 6.81.

5.3 Results and Discussion

5.3.1 Synthesis of New Uranyl Silylamide Complexes

As an entry into this work, the parent amine, $HN(SiHMe_2)^tBu$, was generated using a modified literature procedure, in which Me_2SiHCl is slowly added to a cold solution of excess $NH_2{}^tBu$ (Scheme 5.1).[148] Following workup, analysis by ^1H NMR spectroscopy (C_6D_6, 25 °C) shows a diagnostic resonance at 4.83 ppm as a doublet of septets with an Si-H coupling of 192 Hz (Figure 5.1).

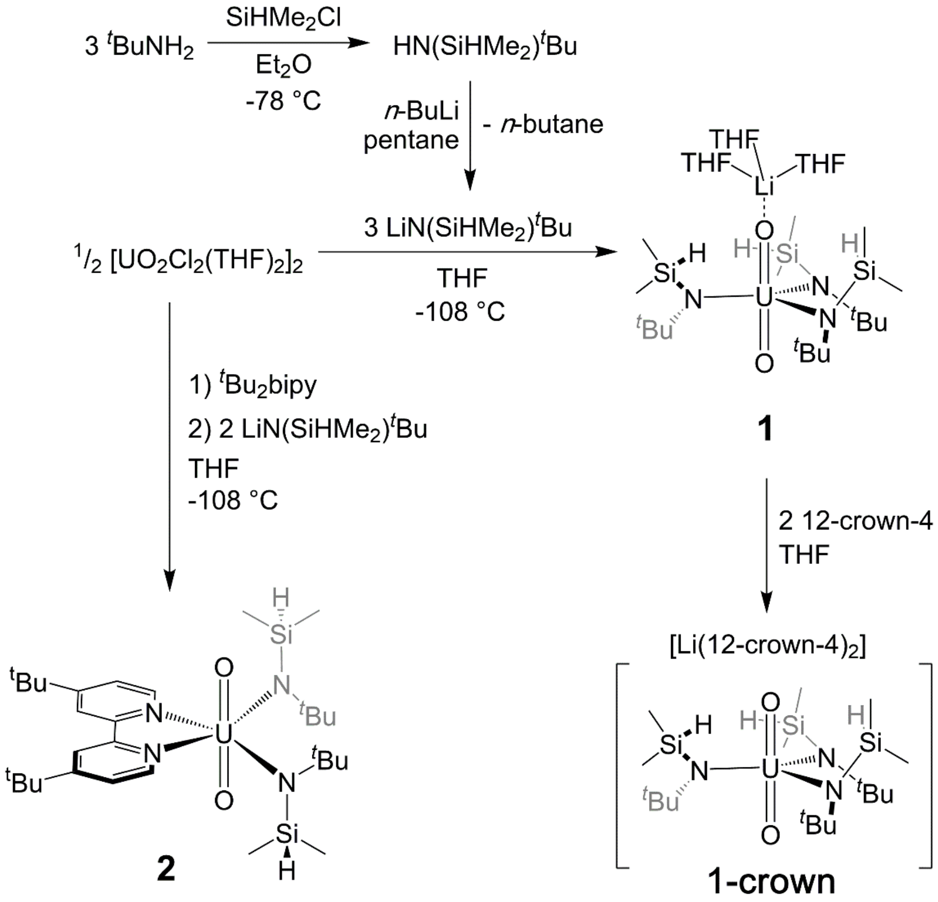

Scheme 5.1. Synthesis of uranyl silylamide complexes **1**, **1-crown**, and **2**.

In order to generate uranyl derivatives using salt metathesis, the lithium amide derivative, $LiN(SiHMe_2)^t Bu$, was synthesized according to a modified literature procedure, furnishing the desired product in high yield.[148] Subjecting half an equivalent of $[UO_2Cl_2(THF)_2]_2$ to two equivalents of $LiN(SiHMe_2)^t Bu$, in anticipation of generating "$UO_2(N(SiHMe_2)^t Bu)_2$", instead produced $[Li(THF)_3][UO_2(N(SiHMe_2)^t Bu)_3]$ (**1**), as determined by X-ray crystallography (*vide infra*), in poor yield. However, when the appropriate equivalents of $LiN(SiHMe_2)^t Bu$ were used, based on the stoichiometric ratio, $[Li(THF)_3][UO_2(N(SiHMe_2)^t Bu)_3]$ (**1**) was obtained in high yield as an orange-red powder (Scheme 5.1).

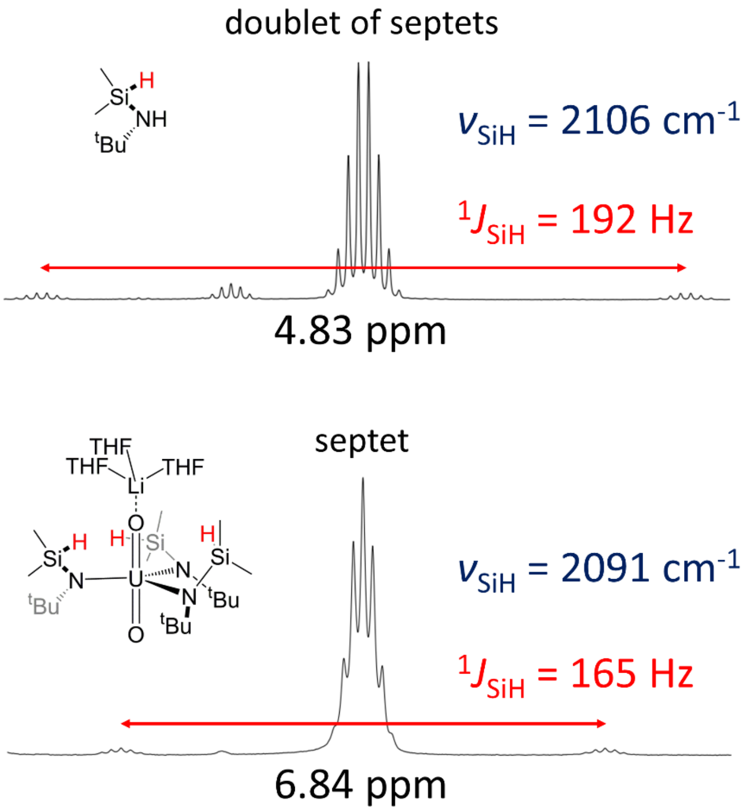

Figure 5.1. Comparison of ^1H NMR spectroscopic data (C_6D_6, 25 °C) for the Si-*H* resonance and IR data for the Si-H stretch in $H(NSiHMe_2)^t Bu$ and **1** highlighting the utility of the Si-H group as a characterization handle.

Single crystals of **1**, formed as red needles, were obtained from a dilute pentane solution cooled to -35 °C. From refinement of the data, the resulting molecular structure shows a C_{3v} symmetric molecule with a trigonal bipyramidal uranium center featuring the characteristic *trans*-oxo ligands in the axial positions (Figure 5.2, structural parameters in Table 5.1). The structure was modelled with exact 1:1 disorder about a crystallographic mirror plane. The three amide ligands are situated in the equatorial plane with 115.6(4)-123.8(4)° angles with respect to each other. The U-N distances of 2.304(6), 2.274(10), 2.348(11) Å and the U-O distance of 1.785(4) Å are all on the order of those observed for $UO_2(N(SiMe_3)_2)_2(THF)_2$[149] and $UO_2(N(SiMe_2Ph)_2)_2$.[131] The other U-O bond shows elongation to 1.853(5) Å, which is likely due to capping by the lithium countercation. A more appropriate comparison is to the uranyl tris(amide), $[Na(THF)_2][UO_2(N(SiMe_3)_2)_3]$.[149] In this case, the U-N distances range from 2.305(4) to 2.318(4) Å, while the U-O distances are 1.781(5) and 1.810(5) Å. Again, elongation of the latter U-O distance is due to the association with the sodium cation to a uranyl oxygen, similar to compound **1**.

Further characterization of **1** by ^1H NMR spectroscopy (C_6D_6, 25 °C) showed a C_{3v} symmetric spectrum in solution, with the largest resonances at 0.66 ($SiH(CH_3)_2$) and 1.89 ppm ($C(CH_3)_3$). The other notable resonance is that for the Si-*H*, appearing as a septet at 6.84 ppm with $^1J_{SiH}$ = 165 Hz, which is substantially shifted downfield compared to the value of the parent amine (4.83 ppm, 192 Hz) (Figure 5.1). The ^{29}Si NMR (C_6D_6, 25 °C) spectrum shows a doublet of septets at -21.89 ppm ($^1J_{SiH}$ = 165.1 Hz) for the silyl group, whereas the ^7Li NMR (C_6D_6, 25 °C) shows a singlet at δ 0.77 (*Li*(THF)$_3$). The strong Si-H coupling constant indicates that, despite the proximity of the Si-H bonds to the uranium center, no secondary Si-H interactions are noted in this case. This is surprising, given the observation of Si-H secondary interactions on lanthanide derivatives of this ligand,[142,143] as well as of C-H agostic bonds of $-N(SiMe_3)_2$ on low-valent uranium,[150] both of which give insight into unique *f*-orbital participation in bonding.[151]

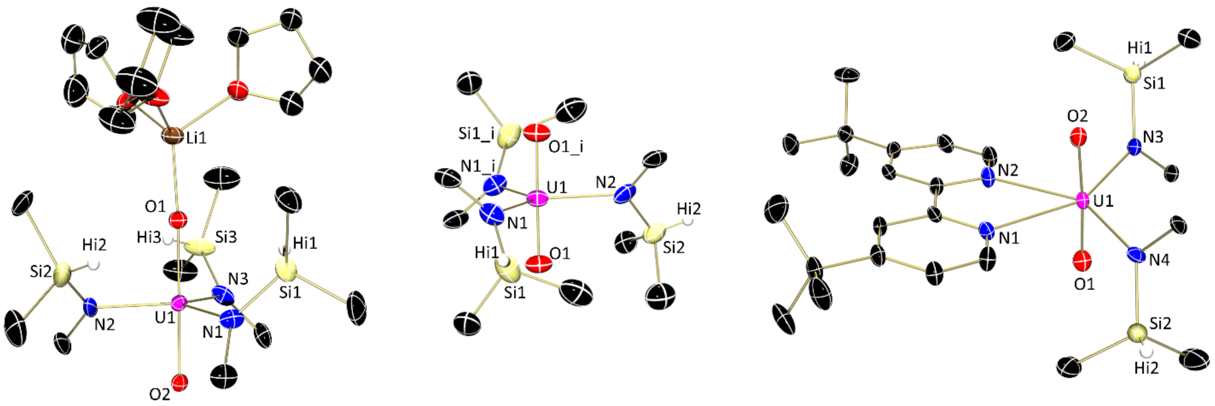

Figure 5.2. Molecular structures of [Li(THF)$_3$][UO$_2$(N(SiHMe$_2$)^{t}Bu)$_3$] (**1**), [Li(12-crown-4)$_2$][UO$_2$(N(SiHMe$_2$)^{t}Bu)$_3$] (**1-crown**), and (^{t}Bu$_2$bipy)-UO$_2$(N(SiHMe$_2$)^{t}Bu)$_2$ (**2**) shown at 30% probability ellipsoids. Disorder, co-crystallized solvent molecules, selected hydrogen atoms, selected ^{t}Bu methyl groups on the amide ligands, and the Li(12-crown-4)$_2$ countercation in **1-crown** have been omitted for clarity.

To remove the lithium countercation from the coordination sphere, **1** was treated with 12-crown-4, which produced [Li(12-crown-4)$_2$][UO$_2$(N(SiHMe$_2$)^{t}Bu)$_3$] (**1-crown**) as an orange solid in quantitative yield. Red block crystals that deposited from a concentrated benzene solution at room temperature were analyzed by X-ray diffraction, showing a disordered amide ligand around a two-fold rotation axis. The molecular structure was very similar to that of **1**, but showed that the lithium was indeed encapsulated and removed from the primary coordination sphere (Figure 5.2, Table 5.1). Again, the uranium appears to be in a trigonal bipyramidal geometry, with two of the amides and both oxygen atoms related by a mirror plane. The U-N bond distances (2.315(7) and 2.352(11) Å) in the equatorial plane are within error of those in parent compound **1**. Significantly, the U-O distances of 1.787(6) Å are now equivalent. The structural parameters for **1-crown** are similar to those noted for [Cp*$_2$Co][UO$_2$(N(SiMe$_3$)$_2$)$_3$], which features an outer sphere pentamethylcobaltocenium cation.[152] In this case, the U-N distances average 2.32 Å, while the U-O distances of 1.811(5) and 1.788(5) Å are signature for uranyls. The inequivalence in these distances is surprising, given that the cobaltocenium is not associated with a uranyl oxygen. In solution, the behavior of **1-crown** is very similar to **1** as well, with little shift (~0.2 ppm or less) in the resonances of the ^{1}H NMR spectrum (C$_6$D$_6$, 25 °C). Again there is no indication of the presence of any secondary Si-H interactions to the uranium ion.

Table 5.1. Bond distances (in Å) for compounds **1**, **1-crown**, **2**, and **3**.

	1	**1-crown**	**2**	**3**
U-O_{uranyl}	1.785(4)	1.787(6)	1.748(5)	1.786(4)
U-O_{uranyl}	1.853(5)	1.787(6)	1.803(5)	1.841(4)
U-N_{amide}	2.304(6)	2.315(7)	2.297(5)	2.292(4)
U-N_{amide}	2.274(10)	2.315(7)	2.332(6)	2.298(4)
U-N_{amide}	2.348(11)	2.352(11)	--	2.308(4)
U-N_{bipy}	--	--	2.636(4)	--
U-N_{bipy}	--	--	2.559(5)	--

Formation of the uranyl tris(amide) derivative **1** likely results from addition of one equivalents of $LiN(SiHMe_2)^tBu$ to transient “$[UO_2(N(SiHMe_2)^tBu)_2]$”. It was hypothesized that this intermediate could be stabilized by the use of a bulky Lewis base, furnishing the neutral uranyl bis(amide) species, rather than an additional equivalent of the lithium amide salt, which produced the ‘ate’ complex. Pre-treating half an equiv. of $[UO_2Cl_2(THF)_2]_2$ with one equiv. 4,4’-di-*tert*-butyl-2,2’- bipyridine followed by addition of $LiN(SiHMe_2)^tBu$ at low temperature resulted in a red-orange solution that was dried to a red powder after workup.

X-ray quality crystals of this product were obtained by cooling a concentrated pentane solution to -35 °C. The structure was modelled with disorder around a crystallographic mirror plane. Analysis confirmed the identity of the product as $(^tBu_2bipy)UO_2(N(SiHMe_2)^tBu)_2$ (**2**), featuring a pseudo-octahedral uranium center with trans-oxo ligands and cis-amides (Figure 5.2, Table 5.1). Notable features of this molecule include the O-U-O angle, which is slightly bent at 175.8(2)°, likely due to the steric pressure imparted by the *cis*-amides. Interestingly, the U-O distances are significantly different from each other at 1.748(5) and 1.803(5) Å, despite the lack of any countercations.

As expected, the U-N distances of 2.297(5) and 2.332(6) Å are within error of those in **1** and **1-crown**, and the dative U-N bond lengths for the bipyridine are much longer at 2.636(4) and 2.559(5) Å. Compound **2** is reminiscent of $UO_2(Ar_2nacnac)(bipy)$ ($Ar_2nacnac = ((2,6-{}^iPr_2C_6H_3)NC(Me))_2CH$), reported by Hayton and co-workers, which features both a 2,2’-bipyridine and a nacnac ligand in the equatorial plane.[153] In this case, the U-N_{bipy} distances of (2.643(6) and 2.636(6) Å) point towards dative bonds, confirming the coordination mode in **2**. By comparison, the U-O bonds of 1.833(5) and 1.821(5) Å in $UO_2(Ar_2nacnac)(bipy)$ are both longer and more similar to each other than those in compound **2**.

Analysis of compound **2** by ^{1}H NMR spectroscopy (C_6D_6, 25 °C) shows very similar parameters to the tris(amide) derivatives, with not more than a difference in chemical shift of ~0.3 ppm for the amide ligand resonances. Additional resonances for the 4,4'-di-*tert*-butyl-2,2'-bipyridine ligand are found at 0.96 ppm for the symmetric *tert*-butyl groups and in the range of 7.14-9.83 ppm for the aromatic protons.

As demonstrated here, use of the bulky 2,2'-bipyridine ligand blocks two coordination sites in the equatorial plane of the uranyl ion, preventing ligand rearrangement and formation of the 'ate' complex. The result is isolation of a neutral, six-coordinate uranyl bis(amide) complex similar to $UO_2(N(SiMe_3)_2)_2(THF)_2$ and $UO_2(N(SiMe_2Ph)_2)_2$. Unavoidable formation of uranyl 'ate' complexes with the $-N(SiMe_3)_2$ ligand is highly dependent on the alkali metal used in the synthesis.[149] For compound **2**, addition of a chelating Lewis base allows for a smaller, harder ion (Li) to be used, while avoiding the apparent driving force for 'ate' complex formation, evident in the preferable formation for **1** (*vide supra*).

The infrared spectra for compounds **1**, **1-crown**, and **2** each display a single band for the Si-H stretch in a narrow range. Compound **1** has the highest energy stretch (ν_{SiH}) at 2091 cm^{-1}, while compound **1-crown** has the lowest energy stretch at 2034 cm^{-1}. The absorption for **2** is between the others with a band at 2081 cm^{-1}. The Si-H stretching modes in the $-N(SiHMe_2)^tBu$ ligands have been shown to trend to much lower energies (<2000 cm^{-1}) upon formation of an interaction with a metal.[142] The ν_{SiH} energies for the uranyl complexes are shifted only slightly from $HN(SiHMe_2)^tBu$ (2106 cm^{-1}) or $LiN(SiHMe_2)^tBu$ (2043 cm^{-1}), supporting the conclusions from Si-H NMR coupling constants that there are no secondary interactions with uranium in these complexes.

Electronic absorption spectroscopy was used to evaluate the $-N(SiHMe_2)^tBu$ series in the ultraviolet (UV), visible, and near-infrared (NIR) regions (Figure 5.3). No absorbances are observed in the NIR region for **1**, **1-crown**, or **2**, consistent an f^0 state of the assigned U(VI) centers. Broad absorbance at the edge of the UV region are observed for **1** (λ_{max} = 360 nm, 4640 M^{-1}cm^{-1}), **1-crown** (λ_{max} = 362 nm, 3721 M^{-1}cm^{-1}), and **2** (λ_{max} = 339 nm, 2576 M^{-1}cm^{-1}). These absorbances extend into the visible region and are consistent with the orange or red colors observed for each complex. Additional absorbances are observed in the UV region for **2** (λ_{max} = 283 nm, 17030 M^{-1}cm^{-1}; λ_{max} = 240 nm, 16319 M^{-1}cm^{-1}), which are likely due to electronic transitions associated with the $^tBu_2$bipy ligand.

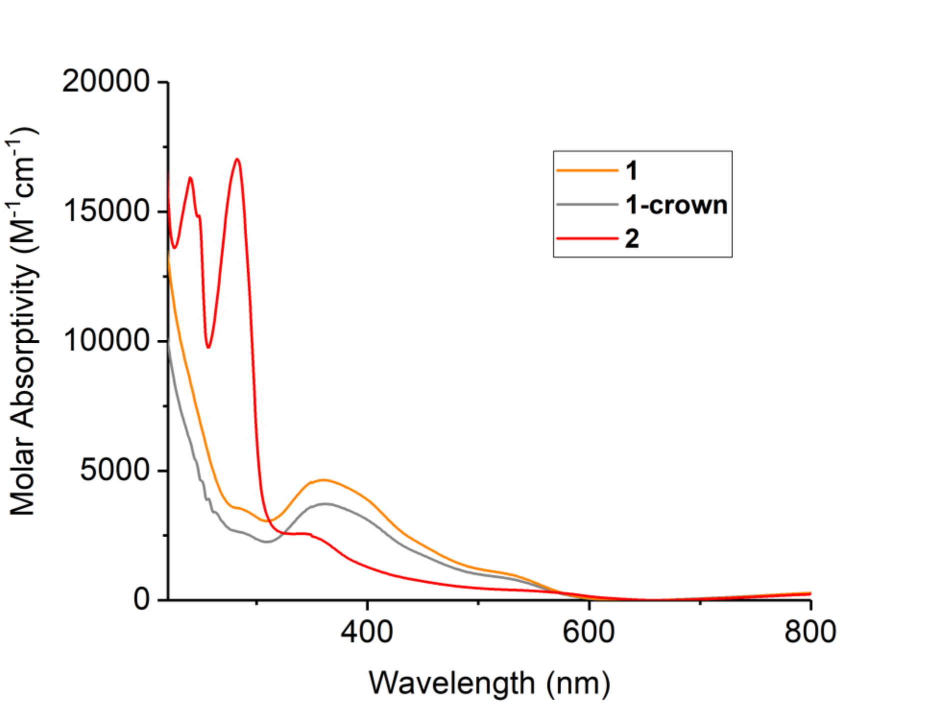

Figure 5.3. UV-vis plot (as THF solutions at ambient temperature) for compounds **1**, **1-crown**, and **2**.

To put the electronic properties of the -N(SiHMe$_2$)^{t}Bu ligand into perspective with known uranyl ligands, a direct comparison of the basicity of [-N(SiHMe$_2$)^{t}Bu]$^{1-}$ and [-N(SiMe$_3$)$_2$]$^{1-}$ was probed (Scheme 5.2). Dissolution of equimolar amounts of LiN(SiHMe$_2$)^{t}Bu and HN(SiMe$_3$)$_2$ in C$_6$D$_6$ resulted in complete conversion to HN(SiHMe$_2$)^{t}Bu and LiN(SiMe$_3$)$_2$ as determined by multinuclear NMR spectroscopy. Analysis of this reaction by ^{1}H NMR spectroscopy validates the utility of the Si-H moiety as a characterization handle. Although it is not possible to definitively distinguish HN(SiMe$_3$)$_2$ (0.10 ppm) from LiN(SiMe$_3$)$_2$ (broad 0.13 ppm), the presence of HN(SiHMe$_2$)^{t}Bu is clearly evident based on the observation of a doublet of septets at 4.79 ppm with a $^1J_{SiH}$ coupling constant of 192 Hz. Resonances for LiN(SiHMe$_2$)^{t}Bu are not observed, which would appear as a broad resonance at 4.86 ppm with a $^1J_{SiH}$ coupling constant of 169 Hz. ^{7}Li NMR spectroscopy confirms the presence of LiN(SiMe$_3$)$_2$ with only one resonance at 1.04 ppm, whereas LiN(SiHMe$_2$)^{t}Bu would be observed at 2.14 ppm. The same product distribution is obtained when equimolar amounts of HN(SiHMe$_2$)^{t}Bu and LiN(SiMe$_3$)$_2$ are mixed.

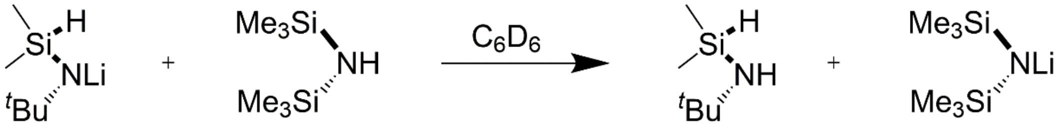

Scheme 5.2. Direct basicity comparison of -N($SiHMe_2$)^{t}Bu and -N($SiMe_3$)$_2$.

To analyze the steric profile of the -N($SiHMe_2$)^{t}Bu ligand, computational analysis via Solid-G was conducted.[154,155] This model quantifies the steric environment imparted by ligands based on the percentage of the metal sphere that is blocked by each ligand. Compound **1** was chosen for analysis based on the structural similarity to both [Li(py)$_2$][UO_2(N($SiMe_3$)$_2$)$_3$] (py = pyridine) and [Li(THF)$_2$][UO_2(N($SiMe_3$)$_2$)$_3$] (**3**).[128] Table 2 shows the results for each of these three complexes. While the uranium-amide bond distances do not change significantly between the three complexes, a clear trend emerges in the G(amide) values. Compound **1** has consistently smaller G(amide) values that range from 21.30% to 22.51%, while the -N($SiMe_3$)$_2$)$_3$ compounds range between 24.85% to 25.55%. This difference indicates that -N($SiHMe_2$)^{t}Bu occupies about 3% less of the uranium coordination sphere compared to -N($SiMe_3$)$_2$.

Table 5.2. Solid-G[154,155] analysis comparing solid angle parameters for compounds **1**, **3**, and [Li(py)$_2$][UO_2(N($SiMe_3$)$_2$)$_3$].[128]

	[Li(THF)$_3$] [UO_2(N($SiHMe_2$)^{t}Bu)$_3$] (**1**)	[Li(THF)$_2$] [UO_2(N($SiMe_3$)$_2$)$_3$] (**3**)	[Li(py)$_2$] [UO2(N($SiMe_3$)$_2$)$_3$]
U-N distances (Å)	2.304(6)	2.292(4)	2.295(11)
	2.274(10)	2.298(4)	2.279(12)
	2.348(11)	2.308(4)	2.280(13)
G(amide), %	21.30	25.15	24.95
	21.86	25.03	25.55
	22.51	24.85	25.17
G(complex), %	92.33	94.18	94.05

5.3.2 Reactivity of Uranyl Silylamide Complexes

5.3.2.1 Substitutional Lability Experiments

With the understanding that -N(SiHMe$_2$)^{t}Bu has increased basicity over -N(SiMe$_3$)$_2$, experiments were developed to demonstrate the subsequent increase in reactivity with the new uranyl complexes. Addition of three equivalents of HN(SiMe$_3$)$_2$ to compound **1** in THF slowly results in conversion to [Li(THF)$_2$][UO$_2$(N(SiMe$_3$)$_2$)$_3$] (**3**) over the course of 48 hours (Scheme 5.3). Compound **3** was characterized by ^{1}H NMR spectroscopy, which showed a singlet at 0.65 ppm, along with resonances for lithium-bound THF observed at 1.18 and 3.24 ppm.

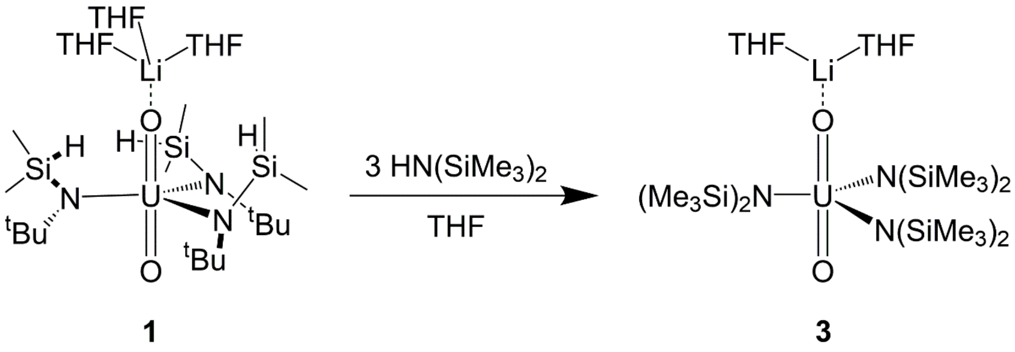

Scheme 5.3. Synthesis of compound **3**.

Orange needle crystals of **3** suitable for X-ray crystallography were grown directly from a benzene solution at room temperature in a sealed tube. Analysis of one of these crystals revealed the expected trigonal bipyramidal uranium center with the expected axial oxo ligands and three equatorial amide ligands (Figure 5.4). Similar to compound **1**, one oxo ligand is capped by a lithium cation. Again, this is evident in the uranyl bond distances as the uncapped oxo ligand has a U-O distance of 1.786(4) Å, and the lithium capped oxo ligand has a longer distance of 1.841(4) Å. The U-N distances for the -N(SiMe$_3$)$_2$ ligands range from 2.292(4) to 2.308(4) Å, similar to the U-N distances observed in **1**. Interestingly, the lithium cation in **3** has only two solvate THF molecules coordinated, similar to the known pyridine solvate [Li(py)$_2$][UO$_2$(N(SiMe$_3$)$_2$)$_3$].[128] This is in contrast to the three lithium-coordinated THF molecules in **1**, a difference that could potentially be an artefact of the differing steric environments of -N($SiMe_3$)$_2$ and -N($SiHMe_2$)^{t}Bu.

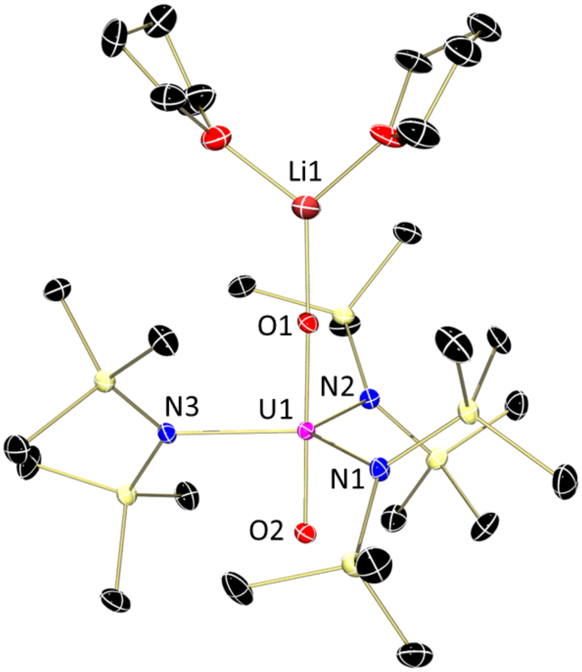

Figure 5.4. Molecular structure of [Li(THF)$_2$][UO_2(N($SiMe_3$)$_2$)$_3$] (**3**) shown at 30% probability ellipsoids. Disorder, hydrogen atoms, and ^{t}Bu methyl groups have been omitted for clarity.

5.3.2.2 Silyl-H Abstraction

One interesting feature of the -N($SiHMe_2$)^{t}Bu ligands is the potential to internally silylate the uranyl, activated by Si-H abstraction from the ligand. The formation of highly reactive silanimines has already been explored through Si-H abstraction of this ligand bound to zirconium.[132] It was rationalized that abstraction of the Si-H would create a highly reactive, oxophilic silicone atom that is unsaturated and could internally silylate onto the uranyl oxygen.

To test this idea, one equivalent of BCF (BCF = tris(pentafluorophenyl)borane) was added to a C_6D_6 solution of compound **1**. This resulted in instant darkening of the solution. Immediate analysis by ^{1}H NMR spectroscopy reveals a new diamagnetic product (labeled with green asterisks in Figure 5.5) along with a small amount of compound **1**. As confirmed by ^{19}F

NMR spectroscopy, the BCF is completely converted to Li[HBCF], signifying that the Si-H abstraction was successful.

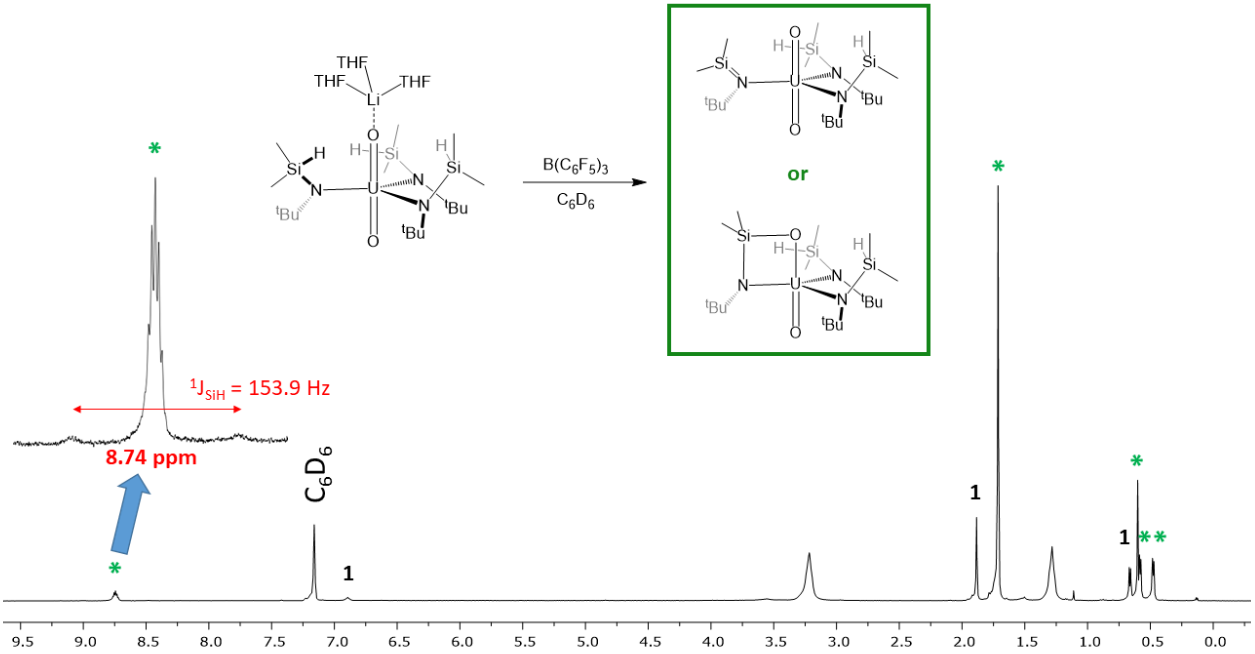

Figure 5.5. ^{1}H NMR spectrum (C_6D_6, 25 °C) showing reaction of compound **1** with BCF. Green asterisks represent new paramagnetic product.

Analysis of the new diamagnetic product in the ^{1}H NMR spectrum (C_6D_6, 25 °C) reveals a pattern that is consistent with either of the two proposed compounds in Figure 5.5. Looking at the silyl-methyl resonances of this new product, three inequivalent resonances are observed in a 1:1:1 ratio (0.47 ppm (d), 0.58 ppm (d), and 0.60 ppm (s)). The resonance at 0.60 ppm appears as a singlet, having lost the coupling to the abstracted Si-H, and is assignable to the new -$NSiMe_2{}^t$Bu ligand. The other two resonances are doublets, having retained their Si-H functionality. In addition, the new S-*H* resonance appears downfield at 8.74 ppm (sept). The lack of coupling to any N-H confirms that these ligands are still deprotonated. Additionally, the $^1J_{SiH}$ is much smaller than that of compound **1**, having a value of 153.9 Hz. This value is the smallest observed for any of the uranyl complexes and is near that of lanthanide examples that exhibit agostic interactions.[132] Overall, the two proposed products cannot be elucidated with ^{1}H NMR spectroscopy, but the ligand splitting pattern is consistent with either one.

Unfortunately, this product isn't stable in solution, and decomposes completely in less than one hour (Figure 5.6). Interestingly, the decomposition product consistently obtained from these reaction is paramagnetic, supporting the possibility of sialylation at the uranyl occurring.

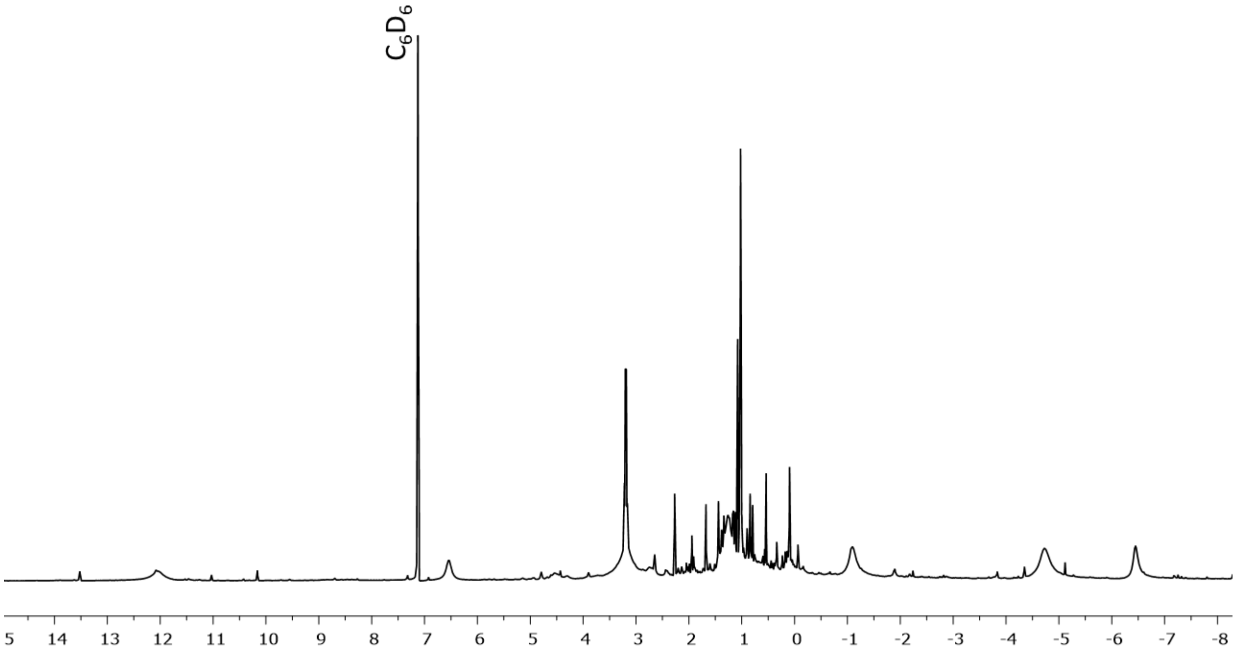

Figure 5.6. ^{1}H NMR spectrum (C_6D_6, 25 °C) showing reaction of compound **1** with BCF after one hour.

Attempts to characterize Si-H abstracted products from compound **2**, or additional Si-H abstractions of compound **1** were unsuccessful. These two instances are common in their formation of $[HBCF]^-$ counterions, which aren't lost as Li[HBCF]. These products weren't soluble in C_6D_6, instead forming a thick clathrate at the bottom of the NMR tube, precluding further characterization. This type of clathrate has been observed with many other salts containing $[HBCF]^-$ counterions.[156,157]

5.3.2.3 Reactivity with Substituted Amines

5.3.2.3.1 NMR Tube Reactions

To test the substitutional lability and basicity of these new uranyl amide complexes, reactions with substituted primary amines were explored. Initial experiments focused on NMR tube reactions in order to fully elucidate the protonation of the -$N(SiHMe_2)^tBu$ ligand, which could easily be monitored by ^1H NMR spectroscopy. To a solution of **1** in C_6D_6, one equivalent of 2,6-diisopropylphenylaniline (H_2NDIPP) was added, causing an instant color change to light brown (Figure 5.7). In order to quantify the resultant products, a known amount of toluene was also added. Analysis of this sample by ^1H NMR spectroscopy reveals complete consumption of both compound **1** and H_2NDIPP. Interestingly, no new peaks assignable to uranyl products or the diisopropylphenyl moiety were observed. In fact, the only new resonances in the spectrum were those for $HN(SiHMe_2)^tBu$, which could be quantified based on the toluene internal standard. Integration of these peaks revealed that 65% of the total -$N(SiHMe_2)^tBu$ was present as $HN(SiHMe_2)^tBu$, indicating that two of the three amide ligands of **1** were protonated. By balancing the reaction, the expected uranyl byproduct would be "$[Li(THF)_3][UO_2(N(SiHMe_2)^tBu)(NDIPP)]$", which again isn't observed in the spectrum, but would be a highly desirable uranyl compound. This reaction is highly reproducible, but inability to elucidate uranium products by this method warranted prep scale reactivity (See Section 5.3.2.3.2).

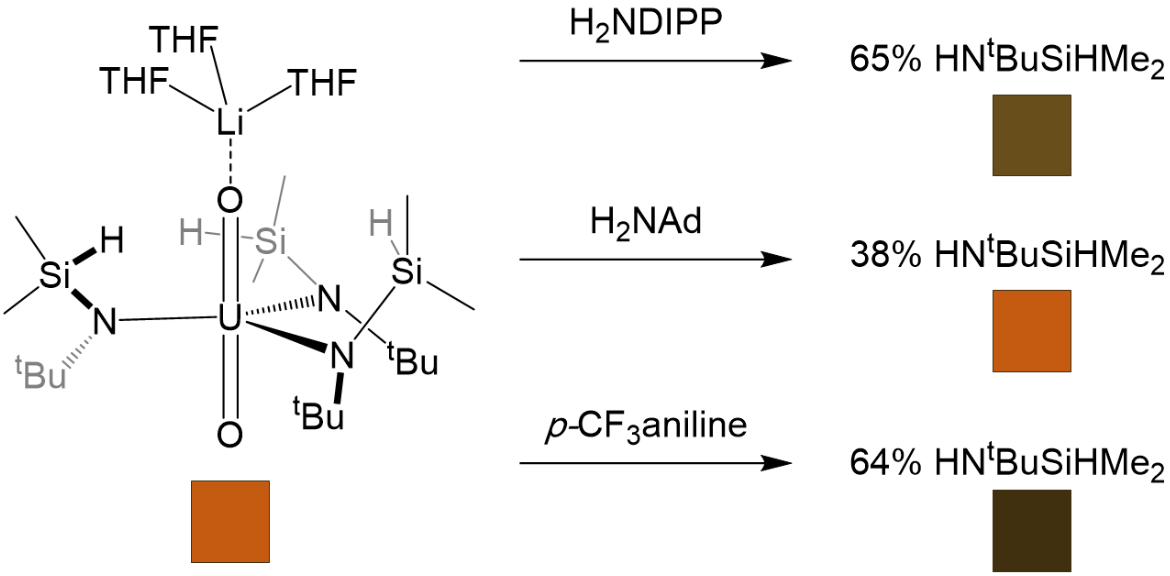

Figure 5.7. Amine quantification from NMR tube reactions (C_6D_6) of **1** with various anilines. Percentage is based off of total -NSi(HMe_2)^{t}Bu present (100% = 3 equivalents based off of **1**).

Repeating this reaction with various types of substituted amines revealed some interesting insights into this reaction. Addition of adamantylamine (H_2NAd), resulted in a similar outcome, where both **1** and H_2NAd were consumed and only HN(SiHMe_2)^{t}Bu was observed (Figure 5.7). However, quantification of the HN(SiHMe_2)^{t}Bu revealed that only 38% of the total -N(SiHMe_2)^{t}Bu was protonated to HN(SiHMe_2)^{t}Bu. This would indicate that only one equivalent of -N(SiHMe_2)^{t}Bu was protonated from the compound **1** and would be consistent with the formation of “[Li(THF)3)][UO2(N(SiHMe_2)^{t}Bu)(NHAd)]”. This result can be rationalized by analyzing the acidity of H_2NDIPP vs H_2NAd. The -Ad moiety is more electron donating than -DIPP, meaning that H_2NAd should be less acidic than H_2NDIPP (both in the first and second deprotonation). This would explain why only one deprotonation occurs in the reaction of **1** with H_2NAd, ideally forming a primary amide, which are extremely rare in uranyl chemistry.[158]

The reaction with *p*-CF_3anilnie was also explored. This aniline was chosen based on its unique electronic properties. The *p*-CF_3phenyl group is even more electron withdrawing than the -DIPP moiety, and the resultant uranyl product may have differing electronic properties.

Addition of one equivalent of *p*-CF_3aniline to a C_6D_6 solution of compound **1** resulted in immediate darkening of the solution to dark brown (Figure 5.7).

Analysis of this sample by ^{1}H NMR spectroscopy reveals complete consumption of both compound **1** and *p*-CF_3aniline. Again, no new peaks assignable to uranyl products or the *p*-CF_3phenyl moiety were observed. In fact, the only new resonances in the spectrum were those for $HN(SiHMe_2)^tBu$, which could be quantified based on the toluene internal standard. Integration of these peaks revealed that 64% of the total $-N(SiHMe_2)^tBu$ was present as $HN(SiHMe_2)^tBu$, indicating that two of the three amide ligands of **1** were protonated. By balancing the reaction, the expected uranyl byproduct would be "$[Li(THF)_3][UO_2(N(SiHMe_2)^tBu)(N(p\text{-}CF_3phenyl)]$", which again isn't observed in the spectrum.

These reaction shows that two equivalents of $HN(SiHMe_2)^tBu$ are liberated from reactions with amines, as long as the amines have a high enough acidity. Although no uranyl products were identified in these studies, they serve as an important starting point to understand these deprotonations, and give insights into the immediate reaction products before any workups were attempted.

Interestingly, in a similar fashion to the other NMR tube reactions, addition of one equivalent of H_2NDIPP to a C_6D_6 solution of **1-crown** produces no immediate color change. Analysis of the reaction mixture by ^{1}H NMR spectroscopy shows no visible signs of a reaction. After two hours, a small amount of $HN(SiHMe_2)^tBu$ is observed, showing that this reaction is much slower than the analogous reaction with **1**. This reaction wasn't analyzed beyond this point due to the likelihood of **1-crown** to decompose over the week long reaction time, which would give erroneous results. This result is surprising, as it was envisioned the sequestration of the lithium cation would create a more reactive uranyl complex.

Reactivity of **2** with H_2NDIPP was also explored (Scheme 5.4). Addition of one equivalent of H_2NDIPP to a C_6D_6 solution of **2** produces no immediate color change. Analysis of the reaction mixture by ^{1}H NMR spectroscopy shows mostly starting material, with a small amount of $HN(SiHMe_2)^tBu$ and another product (Figure 5.8). This product was likely a uranyl product since it contains resonances for $^tBu_2$bipy, $-N(SiHMe_2)^tBu$, and -DIPP groups. New resonances for the $^tBu_2$bipy group are observed at 0.97 (singlet), 7.65 (doublet), 7.72 (singlet) and 9.50 (doublet) ppm, while new resonances for the $-N(SiHMe_2)^tBu$ ligand appear at 0.91

(doublet) and 2.31 (singlet) ppm. The Si-*H* resonance wasn't identified and is likely hidden under the Ar-*H* resonances for toluene. New peaks for the -DIPP group were observed at 1.52 (doublet) and 4.62 (septet) ppm. Again, the Ar-H resonances weren't identified and are likely obscured by the toluene resonance. Interestingly, a singlet is observed at 10.82 ppm, which is likely the N-*H* resonance from a -NHDIPP amide ligand. The extreme downfield shift is likely caused by the proximity to the uranium center. Analysis of this ^{1}H NMR data leads to the assignment of this product as (^{t}Bu$_2$bipy)UO$_2$(N(SiHMe$_2$)^{t}Bu)(NHDIPP) (Scheme 5.4). It appears that the bulk of this complex has allowed the observation of this rare intermediate. Currently, only one primary, aryl amide uranyl complex has boon reported, and its synthesis isn't reproducible. No NMR spectroscopic data was obtained for this complex either.

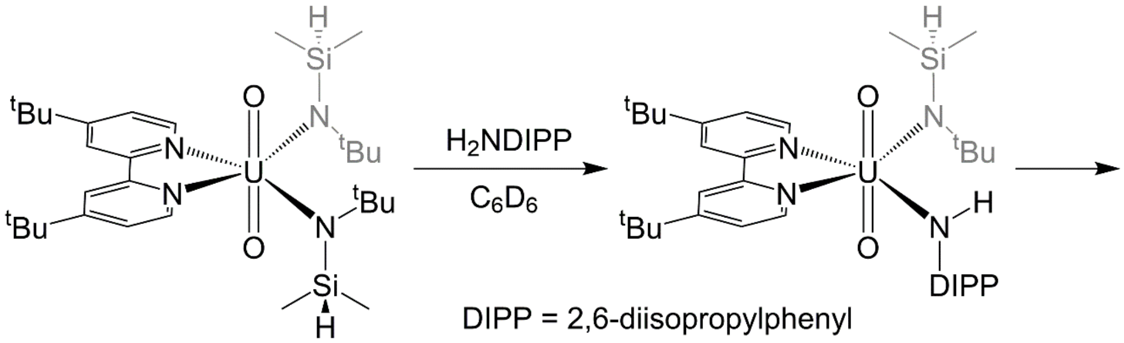

Scheme 5.4. Reaction of compound **2** with H$_2$NDIPP, showing the proposed intermediate, (^{t}Bu$_2$bipy)UO$_2$(N(SiHMe$_2$)^{t}Bu)(NHDIPP).

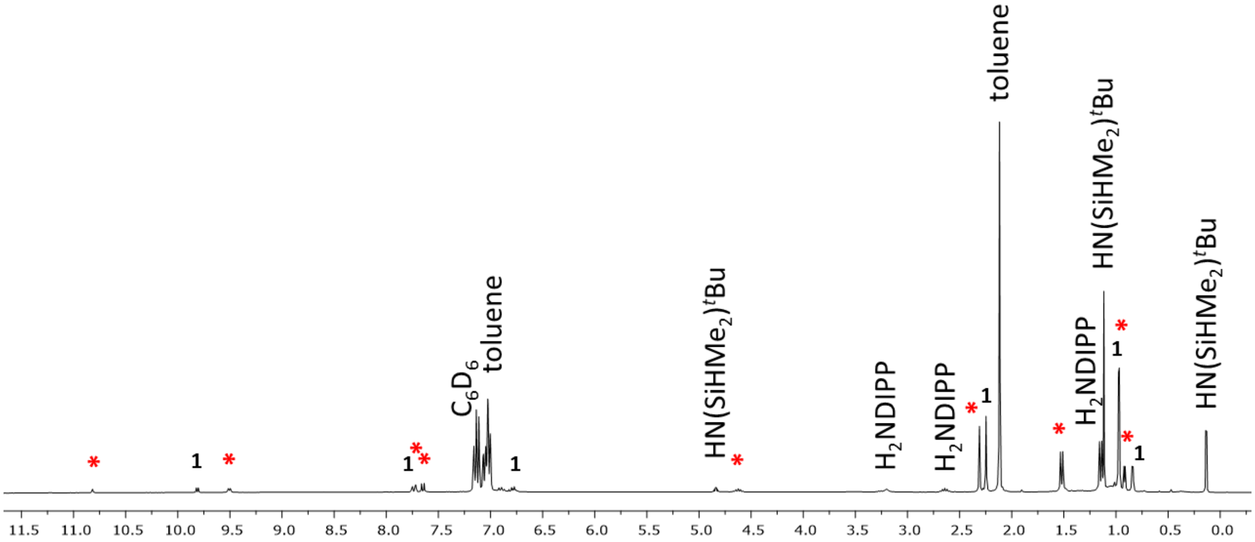

Figure 5.8. ^{1}H NMR spectrum (C_6D_6) showing the reaction of **2** with H_2NDIPP after 10 minutes. Red asterisks represents a new uranyl product.

Unfortunately, as the reaction of **2** plus H_2NDIPP proceeds, this new uranyl product begins to diminish as more HN($SiHMe_2$)^{t}Bu is formed. After two hours, all of the starting materials are consumed, and this new product is absent as well. It appears that the formation of the proposed (^{t}Bu$_2$bipy)UO_2(N($SiHMe_2$)^{t}Bu)(NHDIPP) is an intermediate towards the final product. Quantification of the resultant HN($SiHMe_2$)^{t}Bu that is formed suggest that 1.3 equivalents are liberated from **2**. This is inconsistent with the original theory that **2** reacts with H_2NDIPP to form (^{t}Bu$_2$bipy)UO_2(N($SiHMe_2$)^{t}Bu)(NHDIPP), which then continues to full deprotonation to the uranyl imido. It is currently unclear what the final products are from these reactions; however, it does appear the using a system like **2**, that has steric protection allows for the observation of intermediates in this process.

A similar observation is made when using bulky anilines with compound **1**. Addition of one equivalent of 2,6-dimesitylaniline (mesityl = 2,4,6-trimethylphenyl) to a C_6D_6 solution of **1** produces no immediate color change. Analysis of the reaction mixture by ^{1}H NMR spectroscopy shows mostly starting material, with a small amount of HN($SiHMe_2$)^{t}Bu and another uranyl product similar to the intermediate (Scheme 5.5) observed from the reaction of **2** with H_2NDIPP. New resonances for the -N(SiHMe$_2$)^{t}Bu ligand appear at 0.48 (doublet) and 2.46 (singlet) ppm, and 6.70 (septet) ppm. The peaks for the new, coordinated bulky anilide are observed at 1.70 (singlet), 6.31 (triplet), 7.34 (doublet). A downfield shift is again observed, appearing at 9.27 ppm (singlet), and is presumably from an amide N-*H*. This intermediate is assigned as [Li(THF)$_3$][UO$_2$(N(SiHMe$_2$)^{t}Bu)(NH(2,6-dimesitylphenyl)]. Again, as this reaction proceeds, all products are consumed, until only HN(SiHMe$_2$)^{t}Bu remains.

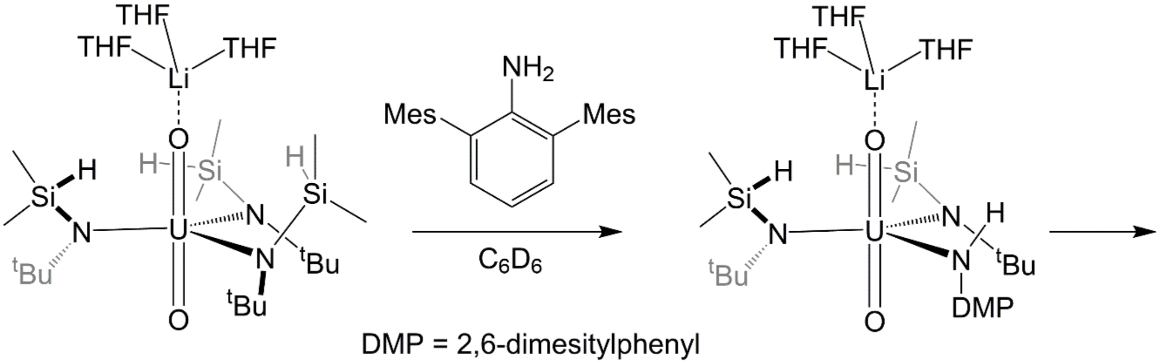

Scheme 5.5. Reaction of compound **1** with 2,6-dimesitylaniline, showing the proposed intermediate, [Li(THF)$_3$][UO$_2$(N(SiHMe$_2$)^{t}Bu)(NH(2,6-dimesitylphenyl)].

5.3.2.3.2 Prep Scale Reactions

For better analysis of the uranyl products from these reactions, prep scale reactions were developed. The reaction of **1** with H_2NDIPP was first examined. Addition of one equivalent of H_2NDIPP to THF or toluene solutions of compound **1** produced dark brown solutions. After stirring for 10 minutes, these reactions were concentrated, yielding orange solids in each case. Analysis of the product by ^{1}H NMR spectroscopy revealed that only starting compound **1** was present in both cases. This is counter to the results of the NMR tube reaction, where all of the starting materials are consumed immediately. It was hypothesized that the isolation of starting material was due to the reversibility of these protonation reactions upon concentration, or perhaps these protonation reactions don't occur the same in THF and toluene.

To address both of these concerns, a prep scale reaction was attempted in C_6H_6 Addition of one equivalent of H_2NDIPP to a C_6H_6 solution of **1** produced the same dark brown color.

After stirring for 10 minutes, this solution was concentrated *in vacuo*. An interesting property of benzene is that it freezes at relatively high temperatures, and often freezes upon concentration due to the absorption of heat upon evaporation. This allows for the slow concentration of frozen samples, and prevents any reactions from occurring during this process. Along these lines, this sample froze upon concentration until a dark-brown powder remained. Analysis of this product by ^{1}H NMR spectroscopy reveals that no resonances are observable, and is likely a similar product obtained from the NMR tube reaction above.

Analysis of this product by IR spectroscopy reveals no N-H stretches are present. Additionally, a Si-H stretch is observed at 2093 cm^{-1}. After brief exposure of this IR sample to ambient atmosphere, a new IR spectrum is obtained. In this spectrum, a large N-H signal is observed, along with a new stretch at 1618 cm^{-1}, consistent with the N-H bend of H_2NDIPP. This data is convincing that the -NDIPP moiety is present without protons. The extreme sensitivity of this compound to air (moisture) is consistent with the tentative assignment as [Li(THF)$_3$][UO$_2$(N(SiHMe$_2$)^{t}Bu)(NDIPP)], which would be the first example of a uranyl-imido. The unusual electronic or dynamic properties that cause the lack of signals in the ^{1}H NMR spectra are not understood. Unfortunately, no single crystals of this product have been obtained.

5.4 Conclusions

In summary, the synthesis and characterization of three new uranyl complexes featuring the -N(SiHMe$_2$)^{t}Bu ligand, which are the first actinide derivatives of this amide has been reported. Successful synthesis was achieved by salt metathesis with LiN(SiHMe$_2$)^{t}Bu, forming compounds that were readily soluble in non-aqueous conditions. Spectroscopic and structural characterization did not reveal any Si-H secondary interactions with the uranium center, contrary to previous examples for rare earth elements. Reactivity studies established that -N(SiHMe$_2$)^{t}Bu is more basic and labile than the established -N(SiMe$_3$)$_2$ derivative.

The Si-H handle is interesting as a reactive site, along with being a useful characterization handle. Si-H abstraction is facile from these uranyl complexes, creating interesting, possibly silylated, products that decompose to paramagnetic products that have yet to be defined. Additionally, these amide ligands have proven useful in diverse ligand substitution chemistry. Reactivity studies show that these complexes may be basic enough to doubly deprotonate substituted anilines to form uranyl imido complexes. Using bulky systems, primary aryl amides are observed as intermediates to these reactions. These molecules will serve as useful synthons for uranyl chemistry for both these and other reactivity studies.

CHAPTER 6. NEW NEPTUNIUM AND PLUTONIUM COMPOUNDS AND REACTIVITY

6.1 Introduction

In the realm of actinide chemistry, studies on uranium and thorium (primarily utilizing the low-specific activity ^{238}U and ^{232}Th α-particle emitting radioisotopes) have dominated.[159] Far less progress has been realized for nuclear fuel cycle relevant transuranic (TRU) elements (Np-Cm) in terms of fundamental research, largely on account of the reduced availability of these elements and the specialized radiological facilities needed to safely handle the TRU materials that are available, which usually comprise high specific-activity α-particle emitters such as ^{237}Np and ^{239}Pu.[159,160]

Recently, neptunium and plutonium have experienced significant advances in the area of nonaqueous chemistry, as demonstrated by the number of new reviews on the topic.[160–162] This has been motivated in part by the development of new nonaqueous actinide-solvento halide starting materials prepared from both An-oxide and An^0 (An = actinide) sources.[163–167] These materials have facilitated the discovery of new oxidation states[167,168] and new bonding motifs including a neptunium bis(imido) complex[169] and neptunium (III) cyclopentadienyl complexes.[167] A parallel can be drawn from the synthesis of $UI_3(THF)_4$ from U^0 by Zwick, Sattelberger, and Clark in 1994, which greatly facilitated the study of low valent uranium chemistry for years to come.[163]

Despite the moderate recent progress, nonaqueous studies of neptunium and plutonium chemistry are still constrained by the limited number of entry routes into well-defined, organic-soluble, starting materials in a specific desired oxidation state. Access to Pu(III) chemistry is typically achieved by oxidation of Pu metal or utilizing $PuCl_3$, sources that are relatively common for facilities that research Pu chemistry. However, neutral, nonaqueous Pu(IV) molecules as synthetic precursors are barely developed, with $PuCl_4(DME)_2$ the only example in the literature.[166] Previous observations have pointing towards difficulty in accessing Pu(IV) under inert atmospheric conditions in dry solvents – for example, oxidation of Pu metal with iodine or bromine in THF does not proceed past the +3 oxidation state,[165] while partial reduction of Pu(VI) or Pu(IV) in THF has been observed without addition of a reductant. In the case of Np, the metal form is very scarce, restricting the utility of the oxidative entry route into Np(III) chemistry. However, solid NpO_2 and acidic aqueous stock solutions of Np(IV) are more readily available, and via dehydration routes, can be converted into materials such as $NpCl_4$ and $NpCl_4(DME)_2$ as suitable reagents for inert atmosphere synthetic chemistry.[166,167] A few studies that reduce Np(IV) to generate Np(III) *in situ* have proven fruitful, but the nature of the Np(III) intermediates are not well-defined. In order to more widely study Np(III) chemistry, development of a facile reductive route that unambiguously yields a Np(III) precursor of known molecular structure would significantly aid progress in the field.

Herein, the solvent exchange and reduction behavior of the An(IV) transuranic starting materials, $PuCl_4(DME)_2$ and $NpCl_4(DME)_2$, in tetrahydrofuran (THF) is reported and the stark differences between these two isostructural compounds is noted.

6.2 Experimental

General Considerations. Caution! ^{237}Np ($t_{1/2} = 2.14 \times 10^6$ y) and ^{239}Pu ($t_{1/2} = 2.41 \times 10^4$ y) are high specific-activity α-particle emitting radionuclides and pose serious health risks if not properly contained. This research was conducted at specialized radiological facilities at Los Alamos National Laboratory, which were designed with appropriate analyses of hazards and implementation of controls for the safe handling of these materials. Multiple levels of containment were utilized when appropriate for safety reasons, and all free-flowing solids containing neptunium or plutonium were handled in negative-pressure gloveboxes. Stock solutions of ^{237}Np and ^{239}Pu were obtained from internal sources at Los Alamos National Laboratory. Due to these radiological hazards, elemental analyses of complexes containing radioisotopes were not possible.

For this study, all reactions were performed under an anaerobic, anhydrous atmosphere inside an Mbraun Labmaster 130 helium atmosphere drybox. The inert atmosphere was maintained with a standalone Vacuum Atmosphere Genesis oxygen and moisture removal system. All solvents were purchased as anhydrous grade, and were further dried over a mixture of 3 Å and 4 Å molecular sieves for several days before use. THF was additionally dried by storing over NaK for several days before it was filtered through dry alumina onto a mixture of 3 Å and 4 Å molecular sieves. $NpCl_4(DME)_2$,[166] $PuCl_4(DME)_2$,[166] and CsC_8 were prepared according to literature procedures.

The solution phase electronic absorption spectrum of $NpCl_3(py)_4$ was collected in a screw-capped quartz cuvette (1 cm path length) that was loaded in a transuranic glovebox using Parafilm to protect the exterior surface of the cuvette and cap from radioactive contamination. The solution was prepared by dissolving 2.1 mg of dried crystalline material in 1.694 g of pyridine (~1.8×10^{-3} M). The spectrum was collected at ambient temperature using a Varian Cary 6000i UV/vis/NIR spectrometer.

To ensure safe handling of radioisotopes during X-ray crystallographic experiments, crystals of each compound were prepared with appropriate layers of containment. Single crystals of $[PuCl_2(THF)_5][PuCl_5(THF)]$, $NpCl_4(THF)_3$, and $NpCl_3(py)_4$ suitable for X-ray diffraction, were coated with Paratone-N oil in a glovebox and mounted inside 0.5 mm capillary tubes, which were subsequently sealed with hot capillary wax. The samples were removed from the glovebox, and the exterior surfaces were coated in a thin film of acrylic dissolved in ethyl acetate (Hard as Nails$^{®}$) to provide structural integrity and appropriate containment of the materials. These contained samples were mounted on the goniometer head on a Bruker D8 diffractometer.

Initial examination and data collection were performed with Mo Kα radiation (λ = 0.71073 Å). All data were collected at 100 K. Data were collected and reflections were indexed and processed using the APEX II software.[52] The data were corrected for absorption using the SADABS program.[54] Frame integration, including Lorentz-polarization corrections, and final cell parameter calculations were carried out using the SAINT+ software.[56] Structure solution and refinement were performed using SHELXTL software.[21] All hydrogen atom positions were idealized and rode on the atom to which they were attached. Final refinements include anisotropic temperature factors on all non-hydrogen atoms. Additional data collection and refinement parameters are given in.

Isolation of $[PuCl_2(THF)_5][PuCl_5(THF)]$. $PuCl_4(DME)_2$ (~3 mg) was dissolved in THF (~1 mL) and was stirred for one hour. No obvious change to the golden colour was noted. This solution was layered with pentane (~0.5 mL) and cooled to -35 °C, producing X-ray quality crystals overnight. Analysis of one of these crystals revealed $[PuCl_2(THF)_5][PuCl_5(THF)]$ instead of the expected THF adduct of plutonium tetrachloride.

Isolation of $NpCl_4(THF)_3$. $NpCl_4(DME)_2$ (20.0 mg, 0.0358 mmol) was dissolved in THF (~2 mL) and was stirred overnight. No obvious change to the solution colour was noted after approximately 16 hours. This solution was layered with pentane (~1 mL) and cooled to -35 °C, producing X-ray quality crystals within 24 hours. Analysis of one of these salmon colored crystals confirmed the assignment as $NpCl_4(THF)_3$.

Preparation of $NpCl_3(THF)_n$. $NpCl_4(DME)_2$ (20.0 mg, 0.0358 mmol) was dissolved in THF (~2 mL) and stirred for 5 minutes. CsC_8 (8.2 mg, 0.036 mmol) was slowly added as a solid, resulting in a colour change of the salmon solution to green. This solution was stirred for one hour before it was filtered, resulting in a translucent yellow solution, which was then concentrated *in vacuo* to a yellow residue. This residue was redissolved in a minimal amount of THF (<1 mL), and the product was precipitated with addition of ~10 mL of pentane. After cooling to -35 °C, the mother liquor was decanted, and the crystalline product was dried *in vacuo* to a free-flowing yellow crystalline powder. 9.9 mg were collected, which would correspond to a 49% yield if the product were $NpCl_3(THF)_3$ or a 44% yield if the product were $NpCl_3(THF)_4$.

Isolation of $NpCl_3(py)_4$. The material from the synthesis of $NpCl_3(THF)_n$ (9.9 mg) was dissolved in pyridine (~2 mL), layered with Et_2O, and cooled to -35 °C, resulting in X-ray quality crystals.

6.3 Results and Discussion

6.3.1 Synthesis of Np and Pu Halide Complexes

Initial studies commenced with experiments to understand the basic solvent exchange chemistry of $PuCl_4(DME)_2$ and $NpCl_4(DME)_2$ with THF. Though these transformations seem trivial, coordinated solvent can be an important synthetic nuance in directing product identity. In fact, unwanted side reactivity of DME was recently reported with neptunium complexes under reducing conditions.[170] Additionally, the chelating nature of DME may be undesirable to other studies that rely on solvent lability to open coordination sites for substrate. Well characterized solution routes to highly soluble solvent adducts of $NpCl_4$ or $PuCl_4$ other than with DME have not yet been reported.

In a negative pressure helium drybox, $PuCl_4(DME)_2$ was dissolved in THF, maintaining the original golden color. Layering the solution with pentane and cooling to -35 °C overnight produced dichroic crystals suitable for X-ray crystallography. Refinement of the data revealed a monoclinic P2/*c* space group. Instead of the expected THF adduct, the structure was the mixed valent plutonium salt $[Pu^{III}Cl_2(THF)_5][Pu^{IV}Cl_5(THF)]$, containing independent Pu(III) and Pu(IV) centers (Figure 6.1). This product, obtained from partial, spontaneous reduction of Pu(IV) (likely through disproportionation) in THF solutions, has been reported as a decomposition product twice before, once from Pu(IV) carbonate in THF/HCl and once from hexane washes of high valent $[PuO_2Cl_2(THF)_2]_2$ synthesized in THF.[165] Isolation of the mixed valent product for the third time highlights that Pu(IV) is prone to reduction in THF. This unusual redox chemistry is counter to examples with other tetravalent actinides earlier in the f-block series, namely U(IV) and Th(IV), which exhibit remarkable thermal stability in most organic solvents. As the actinide series is traversed, increased stability of An(III) ions is expected, but Pu appears to be a transitional element, with Pu(IV) dominant in aqueous/aerobic environments but much more difficult to access in organic solvent/anaerobic environments. Instability of Pu(IV) in THF demonstrates the important of $PuCl_4(DME)_2$ as a well-defined starting material to closely parallel U(IV) entry routes that utilize neutral halide-solvento starting materials.[159,171]

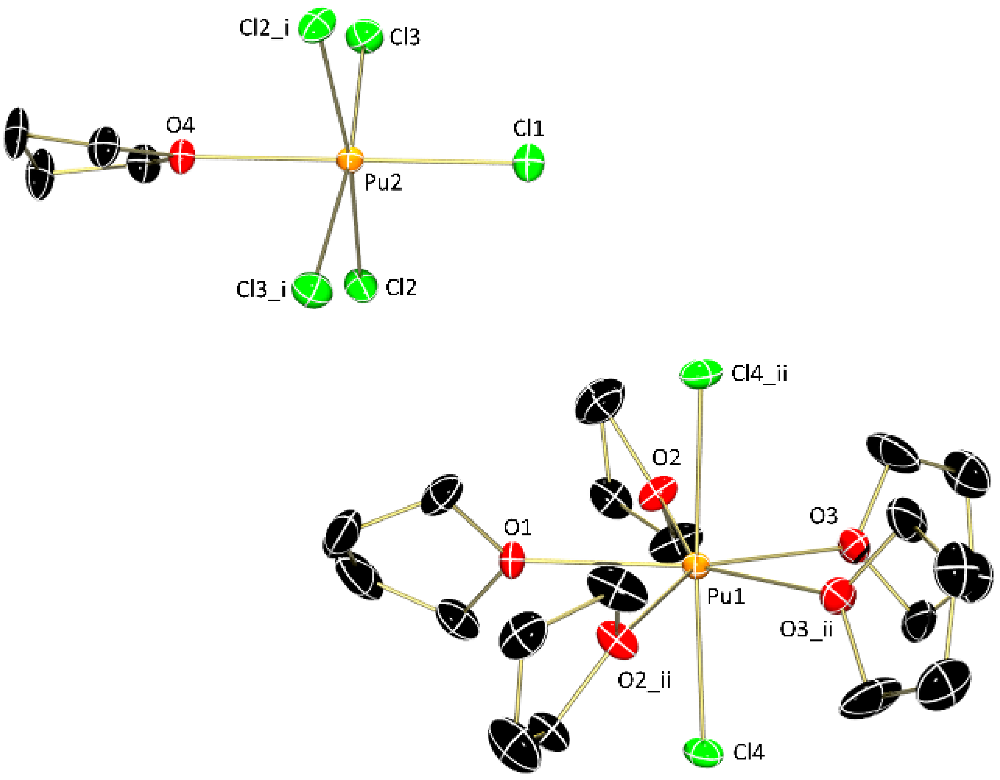

Figure 6.1. Molecular structure of $[PuCl_2(THF)_5][PuCl_5(THF)]$ shown at 30% probability ellipsoids. Hydrogen atoms have been omitted for clarity.

Contrastingly, dissolution of $NpCl_4(DME)_2$ in THF resulted in no obvious change to the initial salmon-pink color. Layering this solution with pentane and cooling it to -35 °C overnight produced salmon colored crystals suitable for X-ray crystallography. Refinement of the data revealed that the compound crystallized in a monoclinic $P2_1$ space group, isomorphous to the structural parameters of $UCl_4(THF)_3$ reported by Sauer and Van Der Sluys.[172] The solid-state structure comprises a Np(IV) metal centre in a pseudo pentagonal bipyramidal geometry with axial chlorides, similar to that of $UCl_4(THF)_3$ (Scheme 6.1, Figure 6.2, Table 6.1). The Np-Cl distances range from 2.568(2) to 2.607(2) Å, similar to those in $NpCl_4(DME)_2$ (2.5878-2.6224 Å).[166] Presumably, this shortening is from the lower coordination number of the Np center and more steric freedom associated with the monodentate THF ligands. The Np-Cl distances are shorter than the U-Cl distances in $UCl_4(THF)_3$ as expected from the change in ionic radii;[37] however, once the errors are taken into account the observed shortening is not statistically significant.

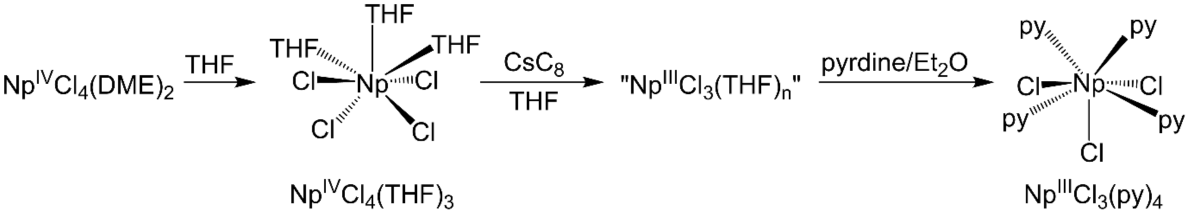

Scheme 6.1. Synthetic route and crystallization conditions that lead to $NpCl_4(THF)_3$ and $NpCl_3(py)_4$.

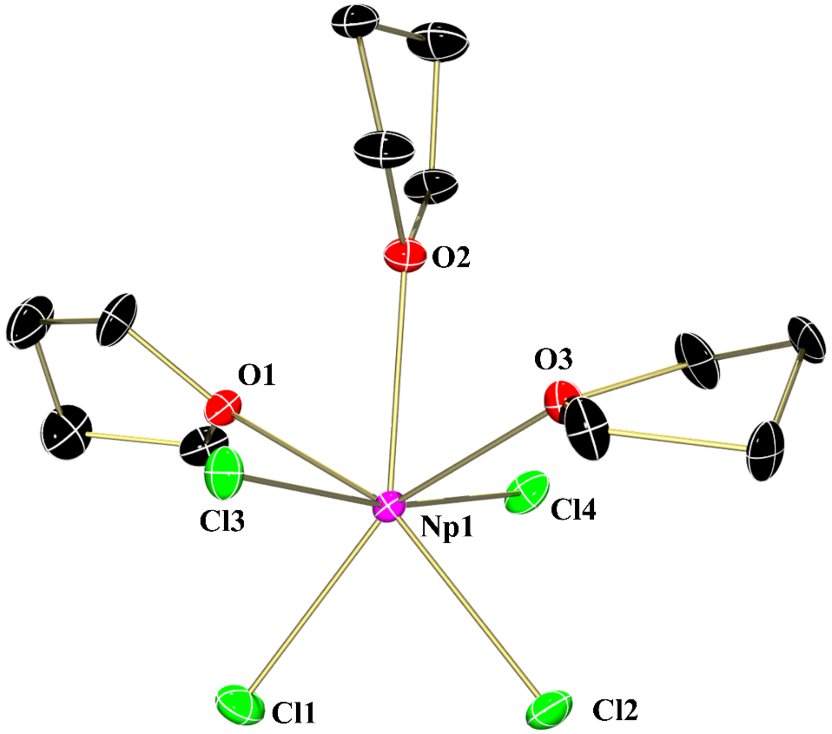

Figure 6.2. Molecular structure of $NpCl_4(THF)_3$ shown at 30% probability ellipsoids. Hydrogen atoms and disorder have been omitted for clarity.

With the successful isolation of $NpCl_4(THF)_3$, a new Np(IV) neutral, organic-soluble, starting material, it was rationalized that this complex, would be ideal for *in situ* reduction routes to trivalent neptunium chemistry without the complication of possible DME reduction to methoxide.[170] Reduction of binary $NpCl_4$ has been demonstrated by Walter, Arnold, and coworkers, who treated polymeric $NpCl_4$ suspension in Et_2O with sodium amalgam to create a highly reactive form of '$NpCl_3$'.[167] Although this material is poorly soluble and undoubtedly polymeric like other forms of anhydrous AnX_3,[173,174] it has proven useful in metathesis reactions as demonstrated by synthesis of homoleptic Np(III) cyclopentadienide complexes. The aim of the reduction study was to gain a better understanding of reduction processes by generating an isolable Np(III) starting material of known molecular formula and structure, thus offering a reliable route into nonaqueous, trivalent neptunium chemistry.

Table 6.1. Np-Cl and Np-solvent (solvent = coordinated THF or py) distances (in Å) for $NpCl_4(THF)_3$ and $NpCl_3(py)_4$.

Bond	$NpCl_4(THF)_3$	$NpCl_3(py)_4$
$Np\text{-}Cl_{ax}$	2.568(2)	2.7097(7)
$Np\text{-}Cl_{ax}$	2.575(2)	2.7097(7)
$Np\text{-}Cl_{eq}$	2.595(2)	2.7303(9)
$Np\text{-}Cl_{eq}$	2.607(2)	--
Np-solvent	2.452(6)	2.620(2)
Np-solvent	2.461(5)	2.620(2)
Np-solvent	2.495(6)	2.641(2)
Np-solvent	--	2.641(2)

As a reductant CsC_8 was chosen since the stoichiometry could be more easily controlled on a small scale than KC_8 (a more common reductant), and the CsCl and graphite byproducts could be easily separated from the product. Slow addition of one equivalent of CsC_8 to a stirring solution of $NpCl_4(THF)_3$ in THF caused a color change from salmon to green. After filtering to remove graphite and CsCl, the solution appeared bright yellow and was subsequently concentrated *in vacuo* to a bright yellow, free-flowing powder. This powder, presumably the THF adduct of $NpCl_3$, was highly soluble in THF but insoluble in pentane. Single-crystals suitable for X-ray diffraction were not obtained, precluding structural confirmation of the putative '$NpCl_3(THF)_n$' product. Starting with 20.0 mg of $NpCl_4(DME)_2$ yielded 9.9 mg of this recrystallized microcrystalline material – corresponding to yields of 44% if $NpCl_3(THF)_4$ or 49% if $NpCl_3(THF)_3$– in either case the yield is synthetically useful and not a minor product. It is worth noting that early lanthanide trichlorides, with large ionic radii, take the formula $LnCl_3(THF)_4$, while smaller, later lanthanide trichlorides have the formula $LnCl_3(THF)_3$.[37,175,176]

There are currently no reports of structurally characterized THF adducts of any An(III) chlorides, including uranium. In fact, the recent accounts of dimeric $[UCl_3(py)_4]_2$ and trimeric $[UCl(py)_4(\mu\text{-}Cl)_3U(py)_2(\mu\text{-}Cl)_3UCl_2(py)_3]$ (py = pyridine) by Meyer and coworkers represented the first crystallographically characterized nonaqueous complexes of UCl_3 in 2014.[177] Therefore, attempts to trap the "$NpCl_3$" product with pyridine in an analogous fashion were conducted. Dissolution of the yellow powder in dry pyridine caused an immediate color change to orange. This solution was layered with Et_2O and cooled to -35 °C, producing orange crystals overnight that were suitable for X-ray crystallography. Refinement of the data revealed that the compound crystallized in a monoclinic C2/*c* space group, and the structure was composed of monomeric $NpCl_3(py)_4$ in a pseudo trigonal bipyramidal geometry with axial chloride ligands (Figure 6.3).

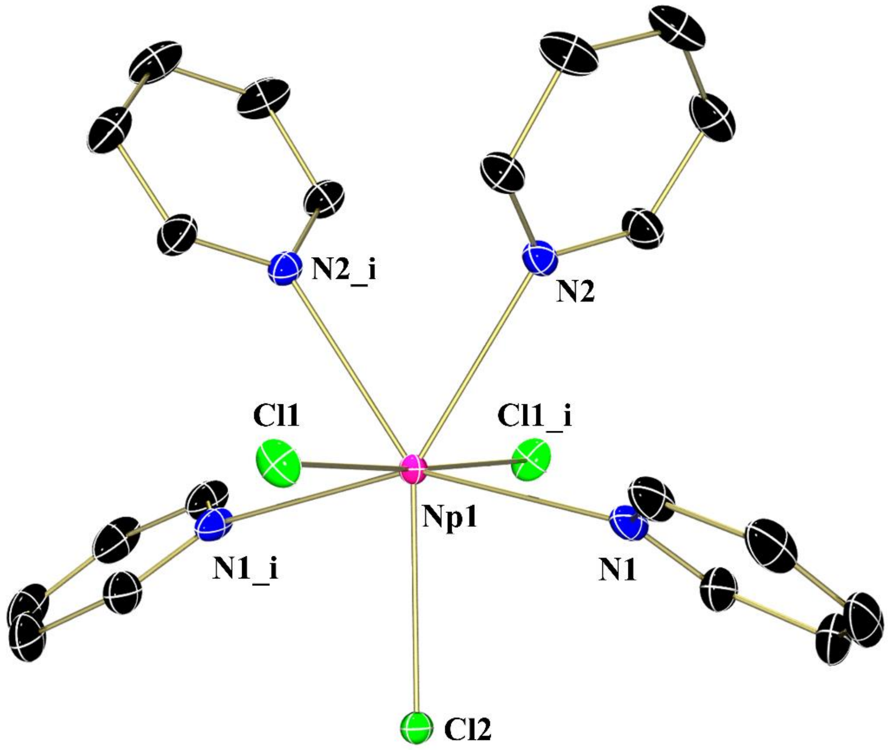

Figure 6.3. Molecular structure of $NpCl_3(py)_4$ shown at 30% probability ellipsoids. Hydrogen atoms have been omitted for clarity.

Notably, the structure of $NpCl_3(py)_4$ is monomeric, while the uranium analogue, grown from similar crystallization conditions, is dimeric through two chloride atoms.[178] This could be an artefact of the larger U(III) ion not completely saturated as a monomer, driving this dimerization.[37] The Np-Cl distances range from 2.7097(7) to 2.7303(9) Å, similar to the Np(III)-Cl distance of 2.6694 Å in $[(L^{Ar})NpCl]$ (L^{Ar} = *trans*-calix[2]benzene[2]pyrrole).[170] The Np-Cl distances in $NpCl_3(py)_4$ are approximately 0.1-0.15 Å longer than the distances in $NpCl_4(THF)_3$, similar to difference in ionic radii of Np(III) vs. Np(IV).[37] The Np-pyridine distances represent the only known Np(III) dative nitrogen distances and range from 2.620(2) to 2.641(2) Å.

$NpCl_3(py)_4$ was also examined by electronic absorption spectroscopy in the visible and near-IR regions. $NpCl_3(py)_4$ was dissolved in dry pyridine to make a 1.8x10^{-3} M solution, and the spectrum was taken with the solution sealed in a quartz screw-capped cuvette. The spectrum, shown in Figure 6.4, shows the electronic "fingerprint" for trivalent neptunium ions with weakly intense 5f-5f and 5f-6d transitions (~10-60 $M^{-1}cm^{-1}$) in the region of 600-1100 nm. There are striking similarities with both the spectrum of Np(III) ions in perchloric acid[177] and also the spectrum of $NpI_3(THF)_4$ in THF.[163] This further validates the oxidation state of Np(III) in $NpCl_3(py)_4$.

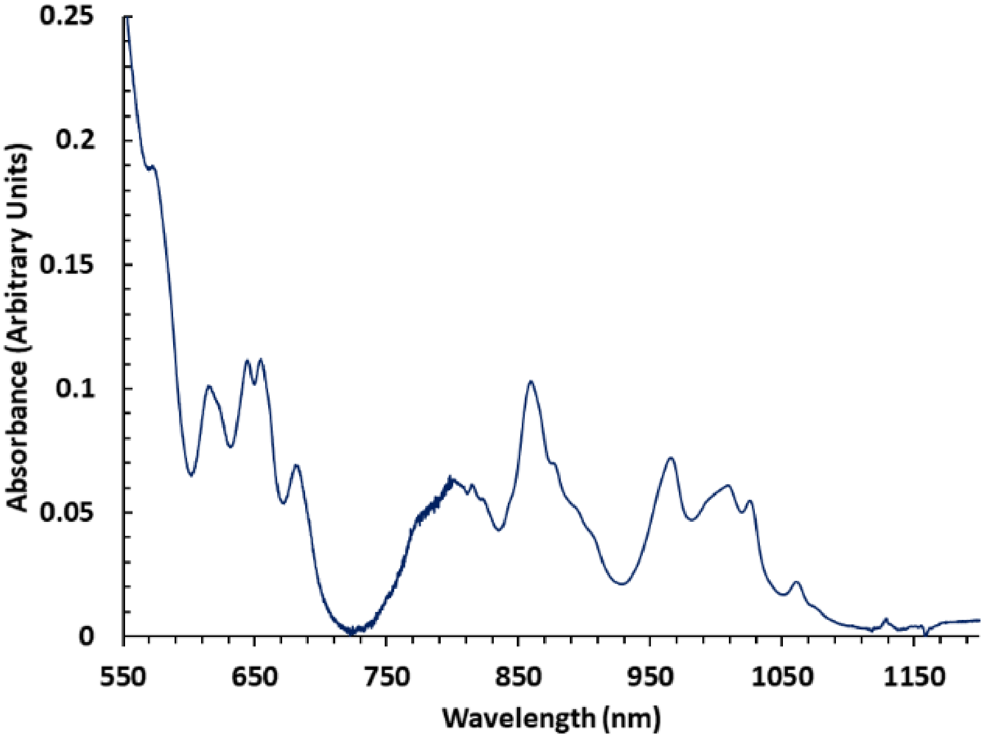

Figure 6.4. Vis-NIR spectrum of $NpCl_3(py)_4$ in pyridine (1.8x10^{-3} M) at ambient temperature.

6.4 Conclusion

In summary, solvent exchange and redox properties of the transuranic starting materials, $NpCl_4(DME)_2$ and $PuCl_4(DME)_2$, in THF were roported. DME is readily displaced in $NpCl_4(DME)_2$ forming the THF adduct $NpCl_4(THF)_3$, which was crystallographically characterized. Contrastingly, $PuCl_4(DME)_2$ was found to be unstable with respect to partial reduction in THF, leading to structural identification of the mixed valent plutonium salt, $[PuCl_2(THF)_5][PuCl_5(THF)]$. This salt has now been reported three times, which highlights the driving force for the formation of Pu(III) under nonaqueous/inert atmosphere conditions. Reduction of $NpCl_4(THF)_3$ with CsC_8 allowed for the isolation of a yellow powder that was presumed to be a molecular THF adduct of $NpCl_3$, and expected to be of great utility for subsequent reactivity studies. Confirmation of reduction to a '$NpCl_3$' species was achieved by 'trapping' the product with pyridine, generating monomeric $NpCl_3(py)_4$, a formulation confirmed by single-crystal X-ray diffraction. Notably, the structure contains the only known Np(III) neutral nitrogen distances. Electronic absorption spectroscopy supports the assignment of the oxidation state as Np(III). These highly soluble, molecular $NpCl_3$-solvento molecules provide easy access to molecular Np(III) chemistry that has previously been hindered by the scarce availability of neptunium metal, and in situ generation routes for which the identity of the reduction products to be used as synthons are not known.

REFERENCES

(1) Stang, S.; Lebkücher, A.; Walter, P.; Kaifer, E.; Himmel, H. J. *Eur. J. Inorg. Chem.* **2012**, 4833.

(2) Guerro, M.; Pham, N. H.; Massue, J.; Bellec, N.; Lorcy, D. *Tetrahedron* **2008**, *64*, 5285.

(3) Olekhnovich, L. P.; Lyubchenko, S. N.; Simakov, V. I.; Shif, A. I.; Kurbatov, S. V.; Lesin, A. V.; Borodkin, G. S.; Ivakhnenko, E. P.; Zhdanov, Y. A. *Dolk. Akad. Nauk* **1999**, *369*, 632.

(4) Ranis, L. G.; Werellapatha, K.; Pietrini, N. J.; Bunker, B. A.; Brown, S. N. *Inorg. Chem.* **2014**, *53*, 10203.

(5) Ivakhnenko, E. P.; Starikov, A. G.; Minkin, V. I.; Lyssenko, K. A.; Antipin, M. Y.; Simakov, V. I.; Korobov, M. S.; Borodkin, G. S.; Knyazev, P. A. *Inorg. Chem.* **2011**, *50*, 7022.

(6) Hananouchi, S.; Krull, B. T.; Ziller, J. W.; Furche, F.; Heyduk, A. F. *Dalt. Trans.* **2014**, *43*, 17991.

(7) Szigethy, G.; Shaffer, D. W.; Heyduk, A. F. *Inorg. Chem.* **2012**, *51*, 12606.

(8) Wong, J. L.; Sánchez, R. H.; Logan, J. G.; Zarkesh, R. A.; Ziller, J. W.; Heyduk, A. F. *Chem. Sci.* **2013**, *4*, 1906.

(9) Matson, E. M.; Opperwall, S. R.; Fanwick, P. E.; Bart, S. C. *Inorg. Chem.* **2013**, *52*, 7295.

(10) Matson, E. M.; Franke, S. M.; Anderson, N. H.; Cook, T. D.; Fanwick, P. E.; Bart, S. C. *Organometallics* **2014**, *33*, 1964.

(11) Pangborn, A. B.; Giardello, M. A.; Grubbs, R. H.; Rosen, R. K.; Timmers, F. J. *Organometallics* **1996**, *15*, 1518.

(12) Andersen, R. A. *Inorg. Chem.* **1979**, *18*, 209.

(13) Schlosser, Manfred; Hartmann, J. *Angew. Chemie Int. Ed.* **1973**, *12*, 508.

(14) Tonzetich, Z. J.; Eisenberg, R. *Inorganica Chim. Acta* **2003**, *345*, 340.

(15) Monreal, M. J.; Thomson, R. K.; Cantat, T.; Travia, N. E.; Scott, B. L.; Kiplinger, J. L. *Organometallics* **2011**, *30*, 2031.

(16) Clark, David L.; Sattleberger, Alfred P.; Andersen, R. A. *Inorg. Synth.* **1997**, *31*, 307.

(17) Berthet, J.-C.; Nierlich, M.; Ephritikhine, M. *Chem. Commun.* **2004**, *2*, 870.

(18) Izod, K.; Liddle, S. T.; Clegg, W. *Inorg. Chem.* **2004**, *43*, 214.

(19) Chakraborty, S.; Chattopadhyay, J.; Guo, W.; Billups, W. E. *Angew. Chemie Int. Ed.* **2007**, *46*, 4486.

(20) Bain, G. A.; Berry, J. F. *J. Chem. Educ.* **2008**, *85*, 532.

(21) Sheldrick, G. M. *Acta Crystallogr. A* **2007**, *64*, 112.

(22) Burla, M. C.; Caliandro, R.; Camalli, M.; Carrozzini, B.; Cascarano, G. L.; De Caro, L.; Giacovazzo, C.; Polidori, G.; Spagna, R. *J. Appl. Crystallogr.* **2005**, *38*, 381.

(23) Berthet, J.-C.; Siffredi, G.; Thuéry, P.; Ephritikhine, M. *Chem. Commun.* **2006**, *8431*, 3184.

(24) Arnold, P. L.; Patel, D.; Blake, A. J.; Wilson, C.; Love, J. B. *J. Am. Chem. Soc.* **2006**, *128*, 9610.

(25) Cladis, D. P.; Kiernicki, J. J.; Fanwick, P. E.; Bart, S. C. *Chem. Commun.* **2013**, *49*, 4169.

(26) Anderson, N. H.; Odoh, S. O.; Yao, Y.; Williams, U. J.; Schaefer, B. A.; Kiernicki, J. J.; Lewis, A. J.; Goshert, M. D.; Fanwick, P. E.; Schelter, E. J.; Walensky, J. R.; Gagliardi, L.; Bart, S. C. *Nat. Chem.* **2014**, *6*, 919.

(27) Kiernicki, J. J.; Newell, B. S.; Matson, E. M.; Anderson, N. H.; Fanwick, P. E.; Shores, M. P.; Bart, S. C. *Inorg. Chem.* **2014**, *53*, 3730.

(28) Castro-Rodríguez, I.; Meyer, K. *Chem. Commun.* **2006**, *13*, 1353.

(29) Kraft, S. J.; Fanwick, P. E.; Bart, S. C. *Inorg. Chem.* **2010**, *49*, 1103.

(30) Zi, G.; Jia, L.; Werkema, E. L.; Walter, M. D.; Gottfriedsen, J. P.; Andersen, R. A. *Organometallics* **2005**, *24*, 4251.

(31) Meyer, K.; Bart, S. C. *Tripodal Carbene and Aryloxide Ligands for Small-Molecule Activation at Electron-Rich Uranium and Transition Metal Centers*; Elsevier Masson SAS, 2008; Vol. 60.

(32) Graves, C. R.; Schelter, E. J.; Cantat, T.; Scott, B. L.; Kiplinger, J. L. *Organometallics* **2008**, *27*, 5371.

(33) Castro-rodriguez, I.; Nakai, H.; Zakharov, L. N. *Science* **2004**, *305*, 1757.

(34) Kindra, D. R.; Evans, W. J. *Chem. Rev.* **2014**, *114*, 8865.

(35) Avens, L. R.; Burns, C. J.; Butcher, R. J.; Clark, D. L.; Gordon, J. C.; Schake, A. R.; Scott, B. L.; Watkin, J. G.; Zwick, B. D. *Organometallics* **2000**, *19*, 451.

(36) Kiernicki, J. J.; Fanwick, P. E.; Bart, S. C. *Chem. Commun.* **2014**, *50*, 8189.

(37) Shannon, R. D. *Acta Crystallogr. A* **1976**, *32*, 751.

(38) Denning, R. G. *J. Phys. Chem. A* **2007**, *111*, 4125.

(39) Nash, K. L.; Nilsson, M. *Introduction to Reprocessing and Recycling of Spent Nuclear Fuels*; Elsevier, 2015.

(40) Herbst, R. S.; Baron, P.; Nilsson, M. *Advanced Separation Techniques for Nuclear Fuel Reprocessing and Radioactive Waste Treatment*; Elsevier: Cambridge, 2011.

(41) Trumm, S.; Geist, A.; Panak, P. J.; Fanghänel, T. *Solvent Extr. Ion Exch.* **2011**, *29*, 213.

(42) Lewis, F. W.; Harwood, L. M.; Hudson, M. J.; Drew, M. G. B.; Desreux, J. F.; Vidick, G.; Bouslimani, N.; Modolo, G.; Wilden, A.; Sypula, M.; Vu, T. H.; Simonin, J. P. *J. Am. Chem. Soc.* **2011**, *133*, 13093.

(43) Panak, P. J.; Geist, A. *Chem. Rev.* **2013**, *113*, 1199.

(44) Neidig, M. L.; Clark, D. L.; Martin, R. L. *Coord. Chem. Rev.* **2013**, *257*, 394.

(45) Kaltsoyannis, N. *Inorg. Chem.* **2013**, *52*, 3407.

(46) Cary, S. K.; Vasiliu, M.; Baumbach, R. E.; Stritzinger, J. T.; Green, T. D.; Diefenbach, K.; Cross, J. N.; Knappenberger, K. L.; Liu, G.; Silver, M. A.; Deprince, A. E.; Polinski, M. J.; Van Cleve, S. M.; House, J. H.; Kikugawa, N.; Gallagher, A.; Arico, A. A.; Dixon, D. A.; Albrecht-Schmitt, T. E. *Nat. Commun.* **2015**, *6*, 1.

(47) Liu, G.; Cary, S. K.; Albrecht-Schmitt, T. E. *Phys. Chem. Chem. Phys.* **2015**, *17*, 16151.

(48) Pattenaude, S. A.; Kuehner, C. S.; Dorfner, W. L.; Schelter, E. J.; Fanwick, P. E.; Bart, S. C. *Inorg. Chem.* **2015**, *54*, 6520.

(49) Ivakhnenko, E. P.; Romanenko, G. V.; Simakov, V. I.; Knyazev, P. A.; Bogomyakov, A. S.; Lyssenko, K. A.; Minkin, V. I. *Inorganica Chim. Acta* **2017**, *458*, 116.

(50) Ivakhnenko, E. P.; Simakov, V. I.; Knyazev, P. A.; Romanenko, G. V.; Bogomyakov, A. S.; Minkin, V. I. *Mendeleev Commun.* **2016**, *26*, 49.

(51) Cantat, T.; Scott, B. L.; Kiplinger, J. L. *Chem. Commun.* **2010**, *46*, 919.

(52) Apex2 v2014.11 Bruker AXS Inc.; Madison (WI), USA, (2013/2014).

(53) Rigaku Crop. CrystalClear, The Woodlands (TX), USA, (2001).

(54) Otwinowski, Z.; Minor, W. *Methods Enzymol.* **1997**, *276*, 307.

(55) Nonius (1998). Collect Users Manual, Nonius Delft, The Netherlands, (1998).

(56) SAINT, Version 6.02a; Bruker AXS Inc.; Madison (WI), USA, (2000).

(57) Cotton, S. *Lanthanide and Actinide Chemistry*; John Wiley and Sons: West Sussex, U. K., 2006.

(58) Feng, J.; Zhang, H. *Chem. Soc. Rev.* **2013**, *42*, 387.

(59) Walter, M. D.; Fandos, R.; Andersen, R. A. *New J. Chem.* **2006**, *30*, 1065.

(60) Behrle, A. C.; Levin, J. R.; Kim, J. E.; Drewett, J. M.; Barnes, C. L.; Schelter, E. J.; Walensky, J. R. *Dalt. Trans.* **2015**, *44*, 2693.

(61) Stults, S. D.; Andersen, R. A.; Zalkin, A. *Organometallics* **1990**, *9*, 1623.

(62) Evans, W. J.; Hozbor, M. A. *J. Organomet. Chem.* **1987**, *326*, 299.

(63) Tian, G.; Shuh, D. K.; Beavers, C. M.; Teat, S. J. *Dalt. Trans.* **2015**, *44*, 18469.

(64) Charushnikova, I. A.; Fedoseev, A. M.; Perminov, V. P. *Radiochemistry* **2015**, *57*, 111.

(65) Gagliardi, L.; Lindh, R.; Karlström, G. *J. Chem. Phys.* **2004**, *121*, 4494.

(66) Spivak, M.; Vogiatzis, K. D.; Cramer, C. J.; Graaf, C. De; Gagliardi, L. *J. Phys. Chem. A* **2017**, *121*, 1726.

(67) Horne, G. P.; Gregson, C. R.; Sims, H. E.; Orr, R. M.; Taylor, R. J.; Pimblott, S. M. *J. Phys. Chem. B* **2017**, *121*, 883.

(68) Singha, D. K.; Majee, P.; Mondal, S. K.; Mahata, P. *Eur. J. Inorg. Chem.* **2016**, *2016*, 4631.

(69) Praneeth, V. K. K.; Ringenberg, M. R.; Ward, T. R. *Angew. Chemie Int. Ed.* **2012**, *51*, 10228.

(70) Kaim, W. *Eur. J. Inorg. Chem.* **2012**, *3*, 343.

(71) Eisenberg, R.; Gray, H. B. *Inorg. Chem.* **2011**, *50*, 9741.

(72) Chirik, P. J. *Inorg. Chem.* **2011**, *50*, 9737.

(73) Chirik, P. J.; Wieghardt, K. *Science* **2010**, *327*, 794.

(74) Broere, D. L. J.; Plessius, R.; van der Vlugt, J. I. *Chem. Soc. Rev.* **2015**, *44*, 6886.

(75) Sarkar, B.; Schweinfurth, D.; Deibel, N.; Weisser, F. *Coord. Chem. Rev.* **2015**, *293*, 250.

(76) Bejger, C.; Tian, Y.-H.; Barker, B. J.; Boland, K. S.; Scott, B. L.; Batista, E. R.; Kozimor, S. A.; Sessler, J. L. *Dalt. Trans.* **2013**, *42*, 6716.

(77) Tezgerevska, T.; Alley, K. G.; Boskovic, C. *Coord. Chem. Rev.* **2014**, *268*, 23.

(78) Warren, L. F. *Inorg. Chem.* **1977**, *16*, 2814.

(79) De Bruin, B.; Bill, E.; Bothe, E.; Weyhermüller, T.; Wieghardt, K. *Inorg. Chem.* **2000**, *39*, 2936.

(80) Bill, E.; Beckmann, U. D. O.; Wieghardt, K. *Hyperfine Interact.* **2003**, 183.

(81) Suarez, A. I. O.; Lyaskovskyy, V.; Reek, J. N. H.; Van Der Vlugt, J. I.; De Bruin, B. *Angew. Chemie Int. Ed.* **2013**, *52*, 12510.

(82) Kiernicki, J. J.; Ferrier, M. G.; Lezama Pacheco, J. S.; La Pierre, H. S.; Stein, B. W.; Zeller, M.; Kozimor, S. A.; Bart, S. C. *J. Am. Chem. Soc.* **2016**, *138*, 13941.

(83) Kiernicki, J. J.; Cladis, D. P.; Fanwick, P. E.; Zeller, M.; Bart, S. C. *J. Am. Chem. Soc.* **2015**, *137*, 11115.

(84) Anderson, N. H.; Odoh, S. O.; Williams, U. J.; Lewis, A. J.; Wagner, G. L.; Pacheco, J. L.; Kozimor, S. A.; Gagliardi, L.; Schelter, E. J.; Bart, S. C. *J. Am. Chem. Soc.* **2015**, *137*, 4690.

(85) Guidal, V.; Camp, C.; Biswas, B.; Pecaut, J.; Dubois, L.; Mazzanti, M. *J. Am. Chem. Soc.* **2013**, *132*, 2.

(86) Fedushkin, I. L.; Maslova, O. V.; Lukoyanov, A. N.; Fukin, G. K. *Comptes Rendus Chim.* **2010**, *13*, 584.

(87) Mullane, K. C.; Cheisson, T.; Nakamaru-Ogiso, E.; Manor, B. C.; Carroll, P. J.; Schelter, E. J. *Chem. - A Eur. J.* **2018**, *24*, 826.

(88) Fang, H.; Cole, B. E.; Qiao, Y.; Bogart, J. A.; Cheisson, T.; Manor, B. C.; Carroll, P. J.; Schelter, E. J. *Angew. Chemie Int. Ed.* **2017**, *56*, 13450.

(89) Bart, S. C.; Chłopek, K.; Bill, E.; Bouwkamp, M. W.; Lobkovsky, E.; Neese, F.; Wieghardt, K.; Chirik, P. J. *J. Am. Chem. Soc.* **2006**, *128*, 13901.

(90) Knijnenburg, Q.; Gambarotta, S.; Budzelaar, P. H. M. *Dalt. Trans.* **2006**, *46*, 5442.

(91) Bill, E.; Bothe, E.; Chaudhuri, P.; Chlopek, K.; Herebian, D.; Kokatam, S.; Ray, K.; Weyhermüller, T.; Neese, F.; Wieghardt, K. *Chem. - A Eur. J.* **2005**, *11*, 204.

(92) Kraft, S. J.; Williams, U. J.; Daly, S. R.; Schelter, E. J.; Kozimor, S. A.; Boland, K. S.; Kikkawa, J. M.; Forrest, W. P.; Christensen, C. N.; Schwarz, D. E.; Fanwick, P. E.; Clark, D. L.; Conradson, S. D.; Bart, S. C. *Inorg. Chem.* **2011**, *50*, 9838.

(93) Schelter, E. J.; Wu, R.; Scott, B. L.; Thompson, J. D.; Cantat, T.; John, K. D.; Batista, E. R.; Morris, D. E.; Kiplinger, J. L. *Inorg. Chem.* **2010**, *49*, 924.

(94) Vasudevan, K.; Cowley, A. H. *Chem. Commun.* **2007**, *33*, 3464.

(95) Cloke, F. G. N.; de Lemos, H. C.; Sameh, A. a. *J. Chem. Soc. Chem. Commun.* **1986**, *17*, 1344.

(96) Ison, E. A.; Ison, A. *J. Chem. Educ.* **2012**, *89*, 1575.

(97) Kiplinger, J. L.; Morris, D. E.; Scott, B. L.; Burns, C. J. *Organometallics* **2002**, *21*, 5978.

(98) Schaub, T.; Radius, U. *Zeitschrift fur Anorg. und Allg. Chemie* **2006**, *632*, 807.

(99) Martins, R. S.; Filgueiras, C. A. L.; Visentin, L. do C.; Bordinhão, J.; Ferreira, L. C. *Acta Crystallogr. E* **2007**, *63*, 4544.

(100) Gonsalvi, L.; Gaunt, J. A.; Adams, H.; Castro, A.; Sunley, G. J.; Haynes, A. *Organometallics* **2003**, *22*, 1047.

(101) Cope-Eatough, E. K.; Mair, F. S.; Pritchard, R. G.; Warren, J. E.; Woods, R. J. *Polyhedron* **2003**, *22*, 1447.

(102) Jantunen, K. C.; Burns, C. J.; Castro-Rodriguez, I.; Da Re, R. E.; Golden, J. T.; Morris, D. E.; Scott, B. L.; Taw, F. L.; Kiplinger, J. L. *Organometallics* **2004**, *23*, 4682.

(103) Marks, T. J. *Progress in Inorganic Chemistry*; John Wiley & Sons: New York, 1979.

(104) Lam, O. P.; Anthon, C.; Heinemann, F. W.; O'Connor, J. M.; Meyer, K. *J. Am. Chem. Soc.* **2008**, *130*, 6567.

(105) Anderson, N. H.; Yin, H.; Kiernicki, J. J.; Fanwick, P. E.; Schelter, E. J.; Bart, S. C. *Angew. Chemie Int. Ed.* **2015**, *54*, 9386.

(106) Smith, A. L.; Martin, P.; Prieur, D.; Scheinost, A. C.; Raison, P. E.; Cheetham, A. K.; Konings, R. J. M. *Inorg. Chem.* **2016**, *55*, 1569.

(107) Kosog, B.; La Pierre, H. S.; Denecke, M. A.; Heinemann, F. W.; Meyer, K. *Inorg. Chem.* **2012**, *51*, 7940.

(108) Den Auwer, C.; Simoni, E.; Conradson, S.; Madic, C. *Eur. J. Inorg. Chem.* **2003**, *2003*, 3843.

(109) Vlaisavljevich, B.; Diaconescu, P. L.; Lukens, W. L.; Gagliardi, L.; Cummins, C. C. *Organometallics* **2013**, *32*, 1341.

(110) Brendebach, B.; Banik, N. L.; Marquardt, C. M.; Rothe, J.; Denecke, M. A.; Geckeis, H. *Radiochim. Acta* **2009**, *97*, 701.

(111) Chiang, M.; Williams, C. W.; Soderholm, L.; Antonio, M. R. *Eur. J. Inorg. Chem.* **2003**, *1*, 2663.

(112) Lukens, W. W. *Organometallics* **1999**, *18*, 1253.

(113) Budzelaar, P. H. M.; De Bruin, B.; Gal, A. W.; Wieghardt, K.; Van Lenthe, J. H. *Inorg. Chem.* **2001**, *40*, 4649.

(114) de Bruin, B.; Peters, T. P. J.; Thewissen, S.; Blok, A. N. J.; Wilting, J. B. M.; de Gelder, R.; Smits, J. M. M.; Gal, A. W. *Angew. Chem. Int. Ed.* **2002**, *41*, 2135.

(115) Schelter, E. J.; Yang, P.; Scott, B. L.; Thompson, J. D.; Martin, R. L.; Hay, P. J.; Morris, D. E.; Kiplinger, J. L. *Inorg. Chem.* **2007**, *46*, 7477.

(116) Newell, B. S.; Rappé, A. K.; Shores, M. P. *Inorg. Chem.* **2010**, *49*, 1595.

(117) Kozimor, S. A.; Bartlett, B. M.; Rinehart, J. D.; Long, J. R. *J. Am. Chem. Soc.* **2007**, *129*, 10672.

(118) Greenwood, N. N.; Earnshaw, A. *Chemistry of the Elements*, 2nd ed.; Butterworth Heinimann: Oxford, 1998.

(119) Giesbrecht, G. R.; Gordon, J. C. *Dalton Trans.* **2004**, *16*, 2387.

(120) Britovsek, G. J. P.; Bruce, M.; Gibson, V. C.; Kimberley, B. S.; Maddox, P. J.; Mastroianni, S.; McTavish, S. J.; Redshaw, C.; Solan, G. A.; Strömberg, S.; White, A. J. P.; Williams, D. J. *J. Am. Chem. Soc.* **1999**, *121*, 8728.

(121) Kepp, K. P. *Inorg. Chem.* **2016**, *55*, 9461.

(122) Vasudevan, K. V.; Smith, N. A.; Scott, B. L.; McKigney, E. A.; Blair, M. W.; Gordon, J. C.; Muenchausen, R. E. *Inorg. Chem.* **2011**, *50*, 4627.

(123) Sugiyama, H.; Korobkov, I.; Gambarotta, S.; Möller, A.; Budzelaar, P. H. M. *Inorg. Chem.* **2004**, *43*, 5771.

(124) Trovitch, R. J.; Lobkovsky, E.; Bouwkamp, M. W.; Chirik, P. J. *Organometallics* **2008**, *27*, 6264.

(125) Levin, J. R.; Cheisson, T.; Carroll, P. J.; Schelter, E. J. *Dalt. Trans.* **2016**, 15249.

(126) Evans, W. J.; Lorenz, S. E.; Ziller, J. W. *Inorg. Chem.* **2009**, *48*, 2001.

(127) Arnold, P. L.; Love, J. B.; Patel, D. *Coord. Chem. Rev.* **2009**, *253*, 1973.

(128) Jones, G. M.; Arnold, P. L.; Love, J. B. *Chem. - A Eur. J.* **2013**, *19*, 10287.

(129) Vaughn, A. E.; Barnes, C. L.; Duval, P. B. *J. Chem. Crystallogr.* **2007**, *37*, 779.

(130) Lewis, A. J.; Carroll, P. J.; Schelter, E. J. *J. Am. Chem. Soc.* **2013**, *135*, 511.

(131) Arnold, P. L.; Jones, G. M.; Odoh, S. O.; Schreckenbach, G.; Magnani, N.; Love, J. B. *Nat. Chem.* **2012**, *4*, 221.

(132) Procopio, L. J.; Carroll, P. J.; Berry, D. H. *J. Am. Chem. Soc.* **1991**, *113*, 1870.

(133) Procopio, L. J.; Carroll, P. J.; Berry, D. H. *J. Am. Chem. Soc.* **1994**, *116*, 177.

(134) Procopio, L. E. O. J.; Carroll, P. J.; Berry, D. H. *Science* **1995**, *14*.

(135) Bi, S.; Zhu, S.; Zhang, Z. *Eur. J. Inorg. Chem.* **2007**, *2007*, 2046.

(136) Ignatov, S. K.; Khalimon, A. Y.; Rees, N. H.; Razuvaev, A. G.; Mountford, P.; Nikonov, G. I. *Inorg. Chem.* **2009**, *48*, 9605.

(137) Yan, K.; Ellern, A.; Sadow, A. D. *J. Am. Chem. Soc.* **2012**, *134*, 9154.

(138) Okazaki, M.; Ebina, S. *Chem. Lett.* **2014**, *43*, 1089.

(139) Yan, K.; Pindwal, A.; Ellern, A.; Sadow, A. D. *Dalt. Trans.* **2014**, *43*, 8644.

(140) McLeod, N. A.; Kuzmina, L. G.; Korobkov, I.; Howard, J. A. K.; Nikonov, G. I. *Dalt. Trans.* **2016**, *45*, 2554.

(141) Rozenel, S. S.; Perrin, L.; Eisenstein, O.; Andersen, R. A. *Organometallics* **2017**, *36*, 97.

(142) Eedugurala, N.; Wang, Z.; Yan, K.; Boteju, K. C.; Chaudhary, U.; Kobayashi, T.; Ellern, A.; Slowing, I. I.; Pruski, M.; Sadow, A. D. *Organometallics* **2017**, *36*, 1142.

(143) Rees, W. S.; Just, O.; Schumann, H.; Weimann, R. *Angew. Chemie Int. Ed.* **1996**, *35*, 419.

(144) Huynh, K.; Anderson, B. K.; Livinghouse, T. *Tetrahedron Lett.* **2015**, *56*, 3658.

(145) Anderson, N. H.; Xie, J.; Ray, D.; Zeller, M.; Gagliardi, L.; Bart, S. C. *Nat. Chem.* **2017**, *9*, 850.

(146) Lewis, A. J.; Williams, U. J.; Carroll, P. J.; Schelter, E. J. *Inorg. Chem.* **2013**, *52*, 7326.

(147) Wilkerson, M. P.; Burns, C. J.; Paine, R. T.; Blosch, L. L.; Andersen, R. A. *Inorg. Synth.* **2004**, *34*, 93.

(148) Kim, J.; Bott, S. G.; Hoffman, D. M. *Inorg. Chem.* **1998**, *37*, 3835.

(149) Burns, C. J.; Clark, D. L.; Donohoe, R. J.; Duval, P. B.; Scott, B. L.; Tait, C. D. *Inorg. Chem.* **2000**, *39*, 5464.

(150) Arnold, P. L.; Prescimone, A.; Farnaby, J. H.; Mansell, S. M.; Parsons, S.; Kaltsoyannis, N. *Angew. Chemie Int. Ed.* **2015**, *54*, 6735.

(151) Katz, J.; Morss, L. R.; Seaborg, G. T. *The Chemistry of the Actinide Elements*; Chapman Hall: New York, 1980.

(152) Brown, J. L.; Fortier, S.; Wu, G.; Kaltsoyannis, N.; Hayton, T. W. *J. Am. Chem. Soc.* **2013**, *135*, 5352.

(153) Schettini, M. F.; Wu, G.; Hayton, T. W. *Inorg. Chem.* **2009**, *48*, 11799.

(154) Guzei, I. A.; Wendt, M. *Dalt. Trans.* **2006**, *33*, 3991.

(155) Guzei, I. A.; Wendt, M. University of Wisconsin: Madison, WI 2004.

(156) Lambert, J. B.; Zhao, Y.; Wu, H.; Tse, W. C.; Kuhlmann, B. *J. Am. Chem. Soc.* **1999**, *121*, 5001.

(157) Holbrey, J. D.; Reichert, W. M.; Nieuwenhuyzen, M.; Sheppard, O.; Hardacre, C.; Rogers, R. D. *Chem. Commun.* **2003**, *4*, 476.

(158) Seaman, L. A.; Schnaars, D. D.; Wu, G.; Hayton, T. W. *Dalt. Trans.* **2010**, *39*, 6576.

(159) Jones, M. B.; Gaunt, A. J. *Chem. Rev.* **2013**, *113*, 1137.

(160) Gaunt, A. J.; Neu, M. P. *Comptes Rendus Chim.* **2010**, *13*, 821.

(161) Arnold, P. L.; Dutkiewicz, M. S.; Walter, O. *Chem. Rev.* **2017**, *117*, 11460.

(162) Kaltsoyannis, N. *Chem. - A Eur. J.* **2017**, 1.

(163) Avens, L. R.; Clark, D. L.; Sattelberger, A. P.; Watkin, J. G.; Zwick, B. D. *Inorg. Chem.* **1994**, *33*, 2248.

(164) Gaunt, A. J.; Enriquez, A. E.; Reilly, S. D.; Scott, B. L.; Neu, M. P. *Inorg. Chem.* **2008**, *47*, 26.

(165) Gaunt, A. J.; Reilly, S. D.; Enriquez, A. E.; Hayton, T. W.; Boncella, J. M.; Scott, B. L.; Neu, M. P. *Inorg. Chem.* **2008**, *47*, 8412.

(166) Reilly, S. D.; Brown, J. L.; Scott, B. L.; Gaunt, A. J. *Dalt. Trans.* **2014**, *43*, 1498.

(167) Dutkiewicz, M. S.; Apostolidis, C.; Walter, O.; Arnold, P. L. *Chem. Sci.* **2017**, *8*, 2553.

(168) Windorff, C. J.; Chen, G. P.; Cross, J. N.; Evans, W. J.; Furche, F.; Gaunt, A. J.; Janicke, M. T.; Kozimor, S. A.; Scott, B. L. *J. Am. Chem. Soc.* **2017**, *139*, 3970.

(169) Brown, J. L.; Batista, E. R.; Boncella, J. M.; Gaunt, A. J.; Reilly, S. D.; Scott, B. L.; Tomson, N. C. *J. Am. Chem. Soc.* **2015**, *137*, 9583.

(170) Dutkiewicz, M. S.; Farnaby, J. H.; Apostolidis, C.; Colineau, E.; Walter, O.; Magnani, N.; Gardiner, M. G.; Love, J. B.; Kaltsoyannis, N.; Caciuffo, R.; Arnold, P. L. *Nat. Chem.* **2016**, *8*, 797.

(171) Liddle, S. T. *Angew. Chemie Int. Ed.* **2015**, *54*, 8604.

(172) Van Der Sluys, W. G.; Berg, J. M.; Barnhardt, D.; Sauer, N. N. *Inorganica Chim. Acta* **1993**, *204*, 251.

(173) Taylor, J. C.; Wilson, P. W. *Acta Crystallogr.* **1974**, *B30*, 2803.

(174) Levy, J. H.; Taylor, J. C.; Wilson, P. W. *Acta Crystallogr.* **1975**, *B31*, 880.

(175) Lin, S. H.; Dong, Z. C.; Huang, J. S.; Zhang, Q. E.; Lu, J. X. *Acta Crystallogr. C* **1991**, *47*, 426.

(176) Deacon, G. B.; Feng, T.; Nickel, S.; Skelton, B. W.; White, A. H. *J. Chem. Soc. Chem. Commun.* **1993**, *261*, 1328.

(177) Hagan, P. G.; Cleveland, J. M. *J. Inorg. Nucl. Chem.* **1966**, *28*, 2905.

(178) La Pierre, H. S.; Heinemann, F. W.; Meyer, K. *Chem. Commun.* **2014**, *50*, 3962.

VITA

Scott Pattenaude received his A.S. in chemistry from Lake Land College in Mattoon, Illinois in the spring of 2010. There he studied chemistry with Dr. Gregory Capitosti, who inspired him to pursue a career in teaching chemistry. Scott then began work on a B.S. in chemistry from the University of Illinois at Urbana-Champaign (UIUC). As an undergraduate at UIUC, Scott joined the organic chemistry research laboratory of Prof. Martin Burke. His work in in the Burke lab involved organic synthesis to create MIDA boronate derivatives that could be used for cross-coupling reactions.

After graduating from UIUC with a B.S. in chemistry in the fall of 2012, Scott pursued his Ph.D. in inorganic chemistry under Suzanne Bart at Purdue University. Scott's projects in the Bart group were diverse and generally focused on understanding structure and bonding properties of elements throughout the f-block. A major component of Scott's work involved the use of redox-active ligands, which were applied to either stabilizing elements throughout the periodic table or to promote new reactivity at lanthanide centers. During his time at Purdue, Scott also had the rare opportunity to collaborate with groups across the nation to perform transuranic chemistry. He has worked directly with Prof. Thomas Albrecht-Schmitt's group to isolate isostructural complexes of plutonium, americium, berkelium, and californium. Through the Seaborg Institute Summer Research Fellowship, Scott also spent two summers working with Dr. Andrew Gaunt at Los Alamos National Laboratory, where he explored neptunium and plutonium imido formation. Scott has presented his work at PINDU conferences, OIW conference, and at and American Chemical Society national meeting.

PUBLICATION

Inorganic Chemistry
Article
pubs.acs.org/IC

Spectroscopic and Structural Elucidation of Uranium Dioxophenoxazine Complexes

Scott A. Pattenaude,[†] Christopher S. Kuehner,[†] Walter L. Dorfner,[‡] Eric J. Schelter,[‡] Phillip E. Fanwick,[†] and Suzanne C. Bart*,[†]

[†]H.C. Brown Laboratory, Department of Chemistry, Purdue University, West Lafayette, Indiana 47907, United States

[‡]P. Roy and Diana T. Vagelos Laboratories, Department of Chemistry, University of Pennsylvania, Philadelphia, Pennsylvania 19104, United States

Supporting Information

ABSTRACT: Uranium derivatives of a redox-active, dioxophenoxazine ligand, $(DOPO^q)_2UO_2$, $(DOPO^{sq})UI_2(THF)_2$, $(DOPO^{cat})UI(THF)_2$, and $Cp^*U(DOPO^{cat})(THF)_2$ (DOPO = 2,4,6,8-tetra-*tert*-butyl-1-oxo-1*H*-phenoxazin-9-olate), have been synthesized from U(VI) and U(III) starting materials. Full characterization of these species show uranium complexes bearing ligands in three different oxidation states. The electronic structures of these complexes have been explored using ^1H NMR and electronic absorption spectroscopies, and where possible, X-ray crystallography and SQUID magnetometry.

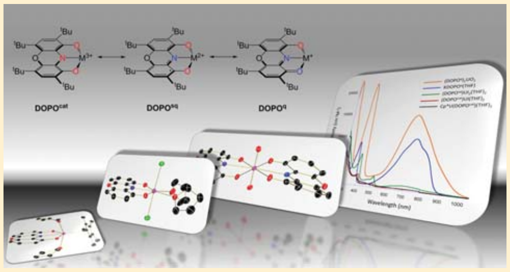

INTRODUCTION

With the recent activity aimed toward understanding redox noninnocent ligands and their cooperative participation in metal mediated transformations, new ligand frameworks have emerged.[1,2] One such class is dioxophenoxazine ligands (DOPO), which have recently been synthesized[3] and studied with transition metals.[4,5] These ligands are an improvement over the related 3,5-di-*tert*-butyl-1,2-quinone-1-(2-oxy-3,5-di-*tert*-butylphenyl)imine frameworks (ONO), as the DOPO class contains an additional ether linkage that introduces rigidity and prevents bending of the π-system needed for electron storage.[6−8] The DOPO ligands are stable in their monoanionic (quinone, $DOPO^q$), dianionic (semiquinone, $DOPO^{sq}$), and trianionic (catecholate, $DOPO^{cat}$) forms, potentially serving to stabilize metals while still being capable of mediating multielectron processes (Scheme 1).

Recently, several studies have reported the utility of the bis(DOPO) ligand framework to support transition metals in a variety of oxidation states. Studies by Minkin and co-workers described the synthesis of divalent, first-row transition metal bis(ligand) complexes, $M(DOPO)_2$ (M = Mn, Fe, Co, Ni, Cu, Zn), bearing the monoanionic $DOPO^q$ form of the ligand.[5] The manganese, iron, and cobalt derivatives are all high spin, and it is hypothesized that the rigid DOPO framework prevents interconversion between the redox-isomeric forms of the complexes. More recently, Brown and co-workers have shown analogous hexavalent octahedral molybdenum and tungsten bis(ligand) species supported by the fully reduced, trianionic form of the dioxophenoxazine ligand, $DOPO^{cat}$.[4] Interestingly, the chromium analogue shows an unusual electronic structure, one ligand in the reduced semiquinone form, DOPOsq, and the other in the oxidized quinone form, DOPOq, generating a C_{2v} symmetric chromium(III) species, $Cr(DOPO^q)(DOPO^{sq})$. Despite this recent interest in the DOPO family of ligands, the ability of this framework to support f-block elements has not yet been explored.

The DOPO class of ligands is related to the iminoquinone (^{R}iq)/iminosemiquinone (^{R}isq)/amidophenolate (^{R}ap) (iq = 4,6-di-*tert*-butyl-2-[(R)-iminoquinone]; ap = 4,6-di-*tert*-butyl-2-[(R)-amidophenolate]; R = ^{t}Bu, Ad, dipp; Ad = 1-adamantyl, dipp =2,6-diisopropylphenyl) family, which has recently been used to perform multielectron oxidative addition[9] and reductive elimination on uranium.[10] For instance, the bidentate amidophenolate ligands in $(^R\text{ap})_2U(THF)_2$ can mediate oxidative addition of chlorine or iodine at monomeric U(IV) complexes, where the two reducing equivalents necessary for bond cleavage are derived from the ligand. Thus, radical iminosemiquinone ligands (^{R}isq) support the products from oxidative addition, which are dimeric, $[(^R\text{isq})_2UCl]_2(\mu\text{-}Cl)_2$, and monomeric, $(^R\text{isq})_2UI_2$.[9] Alternately, radical reductive elimination of bibenzyl occurs from tetrabenzyluranium using the iminoquinone form of the ligand. These are subsequently reduced to generate the corresponding amidophenolate uranium dialkyls, $(^R\text{ap})U(CH_2Ph)_2$.[10] With this multielectron chemistry at U(IV) established, we sought to explore the reactivity with the DOPO ligand, as it has an additional phenoxy substituent to afford more robust tridentate uranium

Received: April 15, 2015
Published: June 23, 2015

DOI: 10.1021/acs.inorgchem.5b00855
Inorg. Chem. 2015, 54, 6520−6527

Scheme 1. Redox Noninnocence of the DOPO Ligand

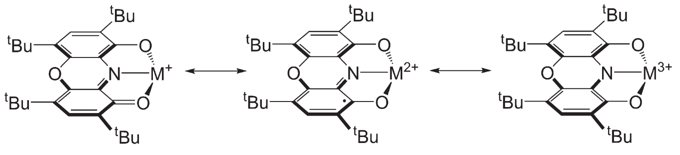

$[DOPO^q]^{-1}$ $[DOPO^{sq}]^{-2}$ $[DOPO^{cat}]^{-3}$

complexes. Herein, we report the synthesis and full characterization of a family of uranium complexes bearing dioxophenoxazine ligands in three different oxidation states.

EXPERIMENTAL SECTION

General Considerations. All air- and moisture-sensitive manipulations were performed using standard Schlenk techniques or in an MBraun inert atmosphere drybox with an atmosphere of purified nitrogen. The MBraun drybox was equipped with a cold well designed for freezing samples in liquid nitrogen as well as two −35 °C freezers for cooling samples and crystallizations. Solvents for sensitive manipulations were dried and deoxygenated using literature procedures with a Seca solvent purification system.[11] Benzene-d_6 and pyridine-d_5 were purchased from Cambridge Isotope Laboratories. Benzene-d_6 was dried with molecular sieves and sodium, and degassed by three freeze−pump−thaw cycles. Pyridine-d_5 was dried with molecular sieves and degassed by three freeze−pump−thaw cycles. 2,4,6,8-Tetra-*tert*-butyl-9-hydroxy-1*H*-phenoxazin-1-one ($HDOPO^q$),[4] $UO_2[N(SiMe_3)_2]_2(THF)_2$,[12] KCH_2Ph,[13] potassium pentamethylcyclopentadienide (KCp*),[14] $UI_3(THF)_4$,[15,16] and KC_8[17] were prepared according to literature procedures.

^{1}H NMR spectra were recorded on a Varian Inova 300 spectrometer at 299.992 MHz. All chemical shifts are reported relative to the peak for $SiMe_4$, using ^{1}H (residual) chemical shifts of the solvent as a secondary standard. The spectra for paramagnetic molecules were obtained by using an acquisition time of 0.5 s; thus, the peak widths reported have an error of ±2 Hz. For paramagnetic molecules, the ^{1}H NMR data are reported with the chemical shift, followed by the peak width at half height in Hertz, the integration value, and, where possible, the peak assignment. Elemental analyses were performed by Complete Analysis Laboratories, Inc., Parsippany, New Jersey. Electronic absorption measurements were recorded at 294 K in THF in sealed 1 cm quartz cuvettes with a Jasco V-6700 spectrophotometer. Infrared spectra were recorded using a Perkin−Elmer FT-IR Spectrum RX I spectrometer. Samples were made by crushing the solids, mixing with dry KBr, and pressing into a pellet.

Single crystals of $Cp^*U(DOPO^{cat})(THF)_2$ (**4**) and $(DOPO^{sq})UI_2(THF)_2$ (**2**) for X-ray diffraction were coated with poly(isobutene) oil in a glovebox and quickly transferred to the goniometer head of a Nonius KappaCCD image plate diffractometer equipped with a graphite crystal, incident beam monochromator. Preliminary examination and data collection were performed with Mo K_α radiation (λ = 0.71073 Å). A single crystal of $(DOPO^q)_2UO_2$ (**1**) was coated with polybutenes oil in a glovebox and quickly transferred to the goniometer head of a Rigaku Rapid II image plate diffractometer equipped with a MicroMax002+ high intensity copper X-ray source with confocal optics. Preliminary examination and data collection were performed with Cu K_α radiation (λ = 1.54184 Å). Cell constants for data collection were obtained from least-squares refinement. The space groups were identified using the program XPREP.[18] The structures were solved by direct methods using either SIR2004[19] or SHELXT.[20] Refinement was performed on a LINUX PC using SHELX-2013.[20] The data were collected at a temperature of either 150(1) K or 200(1) K.

Solid-state magnetic data were collected using a Quantum Design Multi-Property Measurement System (MPMS-7) warmed from 2−300 K and cooled from 300−2 K at 1 T and at 2 K from 0−7 T. Drinking straws were used to contain the samples for measurement and were dried under a dynamic vacuum overnight before use in an inert atmosphere (N_2) drybox. While empty, a straw was crimped using a hot pair of tweezers to melt it together. The samples were added directly into the crimped straw and were massed to the nearest 0.1 mg using a calibrated and leveled Mettler-Toledo AL-204 analytical balance. Approximately 10.0 mg of quartz wool was added to the straw above the sample to hold it in place. The straw was then crimped above the sample and quartz wool with hot tweezers to complete the seal. The samples, contained in the sealed drinking straws for measurement, were transferred to the MPMS under inert atmosphere and immediately loaded into the inert atmosphere of the measurement chamber with three evacuation/purge cycles. Corrections for the intrinsic diamagnetism of the samples were made using Pascal's constants.[21]

The resonance Raman system was based on SpectraCode optical rail design. A Melles-Griot HeNe laser (632.8 nm, 25 mW) was used as an excitation source. The laser was coupled into a SpectraCode optical rail via an optical fiber. Semrock MaxLine Laser-line and Stopline Single-notch filters were used to select and guide the laser beam through an objective lens (Nikon 100x EPlan, Olympus 20x LMPlanFL and Mitutoyo 50x MPlan) to the sample. A video system was used to choose the sample area for data collection. Backscattered Raman photons were guided through a second fiber into an Acton Research SpectraPro 300i spectrograph (1200 g/mm grating). Spectra were collected as a solution in benzene-d_6 in a sealed cuvette between 300 and 1565 rel. cm^{-1} using Roper Scientific WinbSpec software.

Preparation of $KDOPO^q(THF)$ ($KDOPO^q$ = potassium 2,4,6,8-tetra-*tert*-butyl-1-oxo-1*H*-phenoxazin-9-olate). A 100 mL round-bottom flask was charged with $HDOPO^q$ (1.816 g, 4.15 mmol) and 30 mL of THF, and was cooled to −35 °C. An orange solution of KCH_2Ph (0.544 g, 4.15 mmol) in 15 mL of THF was also cooled to −35 °C and added dropwise to the $HDOPO^q$ solution, causing a color change from violet to dark blue. After stirring for 1 h the volatiles were removed *in vacuo* yielding a blue powder (quantitative yield) assigned as $KDOPO^q(THF)$. A small amount of bibenzyl was noted by ^{1}H NMR analysis, but the product was pure enough to use without further purification. Analysis for $C_{32}H_{46}KNO_4$: Calcd C, 70.16; H, 8.46; N, 2.56. Found C, 69.99; H, 8.39; N, 2.76. ^{1}H NMR (C_6D_6, 25 °C): δ = 1.40 (m, 4H, THF−CH_2), 1.58 (br s, 36H, −$C(CH_3)_3$), 3.54 (m, 4H, THF−CH_2), 7.62 (s, 2H, Ar−CH).

Preparation of $(DOPO^q)_2UO_2$ (1). A 20 mL scintillation vial was charged with $UO_2[N(SiMe_3)_2]_2(THF)_2$ (0.050 g, 0.069 mmol) and 5 mL of THF. This orange solution was stirred for 5 min before a solution of $HDOPO^q$ (0.060 g, 0.138 mmol) in 5 mL of THF was added dropwise. The resulting green solution was stirred for 1 h, then the volatiles were removed *in vacuo*. This green powder was taken up in 3 mL of pentane and stirred for 10 min. The solution was then cooled to −35 °C, causing precipitation of a dark-green powder. This was collected by filtration and assigned as $(DOPO^q)_2UO_2$ (0.068 g, 0.059 mmol, 86%). Green crystals suitable for X-ray analysis were grown by slow evaporation from toluene/THF (10:1) overnight at 25 °C. Analysis for $C_{56}H_{76}N_2O_8U$: Calcd C, 58.83; H, 6.70; N, 2.45. Found C, 59.01; H, 6.77; N, 2.62. Raman (C_6D_6, cm^{-1}) 843 (s, U═O symmetric stretch). IR (KBr pellet, cm^{-1}): 2958 (s), 1591 (w), 1498 (s), 1357 (s), 1290 (s), 1253 (s), 1203 (m), 1041 (w), 937 (w, U═O

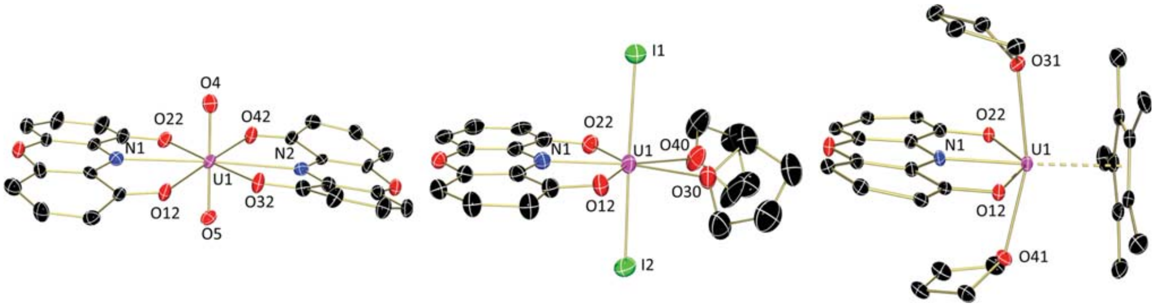

Figure 1. Molecular structures of $(DOPO^{q})_2UO_2$ (**1**) (left), $(DOPO^{sq})UI_2(THF)_2$ (**2**) (center), and $Cp^*U(DOPO^{cat})(THF)_2$ (**4**) (right) shown at 30% probability ellipsoids. Hydrogen atoms, *tert*-butyl groups, and cocrystallized solvent molecules have been omitted for clarity.

asymmetric stretch). ^{1}H NMR (C_6D_6, 25 °C): δ = 1.55 (s, 36H, $-C(CH_3)_3$), 1.93 (s, 36H, $-C(CH_3)_3$), 7.92 (s, 4H, Ar$-$C*H*).

Preparation of $(DOPO^{sq})UI_2(THF)_2$ (2). A 20 mL scintillation vial was charged with $UI_3(THF)_4$ (0.083 g, 0.091 mmol) and $KDOPO^{q}(THF)$ (0.050 g, 0.091 mmol). To this mixture, 8 mL of diethyl ether were added, and the resulting emerald green solution was stirred for 5 min before it was filtered over Celite. After removing volatiles *in vacuo*, an emerald green powder (0.097 g, 0.090 mmol, 99%) was collected and assigned as $(DOPO^{sq})UI_2(THF)_2$. Green crystals suitable for X-ray analysis were grown by slow evaporation from pentane/toluene (5:1) overnight at 25 °C. Analysis for $C_{36}H_{54}I_2NO_5U$: Calcd C, 40.31; H, 5.07; N, 1.31. Found C, 40.47; H, 5.17; N, 1.47. ^{1}H NMR (C_6D_6, 25 °C): δ = −248.69 (141, 2H, Ar−C*H*), −5.38 (9, 18H, $-C(CH_3)_3$), 37.66 (19, 18H, $-C(CH_3)_3$).

Preparation of $(DOPO^{cat})UI(THF)_2$ (3). A 20 mL scintillation vial was charged with $UI_3(THF)_4$ (0.248 g, 0.273 mmol) and $KDOPO^{q}(THF)$ (0.150 g, 0.274 mmol). To this mixture, 15 mL of diethyl ether were added, and the resulting emerald green solution was stirred for 15 min before it was cooled to −35 °C. A suspension of KC_8 (0.033 g, 0.244 mmol) in 5 mL of ether was also cooled to −35 °C and was added to the emerald green solution dropwise, yielding a dark green solution. After stirring for 15 min, the resulting brown solution was filtered over Celite. Upon removal of volatiles *in vacuo*, a yellow-brown powder was collected (0.240 g, 0.253 mmol, 93%) and assigned as $(DOPO^{cat})UI(THF)_2$. To obtain analytically pure sample the compound was taken up in 10 mL of pentane and stirred for 10 min. This solution was cooled to −35 °C and then filtered. Upon removal of volatiles *in vacuo*, a yellow-brown powder was collected (0.105 g, 0.111 mmol, 41%). Analysis for $C_{36}H_{54}INO_5U$: Calcd C, 45.72; H, 5.76; N, 1.48. Found C, 45.67; H, 5.60; N, 1.59. ^{1}H NMR (C_6D_6, 25 °C): δ = −1.73 (4, 18H, $-C(CH_3)_3$), 15.99 (5, 2H, Ar−C*H*), 36.32 (6, 18H, $-C(CH_3)_3$).

Alternative Preparation of $(DOPO^{cat})UI(THF)_2$ (3). A 20 mL scintillation vial was charged with $(DOPO^{sq})UI_2(THF)_2$ (0.050 g, 0.047 mmol) and 15 mL of diethyl ether. This solution was cooled to −35 °C before KC_8 (0.006 g, 0.047 mmol) was added as a solid. After stirring for 15 min, the resulting brown solution was filtered over Celite. Upon removal of volatiles *in vacuo*, a yellow-brown powder was collected (0.038 g, 0.035 mmol, 74%) and assigned as $(DOPO^{cat})UI(THF)_2$ based on ^{1}H NMR spectroscopic data.

Preparation of $Cp^*U(DOPO^{cat})(THF)_2$ (4). A 20 mL scintillation vial was charged with $UI_3(THF)_4$ (0.300 g, 0.331 mmol), KCp* (0.058 g, 0.331 mmol), and 8 mL of THF. This blue solution was stirred for 3 h before a solution of $KDOPO^{q}(THF)$ (0.181 g, 0.331 mmol) in 6 mL of THF was slowly added. After stirring for 1 min, KC_8 (0.045 g, 0.331 mmol) was added quickly as a solid. This brown solution was stirred for 1 h then filtered over Celite. After removing volatiles *in vacuo*, a brown powder (0.272 g, 0.285 mmol, 86%) was collected and assigned as $Cp^*U(DOPO^{cat})(THF)_2$. Brown crystals suitable for X-ray analysis were grown by slow evaporation from pentane overnight at −35 °C. Analysis for $C_{46}H_{69}NO_5U$: Calcd C, 57.91; H, 7.29; N, 1.47. Found C, 57.76; H, 7.40; N, 1.63. ^{1}H NMR (C_6D_6, 25 °C): δ = −65.83 (7, 8H, THF−C*H*$_2$), −20.10 (3, 18H, $-C(CH_3)_3$), −9.70 (13, 8H, THF−C*H*$_2$), 7.20 (4, 15H, Cp*−C*H*$_3$), 7.57 (4, 2H, Ar−C*H*), 16.52 (4, 18H, $-C(CH_3)_3$).

■ RESULTS AND DISCUSSION

Our studies commenced with the synthesis of the protonated $DOPO^{q}$ ligand, $HDOPO^{q}$, which was accomplished using a recently improved procedure[4] that differs from the initial synthesis.[3] Deprotonation of purple $HDOPO^{q}$ was accomplished using benzylpotassium at −35 °C and confirmed by ^{1}H NMR spectroscopy (Figure S1, benzene-d_6), which showed overlapping resonances for the two *tert*-butyl groups at 1.58 ppm and signals for the aryl−C*H* at 7.62 ppm. Two additional resonances (4H each) signify a coordinated THF molecule, making the overall formula, $KDOPO^{q}(THF)$.

With the protonated and deprotonated forms of the ligand in hand, uranium complexes that feature the DOPO ligand in each of its possible oxidation states were planned. To generate a uranium complex with the most oxidized form of the ligand, $DOPO^{q}$, a bis(ligand) uranyl species was targeted. In this case, there are no additional electrons on uranium that can reduce the ligand, thus eliminating ambiguity of ligand oxidation states. Treating an orange toluene solution of $UO_2[N(SiMe_3)_2]_2(THF)_2$[12] with 2 equiv of $HDOPO^{q}$ resulted in a color change to emerald green (eq 1). The concentration of this solution facilitated precipitation of a dark green powder assigned as $(DOPO^{q})_2UO_2$ (**1**) in high yield (86%).

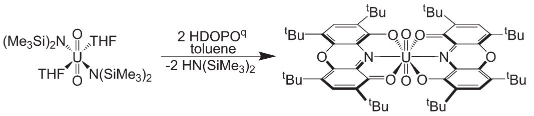

(1)

$(DOPO^{q})_2UO_2$
1

Characterization of **1** by ^{1}H NMR spectroscopy (Figure S2, benzene-d_6) shows a spectrum consistent with a diamagnetic, D_2 symmetric molecule. Two resonances (36H each) for *tert*-butyl groups are visible at 1.55 and 1.93 ppm, as well as a signal for the aryl-C*H* at 7.92 ppm (4H). Vibrational spectroscopic data supports a U(VI) center in **1**, with a O═U═O absorption at 843 cm^{-1} for the symmetric stretch (Raman) as well as one at 937 cm^{-1} for the asymmetric stretch (infrared). These data are as expected based on other uranyl compounds.[22]

In order to provide baseline structural parameters for the $DOPO^{q}$ ligand, a single crystal of **1** was grown from slow evaporation of a concentrated toluene/THF solution (10:1) at 25 °C and analyzed by X-ray crystallography (Figure 1, bond

Scheme 2. Synthesis of DOPO Uranium Complexes

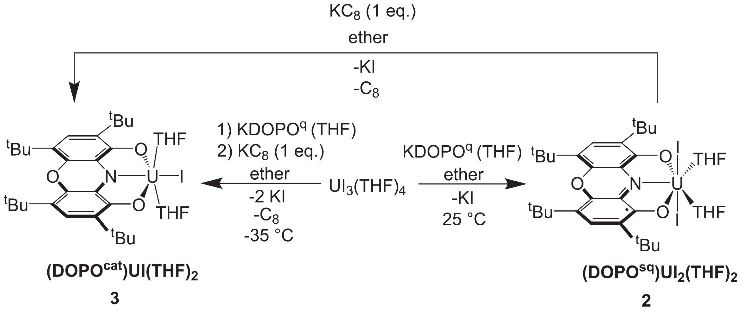

distances in Figure 3). Refinement of the data confirmed the assignment of **1**, showing a molecular structure with two DOPO^q ligands *trans* to one another in the plane perpendicular to the uranyl moiety. The solid-state structure shows a pseudohexagonal bipyramidal uranium center, with some distortions from planarity in the DOPO^q ligands. This distortion likely relieves steric strain from the *tert*-butyl groups on the *trans* DOPO^q ligand. The uranyl U−O bonds of 1.765(4) and 1.768(5) Å are as expected for other uranyl species, including the starting material, $UO_2[N(SiMe_3)_2]_2(THF)_2$.[23]

Previous work has demonstrated that uranium−ligand distances are an accurate gauge for determining the extent of ligand reduction.[24−26] As shown in Scheme 1, the oxidized form of the ligand would have one monoanionic and one dative U−O interaction, which should be delocalized. Thus, the combination of the two resonance structures would produce U−O distances between anionic and dative bonds for uranium, which is observed. The U−O distances of 2.480(4) and 2.518(4) Å (Figure 3) are longer than a typical aryloxide ligand for uranium.[27] The U−N distance of 2.676(6) Å is quite long as compared to a uranium-amide; it is more consistent with a dative uranium−nitrogen bond, as would be expected for the oxidized DOPO^q ligand.[27]

The intraligand parameters for **1** also support the idea that the DOPO ligand is in the quinone oxidation state. For instance, the C−O distances of 1.273(7) and 1.261(7) Å are elongated from C═O double bonds due to the resonance contribution. Similarly, the C−N bond lengths of 1.335(7) and 1.344(7) Å are the same within error. These parameters are on the order of those observed for Pb(DOPO^q)$_2$, which has C−O distances of 1.297(4) and 1.246(4) Å and C−N distances of 1.347(4) and 1.316(4) Å.[4] Similarly, Minkin reports values for Mn(DOPO^q)$_2$ through Zn(DOPO^q)$_2$ with C−O values that range from 1.266(2) to 1.294(5) Å and C−N distances from 1.315(1) to 1.333(5) Å.[5] These structural parameters measured for the ligands in **1** were used to determine the metrical oxidation states (MOS) as established by Brown and coworkers for the DOPO ligand, which is useful due to the sensitivity of this method for the degree of π bonding in a molecule.[4] Applying that model to **1** gave an MOS value of −1.25(19), which is consistent with other reports describing the quinone form of the ligand, including Pb(DOPO^q)$_2$ (MOS = −1.06(15)).[4] Accordingly, the assignment of a hexavalent uranyl with two monoanionic DOPO^q ligands is well supported by crystallographic and spectroscopic data.

Low-valent derivatives of the DOPO ligand were also attempted by metalation with trivalent $UI_3(THF)_4$. Previously, treating $UI_3(THF)_4$ with the related iminoquinone ligand, ^{R}iq, resulted in electron transfer from the uranium to the ligand, forming the uranium(IV) iminosemiquinone product, (^{R}isq)$UI_3(THF)_2$ (R = dipp), as confirmed by magnetometry experiments.[10] Given the similarities between the iminoquinone and the dioxophenoxazine frameworks, it is hypothesized that the analogous uranium oxidation event will occur for the dioxophenoxazine complexes as well. In this case, addition of one equivalent of blue KDOPO^q(THF) to a blue diethyl ether suspension of $UI_3(THF)_4$ at −35 °C (Scheme 2) produced an emerald green powder following workup. Analysis by ^{1}H NMR spectroscopy (Figure S3, benzene-d_6) shows a paramagnetically broadened and shifted spectrum, indicative of a C_{2v} symmetric molecule. Two resonances (18H each) for the *o*- and *p*-*tert*-butyl groups appear at −5.38 and 37.66 ppm, respectively, along with a smaller resonance (2H) shifted drastically to −248.69 ppm for the aryl−C*H* protons. This extreme upfield shift has been noted previously for uranium species bearing radical ligands,[26,28,29] leading to the assignment of the green product as (DOPO^{sq})UI_2, with a semiquinone radical ligand by analogy to (^{R}isq)$UI_3(THF)_2$.

No THF resonances were noted in the ^{1}H NMR spectrum, likely due to dissociation/association of labile THF ligands on the NMR time scale. This hypothesis was tested by addition of pyridine-d_5 to an NMR tube containing a known amount of (DOPO^{sq})UI_2 (Figure S4, benzene-d_6). Immediately, resonances for uncoordinated THF were apparent, indicating ligand substitution was operative. Quantification of the liberated THF was possible by integration against a mesitylene internal standard. This experiment established the presence of two equivalents of THF for each equivalent of (DOPO^{sq})UI_2, leading to the more accurate assignment of (DOPO^{sq})$UI_2(THF)_2$ (**2**).

Confirmation for the assignment of **2** was obtained by X-ray diffraction of a single crystal grown from slow evaporation of a concentrated pentane solution with several drops of toluene at 25 °C. Refinement revealed a pentagonal bipyramidal uranium species with two iodide ligands and two THF molecules, in addition to the DOPO ligand (Figure 1, structural parameters in Figure 3). The idealized C_{2v} symmetry of **2** in the solid state is consistent with the solution structure as determined by ^{1}H NMR spectroscopy. The U−O distances of 2.203(4) and 2.231(4) Å are significantly contracted from those in **1**, pointing toward ligand reduction as indicated by the shorter U−O distance that is *not* expected for the larger uranium(IV) center. These distances are consistent with those for uranium(IV)−aryloxide interactions.[30] Accordingly, the U−N bond distance has also decreased (2.371(4) Å), but it is still in the range for a U(IV)-amide.[26,30,31] The intraligand distances corroborate a higher degree of reduction as compared to **1**, with C−O distances (1.350(6) and 1.355(6) Å) that are elongated by ~0.1 Å, in agreement with single bond character that is expected for the iminosemiquinone resonance structure shown in Scheme 1. The corresponding C−N bonds are very similar to those in **1**, showing that they are less sensitive to ligand oxidation state changes. Accordingly, the iminosemiquinone ligand in Cr(DOPO^{q})(DOPO^{sq}) has respective C−O and C−N averages of 1.335(2) and 1.349(2) Å. Thus, the ligand in **2** is most consistent with a U(IV) center ligated by a dianionic DOPO^{sq} ligand. The calculated MOS value of −2.67(21) for the DOPO ligand in **2** suggests a higher degree of reduction in the ligand than predicted by the U−N and U−O distances. Based on the U(IV) assignment, the U−O$_{THF}$ and U−I distances are as expected compared to UI_4(1,4-dioxane)$_2$.[15]

To further corroborate the presence of the iminosemiquinone in **2**, self-consistent solid-state magnetic measurements of two independently prepared, analytically pure samples were performed (Figure 2). The room temperature moment of 2.87 μ_B was consistent with reported magnetic data for uranium(IV) complexes with ligand radicals.[25,32] It is well established that μ_{eff} decreases monotonically with temperature in the cases of U(IV) cations in low symmetry ligand fields, due to the depopulation of the nine ligand field levels for the ion.[33−35] The data for **2** showed this type of behavior, consistent with its assignment as a uranium(IV) complex (Figure 2). The low temperature effective magnetic moment of **2** was determined to be 1.81 μ_B (2 K), which was close to the expected spin-only moment predicted for a ligand based doublet (1.73 μ_B, assuming g = 2.0).[36] The U(IV) ion is also well-established to have a singlet ground state in low symmetry ligand fields.[37,38] The assignment of a magnetic singlet U(IV) ion and ligand-based doublet for **2** is consistent with the observed moment, where the low temperature contributions approach zero for the uranium(IV) cation and 1.73 μ_B for the ligand radical. Field-dependent data were measured at 2 K and achieved a limit at 0.79 μ_B at 7 T, which also supported assignment of a single ligand-based unpaired electron per molecule. An alternate interpretation of the magnetic data for **2** would be assignment of a catecholate-DOPO ligand in a trianionic, closed shell form, coordinated to a J = 5/2 uranium(V) cation: (DOPO^{cat})-U(V) as the ground state. In this scenario, the uranium would retain paramagnetism at low temperature, consistent with the low temperature and field dependent responses for **2**. However, the room temperature moment for **2** does not support (DOPO^{cat})-U(V) because the observed moment of 2.87 μ_B at 300 K is significantly larger than those typically observed for uranium(V) complexes.[38] Overall the magnetic measurements were most consistent with a configuration of **2** comprising S = 1/2 DOPO$^{sq\bullet}$ radical and a 5f^2 U(IV) singlet at low temperature: (DOPO^{sq})$^{\bullet}$-U(IV).

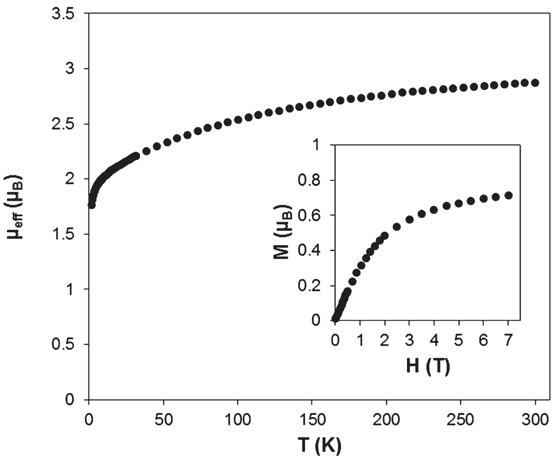

Figure 2. Variable temperature molar magnetic data for **2** collected between 300 and 2 K at 1 T. The inset is a plot of variable field data collected at 2 K.

The synthesis of a uranium species bearing the most reduced form of the ligand, DOPO^{cat}, was attempted by performing the same reaction as for the synthesis of **2** but with an equivalent of potassium graphite (KC_8), which afforded a yellow-brown powder (Scheme 2). As in the case for **2**, ^{1}H NMR spectroscopic analysis (Figure S5, benzene-d_6) showed a C_{2v} symmetric molecule with two resonances at −1.73 and 36.32 ppm for the *tert*-butyl groups on the ligand; however, in this case the C*H* protons for the DOPO aryl groups appeared at 15.99 ppm, indicating loss of radical character. With the addition of an external reductant, the product was assigned as (DOPO^{cat})UI bearing a triply reduced catecholate ligand. By charge balance considerations, a U(IV) ion is hypothesized.

No THF resonances were noted in the ^{1}H NMR spectrum for (DOPO^{cat})UI, again likely due to dissociation/association of labile THF ligands on the NMR time scale. Once again, addition of pyridine-d_5 to (DOPO^{cat})UI caused THF dissociation (Figure S6, benzene-d_6). Quantification by integration (mesitylene internal standard) showed two equivalents of THF were present for each equivalent of (DOPO^{cat})UI; thus, the more accurate assignment is as (DOPO^{cat})UI(THF)$_2$ (**3**). Compound **3** could also be generated by addition of KC_8 to **2** (Scheme 2). Unfortunately, difficulty in obtaining single crystals precluded characterization of **3** by X-ray diffraction.

To circumvent the crystallization issues for **3**, the pentamethylcyclopentadienyl analogue, Cp*U(DOPO^{cat})(THF)$_2$ (**4**), was synthesized. Addition of KDOPO^{q}(THF) to *in situ* generated Cp*UI_2(THF)$_3$,[39] followed immediately by one equivalent of KC_8, generated the desired product as a brown solid after workup (eq 2). Characterization by ^{1}H NMR spectroscopy (Figure S7, benzene-d_6) showed a C_{2v} symmetric molecule, with resonances for the *tert*-butyl protons at −20.10 and 16.52 ppm, along with a resonance at 7.20 ppm assignable to the Cp*−CH_3 protons. The aryl−C*H* resonance appeared close to this at 7.57 ppm, which is on the order of that found for **3** (15.99 ppm). This is in contrast to compound **2**, where the aryl−C*H* resonance appears at −248.69 ppm, pointing to the absence of a ligand radical in **4**.

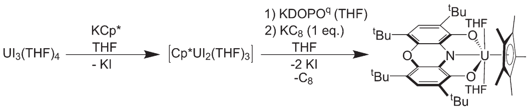

(2)

Cp*U(DOPO^{cat})(THF)$_2$
4

Brown crystals of **4** were obtained from a concentrated pentane solution at −35 °C and analyzed by X-ray crystallography. The molecular structure features a uranium

DOI: 10.1021/acs.inorgchem.5b00855
Inorg. Chem. 2015, 54, 6520−6527

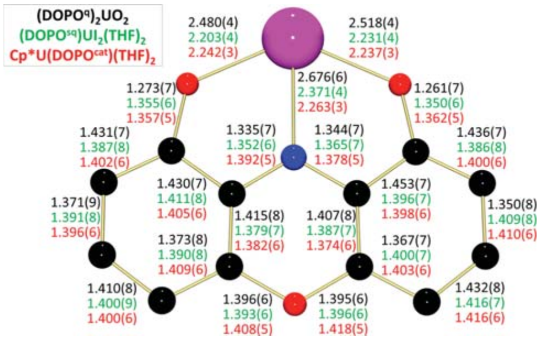

Figure 3. Bond distance comparison (Å) for (DOPO^q)$_2$UO$_2$ (**1**), (DOPO^{sq})UI$_2$(THF)$_2$ (**2**), and Cp*U(DOPO^{cat})(THF)$_2$ (**4**).

with the DOPO and Cp* ligands in a *trans* arrangement (Figure 1, structural parameters in Figure 3). Two THF molecules lie perpendicular to the DOPO ligand plane and are *trans* with respect to each other. The solid state structure shows the THF rings are bent away from the Cp* ring, presumably relieving steric interactions. The U−Cp*$_{cent}$ distance of 2.493 Å is on the order of those for other U(IV)−Cp* complexes.[26,31,40] As in the case for **2**, the U−O distances (2.237(3) and 2.242(3) Å) point to anionic uranium−oxygen bonds, as would be expected for a reduced ligand framework. Divergent from **2**, however, is the U−N distance of 2.263(3) Å, which is 0.1 Å shorter, and reflective of a uranium-amide linkage[31] resulting from a further degree of reduction. The intraligand C−O distances of 1.357(5) and 1.362(5) Å are indistinguishable from those in **2**, once again supporting a reduced ligand. However, the C−N distance of 1.392(5) Å is statistically longer than those in **2**, as would be consistent with C−N single bonds and consistent with the DOPO^{cat} resonance structure. The corresponding distances for Mo(DOPO^{cat})$_2$ and W(DOPO^{cat})$_2$, which have been established to contain trianionic catecholate ligands, have C−O average distances of 1.366(6) and 1.376(4) Å, respectively, which match well with those in **4**.[4] The average C−N distances for these transition metal analogues of 1.362(9) and 1.372(4) Å are within error of those for the uranium species, **4**. This structural support and the similar spectroscopic properties of **3** and **4** point to a trianionic DOPO^{cat} ligand in both cases. This is supported by the value obtained for **4** using the MOS model (−2.87(16)), which is on the order of those for Mo(DOPO^{cat})$_2$ (−2.83(23), −2.60(18)) and W(DOPO^{cat})$_2$ (−3.00(22), −2.80(19)).

Further confirmation for the oxidation states of complexes **1**−**4** was gathered using electronic absorption spectroscopy (Figure 4). Data in the UV−visible regions for the DOPO uranium series and KDOPO^q(THF) showed intense absorptions throughout the UV region, as has been noted previously.[3,4] Striking differences are found in the visible region, which shows an absorption for KDOPO^q(THF) at 735 nm with a high molar absorptivity (9,750 cm^{-1} M^{-1}) similar to what was observed for the corresponding sodium salt (λ_{max} = 695 nm).[3] For the uranium complexes, **1** shows a strong π−π* absorption at 719 nm with a high molar absorptivity (14,400 cm^{-1} M^{-1}). This large absorbance is characteristic of a transition into an empty DOPO^q -based π* orbital. For compound **2**, there is a much weaker (ε = 874 cm^{-1} M^{-1}) π−π* absorption noted at 704 nm, assigned as a transition into the half-filled π* orbital of DOPO^{sq}. In the case of this uranium semiquinone species, the molar absorptivity is significantly lower than that reported for transition metal and main group semiquinone complexes.[7,41] However, the previously established trend for these complexes shows a larger molar absorptivity for the quinone ligands and a lower molar absorptivity for the semiquinone form. While our absolute value for **2** is different than those for transition metal and main group examples, the data still follows this general trend. These bands are absent in complexes **3** and **4**, confirming the closed shell DOPO^{cat} ligand with a filled π* orbital. Data obtained in the NIR region for **2**−**4** show sharp but weak f−f transitions consistent with U(IV), f^2 centers (Figure 4). For **1**, no peaks

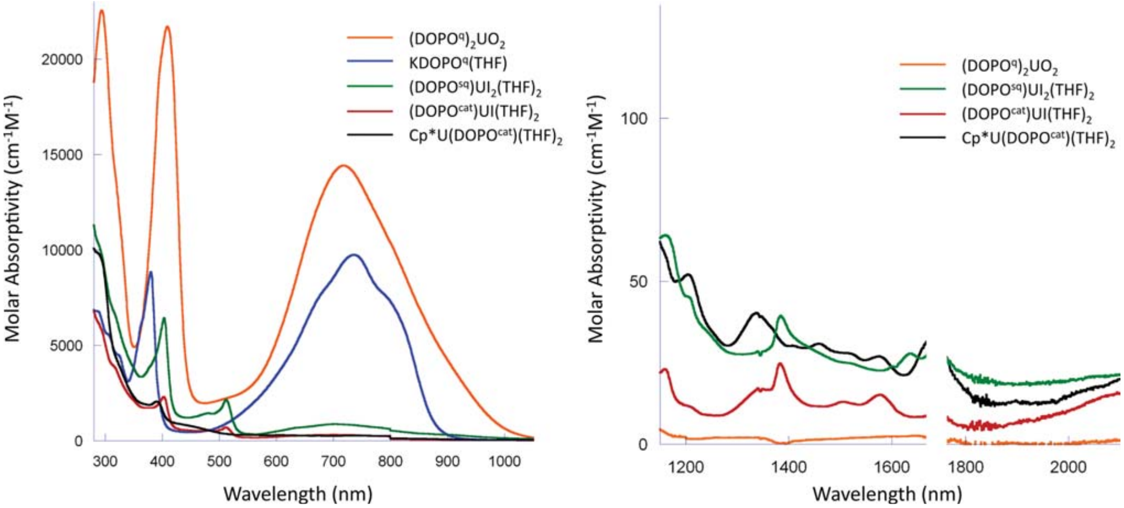

Figure 4. Electronic absorption spectra in the UV/visible region (left) and NIR region (right) for the DOPO series collected as solutions in THF at ambient temperature.

are noted in the NIR region, indicating the absence of f–f transitions, which would be expected for a U(VI), f^0 center.

CONCLUSIONS

A series of dioxophenoxazine uranium complexes, $(DOPO^{q})_2UO_2$, $(DOPO^{sq})UI_2(THF)_2$, $(DOPO^{cat})UI(THF)_2$, and $Cp^*U(DOPO^{cat})(THF)_2$, have been synthesized in high yield and characterized. Data obtained using ^1H NMR spectroscopy, electronic absorption spectroscopy, X-ray crystallography, and SQUID magnetometry suggest that **1** contains two monoanionic $DOPO^{q}$ ligands at a U(VI) center, while **2** has a dianionic $DOPO^{sq}$ chelate and a U(IV) center. Both **3** and **4** feature a trianionic $DOPO^{cat}$ framework, also ligated to a U(IV) center. Ligand oxidation states were also established by using the intraligand bond distances as determined by X-ray crystallography to calculate the Metrical Oxidation State (MOS) of each ligand.[4] These calculations supported, within error, the assignments of the ligand oxidation states based on experimental data as compared to previously established examples with transition metals.[4,5] Near-infrared absorption data support that the uranium center is tetravalent for **2**–**4** and maintains its +6 oxidation state for **1**. The dioxophenoxazine uranium species described here are exciting new additions to the collection of known uranium species bearing redox active ligands, as the oxygen donor atoms make the DOPO ligand a strong chelator for the oxophilic uranium center. Future studies will be aimed at the utility of these complexes for multielectron transformations.

ASSOCIATED CONTENT

Ⓢ Supporting Information

^1H NMR spectroscopic data, X-ray crystallographic experimental details, and cif data. The Supporting Information is available free of charge on the ACS Publications website at DOI: 10.1021/acs.inorgchem.5b00855.

AUTHOR INFORMATION

Corresponding Author

*E-mail: sbart@purdue.edu.

Notes

The authors declare no competing financial interest.

ACKNOWLEDGMENTS

The authors gratefully acknowledge funding from the Division of Chemical Sciences, Geosciences, and Biosciences, Office of Basic Energy Sciences of the U.S. Department of Energy through Grants DE-AC02-12ER16328 (S.C.B.) and DE-SC0006518 (E.J.S.).

REFERENCES

(1) Stang, S.; Lebkuecher, A.; Walter, P.; Kaifer, E.; Himmel, H.-J. *Eur. J. Inorg. Chem.* **2012**, *2012*, 4833–4845.

(2) Guerro, M.; Pham, N. H.; Massue, J.; Bellec, N.; Lorcy, D. *Tetrahedron* **2008**, *64*, 5285–5290.

(3) Olekhnovich, L. P.; Lyubchenko, S. N.; Simakov, V. I.; Shif, A. I.; Kurbatov, S. V.; Lesin, A. V.; Borodkin, G. S.; Ivakhnenko, E. P.; Zhdanov, Y. A. *Dokl. Akad. Nauk* **1999**, *369*, 632–638.

(4) Ranis, L. G.; Werellapatha, K.; Pietrini, N. J.; Bunker, B. A.; Brown, S. N. *Inorg. Chem.* **2014**, *53*, 10203–10216.

(5) Ivakhnenko, E. P.; Starikov, A. G.; Minkin, V. I.; Lyssenko, K. A.; Antipin, M. Y.; Simakov, V. I.; Korobov, M. S.; Borodkin, G. S.; Knyazev, P. A. *Inorg. Chem.* **2011**, *50*, 7022–7032.

(6) Hananouchi, S.; Krull, B. T.; Ziller, J. W.; Furche, F.; Heyduk, A. F. *Dalton Trans.* **2014**, *43*, 17991–18000.

(7) Szigethy, G.; Shaffer, D. W.; Heyduk, A. F. *Inorg. Chem.* **2012**, *51*, 12606–12618.

(8) Wong, J. L.; Sanchez, R. H.; Logan, J. G.; Zarkesh, R. A.; Ziller, J. W.; Heyduk, A. F. *Chem. Sci.* **2013**, *4*, 1906–1910.

(9) Matson, E. M.; Opperwall, S. R.; Fanwick, P. E.; Bart, S. C. *Inorg. Chem.* **2013**, *52*, 7295–7304.

(10) Matson, E. M.; Franke, S. M.; Anderson, N. H.; Cook, T. D.; Fanwick, P. E.; Bart, S. C. *Organometallics* **2014**, *33*, 1964–1971.

(11) Pangborn, A. B.; Giardello, M. A.; Grubbs, R. H.; Rosen, R. K.; Timmers, F. J. *Organometallics* **1996**, *15*, 1518–1520.

(12) Andersen, R. A. *Inorg. Chem.* **1979**, *18*, 209–209.

(13) Schlosser, M.; Hartmann, J. *Angew. Chem., Int. Ed.* **1973**, *12*, 508–509.

(14) Tonzetich, Z. J.; Eisenberg, R. *Inorg. Chim. Acta* **2003**, *345*, 340–344.

(15) Monreal, M. J.; Thomson, R. K.; Cantat, T.; Travia, N. E.; Scott, B. L.; Kiplinger, J. L. *Organometallics* **2011**, *30*, 2031–2038.

(16) Clark, D. L.; Sattelberger, A. P. *Inorg. Synth.* **1997**, *31*, 307–315.

(17) Chakraborty, S.; Chattopadhyay, J.; Guo, W.; Billups, W. E. *Angew. Chem., Int. Ed.* **2007**, *46*, 4486–4488.

(18) Sheldrick, G. M. *Acta Crystallogr.* **2008**, *112*, A64.

(19) Burla, M. C.; Caliandro, R.; Camalli, M.; Carrozzini, B.; Cascarano, G. L.; De Caro, L.; Giacovazzo, C.; Polidori, G.; Spagna, R. *J. Appl. Cryst.* **2005**, *38*, 381–388.

(20) Sheldrick, G. M. *Beta program*.

(21) Bain, G. A.; Berry, J. F. *J. Chem. Educ.* **2008**, *85*, 532.

(22) Berthet, J.-C.; Siffredi, G.; Thuery, P.; Ephritikhine, M. *Chem. Commun.* **2006**, 3184–3186.

(23) Arnold, P. L.; Patel, D.; Blake, A. J.; Wilson, C.; Love, J. B. *J. Am. Chem. Soc.* **2006**, *128*, 9610–9611.

(24) Cladis, D. P.; Kiernicki, J. J.; Fanwick, P. E.; Bart, S. C. *Chem. Commun.* **2013**, *49*, 4169–4171.

(25) Anderson, N. H.; Odoh, S. O.; Yao, Y.; Williams, U. J.; Schaefer, B. A.; Kiernicki, J. J.; Lewis, A. J.; Goshert, M. D.; Fanwick, P. E.; Schelter, E. J.; Walensky, J. R.; Gagliardi, L.; Bart, S. C. *Nat. Chem.* **2014**, *6*, 919–926.

(26) Kiernicki, J. J.; Newell, B. S.; Matson, E. M.; Anderson, N. H.; Fanwick, P. E.; Shores, M. P.; Bart, S. C. *Inorg. Chem.* **2014**, *53*, 3730–3741.

(27) Castro-Rodriguez, I.; Meyer, K. *Chem. Commun.* **2006**, 1353–1368.

(28) Kraft, S. J.; Fanwick, P. E.; Bart, S. C. *Inorg. Chem.* **2010**, *49*, 1103–1110.

(29) Zi, G.; Jia, L.; Werkema, E. L.; Walter, M. D.; Gottfriedsen, J. P.; Andersen, R. A. *Organometallics* **2005**, *24*, 4251–4264.

(30) Meyer, K.; Bart, S. C. *Adv. Inorg. Chem.* **2008**, *60*, 1–30.

(31) Graves, C. R.; Schelter, E. J.; Cantat, T.; Scott, B. L.; Kiplinger, J. L. *Organometallics* **2008**, *27*, 5371–5378.

(32) Anderson, N. H.; Odoh, S. O.; Williams, U. J.; Lewis, A. J.; Wagner, G. L.; Lezama Pacheco, J.; Kozimor, S. A.; Gagliardi, L.; Schelter, E. J.; Bart, S. C. *J. Am. Chem. Soc.* **2015**, *137*, 4690–4700.

(33) Castro-Rodriguez, I.; Olsen, K.; Gantzel, P.; Meyer, K. *J. Am. Chem. Soc.* **2003**, *125*, 4565–4571.

(34) Lewis, A. J.; Williams, U. J.; Kikkawa, J. M.; Carroll, P. J.; Schelter, E. J. *Inorg. Chem.* **2012**, *51*, 37–39.

(35) Lewis, A. J.; Williams, U. J.; Carroll, P. J.; Schelter, E. J. *Inorg. Chem.* **2013**, *52*, 7326–7328.

(36) Castro-Rodriguez, I.; Nakai, H.; Zakharov, L. N.; Rheingold, A. L.; Meyer, K. *Science* **2004**, *305*, 1757–1760.

(37) Boudreaux, E. A.; Mulay, L. N. *Theory and Applications of Molecular Paramagnetism*; Wiley: New York, 1976; p 510.

(38) Kindra, D. R.; Evans, W. J. *Chem. Rev.* **2014**, *114*, 8865–8882.

(39) Avens, L. R.; Burns, C. J.; Butcher, R. J.; Clark, D. L.; Gordon, J. C.; Schake, A. R.; Scott, B. L.; Watkin, J. G.; Zwick, B. D. *Organometallics* **2000**, *19*, 451–457.

(40) Kiernicki, J. J.; Fanwick, P. E.; Bart, S. C. *Chem. Commun.* **2014**, *50*, 8189–8192.

(41) Szigethy, G.; Heyduk, A. F. *Dalton Trans.* **2012**, *41*, 8144−8152.